WAVELET ANALYSIS STUDY OF MICROBUBBLE DRAG REDUCTION IN A BOUNDARY CHANNEL FLOW

A Thesis

by

LING ZHEN

Submitted to the Office of Graduate Studies of
Texas A&M University
in partial fulfillment of the requirements for the degree of

MASTER OF SCIENCE

December 2004

Major Subject: Nuclear Engineering

WAVELET ANALYSIS STUDY OF MICROBUBBLE DRAG REDUCTION IN A BOUNDARY CHANNEL FLOW

A Thesis

by

LING ZHEN

Submitted to Texas A&M University
in partial fulfillment of the requirements
for the degree of

MASTER OF SCIENCE

Approved as to style and content by:

Yassin A. Hassan (Chair of Committee)	Kalyan Annamalai (Member)
William H. Marlow (Member)	William E. Burchill (Head of Department)

December 2004

Major Subject: Nuclear Engineering

ABSTRACT

Wavelet Analysis Study of Microbubble Drag Reduction

in a Boundary Channel Flow. (December 2004)

Ling Zhen, B.S., Zhejiang University, China;

M.S., Zhejiang University, China

Chair of Advisory Committee: Dr. Yassin A. Hassan

Particle Image Velocimetry (PIV) and pressure measurement techniques were performed to investigate the drag reduction due to microbubble injection in the boundary layer of a fully developed turbulent channel flow. Two-dimensional full-field velocity components in streamwise-near-wall normal plane of a turbulent channel flow at Reynolds number of 5128 based on the half height of the channel were measured. The influence of the presence of microbubbles in the boundary layer was assessed and compared with single phase channel flow characteristics. A drag reduction of 38.4% was achieved with void fraction of 4.9%.

The measurements were analyzed by studying the turbulence characteristics utilizing wavelet techniques. The wavelet cross-correlation and auto-correlation maps with and without microbubbles were studied and compared. The two-dimensional and three-dimensional wavelet maps were used to interpret the results.

The following observations were deduced from this study:

1. The microbubble injection within the boundary layer increases the turbulent energy of the streamwise velocity components of the large scale (large eddy size, low frequency) range and decreases the energy of the small scale (small eddy size, high frequency) range.

2. The wavelet cross-correlation maps of the normal velocities indicate that the microbubble presence decrease the turbulent energy of normal velocity components for both the large scale (large eddy size, low frequency) and the small scale (small eddy size, high frequency) ranges.

3. The wavelet auto-correlation maps of streamwise velocity shows that the intensities at low frequency range were increased with microbubble presence and the intensities at high frequency range were decreased.

4. The turbulent intensities for the normal fluctuating velocities at both low frequency and high frequency range were decreased with microbubble injection.

This study presents the modifications in the characteristics of the boundary layer of channel flow which are attributed to the presence of microbubbles. Drag reduction studies with microbubble injections utilizing wavelet techniques are promising and are needed to understand the drag reduction phenomena.

ACKNOWLEDGMENTS

This thesis would not have been possible without the encouragement I received from my academic advisor, committee Chair, Dr. Yassin A. Hassan. From the proposal of this topic to later queries on focus and connection, he was always eager to entertain my ideas and help me solve conceptual difficulties. I appreciate his consistent efforts and true desire to keep me on track. I would also like to thank Dr. Kalyan Annamalai and Dr. William H. Marlow as my committee members.

Also, thanks to my friends and co-workers, Claudia del Carmen Gutierrez Toores, Jose Alfredo Jimenez Bernal, Elvis E. Dominguez Ontiveros and Carlos E. Estrada Perez.

Special thanks to my mother and my father for their love and motivation during my whole life. Thanks to my mother-in-law for her love.

And last but not least, thanks to my husband for encouraging me to seek a demanding and meaningful education. This study could not have taken place without that precious gift from my husband.

Thanks to the Nuclear Engineering Department of Texas A&M University for its support during my studies.

NOMENCLATURE

d	Diameter of microbubbles
ΔP	Differential pressure
DR	Drag reduction
g	Acceleration due to gravity
h	Half height of the channel
k_1	Wavenumber in the streamwise direction
k_2	Wavenumber in the normal direction
l	Wall layer thickness or viscous length scale
N	Total number of samples
P	Pressure field
Q_a	Volume flow rate of air
Q_w	Volume flow rate of water
Re	Reynolds number
$R(x, x)$	Auto correlation of signal x
$R(x, y)$	Cross correlation of signal x and y
$R_{i,j}(\Delta r)$	Cross correlation coefficient between two-point signal
$R_{i,j}(\Delta t)$	Auto correlation coefficient of one point signal
s	Riblet space
s^+	Riblet space in wall units
t_τ	Viscous time scale

T_τ	Integral time scale
u	Streamwise velocity
u’	Streamwise fluctuating velocity
u_{rms}	Turbulent intensity of the streamwise component
U_b	Bulk velocity
$\bar{u}_i$	Mean velocity
v	Normal velocity
v’	Normal fluctuating velocity
v_{rms}	Turbulent intensity of the normal velocity
w	Spanwise velocity
x	Distance in streamwise direction
y	Distance in normal direction
z	Distance in spanwise direction
x^+	Dimensionless distance in streamwise direction
y^+	Dimensionless distance in normal direction
z^+	Dimensionless distance in spanwise direction
$E_{ij}(k_1)$	One dimensional spectra in the streamwise wavenumber direction
$E_{ij}(k_2)$	One dimensional spectra in the normal wavenumber direction
$E_{ij}(k_1,k_2)$	Two dimensional spectra in the streamwise and normal wavenumber direction

$-\rho\overline{u'v'}$	Reynolds stresses
u_τ	Friction velocity
Greek letter	
ω	Vorticity
μ	Water viscosity
ν	Water kinematics viscosity
ρ	Water density
τ	Shear stress
η	Kolmogorov length scale
τ_w	Shear stress at the wall
Superscript	
$\sim$	Instantaneous
-	Average or mean

TABLE OF CONTENTS

Page

CHAPTER

Page

LIST OF FIGURES

Page

Page

Page

Page

Page

Page

Page

Page

Page

Page

Page

Page

Page

Page

LIST OF TABLES

Page

CHAPTER I

INTRODUCTION

1.1 Background

According to Wood (2003), existing data indicates that up to 25% of the total energy consumed in the United States is used to overcome aerodynamic drag, 27% of the total energy used in the United States is consumed by transportation systems, and 60% of the transportation energy or 16% of the total energy consumed in the United States is used to overcome aerodynamic drag in transportation systems. This energy consuming correlates to a yearly cost savings in the 30 Billion dollar range. To save energy in engineering applications such as hydraulic machines, aircraft, pumping systems, automobiles, slurry pipeline systems, oil pipeline transport, oil well operations, marine applications etc, drag reduction technologies need to be investigated and developed. The benefits of obtaining a decrease in drag can have environmental and economic impacts. Actually, drag reduction by use of additives such as polymers and microbubbles have already obtained great success in the laboratory and some industries. A similar application is the addition of polymers to oil being pumped from offshore platforms to shore facilities (Beaty *et al*., 1984).

This dissertation follows the style and format of the *Journal of Fluid Mechanics.*

Also, in sewerage pipes and storm-water drains polymers have been used to increase the flow rates so that the peak loads do not result in over flowing and this can be much cheaper than constructing new pipes (Sellin 1988).

And there is even a possible medical application: the addition of low concentrations of polymers might be capable of improving blood flow without altering flow through normal vessels, as is suggested by a study by Unthank *et al*., (1992). Though the drag reduction effect is extremely interesting from a practical point of view, it is still not ready to practice on shipboard systems. Transition from the laboratory to full-scale has been severely limited because the physical mechanisms underlying additive-based drag reduction are still poorly understood.

1.2 Turbulence

A drag force has two components. One is the drag that is directly related to the wall shear stress, which means the skin friction drag. The other one is pressure drag associated with the normal stresses or pressure variation over the surface. Most of the industries systems have very large Reynolds numbers and are in turbulent flow conditions where skin friction is very large. Hence, to implement drag reduction schemes at full-scale in industry, the dynamics of the turbulence must be understood.

As an old but challenging topic, turbulence has attracted the attention of the world's greatest scientists over the last hundred years, and yet our understanding is far from complete. According to Tsinober, 2001, turbulence is a fluctuating and chaotic state of

fluid motion when non-linear inertial effects dominate over viscous effects. Turbulence has irregular fluctuation of velocity in all three directions. A time history of the velocity at a point looks like a random signal. Nevertheless, there is structure to the fluctuations, so it is not absolutely accurate to say that the fluctuations are random. The irregularities in the velocity field have certain spatial structures known as eddies. An eddy may be like a vortex, an imbedded jet, a mushroom shape, or any other recognizable form. Small eddies exist inside larger eddies, and even smaller eddies exist inside the small eddies. The turbulence is also self-sustaining, once a flow becomes unstable and turbulence develops. Turbulence, once initiated, continues and perpetuates itself without diminishing. A gradient in the mean velocity profile exists as the mean shear for the turbulence to be self-sustaining. The rigorous way to decide whether fluid is turbulent or nonturbulent is based on vorticity. Turbulent flow also involves processes that change the length scale of the eddies. Turbulent eddies are continually formed with smaller and smaller length scales. There is also a limit to this process. When the spatial extent of an eddy becomes very small, viscous forces, because of the steep velocity gradient, become very important. They tend to destroy the smallest eddies, and hence viscosity puts a lower limit on the eddy size. Any flow with viscosity has viscous dissipation, but turbulent flows have much more of it because the small-scale eddies have sharp velocity gradients. The energy dissipated in the small-scale eddies dominates that dissipated in the largest eddies and in the mean flow. Since the small eddies dissipate energy and tend to destroy themselves, the scale-changing process that produces smaller eddies is a necessary element of self-sustaining turbulence.

It has already been discovered that turbulence production and self-sustainment in a boundary layer are organized phenomena and it could be discovered by using visualization techniques. These are generally called “coherent structures". It is assumed that the coherent structures, evolving in time and in space, play an important role in the dynamics of turbulence. However, it is quite difficult to determine the properties of the coherent structures with traditional measurement techniques. In the past decade there have been some developments in turbulence research that hold some promise for the future. One of these is Particle Image Velocimetry (PIV), which is an optical technique that opens the possibility to study the coherent structures quantitatively (see Adrian 1991, Hassan 1992). Another important technique is Direct Numerical Simulation (DNS). It is based on solving the governing equations that describe the spatial and temporal evolutions of flows numerically. However, to solve the Navier-Stokes equation numerically, the size of grid mesh and time increment of solution must be carefully considered. The calculations would have to be made on the grid at a frequency greater than the frequency of the passage of a small eddy by a fixed position. Considering the number of the grid points and the time dependent nature of the solution, the number of arithmetic operations is immense and impractical for any normal computer. For the additives drag reduction analysis, DNS will become more impractical since a lot of assumptions have to be made for the size, distribution of the polymers or microbubbles.

1.3 Review of drag reduction research

Wall turbulence physics fundamental advances and drag reduction methodologies need to be coupled to solve the challenges of full scale drag reduction. Many techniques have been approved numerically and experimentally to pursue drag reduction. Some hypotheses have been made to elucidate the mechanics of the drag reduction. However, there is no consensus between them. Further experiments and analysis still need to be continued. An extensive review on different techniques has been carried out in order to better understanding the mechanism of drag reduction effect happened on the boundary layer. Turbulent drag reduction methods-including polymer, microbubbles, riblets on the wall and biology based methods are discussed as follows.

1.3.1 Drag reduction by polymer

In 1946, Toms (1977) conducted one of the most famous experiments for drag reduction by addition of polymers. The flow was kept the same pressure at inlet and outlet which were glass aspirator jars and the fluid was moved from one jar to the other. Both jars were submersed in a water tank to maintain the same constant temperature (25^{o} C). The time required for one liter of solution to pass through the tube under a known pressure (showed by a mercury U-tube manometer) was measured. It was found that the flow rate was increased in the condition that polymer solution was offered.

From then on, there was a substantial research on this drag reduction phenomenon, including theoretical, experimental and numerical approaches in different countries and in thousands of institutions. Research of the effect of polymer additives on turbulent drag is described leading to a number of significant findings and possible explanation of the mechanism of drag reduction. Tests of the turbulence characteristics in the boundary layer with and without the polymer injection was conducted.

The two most important findings from experimental studies by Virk (1975) were the onset of drag reduction and the existence of maximum drag reduction (MDR). De Gennes (1990) suggested that drag reduction does not come from a purely viscous effect of the dilute polymer solution. Experiments showed that the drag reduction had a threshold regardless of the amount of polymer concentration. So the viscosity could not be a dominant parameter for drag reduction.

Among the studies for drag reduction by laser Doppler velocimetry (LDV) measurement were for example the contributions of Pinho & Whitelaw (1990), Harder & Tiederman (1991) and Wei & Willmarth (1992). Pinho & Whitelaw (1990) measured all three velocity components in a pipe flow, while the other two studies used a two-dimensional LDV system in a channel flow. Wei & Willmarth (1992) gave special attention to the power spectra. One of the most striking results found in these papers, and also in the majority of other studies reported in the literature, was that polymer additives do not simply suppress the turbulent motion. On the contrary, the streamwise turbulence intensity is increased, while the normal turbulence intensity is decreased. This means that the turbulence structure was changed, rather than attenuated. Wei & Willmarth

(1992) found that the energy in the normal velocity component was dramatically suppressed over all frequencies, while there is a redistribution of energy from high frequencies to low frequencies for the streamwise component.

Den Toonder *et al*., (1997) studied the roles of stress anisotropy and of elasticity in the mechanism of drag reduction by polymer additives in numerical and laboratory experiments. In their DNS two different models were used to describe the effects of polymers on the flow. The first was a constitutive equation based on Batchelor's theory of elongated particles suspended in a Newtonian solvent which models the viscous anisotropic effects caused by the polymer orientation. The second was an extension of the first model with an elastic component, and can be interpreted as an anisotropic Maxwell model. The LDV experiments had been carried out in a reticulating pipe flow facility by using of a solution of water and 20 w.p.p.m Superfloc A110. Turbulence statistics up to the fourth moment, as well as power spectra of various velocity components, were measured. The results of the numerical simulation and of the measurements were compared in order to elucidate the role of polymers in the phenomenon of drag reduction. For the case of the viscous anisotropic polymer model, almost all turbulence statistics and power spectra calculated agreed in a qualitative sense with the measurements. The addition of elastic effects, on the other hand, had an adverse effect on the drag reduction, i.e. the viscoelastic polymer model showed less drag reduction than the anisotropic model without elasticity. Moreover, for the case of the viscoelastic model not all turbulence statistics showed the right behavior. On the basis of

these results, they proposed that the viscous anisotropic stresses introduced by extended polymers played a key role in the mechanism of drag reduction by polymer additives.

By using LDV system and pressure measurement, Warholic *et al*., (1999) investigated on experiments for drag reduction of 14, 19, 27, 33, 64 and 69% by addition of Percol 727 (Copolymer of polyacylamide and sodium acrilate). It was conducted on a channel with a length of 1100 cm, a height of 5.1 cm, and 61 cm wide, and several polymer concentration (from 5 to 200 ppm) were used. A Validyne pressure transducer (DP103) was used to evaluate the pressure drop (Δp) with polymer and without polymer over a distance (Δx) of 154 cm. In 2001, Warholic used Particle image Velocimetry to study the effect of drag-reducing polymers on the structure of turbulence in a channel flow. The polymer choose at this time was Percol 727. The PIV system was composed of a pulsed ruby-laser with energy of 1 J/pulse, and time difference between pulses of 4 ms, and a CCD camera with a resolution of 256 x 256 pixels. Because of the non-intrusive and 2-dimension characteristic of PIV, this time the measurements could be carried on in the x-y plane and in the x-z plane. In both LDV (Warholic *et al*., 1999) and PIV (Warholic *et al*., 2001), it was found that the root-mean square of the streamwise velocity fluctuation, u_{rms}, made dimensionless with the friction velocity increased and was displaced outward with increasing drag reduction. The root-mean square of the normal velocity fluctuation v_{rms}, decreased systematically with increasing drag reduction for $y^+ <100$. Furthermore, Reynolds stress made dimensionless by τ_w, show a decrease when the drag reduction increases. Frequency spectra for different cases were also given. The addition of polymer was seen to decrease drastically the contribution of high

frequency fluctuations to the turbulence. Furthermore, by using PIV, a notable difference between turbulence structures of Newtonian fluids and of polymer solutions with high drag reduction is the reduction of small scale fluctuations and this 2-dimensional visual comparison could not be given by the tradition 1-dimensional measurement. The small scale fluctuation reduction effect was also evidenced by the spectral functions vs. wave numbers. The result from PIV measurement showed a damping effect for the turbulence activity near the wall which means a decrease of bursts event happened due to the injected polymers. Suppression of small scale eddies and shift of the turbulence spectrum towards the larger eddy sized were observed.

The structure of turbulence in a drag-reduced flat-plate boundary layer flow has also been studied with particle image velocimetry (PIV) by White *et al.*, (2003). Drag reduction was achieved by injection of a concentrated polymer solution through a spanwise slot along the test wall at a location upstream of the PIV measurement station. Planes of velocity were measured parallel to the wall (x–z plane), for a total of 30 planes across the thickness of the boundary layer. For increasing drag reduction, it was found a significant modification of the near-wall structure of turbulence with a coarsening of the low-speed velocity streaks and a reduction in the number and strength of near-wall vortical structures.

Min (2003) carried out a DNS simulation using an Oldroyd-B model for the linear elastic behavior of the polymer solution. Simulations were carried out by changing the Weissenberg number at the Reynolds numbers of 4000 and 20000 based on the bulk velocity and channel height. The onset criterion for drag reduction predicted in this study

showed a good agreement with previous theoretical and experimental studies. In addition, the flow statistics such as the r.m.s value of velocity fluctuations were also in good agreement with previous experimental observations. The onset mechanism of drag reduction was interpreted based on elastic theory, which was one of the most plausible hypotheses suggested in the past. It was observed that the polymer stores the elastic energy from the flow very near the wall and then releases it there when the relaxation time was short, showing no drag reduction. However, when the relaxation time was long enough, the elastic energy stored in the very near-wall region was transported to and released in the buffer and log layers, showing a significant amount of drag reduction.

1.3.2 Drag reduction by injection of microbubbles

In the US, the first study on drag reduction by injection of bubbles was conducted by Mccormick & Bhattacharyya (1973). In their experiment, hydrogen bubbles were produced by driving an electrical current through a wrapped wire (0.6 cm in diameter). A fully submersed axisymetric body of revolution (SABR) with 91.44 cm in length and 12.7 cm in maximum diameter was used. The total drag force was measured by a dynamometer. The bubbles were injected beneath the boundary layer, and a maximum total drag reduction of approximately 30 % was measured. The author attributed the drag reduction to the decrease of the viscosity near the wall, which could also stop transmission of the small viscous shear stresses from the turbulent region of the boundary layer to the wall. As the bubbles distributed from the surface to the outer

regions of the boundary layer, it was proposed that micro bubbles reduced the Reynolds stresses by absorbing the momentum by their elasticity.

Madavan *et al*., (1984) used Laser Dopler anemometer (LDA) technique to measure velocity profiles in drag reduction conditions. Experiments were carried out at the top and bottom of a rectangular test section with a length of 76.2 cm and a cross section of 50.8 cm x 11.4 cm of a water channel. Microbubbles were injected in the boundary layer by driving air into a sintered stainless steel plate. A floating element force balance was used for the integrated skin friction evaluation, and a flush mounted hot film probe was used to measure the local skin friction. The maximum integrated skin friction reduction was more than 80%. It showed that the differences of the velocity and turbulent intensities with and without bubbles were small outside the boundary layer. Spectra results showed a shifting effect of the turbulent energy toward lower frequencies in bubbles injected conditions.

Madavan *et al*., (1985) investigated a numerical study in microbubble drag reduction. The mixing length model was used. The viscosity and density were locally changed as a function of a trapezoidal concentration profile. The results obtained indicated that the skin friction depends on not only the concentration of the bubbles, but also in their location, and distribution in the boundary layer. Bubbles were most efficacious when they are located in the buffer layer.

Kato *et al*., (1994) conducted frictional drag reduction experiments by injecting bubbly water into turbulent boundary layer. The tunnel had 120 mm x 50 mm in cross section. A circular rod of 5 mm diameter was set on the tunnel wall 115 mm upstream of

the test section and it acted as a turbulence stimulator. LDV was used to measure the velocity. The shear stress was measured using five shear-stress sensors on the flat wall of the test sections. The results showed that the position of the microbubbles within the boundary layer had a determinant role in the drag reduction phenomenon.

Fontaine *et al*., (1999) injected micro bubbles with homogeneous solution of surfactant or drag reduction polymers for drag reduction experiment. It was performed on an axisymmetric body with a length of 63.2 cm and a diameter of 8.9 cm. A wire with a diameter of 0.035 was located at 4.6 cm from the leading edge of the body to assure fully developed flow in test section. It was observed that reduction of drag for a combination of polymer and microbubbles is greater than that obtained by polymer and microbubbles lonely. A drag reduction higher than 80 % was measured with a polymer concentration of 20 ppm and 10 m^3/s of gas. It was proposed that polymers modify the turbulence close to the wall in such way that the effectiveness of the microbubbles is increased.

Kodama *et al*., (2000) performed microbubble experiments in a water tunnel. The test section has 100 mm width, 15 mm height and 3000 mm length. Microbubbles were generated in an air injection chamber by injecting air through a porous plate. It was found that the local void fraction is an important factor for the drag reduction. It was also indicated that the interaction between the bubbles and the wall turbulence near the wall contributes to the reduction of turbulent energy. The drag reduction effect was attributed to the prevention of the formation of the sheet-like structure of the spanwise vorticity near the wall due to the bubbles' presence. The streamwise vorticity was weakened,

depressing the bursting phenomenon. The low-speed streaks of the spanwise vorticity was found to be disappeared in the drag reduction condition.

Kitagawa *et al*., (2003) investigated the turbulence structure of flow field with microbubbles injected. Both particle tracking velocimetry and Laser Induced Fluorescence (PTV/LIF) technique were used. The channel had 15 mm in height, 100mm in width and 3000 mm in length. Air bubbles were injected through an array of holes installed at the upper wall. The turbulence intensity was found to be increased and the Reynolds stress was decreased with the increasing of void fraction.

1.3.3 Drag reduction by riblets

In addition to Polymers, Bubbles injections, riblets are also used for turbulent drag reduction. This technique has already been studied for more than two decades by different institutions. The most significant parameters to describe a riblet are spacing riblet (s), height of the riblet (h), and the spacing of the riblet in wall units, which is shown in the equation (1), where u_τ is the friction velocity and ν is the kinematic viscosity of the fluid.

$$s^+ = \frac{s u_\tau}{\nu} \qquad (1)$$

The same method to define the dimensionless normal distance y+= yuτ/ν.

Baron & Quadrio (1993) performed some experiments using V riblets in a wind tunnel with a length of 170 cm, width of 30 cm, and a height of 9.3 cm. The test section

was located at 65 cm downstream of the leading edge of the lower wall of the tunnel. Smooth and V shape riblets were flushed to the wall. The velocity field was measured by a hot wire anemometer. The best performance of the riblets was achieved at $s^+ = 12$ for a skin friction coefficient of 6 percent.

The turbulent intensity with riblets is lower than without them and the maximum value is achieved about $y^+ \approx 10$. Using hot wire anemometer, Choi & Orchard (1997) performed another similar experiment in the lower wall of a flat plate with V-riblets mounted the surrounding flat plate. Riblets with an s/h =1 and s = 0.183 cm was tested using a free stream velocity of 250 cm/s. It was founded again that nearly 6 % of drag reduction achieved. The turbulent intensity profile for the riblets case is lower than without them, and the maximum value was reported for $y^+ = yu_\tau/\nu = 13$ (where y is the distance from the wall). Turbulent energy of the spectra with riblets was found to be reduced compared to the energy spectra without riblets. Using Laser Doppler Velocimetry (LDV), Wang *et al*., (2000) performed experiments of V type riblets. The maximum value was reported around $y^+ = 10.9$.

Experiments with semicircular riblets were carried out in a closed type subsonic wind tunnel by Lee & Lee (2001). A sharp flat plate with a length of 620 cm was installed in the test section of a wind tunnel. Roughness elements were situated at 50 cm downstream the leading edge of the flat plate to get a fully developed flow at the measurement station, which is located at 541 cm downstream the leading edge. The measurements are performed in two exchangeable plates with 30 cm wide and 60 cm long, one of them is smooth and the other has riblets, which was aligned to the flat plate

by using the virtual origin of the riblets. They have semicircular grooves with an s = 0.3 cm. Instantaneous velocity fields in y-z plane (vertical plane) with an area of 6.75 x 6.75 mm^2 were obtained by Particle Image (PIV) measurement technique. Their PIV system is in general composed of Nd:YAG laser with a maximum frequency of 40 Hz (width pulse about 7ns, and approximately 25 mJ/pulse), and high speed CCD camera with a frame rate from 31-1000 frames per second and a resolution of 512x512 pixels. Drag reduction was obtained at the lower velocity at $s^+ = 25.2$. However, the opposite trend occurs for the highest velocity at $s^+ = 40.6$.

1.3.4 Drag reduction by biology based methods

Evolutionary adaptations of animals to sustained fast flying and swimming face the same challenges as engineering of modern aircraft, cars, ships and submarines. Contrary to engineering, nature had a huge experimental ground. Only optimal combinations of mechanically highly efficient propulsion systems and extraordinary complex drag reduction measures can explain the spectacular achievements of animal locomotion in air and water. Videler (1992) did a comparison of the costs of transport of animal flight with that of aircraft and helicopter in a dimensionless way showed that nature was found to have much more economic solutions. However, due to the enormous diversity in life styles, feeding and survival strategies, principles of force generation and the many other functions incorporated in the animal's body, many details and structural solutions to the problem of natural drag reduction still remained undiscovered or ill-understood (Bannasch 1998).

Experimental studies of the fluid dynamic properties of live swimming animals are crucial. Their flexible bodies were adaptable to particular flow conditions. In fish and dolphins the body was strongly involved in the process of thrust generation and is thus exposed to highly unsteady effects, which can hardly be reproduced in labs. Studies with rigid models had been rather disappointing, and various numerical approaches to discover the secrets of the dolphin swimming, namely to solve Gray's Paradox (1936), led to controversial results. Gray stated that "If the resistance of an actively swimming dolphin is equal to that of a rigid model towed at the same speed, the muscles must be capable of generating energy at a rate at least seven times greater than that of other types of mammalian muscle." Gray went on to identify the proposition that the rhythmic movements of the dolphin in some way that prevent the fluid from generating turbulence along the body. Gray proposed the paradox and speculated that laminar flow exited along the body. However, some other authors reject the existence of any drag reducing mechanisms in dolphins, but concluded that dolphins swim fast, but do not exceed what they would be able of doing without exotic drag reduction mechanisms (Fein 1998, Fish 1991). After respective correction, it turned out that, Gray was right (Bannasch 1998). These animals must be able to use special methods for drag reduction. Apart from the ability to delay considerably the laminar-turbulent transition in the boundary layer by compliant wall effects (Carpenter P.W. 1990), other authors proposed that dolphin used secretion on the skin or wave-like body motion to get drag reduction Bannasch (1998). Rosen (1971) reported that the dilute solutions of fish mucus in turbulent pipe flow exhibited as much as 66% in friction drag. The mucus secreted by fish over the body

surface was believed to reduce the rate of momentum transfer from the free-stream flow to the surface of the fish. The development of riblets to reduce turbulent skin friction came from the study of shark scales. For instance sharks have small riblets (parallel, converging and diverging patterns) on their skin, which are assumed to improve the performance (Koeltzsch *et al*., 2002, Bechert *et al*., 1997, Bechert *et al*., 2000). Some species also deploy roughness by projecting bands near the position of maximum body girth to ensure the presence of turbulent flow over the body to avoid flow separation, which would increase the pressure drag. Likewise, investigations indicate most fish slime, which contains high molecular weight polymer and surfactants, manifest a considerable drag reduction behavior with maximum effectiveness taking place close to the wall region, which suggest that drag reduction by addition of additives and surfactants is present in nature (Bushnell & Moore, 1991). A diversity of drag reducing mechanisms existed in aquatic animals in association with their habits and restrictions on body design (Fish, 1998).

As matters of energy economy and greater speeds are desired in engineered systems (Bushnell & Moore, 1991), imaginative solutions for drag reduction from nature may serve as the inspiration for new technologies. It can be believed that the combination between biology and engineering and modern computational approaches (Moin, 1997) can achieve a promising future for the industry drag reduction techniques.

1.4 Aim and framework of this thesis

The aim of the present thesis is to shed more light on the mechanism of drag reduction by micro bubbles. We use two different techniques measurement technology to reach our goal, the first being laboratory experiments using Particle Image Velocimetry (PIV) and the second differential pressure measurement using Validyne DP-103 transducer. Both techniques are applied to turbulent flow in a rectangular pipe. The plan of the remainder of this thesis is as follows. First, in Chapter II we mention the description of our laboratory experimental setup followed by the PIV system description. Then in Chapter III, basic equations in turbulence analysis that apply to our problem are discussed. Then we come to the main body of this thesis that is application of the wavelet analysis on drag reductions. In Chapter IV, the wavelet theory was discussed, including the literatures on the wavelet application in turbulence study, and the different wavelet algorithms were discussed. In Chapter V, we present the results by using wavelet based algorithms from the experiment data were shown. We end this thesis with some closing remarks and conclusions in Chapter VI.

CHAPTER II

EXPERIMENTAL SETUP AND THE PIV SYSTEM

Our experiments were performed in two series. Single phase flow condition without bubbles was measured for the first series, and micro bubbles at different void fractions – for another series. The instantaneous velocity fields near the wall were measured by PIV at streamwise-normal plane and in the upper wall region. The differential pressure was measured at both cases. For the facility, a rectangular cross section channel was built and the upper water tank was designed to achieve constant water head pressure. Water was used as a working fluid and microbubbles were produced by electrolysis.

2.1 Channel flow setup

The experimental measurements for this study took place in a rectangular channel flow at Reynolds Number of 5128. The channel was build with Plexiglas. The dimensions of the channel are 5.6 cm high, 20.5 cm wide and 4.8 m long. Water was used as our working fluid. Water was pumped from the lower tank to the upper tank by 3 pumps with power of 1/6, 1/4, 1/2 hp respectively. Then water was driven trough the channel by gravity from the upper tank and this tank is located 3m above the channel. The water flows from the channel to the lower tank back and thus formed a close loop. Upper tank's water level was kept constant through the tests to ensure constant flow rate

through the channel. The flow of water was controlled by two spherical valves and one butterfly valve. Water runs through the channel by gravity and is quantified by two digital turbine flow meters (GPI, 0-50 GPM), and a float rotameter (Dwyer, 0-10 GPM). The schematic diagram of the experimental set up is shown in figure 2.1.

The water flow was seeded by polystyrene neutrally buoyant particles with a diameter that goes from 6 to 9 μm, and a density of 1.050 g/cm^{-3}. This type of particle can reflect enough light to be detected by the CCD cameras and they were injected and mixed thoroughly in the lower tank before going to the channel. The channel was filled smoothly to avoid air bubbles entering into the flow.

Microbubbles was produced by electrolysis at 10 cm upstream the test zone. Two parallel platinum wires with a diameter of 76 μm are used as cathode an anode and their distance is 2.54 cm. The anode is 0.5 cm far from the upper wall and the cathode is separated 1 cm far from the wall. The ratio between the distance from the closest wire to test station and the wire's diameter is $0.1/76 \times 10^{-6} = 1315$. Hence, the wire effect on the test station can be neglected. To produce hydrogen microbubbles of 30 μm diameter a current of 25 mA is conducted trough the electrodes.

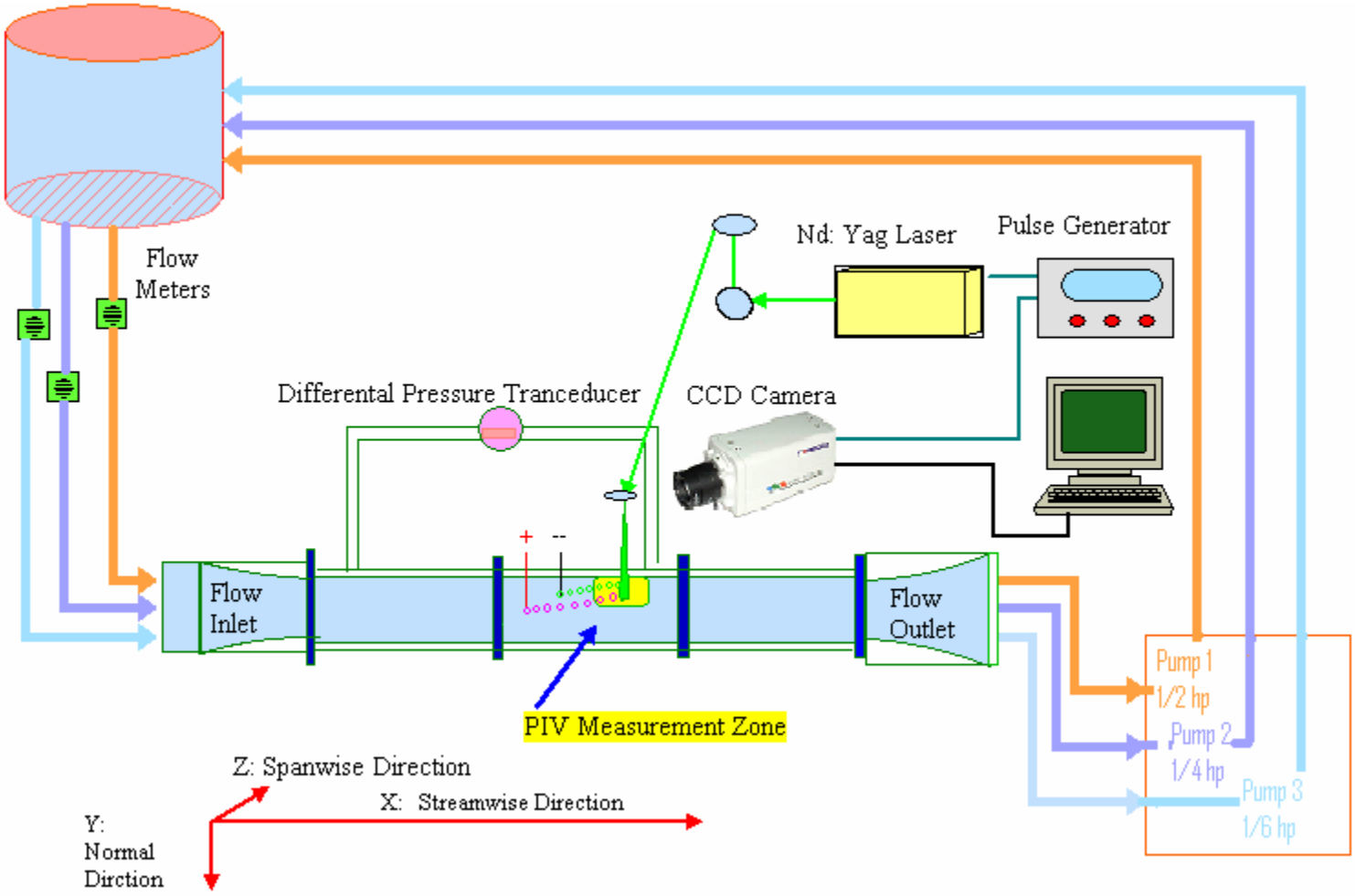

FIGURE 2.1 Schematic diagram of the experimental set up.

2.2 Pressure measurement

As mentioned in Chapter I, Warholic *et al.* (1999) reported an investigation on drag reduction by addition of polymer. In their experiment, a Validyne pressure transducer (Model DP103) was used to evaluate the pressure drop (Δp) with polymer and without polymer over a distance (Δx) of 154 cm. As a differential pressure transducer, (Validyne DP-103) is able to measure a pressure drop range from 0-35 Pa. This device was installed in the upper wall of the channel. The same method was used in our experiment. The differential pressure was measured through pressure taps positioned on the top wall of the channel over a distance of 157.5 cm.

$$\tau_w = -H \frac{\Delta P}{\Delta x} \qquad (2)$$

where τ_w is the wall shear stress, ΔP is the pressure drop measured by the pressure transducer; Δx is the axial distance between the pressure connection tabs and H is the half height of the channel.

The wall shear stress was defined as

$$\tau_w = \mu \left. \frac{dU}{dy} \right|_{y=0} \qquad (3)$$

The wall shear stresses were obtained by extrapolating measured Reynolds stresses at different y in the outer part of the flow or by using measured pressure drops and the force balance equation. For a Newtonian fluid the same τ_w is obtained by both methods. However, for flows with large drag-reductions smaller values of τ_w were

obtained by equation (2) because of the existence of large stress deficits τ_p . Consequently, pressure drop measurements were used in all experiments to determine τ_w . Percent drag-reductions, was defined as the ratio of τ_w for a polymer solution to that for water. The drag reduction percentage can be calculated by

$$DR\% = 100 * \left[1 - \left(\frac{\tau_w}{\tau_{w0}} \right) \right] \qquad (4)$$

where τ_{w0} is obtained in single phase flow condition and τ_w is obtained at different void fractions.

The estimate of void fraction values can be evaluated from

$$\alpha = \frac{V_g}{V_g + V_l} \qquad (5)$$

where V_g is the volume for injected bubbles and V_l is the volume for water. τ_w, τ_{w0}, V_g and V_L could be obtained from the PIV measurement.

2.3 Common velocity measurement technique

To investigate the drag reduction mechanism, it is very important to study the velocity field in the near wall region. Most of the instantaneous flow information were reported using Hot film or Hot-wire anemometry, Doppler Velocimetry (LDV) or Laser Doppler Anemometry (LDA). Hot-wire or hot-film is a one-point intrusive technique measurement. The principle of this technique is based on the relationship between the heat removed from the wire by convection and the velocity of the fluid.

However, fluid temperature is hard to keep exactly constant. And the impurities in the fluid can easily adhere to the wire. All these kind of factors can destroy the calibration of the hot-film system. The measurement is not flexible since one sensor can only be located at one point at one time. LDA or LDV is a non-intrusive measurement technique, which will not impact the fluid field by installation. LDA or LDV is designed by Doppler effect. When a particle passes through the intersection volume formed by the two coherent laser beams, the scattered light received by a detector has components from both beams. The components interfere on the surface of the detector. Due to the changes in the difference between the optical path lengths of the two components this interference produces pulsating light intensity as the particle moves through the measurement volume. Thus the velocity can be measured. A velocity field can be obtained by moving the measuring volume, which has the size of the region intersected by the laser beams. However, this technique is still for one point measurement. To discern the real information and capture the coherent structure in the near wall region of a turbulent channel flow, more advanced technique is still needed.

2.4 Particle image velocimetry

As an optical and non-intrusive measurement technique, Particle Image Velocimetry (PIV) provides both temporal and spacial information for instantaneous velocity fields. Thus, more valuable turbulence statistics parameter could be calculated based on two dimensional velocity field U(x, y, t) and V(x, y, t). Important turbulence

study parameters such as velocity profiles, turbulent intensities, Reynolds stress, vorticity, entropy, spatial derivatives, wavenumber-spectrum could be achieved etc. Meanwhile, the PIV has some limitation due to the memory size, and hard disk size of the computer and the performance of recording devices. The power and sampling frequency of the Laser can also impede the good performance of the whole PIV system.

2.4.1 PIV sampling system

The early discussion about PIV can be referred to Adrian (1991) and Hassan (1992). The detailed information about PIV can be found in Markus (1998). In our experiment, PIV was used to estimate instantaneous velocity fields in the x-y plane. Optical access in x-z plane is required to place a sheet of light and the camera. Pictures were recorded by a CCD Kodak camera (model Megaplus ES 1.0/1.0) with a resolution of 1008 x 1018 pixels. The camera has the trigger double exposure mode, which permits measurements at high velocity flows. The seeded flow is illuminated by a high power, dual oscillator Nd:Yag laser with a power of 300-350 mJ/pulse, and a wavelength of 532 nm (green light). The incident laser beam is transformed into a 1 mm thickness sheet of light by an array of cylindrical and spherical lenses. The viewing area was 1.28 cm^2 in x-y plane. 60 images were taken in one second and 30 pairs velocity field was given. Each velocity field was obtained from two successive images and the elapsed time between the two pictures is 1 ms. Total sets of velocity fields per run were 100 and images were recorded for a time span of approximately 3.3 second.

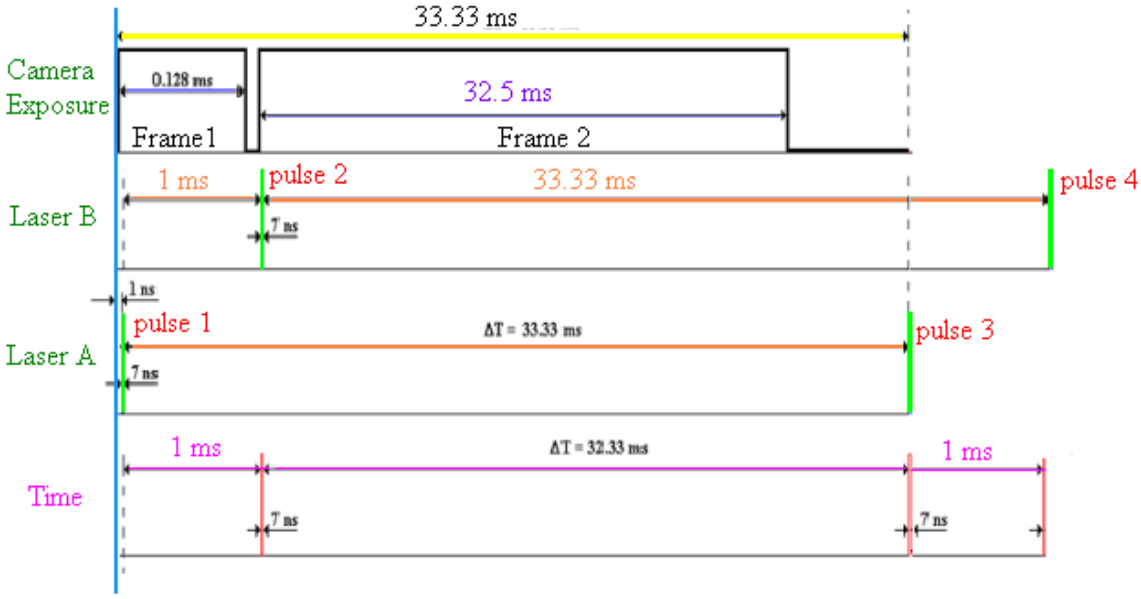

FIGURE 2.2 Time synchronization process.

A high accuracy pulse generator (Stanford Research System Inc., model DG535) with a four channels digital delay/ pulse and accuracy of picoseconds is used to synchronize the PIV system. The commercial frame rate of the CCD camera is increased from 30 to 60 fps by doing a precise synchronization between the laser light pulsing and the double exposure capability of the CCD camera.

To have a better idea of the image sampling sequence, a diagram is given in Fig 2.2 to show the synchronization system. Two exposure times, are used for the odd and even frames in order to attain the 60 fps. The exposure time for the first frame is 0.128 ms and for the second frame the CCD array was exposed for 32.4 ms, respectively. The diagram of the synchronization and timing used on this study is shown in figure 2.2. The time length between pulse 1 and pulse 2 was 1 ms. The time duration between

pulse 2 and pulse 3 is 32.33 ms. The pictures taken at frame 1 and frame 2 were processed to get the vector field. And the pictures taken at frame 3 and frame 4 were processed to get the next vector field. So the time duration between two consecutive vector fields is 33.33 ms.

A calibration grid with adjacent white dots regularly divided, is located at the viewing plane, in order to obtain a scale for the physical measurement.

2.4.2 Image processing after PIV sampling

Step 1, preprocessing needed to be done before getting velocity vectors. Since the illumination time of odd frame (Laser A) and even frame (Laser B) is different, two average image from the whole set of the original images are evaluated separately for the odd images and another for the even images. Then, the odd/even average is subtracted respectively from the original odd/even images. After this, the images from the subtraction process are equalized.

Step 2, two different PIV processing software are used for the tracking process. One is a Windows based application (Uemura *et al*., 1989) and can be used directly to process the images from the preprocessing process. This software is flexible since it allows the user to set different image threshold and tracking parameter for each pair of images. The second software is an in-house code (Hassan *et al*., 1992). First, the image files from the preprocessing process was transformed to ASCII files by a program developed in Lab-View. Then, the ASCII files were processed by our in-house code in

Unix systems. The resulting velocity vectors from these two applications were compared, corrected and combined. This hybrid technique widely increment the number of vectors used for the flow field analysis.

Steps 3, the velocity vectors from step 2 were filtered by two processes. The first filter got rid of the vectors that have a lower cross-correlation value than the average value (~50% of the vectors). The second filter took away the vectors that are not within +/- a standard deviation value of the magnitude and direction of the representative velocity vector of within a small window (~20 X 20 pixels). About 40% of the initial vectors of each velocity field remain after performing the filtering processes. Then, the vectors of both filtering process for each velocity field, are combined to get one single file, and compared to remove repeated vectors. Finally, these vectors are interpolated using the inverse distance algorithm in a window of 20 x 20 pixels to obtain instantaneous velocity fields in an ordered grid of 50 x 50 vectors.

CHAPTER III

TURBULENT BOUNDARY LAYERS

The problems of fully developed turbulence have fascinated people for centuries. Interest has been fueled both by the abundance of turbulent flows which require prediction and control and by the persistent belief that out of the limit of many compounded instabilities should arise a universal statistical state. Many mathematical models have been developed for the study of the turbulent boundary layer. However, turbulence has the character of 3-dimensional, time-dependent, eddy motions with various scales, a lot of difficulties still arise even using the most advanced technology. It is extremely complex if not impossible to obtain a deterministic solution because of their irregularities (randomness). To investigate the turbulent drag reduction mechanism, the turbulent boundary layers need to be studied combining the previously discussed measurement technique. In this chapter, the classical turbulence analysis methods such as the mean velocity profiles, the turbulent intensity, Reynolds stress, spectra and correlation were discussed.

3.1 Equation of motion

For the adiabatic, incompressible, and Newtonian fluid, the Navier-Stokes equation could be expressed in this way:

Continuity equation: $$\frac{\partial u_i}{\partial x_i} = 0 \quad (6)$$

Momentum conservation equation: $$\frac{\partial u_i}{\partial t} + u_j \frac{\partial u_i}{\partial x_j} = -\frac{1}{\rho}\frac{\partial p}{\partial x_i} + \nu \frac{\partial^2 u_i}{\partial x_j^2} \quad (7)$$

where u_i is the instantaneous velocity component in the direction of x_i, p is the instantaneous static pressure, ν represents the kinematics viscosity, and ρ is the density of the fluid.

Reynolds decomposition is a very common used technology for turbulence statistics. The instantaneous component of the velocity was decomposed into an average and a fluctuating component:

$$u = U + u' \quad (8)$$

The average value of the velocity or pressure over an interval of time can be obtained from

$$U_i(x, y) = \frac{1}{N_T}\sum_{i=1}^{N_T} u_i(x, y) \quad (9)$$

Substituting equation (8) into equation (5) and (6), making the time average for each term and enforcing conservation of mass the mean momentum equation in the streamwise direction:

$$U_j \frac{\partial U_i}{\partial x_j} = -\frac{1}{\rho}\frac{\partial P}{\partial x_i} + \frac{\partial}{\partial x_j}\left(\nu \frac{\partial U_i}{\partial x_j} - \overline{u'v'}\right) \quad (10)$$

The second term on the right hand represents the transport of momentum due to fluctuating velocities. The term $\overline{u_i v_j}$ is called the Reynolds stress, which is the

contribution of the turbulent motion to the mean stress tensor. The Newtonian viscous stress is important in a region close to the wall. Far from the wall, the Reynolds stress will suppress the Newtonian viscous stress. When the N-S equations are time averaged information about the structures of the flow is lost and to discern the coherent structure inside the turbulent flow, more advanced technology is still needed.

3.2 Commonly used turbulent quantities

The region close to the wall ($0 \leq y^+ < 5$) is known as the viscous sublayer; from $y^+=5$ to $y^+= 70$ is the buffer layer; the overlap layer is located at $y^+>70$. The study of the region close to the wall is very important to clarify skin friction reduction. The comparison between the near wall region parameters with drag reduction and without drag reduction could give us a direct result for drag reduction analysis.

The kinematic viscosity and the wall shear stress are the most important parameters near the wall region. The wall shear stress can be represented by

$$\tau_w = \mu \left(\frac{du}{dy} \right)_{y=0} \qquad (11)$$

For a fully developed channel flow, which is homogeneous in the streamwise direction, there is an exact balance between the wall shear stress acting on the walls and the net pressure force acting across the flow. Thus the shear stress can also be calculated by equation (1).

In a turbulent flow several scales exist. Most of them are scaled by the friction velocity u_τ, which is also associated with the wall shear stress τ_w. The evaluation of the friction velocity can be done by equation (11), where ρ is the density of the fluid.

$$u_\tau = \sqrt{\frac{\tau_w}{\rho}} \qquad (12)$$

A corresponding length scale for this region is defined as wall layer thickness or viscous length scale (Schlichthing & Gersten, 2000):

$$l = \frac{\upsilon}{u_\tau} \qquad (13)$$

For the viscous region, the time scale is defined as

$$t_o = \frac{\upsilon}{u_\tau^2} \qquad (14)$$

The velocity $\bar{u}$ and the distance from the wall y can be made dimensionless in wall units by the friction velocity.

$$u^+ = \frac{\bar{u}}{u_\tau} \qquad (15)$$

$$y^+ = \frac{y\nu}{u_\tau^2} \qquad (16)$$

Since our velocity field was measured by PIV in the x-y plane, all the following calculation are based on the instaneous velocity $u_i(x, y)$ and $v_i(x\ y)$.

Averaged streamwise velocity: $$\overline{U(x,y)} = \frac{1}{N}\sum_{i=1}^{N} u_i(x,y) \qquad (17)$$

Averaged normal velocity: $$\overline{V(x,y)} = \frac{1}{N}\sum_{i=1}^{N} v_i(x,y) \quad (18)$$

Streamwise turbulence intensity: $$u_{rms}(x,y) = \sqrt{\frac{1}{N}\sum_{i=1}^{N}[u_i(x,y) - U(x,y)]^2} \quad (19)$$

Normal turbulence intensity: $$v_{rms}(x,y) = \sqrt{\frac{1}{N}\sum_{i=1}^{N}[v_i(x,y) - V(x,y)]^2} \quad (20)$$

Reynolds shear stress: $$\overline{u'v'(x,y)} = \frac{1}{N}\sum_{i=1}^{N}\{[u'_i(x,y)][v'_i(x,y)]\} \quad (21)$$

Spanwise vorticity: $$\omega_z = \left(\frac{\partial v}{\partial x} - \frac{\partial u}{\partial y}\right) \quad (22)$$

Two point correlation coefficient: $$R_{ij}(\Delta r) = \frac{\overline{u'_i(r)u'_j(r+\Delta r)}}{u_{rms_i}(r)u_{rms_j}(r+\Delta r)} \quad (23)$$

The integral length scale: $$L_u = \int_0^b R_{ij}(\Delta r)dr \quad (24)$$

One point auto-correlation coefficient: $$R_{ij}(\Delta t) = \frac{\overline{u'_i(t)u'_j(t+\Delta t)}}{u_{rms_i}(t)u_{rms_j}(t+\Delta t)} \quad (25)$$

The integral time scale: $$T_L = \int_0^b R_{ij}(\Delta t)dt \quad (26)$$

Wavenumber spectra: $$E(k_1) = 2\int_{-\infty}^{\infty} R(\Delta r)e^{-i2\pi k_1 \Delta r}dr = 4\int_0^{\infty} R(\Delta r)e^{-i2\pi k_1 r}dr \quad (27)$$

All the detailed information about the above equations could be referred to Gutierrez Torres (2004) and Jimenez Bernal (2004). In their work, the extensive

discussion about the turbulence statistic theory was done and the application of turbulence intensity, Reynolds stress, both integral time scale and integral length scale, wavenumer spectra in streamwise direction and normal direction were applied to full data sets from the turbulent measurements. Both the results from single phase flow and micro bubbles injected two phase flow were compared. Good and consistent conclusions were reached. Mechanisms about drag reduction by microbubbles were discussed and good suggestions about drag reduction control were given.

Based on their extensive work in the microbubbles drag reduction studies, my thesis focused on the wavelet technique to process our lab data. Basic turbulence statistic theory was applied both in Gutierrez Torres (2004) and Jimenez Bernal (2004). However, Gutierrez Torres (2004) focused on time domain or space domain processing by using correlation calculation for the temporal correlation or the space correlation while Jimenez Bernal (2004) focused on frequency domain or wavenumber domain processing by using Fourier transform. As a time-frequency or space-wavenumber 2-Dimensional analysis method, Wavelet is powerful to decompose the signals of turbulence measurement into 2-D plane. My thesis followed this idea and does the following studies for the drag reduction research.

CHAPTER IV

WAVELET ANALYSIS ON TURBULENCE STUDY

4.1 Review of wavelet analysis on turbulence study

PIV technique provides us a lot of information about the velocity field distribution and it is very powerful to capturer the 2-dimensional information about the velocity fluctuation, vorticity formation. The quantities such as Reynolds Stress, turbulence intensity, spatial correlation, the integral length scale, the integral time scale, vortices and spectra can all be calculated from the PIV measurement. However, it is still hard to classify fluid structure patterns and capture the coherent structure by the previous mentioned parameters since the classical theory of turbulence is blind to the presence of coherent structures because they are advected by the flow in a homogeneous and isotropic random fashion, and hence they are lost by ensemble averaging. Moreover, the spatial support of coherent structures becomes smaller and smaller when Reynolds number increases.

The wavelet transform was first introduced by Grossman & Morlet (1984) for the applications of the analysis of seismic data. As a useful tool for analysis of non-stationary signals such as seismic signals, wavelet showed its ability of resolving features at various scales. The theory and applications of wavelets have undoubtedly dominated the journals in all mathematics, engineering and related fields. Few other

theoretical developments in mathematical sciences have enjoyed this huge attention and popularity. A mathematician comes up with a good idea, develops a concrete theory, faces great opposition from other prominent figures in the area, but continues to work nevertheless. Then come in engineers and physicists, reformulate and modify that theory to make it more accessible, and eventually that idea becomes a standard tool for many researchers in many fields. Wavelet theory has now already enjoyed a tremendous attention and success over the last decade, and almost all signals encountered in practice call for a time-frequency analysis, and wavelets provide a very simple and efficient means of performing such an analysis. And now the application areas for wavelets have been growing for the last ten years at a very rapid rate. Reviewing all of them in our paper is certainly not possible. The purpose of our review is to point out to various areas that wavelets can be used, and especially be a source of inspiration for research on turbulence.

Applications have already been taken on image processing and compression. Due to the compact support of the basis function used in wavelet analysis, DWT have good energy concentration properties. By discarding some coefficients using threshold and reconstructing the data, the image data can be largely compressed without significant error. Since most of the noise distribute on some specific scales like fine scales, discarding the coefficients at these scales can remove the noise for the reconstruction of the signals. Due to the very nature of all biological signals being non-stationary, wavelets have enjoyed great success in biomedical engineering. Wavelets have been used for the analysis of electrocardiogram for diagnosing cardiovascular disorders, and

of electroencephalogram for diagnosing neuropsychological disorders, such as seizure detection, or analysis of evoked potentials for detection of Alzheimer's disease (Polikar *et al*., 1997). Another interesting area of applications has been nondestructive evaluation. Wavelets have been successfully used for the analysis of ultrasonic and eddy current signals for flaw detection in various media such as nuclear power plant tubings (Polikar et al., 1998), gas pipelines, aircraft components, etc. Wavelets have even been used on hierarchical organization of distant galaxies. Bijaoui *et al.* (1996) developed a multi-scale vision model using wavelets for classifying each component in the hierarchical structures at various scales. Jordan *et al.* (1997) characterized the turbulence scales in the atmospheric surface layer with the continuous wavelet transform.

Although the wavelet theory has been very successfully applied in various fields for a long time, the application of the wavelet analysis to turbulence started not a long time ago. Argoul *et al*., (1989) firstly used the wavelet transform to analyze the wind-tunnel turbulence data and provided the visual evidence of the Richardson cascade. Liandrat & Moret-Bailly (1990) showed that the wavelet transform is very well adapted to fluid dynamics and turbulence study and is much more powerful comparing with the VITA (Variable Interval Time Averaging) technique. Everson & Sirovich, (1990) analyzed two-dimensional dye concentration data from a turbulent jet by wavelet transform, and revealed the nature and self-similarity of the inner structure of the jet. Yamada & Ohkitani (1990) applied the orthogonal wavelet expansion to the experimental data of turbulence and found a direct relation between the wavelet

spectrum and the Fourier spectrum. Muzy *et al*., (1991) used wavelet transform to the fully developed turbulence data and characterized the local multifractal behavior of turbulence in the range of inertial scales. Dallard & Browand (1993) have reported extensive results of wavelet analysis from phase-averaged 2-D velocity fields in an acoustically forced mixing layer. Dallard & Browand (1993) also extended 1-D wavelet functions to the 2-D case for the application of the experimental data in fluid mechanics. And now, the wavelet transform was already widely used to reveal various turbulent or eddy structure, such as in jets (Li & Nozaki, 1995), multiphase flows (Li & Tomita, 1998) and others. Now, the wavelet transform has already become a standard tool or software kit in identification of flow structure. Several new diagnostics (Farge, 1992, Farge *et al*., 2001, Farge *et al*., 2003, Protas *et al*., 2002) developed from the wavelet transform were employed to analyze structure of turbulence and eddy analysis. They offer the potential of extracting the essence of structure feature from flow fields, which are lost if using traditional statistics methods.

Wavelet technique allows tracking turbulent structures in terms of time and scale, and extracts new information on turbulence scale. Li did a lot of work combining wavelet with fluid mechanics. In 1997, Li (1997a) used wavelet to analyze the coherent structure dynamics in a plane turbulent jet. Li (1997b) also gave wavelet Reynolds stress analysis to two-dimensional vortex flow. Furthermore, Li (1997c) gave wavelet velocity correlation analysis in a plane turbulent jet. The turbulent structure analysis of a two-dimensional jet using wavelets was given by Li (1997d). Li & Nozaki (1995) made wavelet analysis for the plane turbulent jet (analysis of large eddy structure) and

the flow structure in a bounded jet (Li *et al*., 1997). The velocity correlation analysis was made in the near-field of a turbulent jet with help of discrete wavelet transform by Li *et al*., (1998a). Li *et al*., (1998b) also used orthogonal wavelet basis on multi-resolution image analysis for a turbulent flow. For PIV measurement, Li *et al*. (2000, 2001a, 2001b, 2002) gave wavelet multi-resolution analysis for dual-plane stereoscopic PIV measurement results in a lobed jet.

Though wavelet is widely applied in turbulent study, few papers discussed the drag reduction phenomena in bubbly channel turbulent flow by wavelet analysis. The aim of this paper is to apply the wavelets to analyzing the coherent structures in the near wall region of a turbulent channel flow. Camussi (2002) identificated the coherent structure from wavelet analysis of particle image velocimetry data. Coherent structures are known to exist and be responsible for most of the momentum transfer in the boundary layers. Turbulent flows are characterized for showing incoherent structures and coherent structures (vortices) lying parallel and close to the wall, and oriented in the streamwise direction. These coherent structures account for 80% of the turbulent fluctuating energy (Lumley & Blossey, 1998). Many identification techniques such as visualization, spectra analysis, spatial correlation functions, and temporal correlation functions are well established in theory for turbulence analysis. In our lab, all the above identification methods have already been used to extract coherent structures in the turbulent flows. However, the local frequency with respect to space-time changes continuously for the turbulence and large-scale eddy motion, and the coherent structure in both time and frequency or in both space and wavenumber has not been clarified. Li

(2000, 2001a, 2001b) extracted multi-scale turbulent structure from PIV results based on wavelet vector multiresolution technique. Identification of coherent structure requires the acquisition of detailed quantitative data on such structure characteristics as size, strength, convection velocity, etc. Neither the Fourier analysis nor the traditional correlation method gives us sufficient information.

4.2 Wavelet analysis theory

4.2.1 One dimensional continuous wavelet transform

As we know that the Fourier transform is a mathematical prism that breaks up a signal into the frequencies that compose it (Hubbard, 1996), as a prism breaks up light into colors. It transforms a function that depends on time or space into a new function that depends on frequency or wave number.

$$F(\overline{w}) = \int_{-\infty}^{\infty} e^{-iwt} f(t)dt \qquad (28)$$

The new function is called the Fourier transform of the original function. The function and new function display the information in time domain and frequency domain separately. The Fourier transform of music tells what notes (frequencies) is played, but it is virtually impossible to discern when the notes are played.

Wavelets are an extension of Fourier analysis and the basic approach is the same. The coefficients tell in what way the analyzing function (sine and cosines, or wavelets)

needs to be modified in order to reconstruct a signal. But wavelet automatically adapt to the different components of a signal, using a small window to look at brief, high frequency components and a large window to look at long-lived, low-frequency components. This procedure is called multiresolution; the signal is studied at a coarse resolution to get an overall picture and at higher and higher resolutions to see increasingly fine details. So wavelets have been called a "mathematical microscope"; compressing wavelets increases the magnification of this microscope, enabling us to take a closer look at small details in the signal.

Wavelets are obtained from a single prototype wavelet ψ(t) called mother wavelet by dilations and shifting:

$$\psi_{a,b}(t) = \frac{1}{\sqrt{a}}\psi(\frac{t-b}{a}) \qquad (29)$$

, where a is the scaling parameter and b is the shifting parameter.

The continuous wavelet transform (CWT) of a function f is defined as

$$Tf(a,b) = < f, \psi_{a,b} > = \frac{1}{\sqrt{a}}\int f(t)\psi^{*}(\frac{t-b}{a})dt \qquad (30)$$

If ψ is such that

$$C_{\Psi} = \int_{-\infty}^{+\infty} \frac{\left|\Psi(\omega)\right|^{2}}{\omega}\, d\omega < +\infty \qquad (31)$$

f can be reconstructed by an inverse wavelet transform:

$$f(t) = C_{\Psi}^{-1}\int_{0}^{+\infty}\int_{-\infty}^{+\infty} Tf(a,b)\psi_{a,b}(t)db\frac{da}{a^{2}} \qquad (32)$$

4.2.2 One dimensional discrete wavelet transform

The main idea of DWT is the same as it is in the CWT. A time-scale representation of a digital signal is obtained using digital filtering techniques. Recall that the CWT is a correlation between a wavelet at different scales and the signal with the scale (or the frequency) being used as a measure of similarity. The continuous wavelet transform was computed by changing the scale of the analysis window, shifting the window in time, multiplying by the signal, and integrating over all times. In the discrete case, filters of different cutoff frequencies are used to analyze the signal at different scales. The signal is passed through a series of high pass filters to analyze the high frequencies, and it is passed through a series of low pass filters to analyze the low frequencies. The resolution of the signal, which is a measure of the amount of detail information in the signal, is changed by the filtering operations, and the scale is changed by upsampling and downsampling (subsampling) operations. Subsampling a signal corresponds to reducing the sampling rate, or removing some of the samples of the signal. For example, subsampling by two refers to dropping every other sample of the signal. Subsampling by a factor n reduces the number of samples in the signal n times. Upsampling a signal corresponds to increasing the sampling rate of a signal by adding new samples to the signal. For example, upsampling by two refers to adding a new sample, usually a zero or an interpolated value, between every two samples of the signal. Upsampling a signal by a factor of n increases the number of samples in the signal by a factor of n.

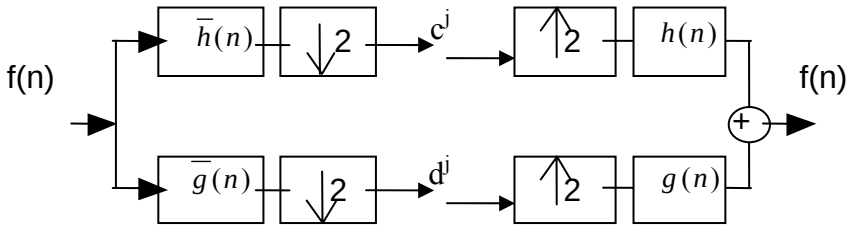

FIGURE 4.1 Decomposition and reconstruction of a signal.

The 1-D decomposition process can be clearly seen in Fig 4.1. The original signal is labeled as f(n). The boxes represent convolution with either g or h. The box with downward arrows represents down sampling by a factor of two. The outputs, cj and dj are known as scaling coefficients and wavelet coefficients. This process can be repeated for the number of scales desired. Repeat the convolution to the next step to our desired scale number, we can get the scaling coefficients and the wavelet coefficients in different scales. This method is called multi-resolution analysis or pyramid decomposition. The box with upward arrows represents up sampling by a factor of two, which means that a zero is inserted between each sample. g is known as the wavelet filter and h is the scaling filter. In the reverse direction, the reconstruction of the original signal can be achieved using the wavelet coefficients and the scaling coefficients.

The scaling coefficients can be given by:

$$c^{j+1}[n] = \sum_m h[2n - m]c^j[m] \qquad (33)$$

And the wavelet coefficients can be given by:

$$d^{j+1}[n] = \sum_{m} g[2n - m]c^{j}[m] \qquad (34)$$

The unit of frequency is of particular importance at this time. In discrete signals, frequency is expressed in terms of radians. Accordingly, the sampling frequency of the signal is equal to 2π radians in terms of radial frequency. Therefore, the highest frequency component that exists in a signal will be π radians, if the signal is sampled at Nyquist's rate (which is twice the maximum frequency that exists in the signal); that is, the Nyquist's rate corresponds to π rad/s in the discrete frequency domain. Therefore using Hz is not appropriate for discrete signals. However, Hz is used whenever it is needed to clarify a discussion, since it is very common to think of frequency in terms of Hz. It should always be remembered that the unit of frequency for discrete time signals is radians.

After passing the signal through a half band lowpass filter, half of the samples can be eliminated according to the Nyquist's rule, since the signal now has a highest frequency of $\pi/2$ radians instead of π radians. Simply discarding every other sample will subsample the signal by two, and the signal will then have half the number of points. The scale of the signal is now doubled. Note that the lowpass filtering removes the high frequency information, but leaves the scale unchanged. Only the subsampling process changes the scale. Resolution, on the other hand, is related to the amount of information in the signal, and therefore, it is affected by the filtering operations. Half band lowpass filtering removes half of the frequencies, which can be interpreted as losing half of the information. Therefore, the resolution is halved after the filtering

operation. Note, however, the subsampling operation after filtering does not affect the resolution, since removing half of the spectral components from the signal makes half the number of samples redundant anyway. Half the samples can be discarded without any loss of information. In summary, the lowpass filtering halves the resolution, but leaves the scale unchanged. The signal is then subsampled by 2 since half of the number of samples are redundant. This doubles the scale.

4.2.3 Wavelet auto-correlation transform

Wavelet correlation analysis can overcome limitations of the traditional correlation method which only describes the correlation of signals in terms of time delay and assist analysis of the similarity structure of signals in terms of scale and time delay. The traditional auto-correlation method still plays an important role, but it had been hiding the essence of the similarity structure since it lacks frequency resolution. Then the experimental fluctuating velocities at some spatial locations in the near wall region of the channel turbulent flow are analyzed by the wavelet auto-correlation analysis to reveal coherent structures over a two-dimensional time-period plane, and to extract the most essential scales governing the features of eddy motions.

From 4.2.1, we have the definition of continuous wavelet transform. And equation (28) can be expressed as

$$Tf(a,b) = \frac{1}{2\pi}\int_{-\infty}^{\infty} \hat{f}(w)\overline{\hat{\psi}_{b,a}(w)}e^{ibw}dw \qquad (35)$$

where $\hat{f}$ and $\hat{\psi}$ are the Fourier transforms of f and ψ respectively.

In nonstationary situation, velocity signals of turbulence and others, signals contain various frequency components that rapidly change with time in complex ways. The traditional auto-correlation method is quite capable in identifying the self-similarity structure. However, it cannot extract the information of the self-similarity structure in frequency space and had been hiding the essence of the self-similarity feature since it lacks frequency resolution. The traditional correlation method is well suited to analyze the periodic signals and is not suited for complex signal analysis. From CWT, the wavelet coefficients can describe a signal as localized strength of the signal in both time and period or frequency spaces. The modulus of wavelet coefficients has been employing to describe the characteristics of a signal. Therefore the all traditional statistics method may be applied. In order to obtain the self-similarity structure of a signal for various scales at any given time delay, at first, the original signal is unfolded into time-frequency plane using equation (28). Then the following correlation function was applied to the wavelet coefficient:

$$TC(a,\tau) = \lim_{T\to\infty} \frac{1}{T} \int_{-2/T}^{2/T} \overline{Tf(a,b)}\, Tf(a,b+\tau)\, db \qquad (36)$$

where τ is time delay of wavelet coefficients in the wavelet space, or the time delay of the signal f(t). It is evident that the wavelet auto-correlation function can provide important self-similarity features on a two-dimensional period-time delay plane and then extracts the most essential frequencies governing the self-similarity features of signals.

4.2.4 Wavelet cross-correlation transform

In identifying the spatial turbulent structure or coherent structures and its evolution in time, the cross-correlation analysis between velocities components measured at two separated points in flow filed is most used. A difficulty with the traditional cross-correlation function only provides information about the cross-cross correlation behaviors in scale space at each scale due to lack of scale resolution.

Similar to the wavelet auto-correlation, the original signal f_x(t) and f_y(t) are unfolded into time-frequency plane using equation (28). Then the following cross-correlation function was applied to the wavelet coefficient:

$$TC(a,\tau) = \lim_{T\to\infty} \frac{1}{T} \int_{-2/T}^{2/T} \overline{Tf_x(a,b)} Tf_y(a,b+\tau) db \qquad (37)$$

where τ is time delay of wavelet coefficients in the wavelet space, or the time delay of the signal f_x(t) and f_y(t) . It is evident that the wavelet cross-correlation function can separate different period of the time domain correlation. And this separation is achieved without excessive loss of resolution in time variable due to use of the wavelet transform. Therefore, the wavelet cross-correlation function can describe important statistical correlation features between two different signals on a two-dimensional scales time delay plane, and extract the most essential scales governing the correlation features, which is lost if using traditional method.

4.2.5 Two dimensional discrete wavelet transform

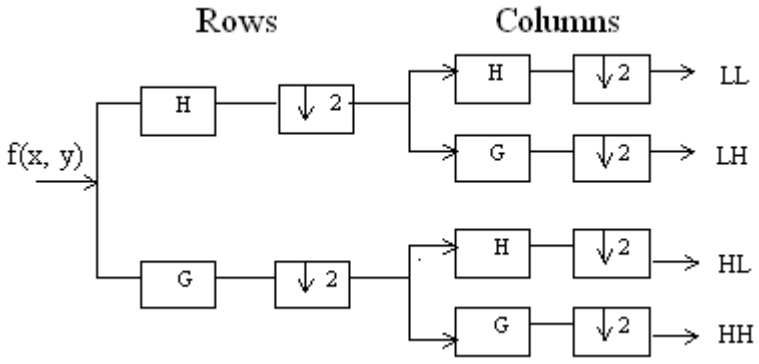

FIGURE 4.2 Two-dimensional wavelet decomposition.

For our study, we also need to analyze two-dimensional signals by two-dimensional wavelet analysis. We perform the two-dimensional wavelet transform by applying one-dimensional wavelet transform first on rows firstly and on columns secondly as shown in figure 4.2. Then the original two-dimensional signal is decomposed to the coarse mesh approximation space (LL), horizontal detail (LH) approx space, vertical detail approx space (HL) and diagonal detail approx space (HH) for the first level decomposition. And the two-dimensional wavelet decomposition can be finished.

Related to turbulence study, we are interested in the multi-resolution of wavelet which can decompose the original signal into different scales. By combining the obtained coefficents at different scales, we get the reconstrution velocity field and then by using eqn (21) the spanwise vorticies field is also obtained. The reconstruction can be realized by the following equation:

$$f(x,y) = \overline{f}_{0,0,0}\phi_{0,0,0}(x,y) + \sum_{j=0}^{J-1}\sum_{i_x=0}^{2^{j-1}}\sum_{i_y=0}^{2^{j-1}}\sum_{\mu=1}^{3} f^{\mu}{}_{j,i_x,i_y}\psi^{\mu}{}_{j,i_x,i_y}(x,y)$$

$$\text{and} \quad \phi_{j,i_x,i_y}(\vec{x}) = \phi_{j,i_x}(\vec{x})\phi_{j,i_y}(\vec{x}) \longrightarrow LL \qquad (38)$$

$$\psi^{\mu}{}_{j,i_x,i_y}(\vec{x}) = \begin{cases} \phi(x)\psi(y); \mu = 1, \longrightarrow LH \\ \psi(x)\phi(y); \mu = 2, \longrightarrow HL \\ \psi(x)\psi(y); \mu = 3, \longrightarrow HH \end{cases}$$

For our two dimensional vector field, we process our data in 4 steps:

First, the wavelet coefficients of instaneous velocity vector u(x, y) was computed as figure 4.2. Second, velocity field reconstruction in coarse scale and fine scale were realized from the wavelet coefficients by equation (37). Third, using the reconstructed velocity field to caculate the vorticities field by equ (5) and calculate the dimensionless coordinates by equ (3) and (4). Finally, the original velocity field was projected into its components in fine scale and coarse scale, which help us to discern the coherent structure hided in original turbulence flow.

4.2.6 Wavelet function selection

According to equation (29), any arbitrary function satisfying the admissibility condition of wavelet may be used as an analyzing wavelet. Several well-defined wavelet functions such as Haar, Mexican hat, Morlet, Db 2 wavelet are commonly used as the analyzing wavelet. The choice of the appropriate wavelet function is at the user's disposal and depends on the kind of information that we want to extract from the signal.

We will start with a simple wavelet: the `Mexican hat', shown on Fig. 4.3.

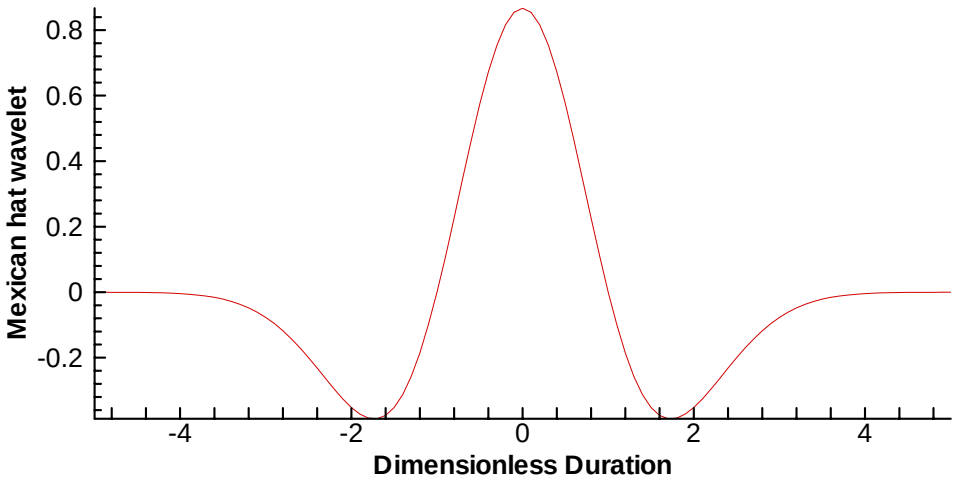

FIGURE 4.3 The Mexican hat wavelet.

It is important to note that, for this to be a wavelet, the positive and negative areas `under' the curve must cancel out. This is known as the admissibility condition. The admissibility condition, spelled out in mathematical references (Daubechies, 1992), is satisfied as long as

$$\int_{-\infty}^{+\infty} \Psi(\omega) d\omega = 0 \qquad (39)$$

The admissibility condition ensures that the inverse transform and Parseval formula are applicable. Analytically, the Mexican hat wavelet is represented by

$$\psi(x) = \frac{2}{\sqrt{3} * \pi^{1/4}} \exp(-x^2/2) * (1 - x^2) \qquad (40)$$

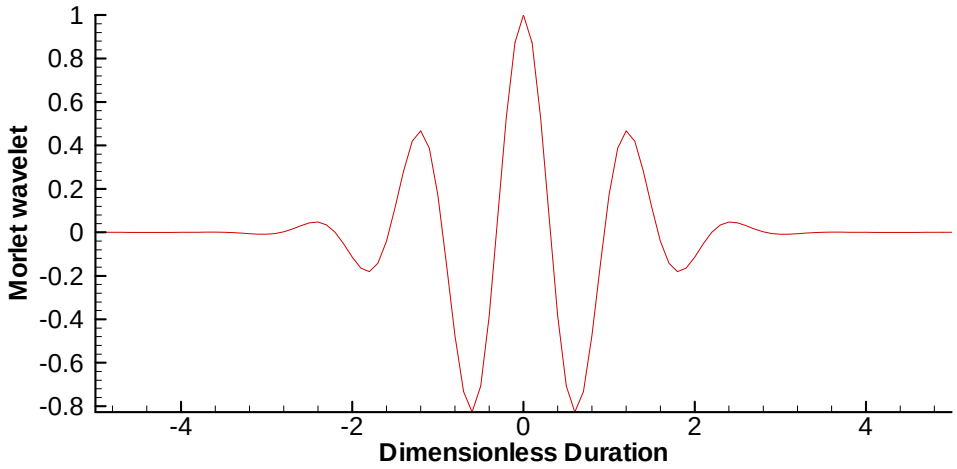

FIGURE 4.4 The Morlet wavelet.

Selection of the wavelet shape is one of the important decisions on the user's part. It is similar to the choice of instruments of observation, like X-rays or filtered colored light or infra-red; or again like the selection of dyes as specific markers of biological tissues: each will show a part of the reality with specificity, and each reveals something that the others had concealed.

Although the discrete Haar wavelets predate Morlet's, it was only as a consequence of Morlet's work that the mathematical foundations of wavelets as a better formulation of time-frequency methods were laid. Conceptually related to windowed-Fourier analysis, the Morlet wavelet is a locally periodic wave train. It is obtained by taking a

complex sine wave, and by localizing it with a Gaussian (bell-shaped) envelope. As shown in figure 4.4, the Morlet wavelet is represented by

$$\psi(x) = \exp(-x^2/2) * \cos(5x) \qquad (41)$$

4.3 Wavelet application methods in our work

Farge (1992) gave recent summaries of applications of wavelet analysis in the fluid mechanics. Numerous papers on this topic have been published rapidly, but from the view of fluids engineering these researchers can be broadly split into two categories: (1) Extracting the characters of turbulent or eddy structure from the wavelet analysis of experimental data and simulation data (2) developing turbulence modeling and numerical methods based on wavelet analysis. In our research, we focused on the wavelet analysis of our experimental data, which means differential pressure and velocity vectors from PIV measurement.

4.3.1 One-dimensional continuous wavelet time-frequency map

We can identify the individual peaks and troughs of the cosine wave as well as their frequency: this compromise between the temporal domain and the spectral domain is the hallmark of wavelet transforms. The cost of this compromise is the need to map the signal as a function of both time and duration. Therefore, we see that some spectral

resolution is achieved by selection of the wavelet size, and some temporal resolution follows from the location of the wavelet relative to the signal. One of the most widely used tools of Fourier analysis is the Parseval theorem. It enables the experimentalist to view how the `energy' in the signal is distributed among frequencies. The Fast Fourier Transform (FFT) algorithms have made power spectra one of the obvious diagnostics tools during data acquisition, and energy maps are a versatile alternative.

Wavelet transforms are endowed with a similar theorem. This time, the energy density is distributed in the wavelet half-plane *(k,t)*, according to the expression

$$E(k,t) = \left| f(k,t) \right|^2 \Big/ \pi \qquad (42)$$

The result is an energy map, showing the distribution of energy corresponding to the wavelet map.

For non-periodic signals, the mean wavelet spectrum is similar to the Fourier spectrum. Of course, the energy map can be integrated in time at each duration. The result of this operation is to distribute the energy of the signal among the durations - a concept identical to that of the Fourier power spectrum. The content of the Parseval formulae for Fourier and wavelet transforms needs to be reexamined.

What the equations say is the following

$$\int_{+\infty}^{-\infty} \left| f(t) \right|^2 dt \ \textit{total energy in signal}$$

$$= \int_{+\infty}^{-\infty} \left| f(z) \right|^2 dz \ \textit{total energy in Fourier spectrum}$$

$$= \int_{-\infty}^{\infty}\int_{0}^{\infty} \left| f(k,t) \right|^2 \Big/ \pi \; dtdk \quad \textit{total energy in the energy map}$$

$$= \int_{0}^{\infty} E(k)dk \quad \textit{total energy in the mean spectrum} \qquad (43)$$

The integrals have the same value. Clearly, this does not imply that the integrands should be equaled point-by-point; in fact, there is infinity of integrands that would meet the integral criterion, each for a different functional basis. It is a matter of interpretation to associate the integrands with an energy density. By using the Fourier spectra exclusively, the user may have developed a false sense of security in this regard, and the clear interpretation in the case of periodic signals provides no hint of trouble. However, in the case of broadband spectra associated with a sequence of square waves, say, the particular spectral content at a given frequency is clearly an artifact of the sine wave decomposition. As the signal becomes more intermittent or modulated, no functional basis seems privileged, least of all a periodic one covering the entire time axis.

Now with the method discussed above, we show the standard signals and their corresponding results of wavelet time frequency map, wavelet energy map, and wavelet density spectrum.

Figure 4.5 (a) gives the standard periodical cosine periodical signal and the frequency of this signal is 10 Hz.

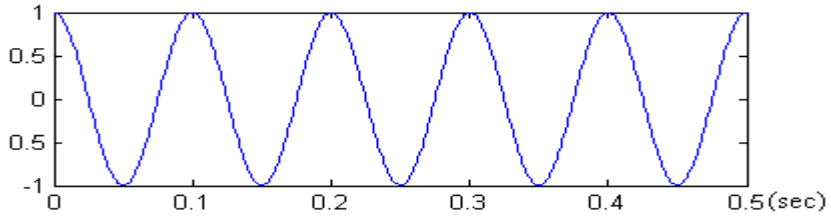

FIGURE 4.5 (a) Standard cosine periodical signal $\cos(2\pi * 10 * t)$.

Figure 4.5 (b) gives the wavelet time frequency map of the signal in figure 4.5 (a). It can be seen that the strong red color corresponds to the peak of the signal 4.5 (a) and the strong blue color corresponds to the valley of the signal 4.5(b). And the center line of the vortex structure of figure 4.5 (b) is related to 10 Hz. Figure 4.5 (c) gives the wavelet energy map of the signal in figure 4.5 (a). The red color represents the strongest intensity of the energy and the blue color represents the weakest intensity of the energy. By this way, the energy distribution can be shown in a two-dimensional plane. The horizontal axis is time and the vertical axis is scale which also corresponds to frequency. The center line of the vortex structure of figure 4.5 (c) is related to 10 Hz.

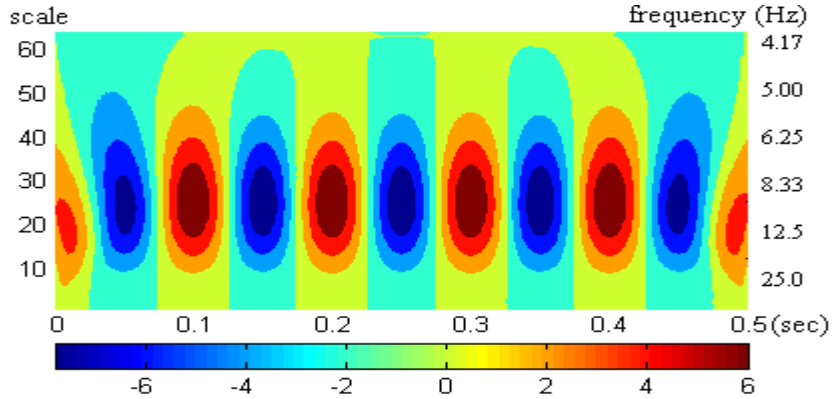

FIGURE 4.5 (b) Wavelet time frequency map of the signal in figure 4.5 (a) using Mexican hat wavelet.

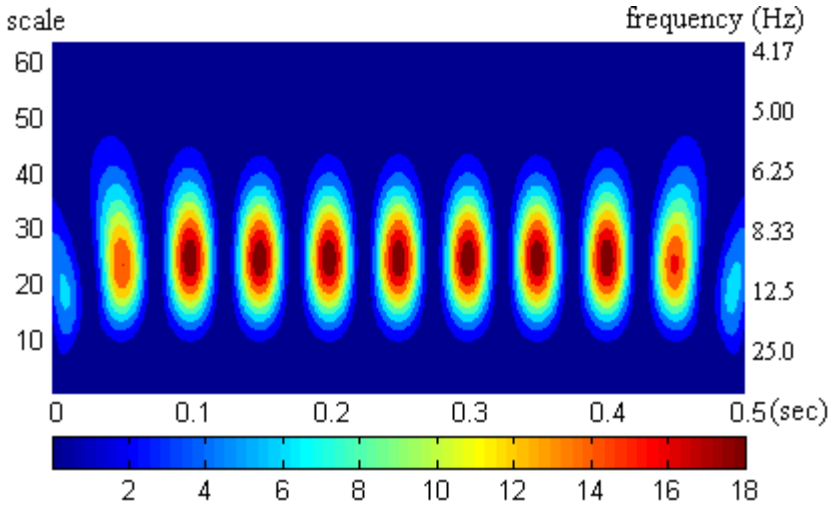

FIGURE 4.5 (c) Wavelet energy map of the signal in figure 4.5 (a) using Mexican hat wavelet.

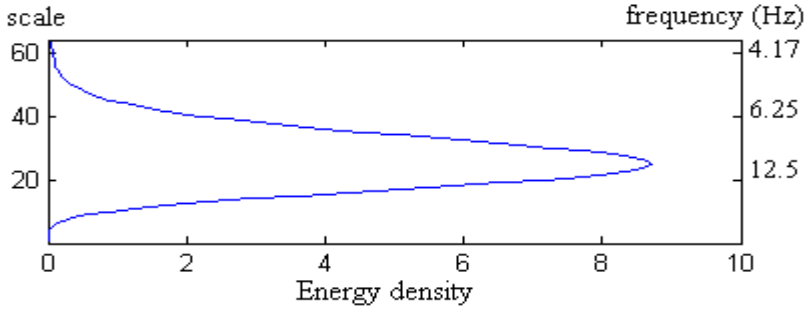

FIGURE 4.5 (d) Wavelet density spectrum of the signal in figure 4.5 (a) using Mexican hat wavelet.

Figure 4.5 (d) gives the wavelet density spectrum of the signal in figure4.5 (a). The peak of the energy density corresponds to 10 Hz.

Figure 4.5 (e) gives the wavelet time frequency map of the signal in figure4.5 (a) using Morlet wavelet. It can be seen that the strong red color corresponds to the peak of the signal 4.5 (a) and the strong blue color corresponds to the valley of the signal 4.5(b).

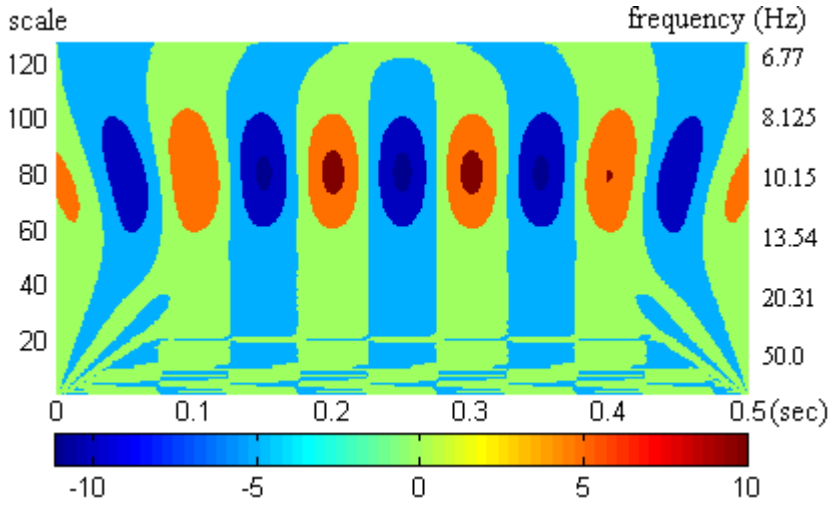

FIGURE 4.5 (e) Wavelet time frequency map of the signal in figure 4.5 (a) using Morlet wavelet.

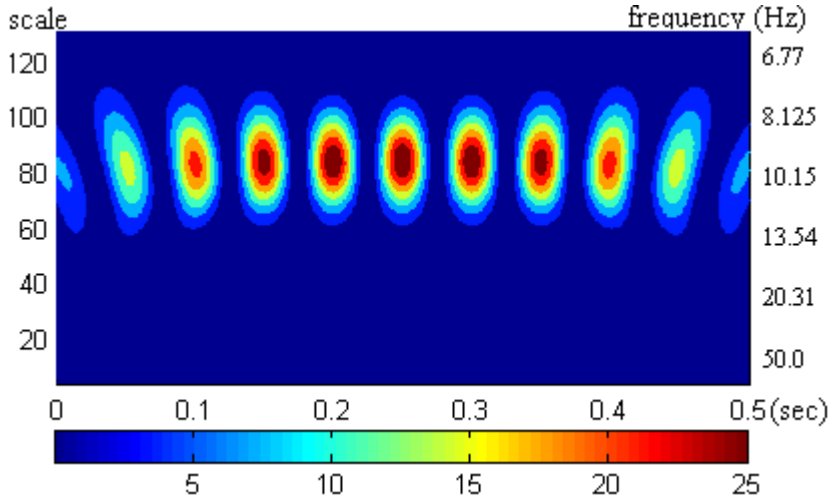

FIGURE 4.5 (f) Wavelet energy map of the signal in figure 4.5 (a) using Morlet wavelet.

Figure 4.5 (f) gives the wavelet energy map of the signal in figure 4.5 (a) using Morlet wavelet. For a simple signal like signal 4.5 (a) which is a single cosine wave, the difference of using Mexican hat wavelet and Morlet wavelet is not shown.

Figure 4.5 (g) gives the wavelet time frequency map of the signal in figure 4.5 (a) by using Morlet wavelet. Again, the main frequency of 10 Hz can be detected by this figure.

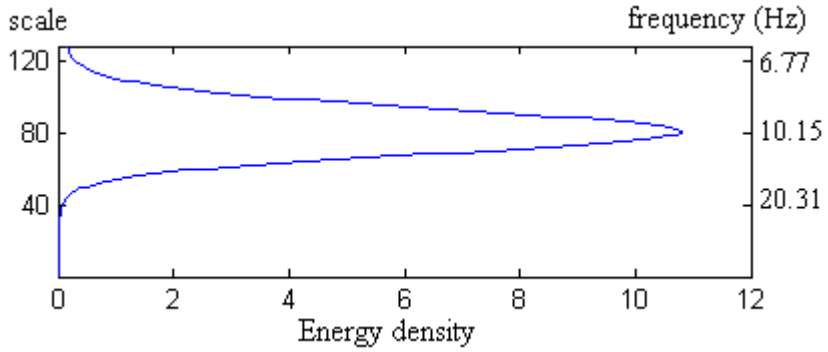

FIGURE 4.5 (g) Wavelet density spectrum of the signal in figure4.5 (a) using Morlet wavelet.

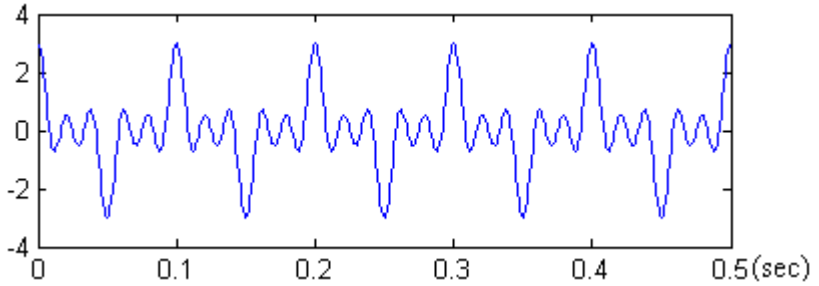

FIGURE 4.6 (a) $\cos(2\pi*10*t)+\cos(2\pi*30*t)+\cos(2\pi*50*t)$.

Now we need to discuss some relatively complex signals of three frequencies: $\cos(2\pi*10*t)+\cos(2\pi*30*t)+\cos(2\pi*50*t)$ in Figure 4.6 (a). Figure 4.6 (b) gives the wavelet time frequency map of the signal in figure 4.6 (a) using Mexican hat. In this figure, the frequency of 10 Hz can be clearly seen. The frequency of 30 Hz can still be seen. However, the frequency of 50 Hz can hardly be detected in this figure.

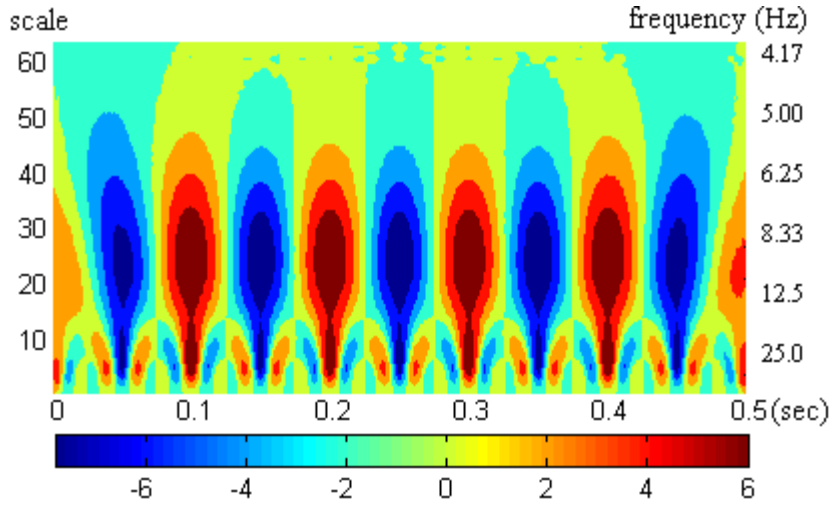

FIGURE 4.6 (b) Wavelet time frequency map of the signal in figure 4.6 (a) using Mexican hat wavelet.

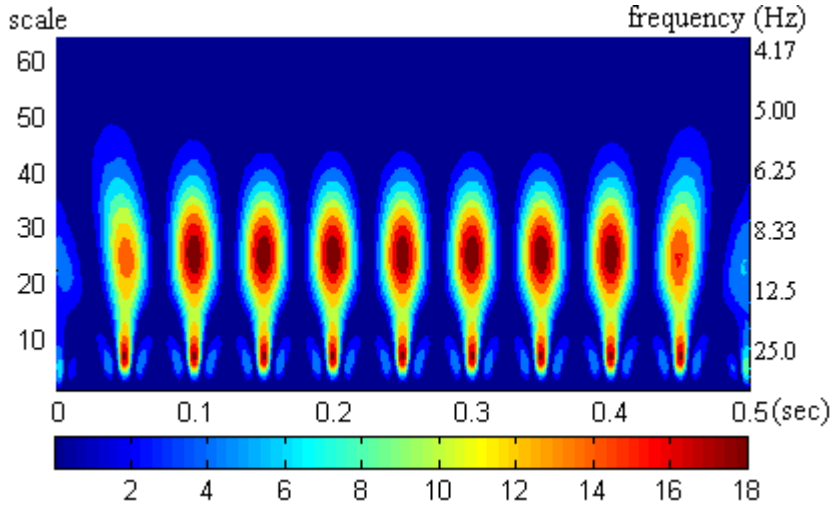

FIGURE 4.6 (c) Wavelet energy map of the signal in figure 4.6 (a) using Mexican hat wavelet.

Figure 4.6 (c) gives the wavelet energy map of the signal in figure 4.6 (a). The frequency of 10 Hz and 30 Hz can be seen, but the 50 Hz signal could not be found. Figure 4.6 (d) gives the wavelet density spectrum of the signal in figure 4.6 (a). To

detect the 50 Hz signal hided inside the original signal, other wavelet function needs to be tested.

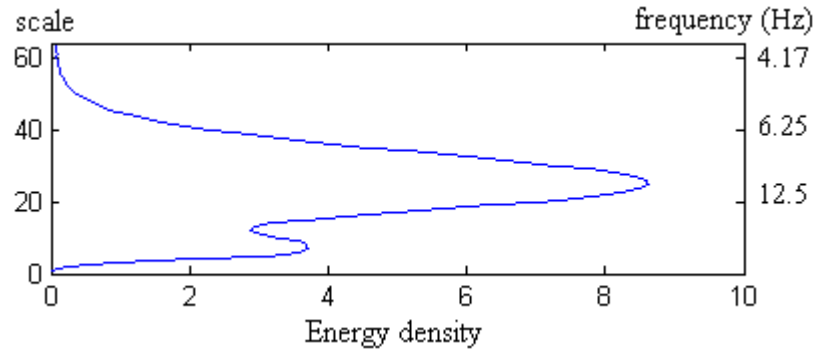

FIGURE 4.6 (d) Wavelet density spectrum of the signal in figure 4.6 (a) using Mexican hat wavelet.

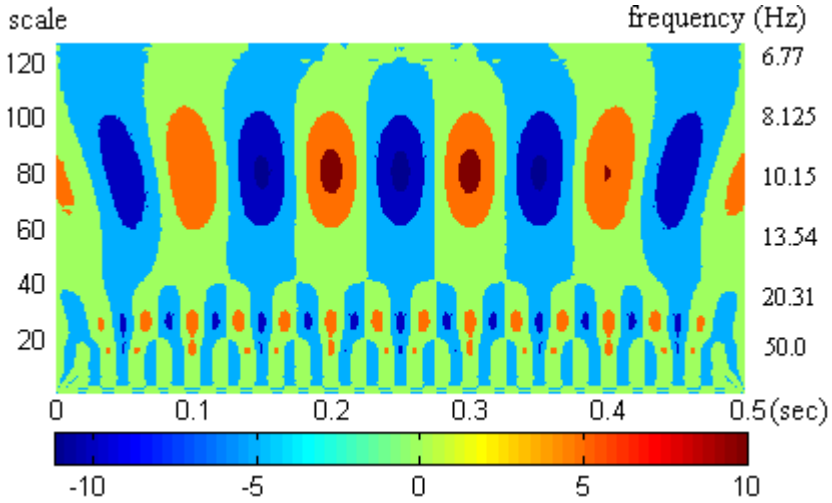

FIGURE 4.6 (e) Wavelet time frequency map of the signal in figure 4.6 (a) using Morlet wavelet.

Figure 4.6 (e) gives the wavelet time frequency map of the signal in figure 4.6 (a) using Morlet wavelet. Now, the three frequencies can be seen in this figure. So in figure 4.6 (f), the wavelet energy map gives the energy distribution at both time and

frequency domain. The frequency of 10 Hz, 30 Hz and 50 Hz can all be found in the figure.

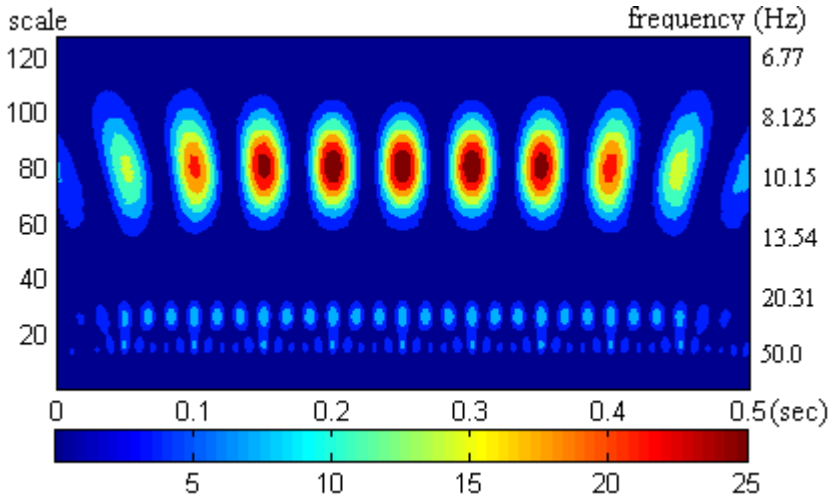

FIGURE 4.6 (f) Wavelet energy map of the signal in figure 4.6 (a) using Morlet wavelet.

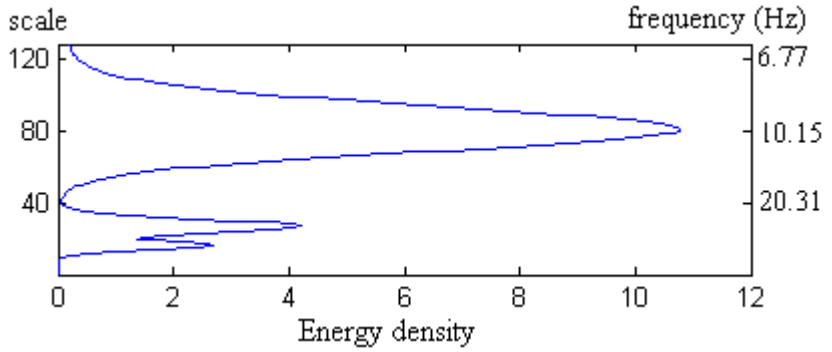

FIGURE 4.6 (g) Wavelet density spectrum of the signal in figure 4.6 (a) using Morlet wavelet.

Figure 4.6 (g) shows that Morlet wavelet is good to distinguish the different frequencies in the high frequency range. However, in the low frequency range, Morlet wavelet may have some problems of aliasing as shown in figure 4.6 (e). For real

signals measured in labs, the noise disturbance must be considered. Now we generate some white noise and add them to the signal 4.6 (a). Figure 4.7 (a) shows the signal.

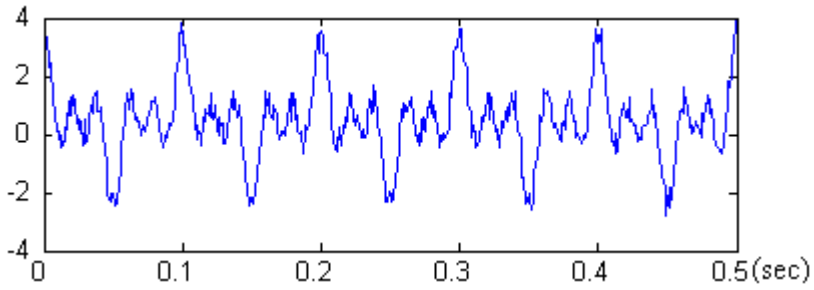

FIGURE 4.7 (a) $\cos(2\pi * 10 * t) + \cos(2\pi * 30 * t) + \cos(2\pi * 50 * t)$ +white noise.

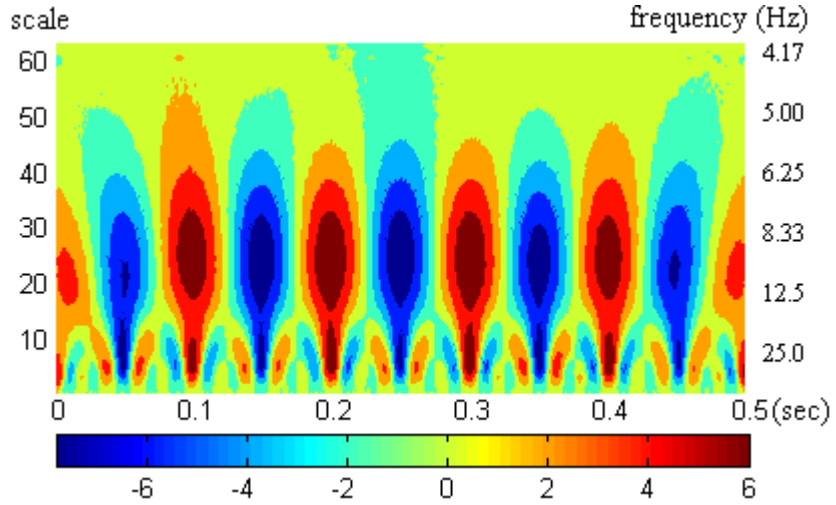

FIGURE 4.7 (b) Wavelet time frequency map of the signal in figure 4.7 (a) using Mexican hat wavelet.

The wavelet time frequency map of the signal in figure 4.7 (a) is given in figure 4.7 (b). Comparing figure 4.7 (b) with figure 4.6 (b), the vortex structures fade in the left and right boundary of the map. This effect is caused by the noise distribution. For the

simple signals like $\cos(2\pi*10*t)+\cos(2\pi*30*t)+\cos(2\pi*50*t)$ +white noise, the structures can still be detected. For real complex signals from turbulence measurement, new algorithm is still needed.

Figure 4.7 (c) gives the wavelet energy map of the signal in figure 4.7 (a). Comparing figure 4.7 (c) with figure 4.6(c), the disturbance of noise is more obvious.

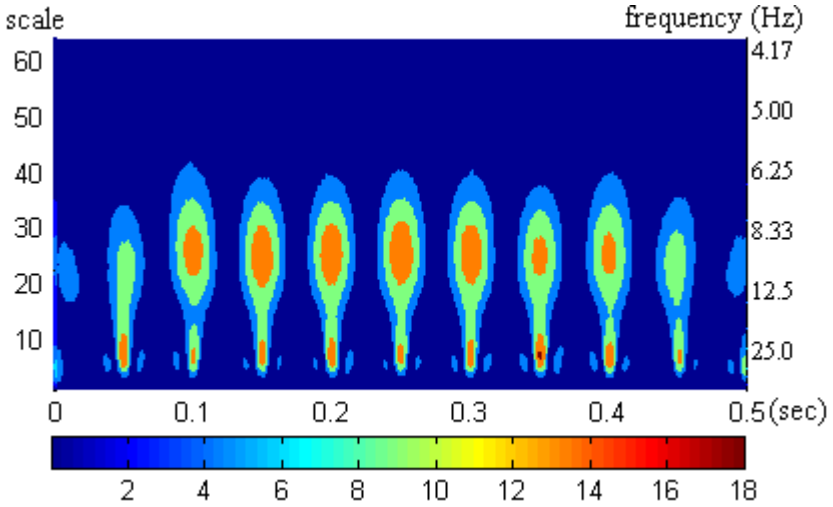

FIGURE 4.7 (c) Wavelet energy map of the signal in figure 4.7 (a) using Mexican hat wavelet.

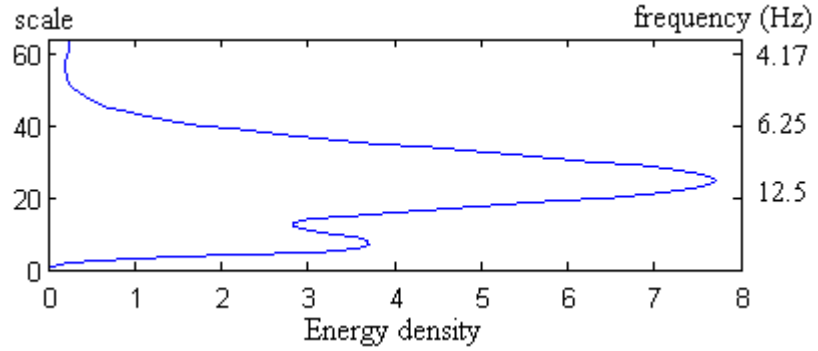

FIGURE 4.7 (d) Wavelet density spectrum of the signal in figure 4.7 (a) using Mexican hat wavelet.

Figure 4.7 (d) gives the density spectrum of the signal in figure 4.7 (a) using Mexican hat wavelet.

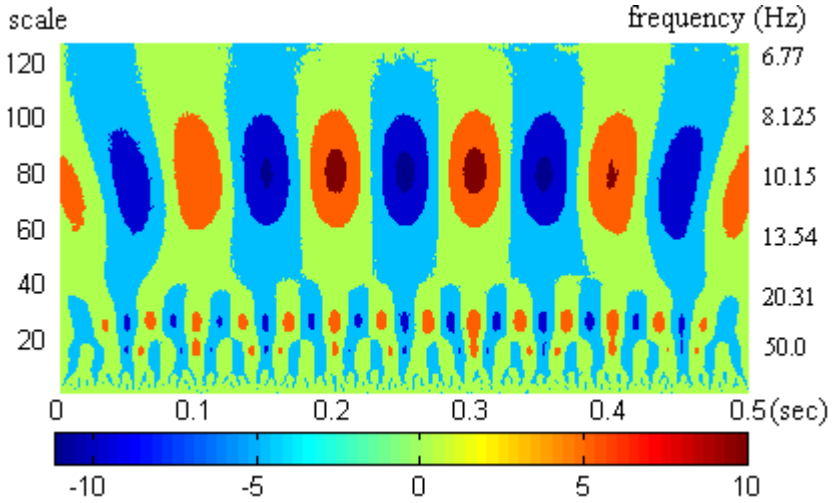

FIGURE 4.7 (e) Wavelet time frequency map of the signal in figure 4.7 (a) using Morlet wavelet.

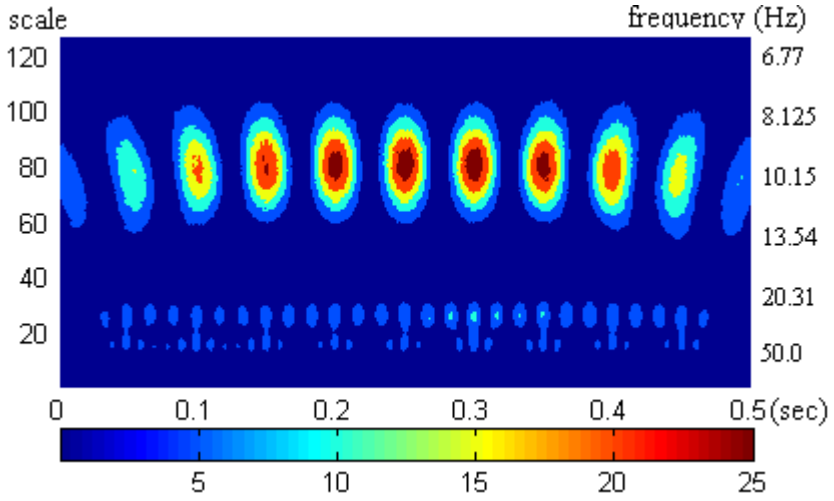

FIGURE 4.7 (f) Wavelet energy map of the signal in figure 4.7 (a) using Morlet wavelet.

Comparing figures 4.7 (e), 4.7 (f) with figures 4.6 (e), 4.6 (f), the disturbance of noise can be clearly seen. Choosing Mexican hat wavelet or Morlet wavelet can not

remove the disturbance of noise at this time. Figure 4.7 (g) gives the wavelet density spectrum of the signal in figure 4.7 (a) using Morlet hat wavelet. The three frequency can be detected.

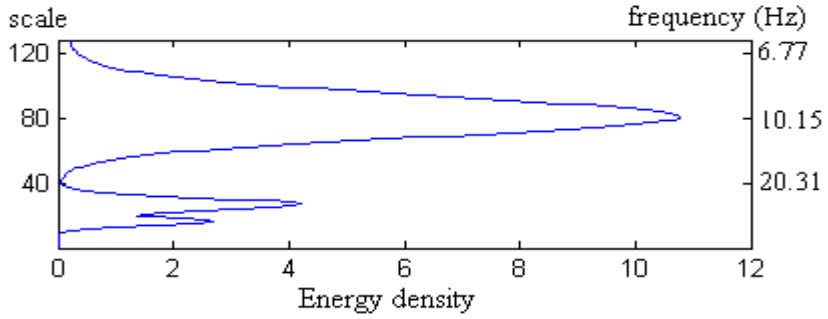

FIGURE 4.7 (g) Wavelet density spectrum of the signal in figure 4.7 (a) using Morlet wavelet.

4.3.2 Wavelet auto-correlation map

In Section 4.2.3, the wavelet auto-correlation map algorithm was discussed. In figures 4.5, 4.6, 4.7, the standard cosine signal was processed directly by one-dimensional continuous wavelet transform. From the wavelet time frequency map, wavelet energy map and wavelet density spectrum using Mexican hat and Morlet wavelet, it can be found that the time-frequency information was projected into two-dimensional plane. The different period components of the original signal were clearly discerned. However, when the original signal was not standard signals like sine or cosine and when a lot of noise disturbs the experiment measurement, it is hard to use the one-dimensional continuous wavelet transform to capture the essence information

inside the original signal. For signals from turbulence measurement, the problem will be more severe. Traditional method like autocorrelation, cross-correlation and Fourier transform just provide the decomposition of signal only in time domain or in frequency domain. Just like playing a piano, using correlation method, you can only know how often a key was played without knowing which key was played. Using Fourier transform, you can only know which key was played without knowing when it was played. With the idea of wavelet auto-correlation map, wavelet cross-correlation map, the correlation information of the signal can be clearly observed in both time domain and frequency domain. Comparing figures 4.6 (b), (c) with figures 4.6 (e), (f), it can be found that the frequency resolution by using Morlet wavelet is better than using Mexican hat wavelet since the component of 50 Hz can be discerned from figures 4.6 (e), (f). However, Morlet wavelet can cause aliasing problem, which can be seen, from figure 4.6 (e). Wavelet energy map tells us the energy evolution process at each frequency. Comparing figure 4.6 with figure 4.7, the only difference of the original signal is the white noise. However, the white noise brings the bad resolution in high frequency domain in figure 4.7 (e) and figure 4.7 (f). Using wavelet auto-correlation map method, the noise disturbance was removed when comparing figure 4.8 (a) with figures 4.6 (b) and 4.7 (b).

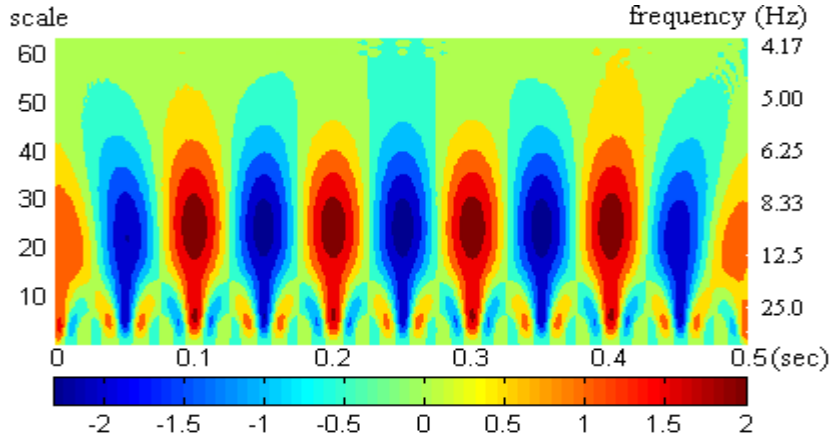

FIGURE 4.8 (a) Wavelet auto-correlation map of the signal in figure 4.7 (a) using Mexican hat wavelet.

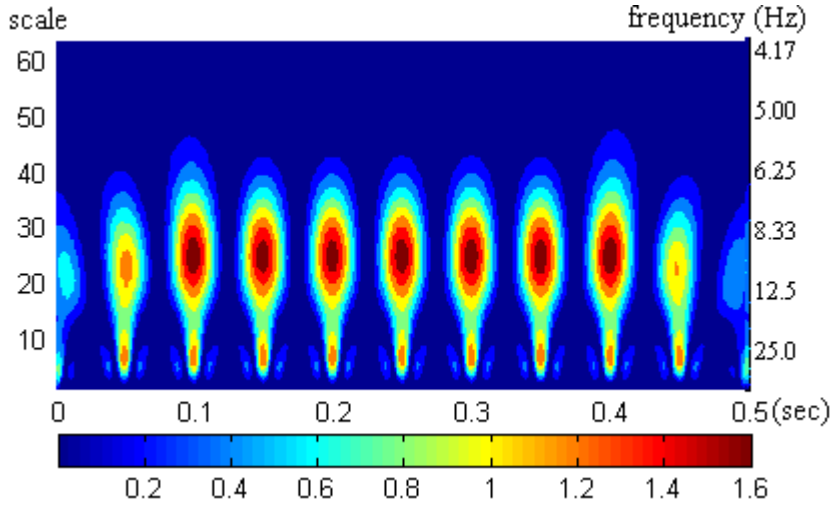

FIGURE 4.8 (b) Wavelet auto-correlation energy map of the signal in figure 4.7 (a) using Mexican hat wavelet.

Using wavelet auto-correlation energy map method, the noise disturbance was also removed when comparing figure 4.8 (b) with figure 4.7(c), figure 4.6 (c). Figure 4.8 (c) gives the wavelet auto-correlation density spectra of the signal in figure 4.7 (a) using Mexican hat wavelet.

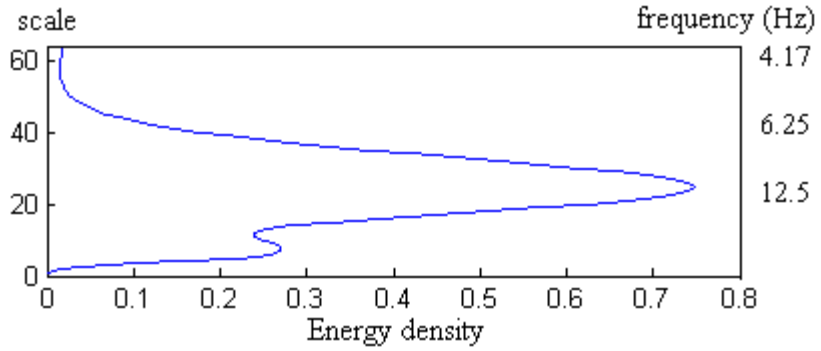

FIGURE 4.8 (c) Wavelet auto-correlation density spectra of the signal in figure 4.7 (a) using Mexican hat wavelet.

Using wavelet auto-correlation map method by Morlet wavelet, the noise disturbance was also removed when comparing figure 4.8 (d) with figure 4.7(e), figure 4.6 (e).

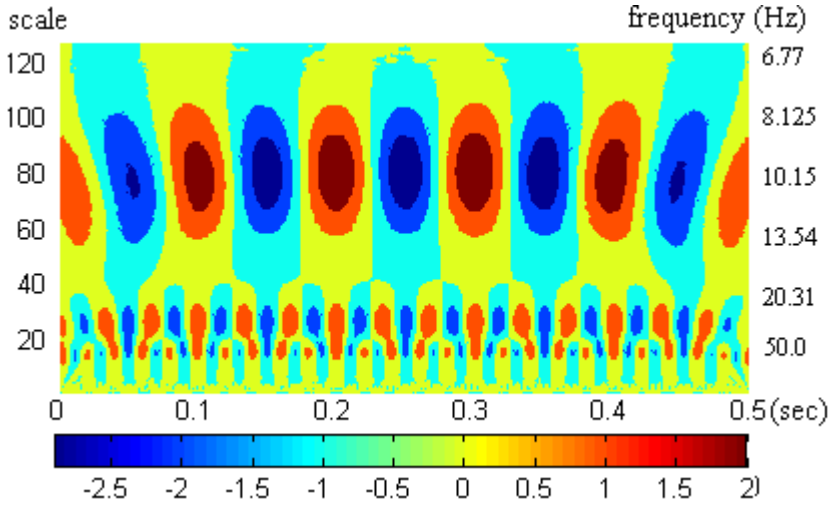

FIGURE 4.8 (d) Wavelet auto-correlation map of the signal in figure 4.7 (a) using Morlet wavelet.

Using wavelet auto-correlation energy map method by Morlet wavelet, the noise disturbance was also removed when comparing figure 4.8 (e) with figures 4.6 (f) and 4.7 (f).

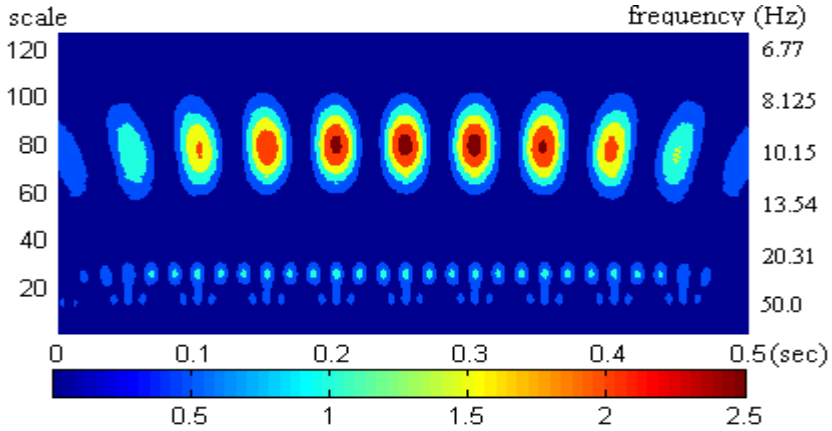

FIGURE 4.8 (e) Wavelet auto-correlation energy map of the signal in figure 4.7 (a) using Morlet wavelet.

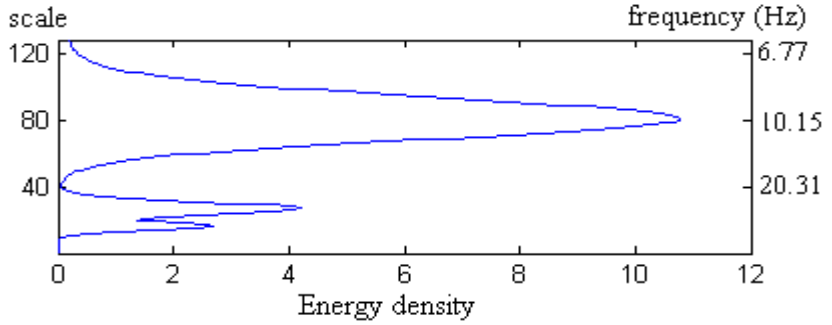

FIGURE 4.8 (f) Wavelet auto-correlation density spectra of the signal in figure 4.7 (a) using Morlet wavelet.

Figure 4.8 (f) gives the wavelet auto-correlation density spectra of the signal in figure 4.7 (a) using Morlet wavelet.

4.3.3 Wavelet cross-correlation map

Figures 4.9 (a) and 4.9 (b) provide two generated signals. To detect the correlation information between these two signals, the wavelet cross-correlation map could be used. In figures 4.9 (c), 4.9 (d), 4.9 (e) and 4.9 (f), it can be found that not only the white noise disturbance was removed but also the frequency domain information of the similarity between two different signals was provided. From the original signal, we know that these two signals both have 10 Hz and 30 Hz cosine signals in common. Figure 4.9 (c) gives the wavelet cross-correlation map of the signals in figures 4.9 (a) and 4.9 (b) using Mexican hat wavelet. Figure 4.9 (d) gives the wavelet cross-correlation energy map of the signals in figures 4.9 (a) and 4.9 (b) using Mexican hat wavelet.

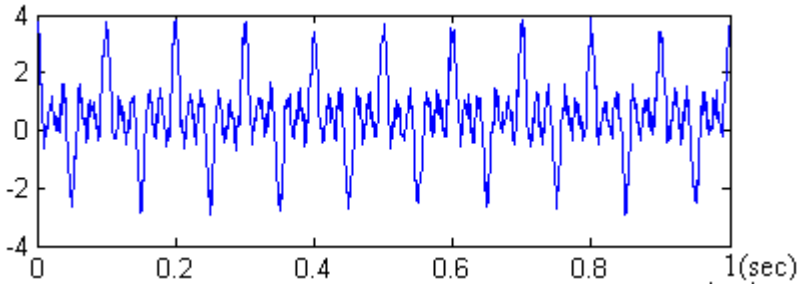

FIGURE 4.9 (a) $\cos(2\pi * 10 * t) + \cos(2\pi * 30 * t) + \cos(2\pi * 50 * t)$ + white noise in 1 second.

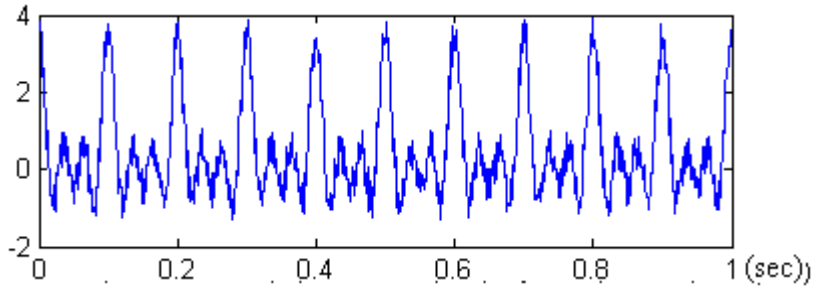

FIGURE 4.9 (b) $\cos(2\pi * 10 * t) + \cos(2\pi * 30 * t) + \cos(2\pi * 20 * t) +$ white noise in 1 second.

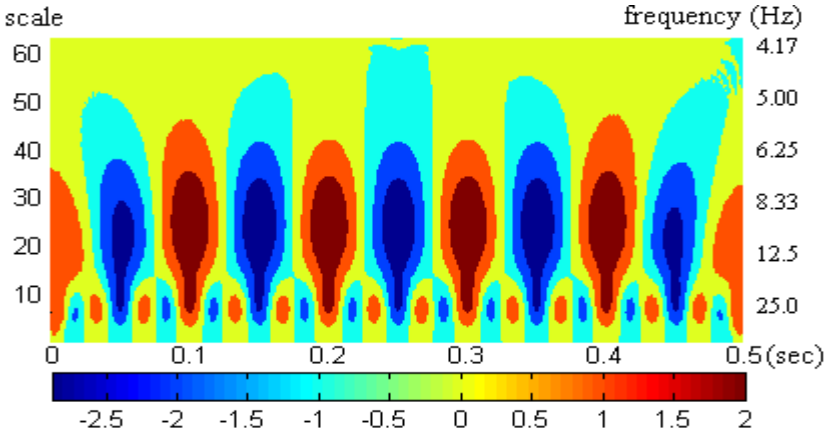

FIGURE 4.9 (c) Wavelet cross-correlation map of the signals in figure 4.9 (a) and figure 4.9 (b) using Mexican hat wavelet.

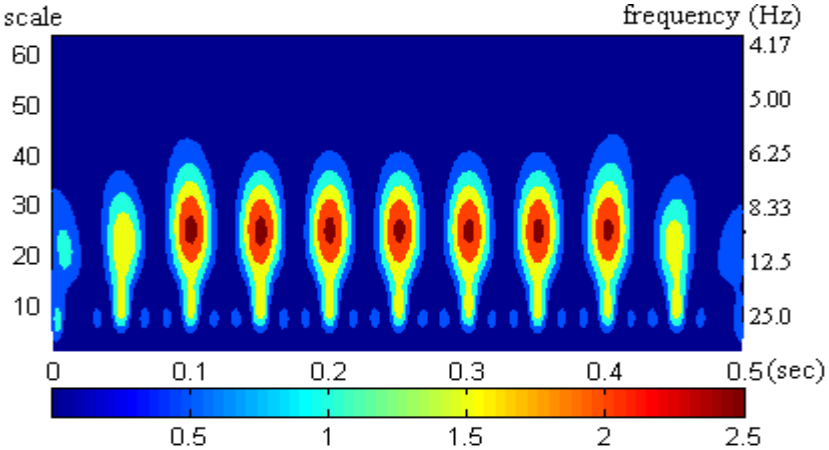

FIGURE 4.9 (d) Wavelet cross-correlation energy map of the signals in figures 4.9 (a) and 4.9 (b) using Mexican hat wavelet.

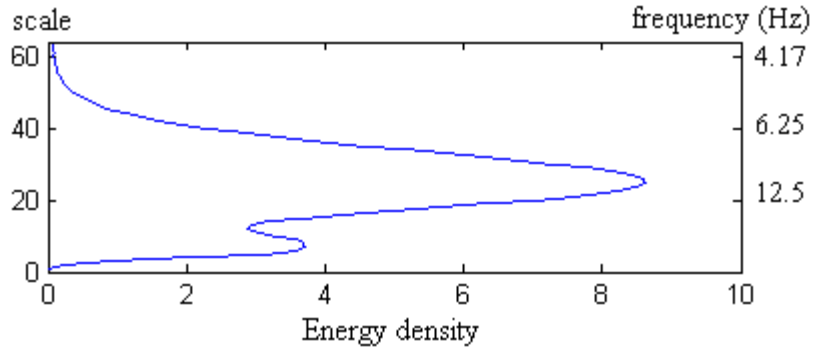

FIGURE 4.9 (e) Wavelet cross-correlation density spectra of the signals in figures 4.9 (a) and 4.9 (b) using Mexican hat wavelet.

Figure 4.9 (e) gives the wavelet cross-correlation density spectra of the signals in figures 4.9 (a) and 4.9 (b) using Mexican hat wavelet.

Figure 4.9 (f) gives the wavelet cross-correlation map of the signals in figures 4.9 (a) and 4.9 (b) using Morlet wavelet. Figure 4.9 (g) gives the wavelet cross-correlation energy map of the signals in figures 4.9 (a) and 4.9 (b) using Morlet wavelet.

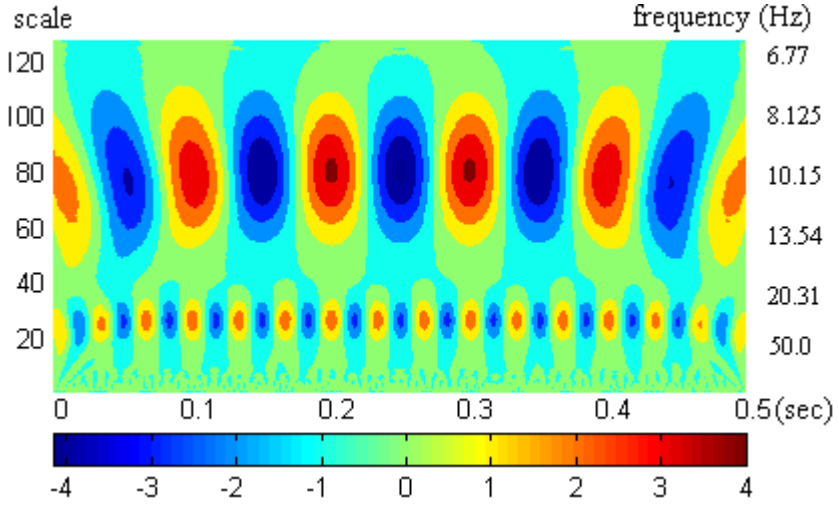

FIGURE 4.9 (f) Wavelet cross-correlation map of the signals in figures 4.9 (a) and 4.9 (b) using Morlet wavelet.

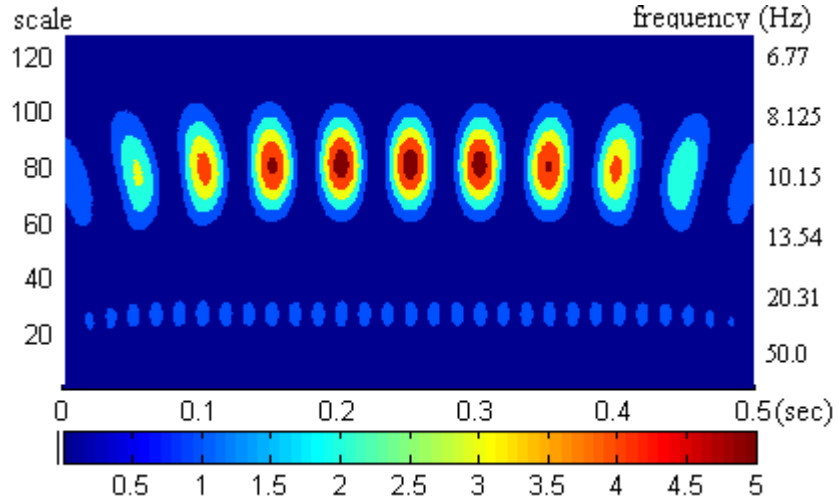

FIGURE 4.9 (g) Wavelet cross-correlation energy map of the signals in figures 4.9 (a) and 4.9 (b) using Morlet wavelet.

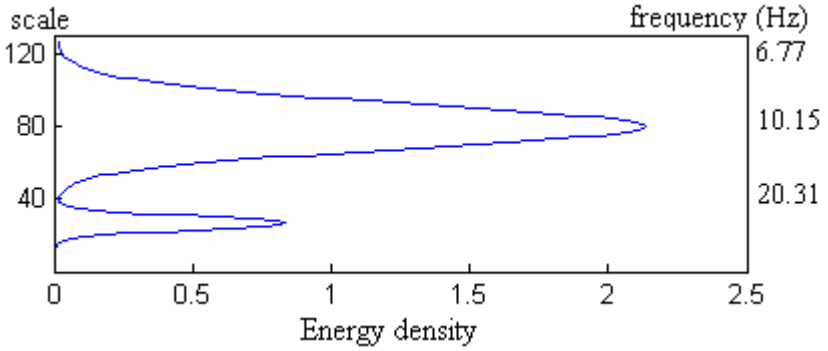

FIGURE 4.9 (h) Wavelet cross-correlation density spectra of the signals in figures 4.9 (a) and 4.9 (b) using Morlet wavelet.

Figure 4.9 (h) gives the wavelet cross-correlation density spectra of the signals in figures 4.9 (a) and 4.9 (b) using Morlet wavelet.

From figures 4.9 (c), 4.9 (d), 4.9 (f) and 4.9 (g), it can be clearly seen that 10 Hz and 30 Hz signals coexist. In our turbulence measurement, we get velocity information at different locations. Applying this wavelet cross-correlation map method, it can be

believed that the coherent structure could be discerned and more information in the boundary layer of the turbulence field could be found.

All these methods were applied for data measured from single phase flow and micro-bubbles injected two phase flow at the same Reynolds number.

CHAPTER V

EXPERIMENTAL RESULTS AND ANALYSIS

In our lab, the extensive study of drag reduction using microbubbles within the boundary layer has been studied for a long time. And consistent results have been obtained from different researchers over a period of time (Gutierrez Torres 2004, Jimenez Bernal 2004, Hassan, 2003) Some preliminary results about modification of the boundary layer structure by microbubbles have been already presented in their papers. The non-dimensional mean streamwise U^+ velocity versus the non-dimensional y location, y^+ agreed well with the results for a fully developed channel flow obtained form LDV (Warholic 1997) at very similar conditions in the single phase flow condition. Still in single phase condition, the calculation of shear stress using equation (2) and equation (10) agrees well. And these two agreements can validate the accuracy of our PIV measurement.

The drag reduction percentage can be calculated by equation (3) and the corresponding void fraction can be calculated by equation (4). The calculation result is listed in Table 5.1. The maximum drag reduction, 38%, was obtained with a local void fraction of 4.8%. The wavelet cross-correlation map and wavelet auto-correlation map for single phase and maximum drag reduction are compared at several locations. The diameter, d, of the bubble is presented in wall units $\left(d^+ = \frac{du_\tau \rho}{\mu} \right)$, where u_τ is the friction velocity.

u_τ [m/s]	d+	Void fraction (α)	Drag Reduction
0.0091	0.27	4.90%	38.40%

TABLE 5.1 Drag reduction at various void fraction conditions

All the streamwise and normal turbulence intensities, Reynolds stresses from single phase flow and two phase were showed and discussed both in Gutierrez Torres (2004) and Jimenez Bernal (2004). A significant decrease in the Reynolds stress with increasing local void fraction is obtained. This effect is sometimes called Reynolds stress defect in different experiments with drag-reducing polymers. A decorrelation between the streamwise (u') and the normal (v') velocity fluctuating components is the source of this decrease of the Reynolds stresses.

Spectra is one of the most essential parameters that are evaluated to give an idea about the distribution and interchange of fluctuating turbulent kinetic energy between eddies of different size with and without microbubbles in the near wall region. The spectra for the streamwsie fluctuating velocity $E_{uu}(k_1)$, for normal fluctuating component $E_{vv}(k_1)$ and for the product of the two components $E_{uv}(k_1)$ are evaluated in the streamwise wavenumber direction k_1 in Jimenez Bernal (2004).

To elucidate the changes that the presence of microbubbles originates within the turbulent boundary layer, two-point correlation coefficients and auto correlation coefficients were both calculated in longitudinal and transverse direction at different locations for the streamwise and normal fluctuating components of the velocity in Gutierrez Torres (2004) thesis. Furthermore, the integral length scale for each case is computed and presented in her study.

However, Fourier transform can only give spectrum information in frequency domain and the time domain information is lost in the spectra. Cross correlation and auto correlation can only give time domain information. Both methods are limited on the time-frequency or space-wavenumber analysis. For turbulence study, we believe that new technique is necessary to be used to elucidate the coherent structures near the boundary layers. As discussed in Chapter IV, wavelet analysis is a powerful tool for this purpose. We apply the algorithms of Wavelet cross-correlation map, Wavelet cross-correlation Energy map, Wavelet cross-correlation density spectra, Wavelet auto-correlation map, Wavelet auto-correlation Energy map and Wavelet auto-correlation density spectra to the PIV measurement data from single phase flow and two phase flow.

The turbulence quantities such as the streamwise and normal turbulent intensities, the Reynolds shear stresses, correlation and spectra calculations were always calculated to quantitie the difference between single phase flow and microbubble injected two phase flow to see the effects of microbubble injections. Good and relatively consistent conclusions were achieved. However, the shortcomings of these techniques are the lacking of detection for coherent structures. Whatever correlation or spectra, the processing for the turbulent data could only be done in time domain or in frequency domain.

5.1 Wavelet cross-correlation map in the longitudinal direction

Figures 5.1(a) and 5.1 (b) give the cross correlation coefficient in the longitudinal direction at y+ = 9.2 for streamwise fluctuating velocity and normal fluctuating velocity.

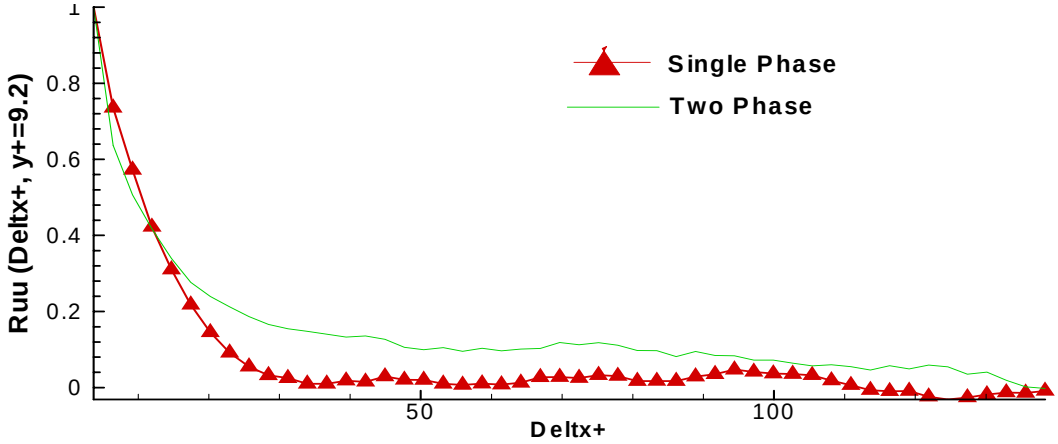

FIGURE 5.1 (a) Cross correlation coefficient in the longitudinal direction at y+ = 9.2 for streamwise fluctuating velocity.

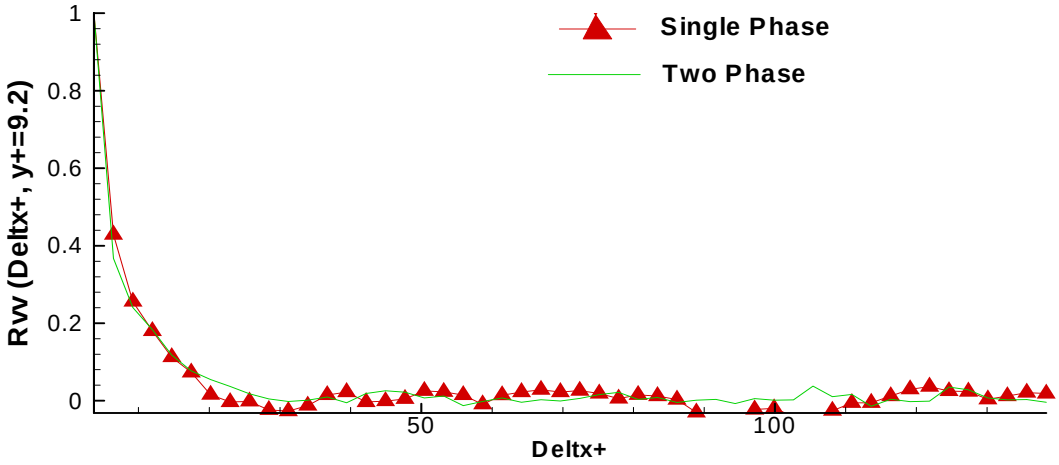

FIGURE 5.1 (b) Cross correlation coefficient in the longitudinal direction at y+ = 9.2 for normal fluctuating velocity.

Figures 5.2 (a) and 5.2 (b) give the wavelet cross-correlation map of (u u) using Mexican hat wavelet and Morlet wavelet in the longitudinal direction at y+ = 9.2 for streamwise fluctuating velocity.

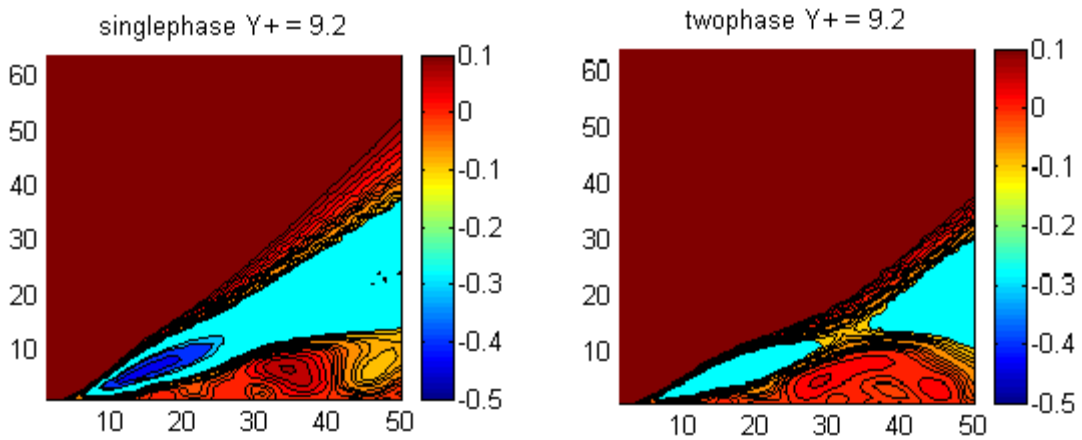

FIGURE 5.2 (a) Wavelet cross-correlation map of (u u) using Mexican hat wavelet in the longitudinal direction at y+ = 9.2 for streamwise fluctuating velocity.

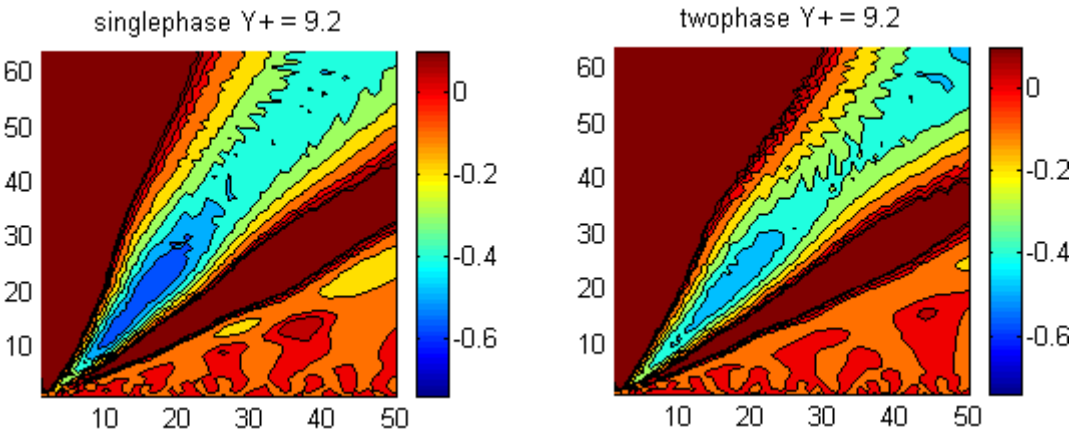

FIGURE 5.2 (b) Wavelet cross-correlation map of (u u) using Morlet wavelet in the longitudinal direction at y+ = 9.2 for streamwise fluctuating velocity.

Figures 5.3 (a) and 5.3 (b) give the wavelet cross-correlation map of (v v) using Mexican hat wavelet and Morlet wavelet in the longitudinal direction at y+ = 9.2 for normal fluctuating velocity.

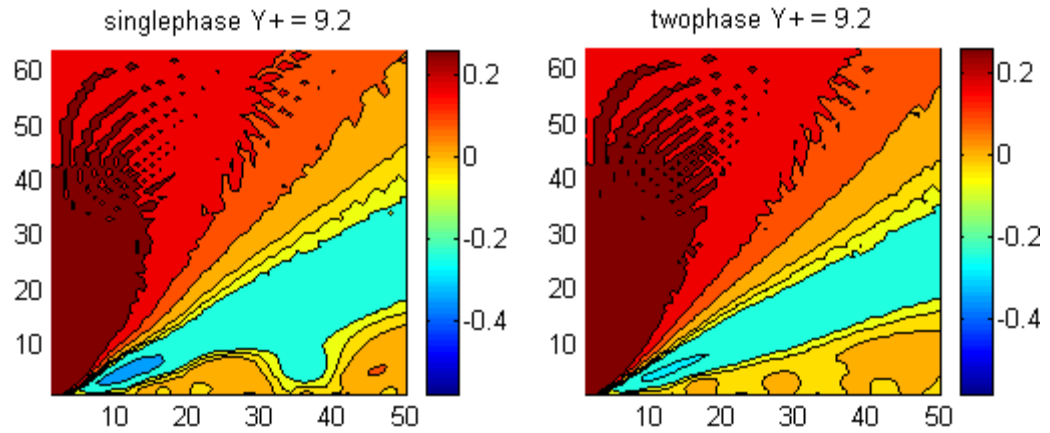

FIGURE 5.3 (a) Wavelet cross-correlation map of (v v) using Mexican hat wavelet in the longitudinal direction at y+ = 9.2 for normal fluctuating velocity.

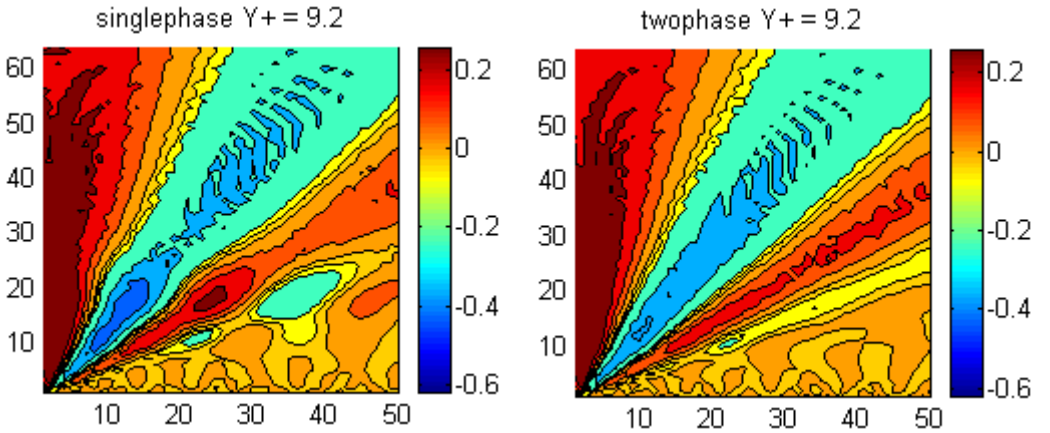

FIGURE 5.3 (b) Wavelet cross-correlation map of (v v) using Morlet wavelet in the longitudinal direction at y+ = 9.2 for normal fluctuating velocity.

Figures 5.4(a) and 5.4 (b) give the cross correlation coefficient in the longitudinal direction at y+ = 14.7 for streamwise fluctuating velocity and normal fluctuating velocity.

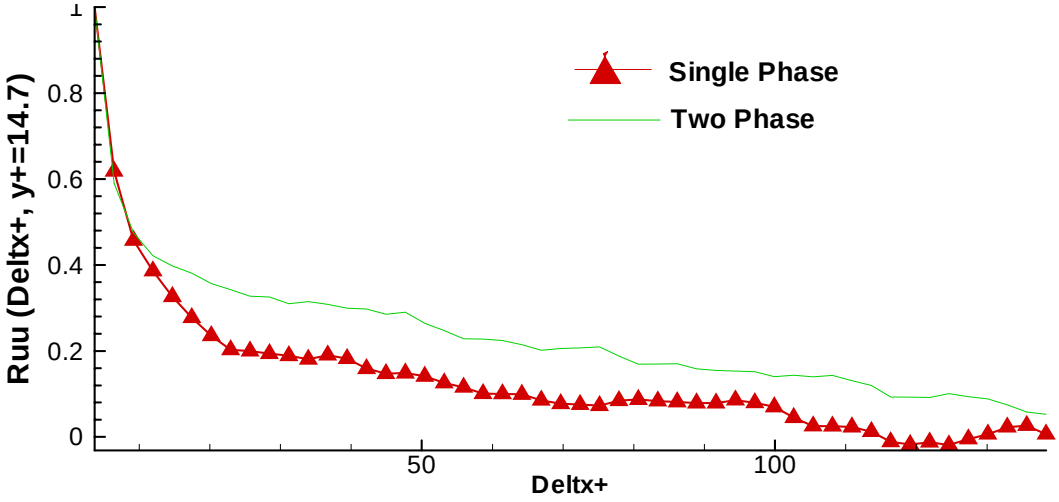

FIGURE 5.4 (a) Two-point correlation coefficient in the longitudinal direction at y+ = 14.7 for streamwise fluctuating velocity.

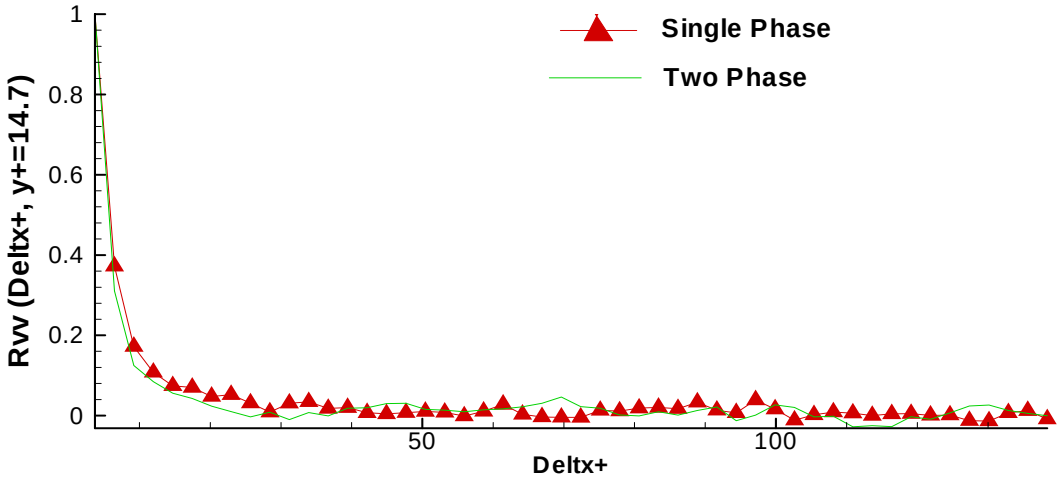

FIGURE 5.4 (b) Two-point correlation coefficient in the longitudinal direction at y+ = 14.7 for normal fluctuating velocity.

Figures 5.5 (a) and 5.5 (b) give the wavelet cross-correlation map of (u u) using Mexican hat wavelet and Morlet wavelet in the longitudinal direction at y+ = 14.7 for streamwise fluctuating velocity.

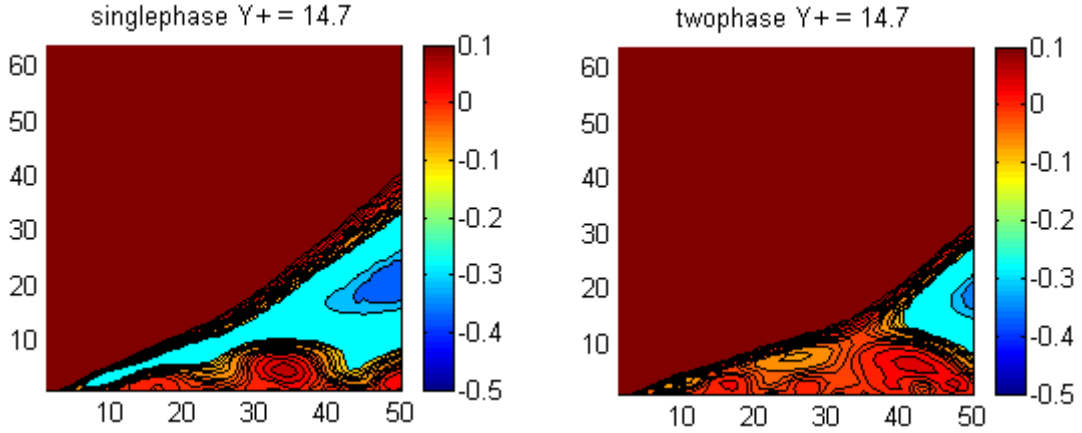

FIGURE 5.5 (a) Wavelet cross-correlation map of (u u) using Mexican hat wavelet in the longitudinal direction at y+ = 14.7 for streamwise fluctuating velocity.

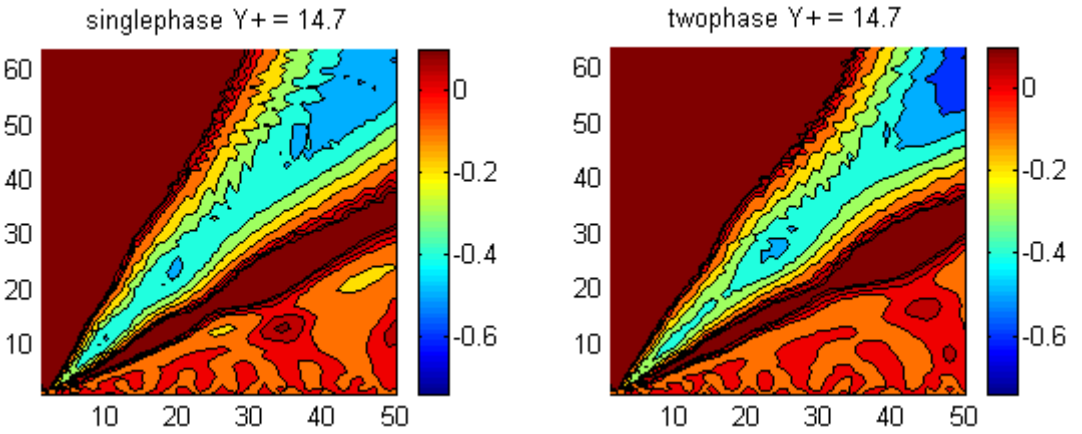

FIGURE 5.5 (b) Wavelet cross-correlation map of (u u) using Morlet wavelet in the longitudinal direction at y+ = 14.7 for streamwise fluctuating velocity.

Figures 5.6 (a) and 5.6 (b) give the wavelet cross-correlation map of (v v) using Mexican hat wavelet and Morlet wavelet in the longitudinal direction at y+ = 14.7 for normal fluctuating velocity.

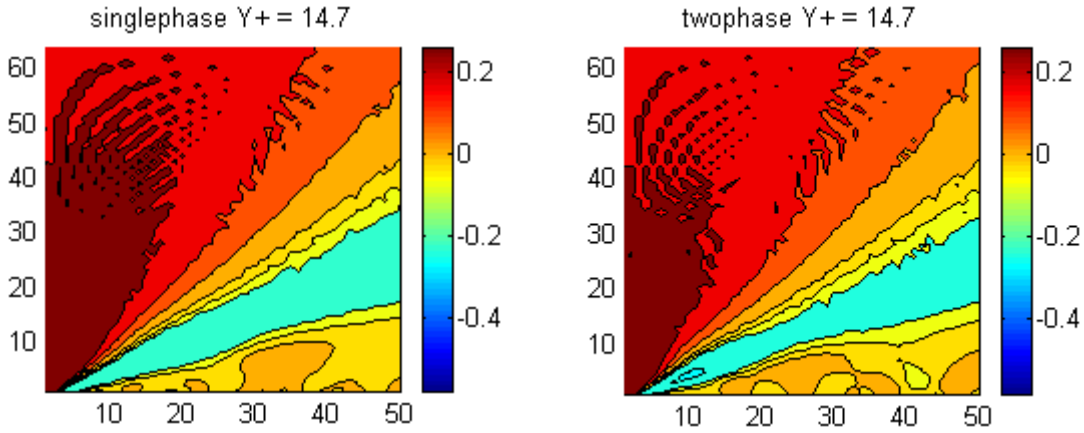

FIGURE 5.6 (a) Wavelet cross-correlation map of (v v) using Mexican hat wavelet in the longitudinal direction at y+ = 14.7 for normal fluctuating velocity.

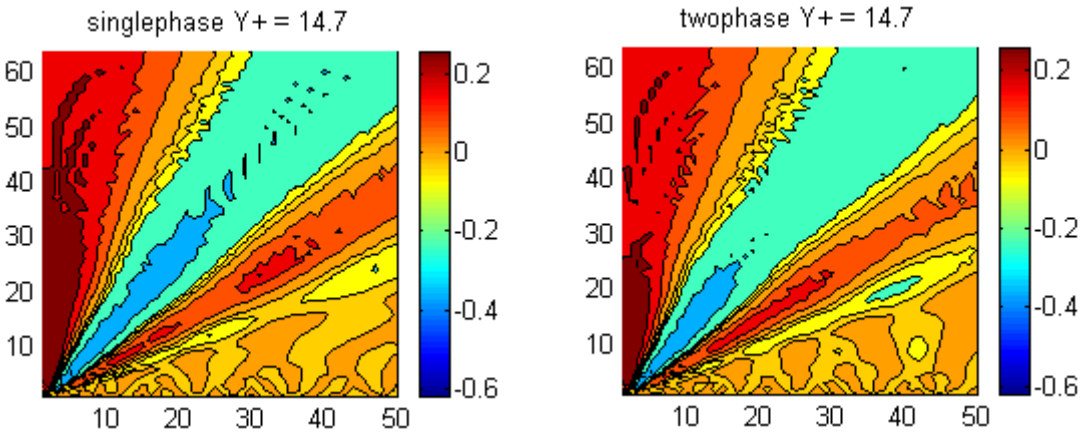

FIGURE 5.6 (b) Wavelet cross-correlation map of (v v) using Morlet wavelet in the longitudinal direction at y+ = 14.7 for normal fluctuating velocity.

Figures 5.7(a) and 5.7 (b) give the cross correlation coefficient in the longitudinal direction at y+ = 17.4 for streamwise fluctuating velocity and normal fluctuating velocity.

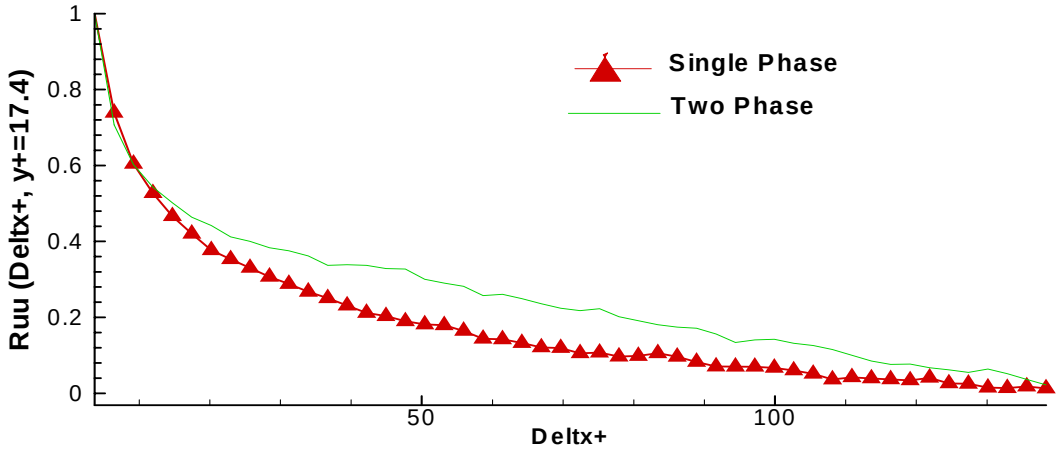

FIGURE 5.7 (a) Two-point correlation coefficient in the longitudinal direction at y+ = 17.4 for streamwise fluctuating velocity.

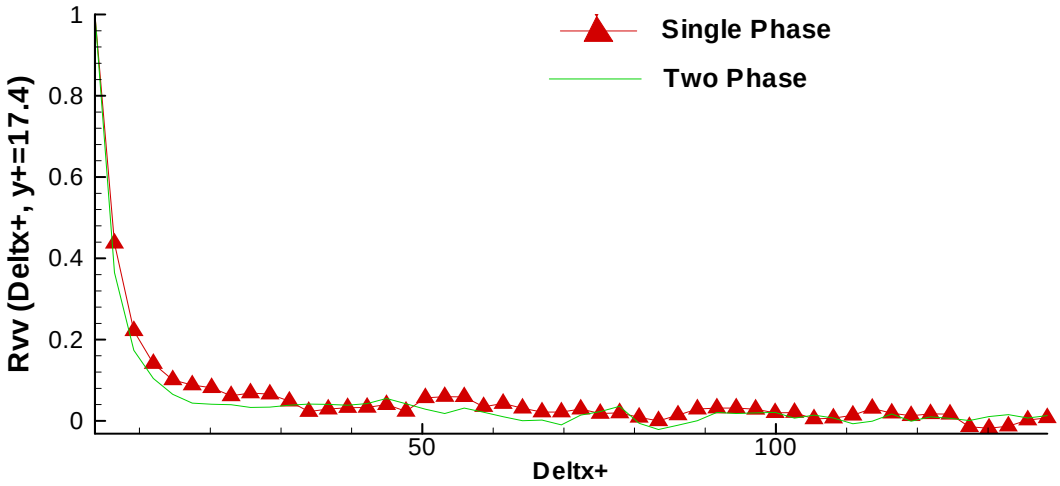

FIGURE 5.7 (b) Two-point correlation coefficient in the longitudinal direction at y+ = 17.4 for normal fluctuating velocity.

Figures 5.8 (a) and 5.8 (b) give the wavelet cross-correlation map of (u u) using Mexican hat wavelet and Morlet wavelet in the longitudinal direction at y+ = 17.4 for streamwise fluctuating velocity.

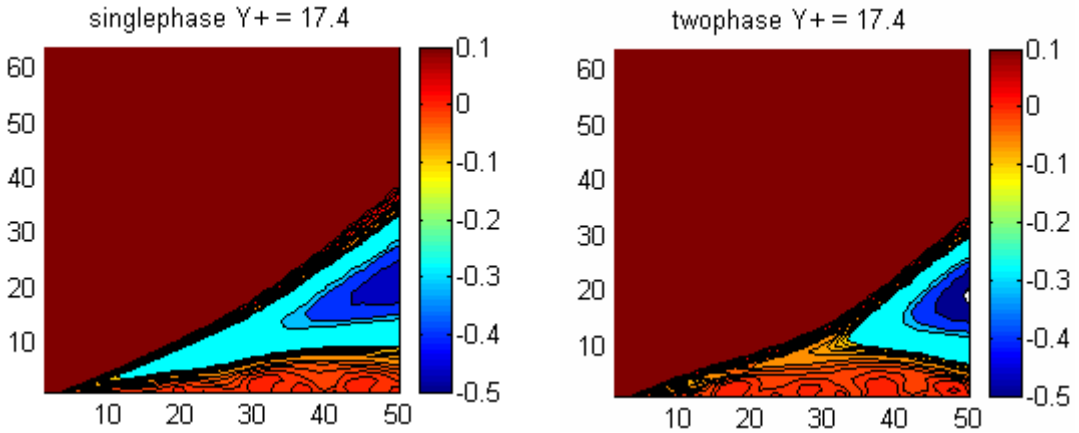

FIGURE 5.8 (a) Wavelet cross-correlation map of (u u) using Mexican hat wavelet in the longitudinal direction at y+ = 17.4 for streamwise fluctuating velocity.

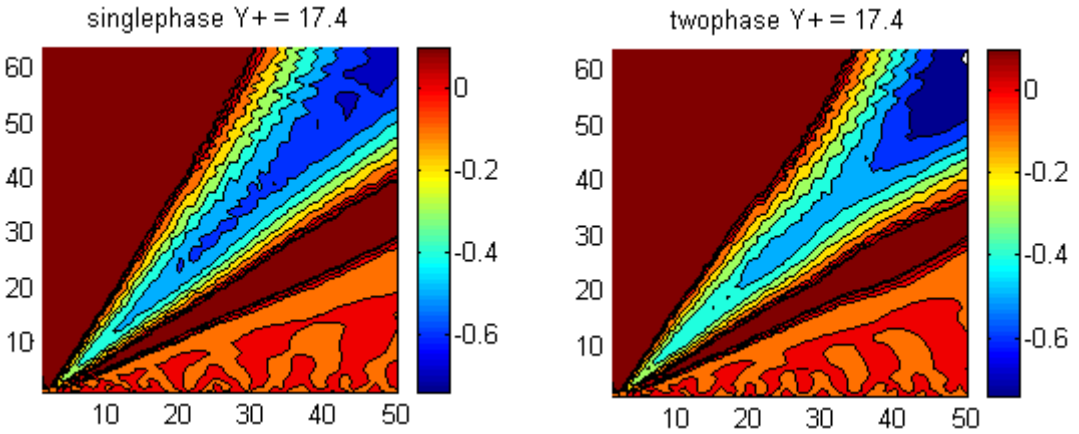

FIGURE 5.8 (b) Wavelet cross-correlation map of (u u) using Morlet wavelet in the longitudinal direction at y+ = 17.4 for streamwise fluctuating velocity.

Figures 5.9 (a) and 5.9 (b) give the wavelet cross-correlation map of (v v) using Mexican hat wavelet and Morlet wavelet in the longitudinal direction at y+ = 17.4 for normal fluctuating velocity.

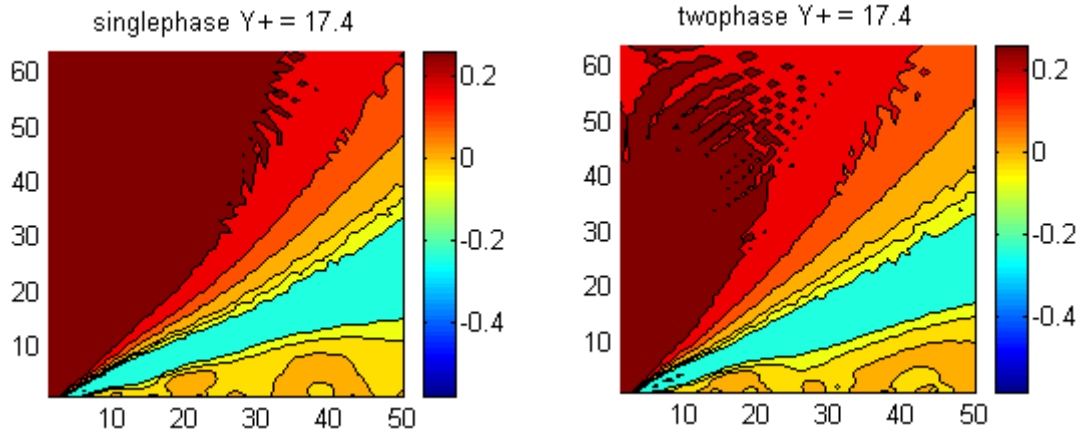

FIGURE 5.9 (a) Wavelet cross-correlation map of (v v) using Mexican hat wavelet in the longitudinal direction at y+ = 17.4 for normal fluctuating velocity.

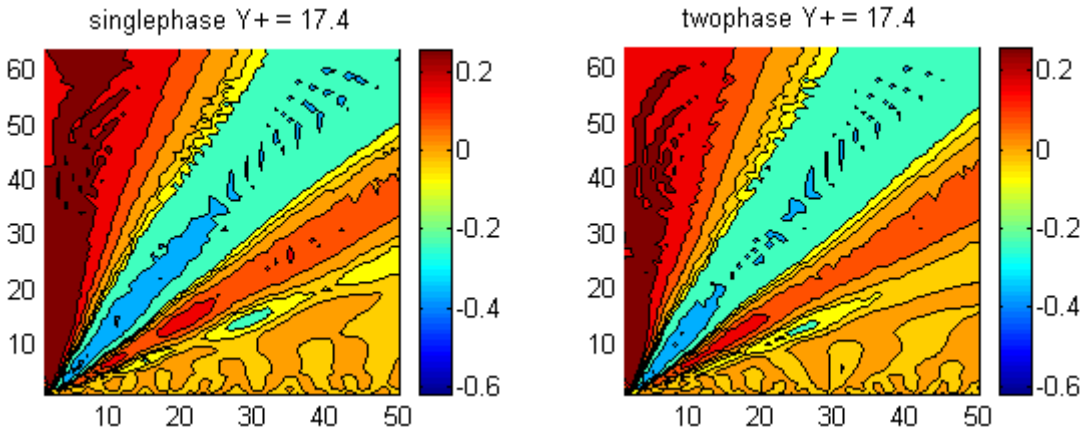

FIGURE 5.9 (b) Wavelet cross-correlation map of (v v) using Morlet wavelet in the longitudinal direction at y+ = 17.4 for normal fluctuating velocity.

Figures 5.10(a) and 5.10 (b) give the cross correlation coefficient in the longitudinal direction at y+ = 25.7 for streamwise fluctuating velocity and normal fluctuating velocity.

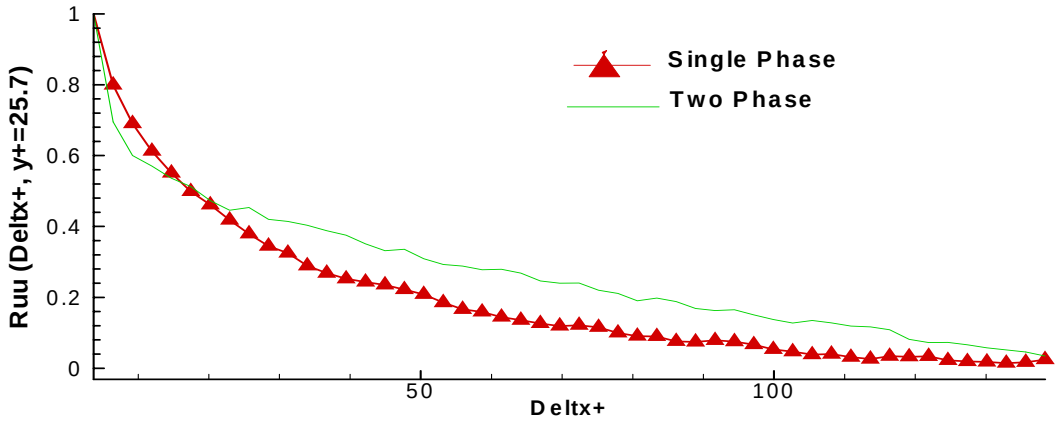

FIGURE 5.10 (a) Two-point correlation coefficient in the longitudinal direction at y+ = 25.7 for streamwise fluctuating velocity.

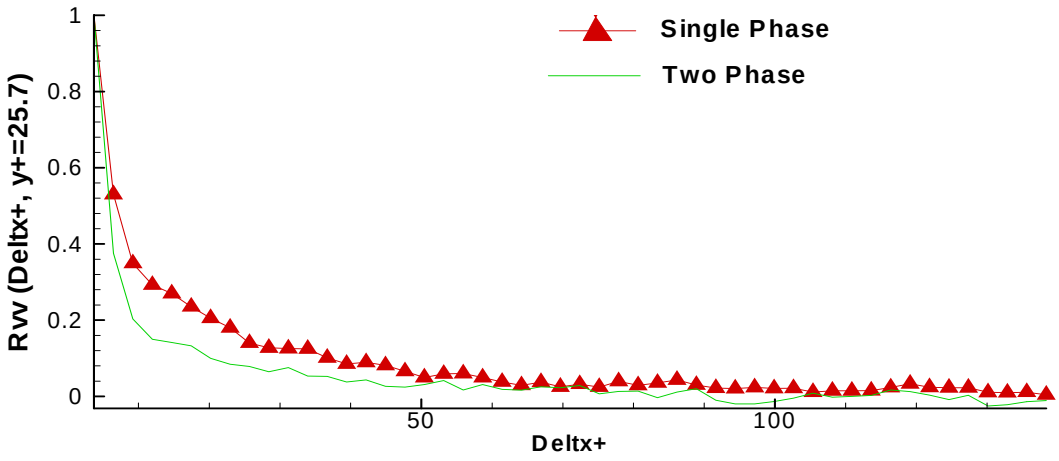

FIGURE 5.10 (b) Two-point correlation coefficient in the longitudinal direction at y+ = 25.7 for normal fluctuating velocity.

Figures 5.11 (a) and 5.11 (b) give the wavelet cross-correlation map of (u u) using Mexican hat wavelet and Morlet wavelet in the longitudinal direction at y+ = 25.7 for streamwise fluctuating velocity.

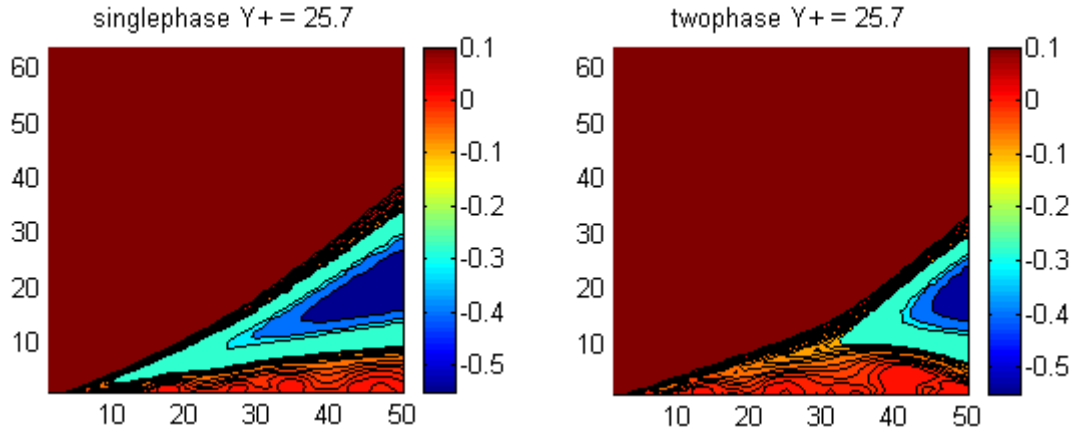

FIGURE 5.11 (a) Wavelet cross-correlation map of (u u) using Mexican hat wavelet in the longitudinal direction at y+ = 25.7 for streamwise fluctuating velocity.

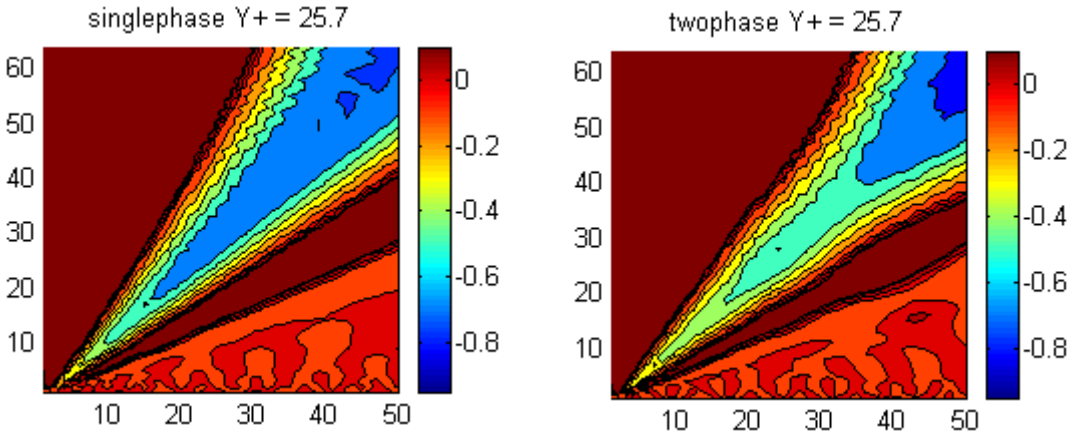

FIGURE 5.11 (b) Wavelet cross-correlation map of (u u) using Morlet wavelet in the longitudinal direction at y+ = 25.7 for streamwise fluctuating velocity.

Figures 5.12 (a) and 5.12 (b) give the wavelet cross-correlation map of (v v) using Mexican hat wavelet and Morlet wavelet in the longitudinal direction at y+ = 25.7 for normal fluctuating velocity.

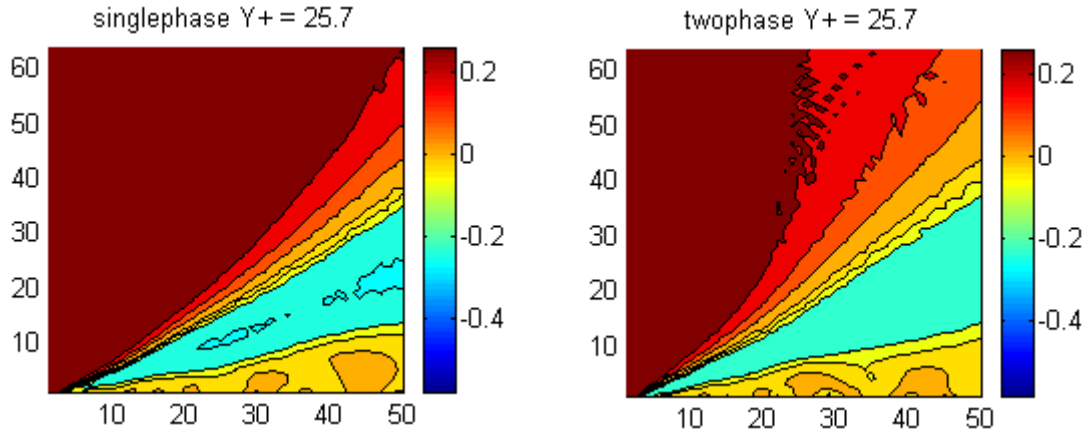

FIGURE 5.12 (a) Wavelet cross-correlation map of (v v) using Mexican hat wavelet in the longitudinal direction at y+ = 25.7 for normal fluctuating velocity.

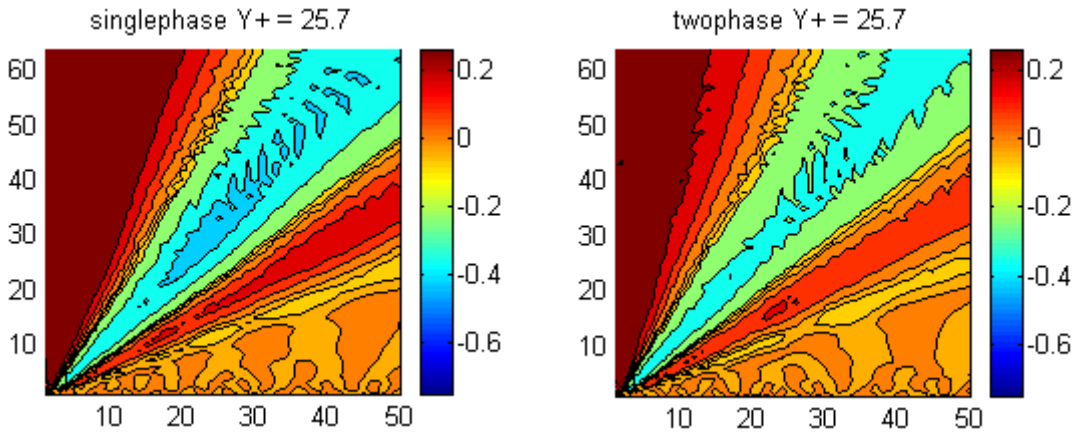

FIGURE 5.12 (b) Wavelet cross-correlation map of (v v) using Morlet wavelet in the longitudinal direction at y+ = 25.7 for normal fluctuating velocity.

Figures 5.13(a) and 5.13 (b) give the cross correlation coefficient in the longitudinal direction at y+ = 69.7 for streamwise fluctuating velocity and normal fluctuating velocity.

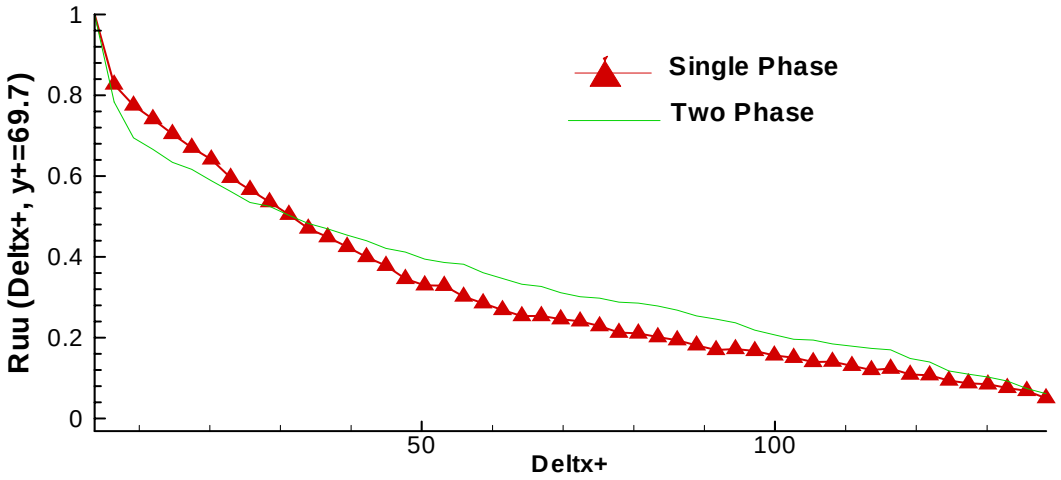

FIGURE 5.13 (a) Two-point correlation coefficient in the longitudinal direction at y+ = 69.7 for streamwise fluctuating velocity.

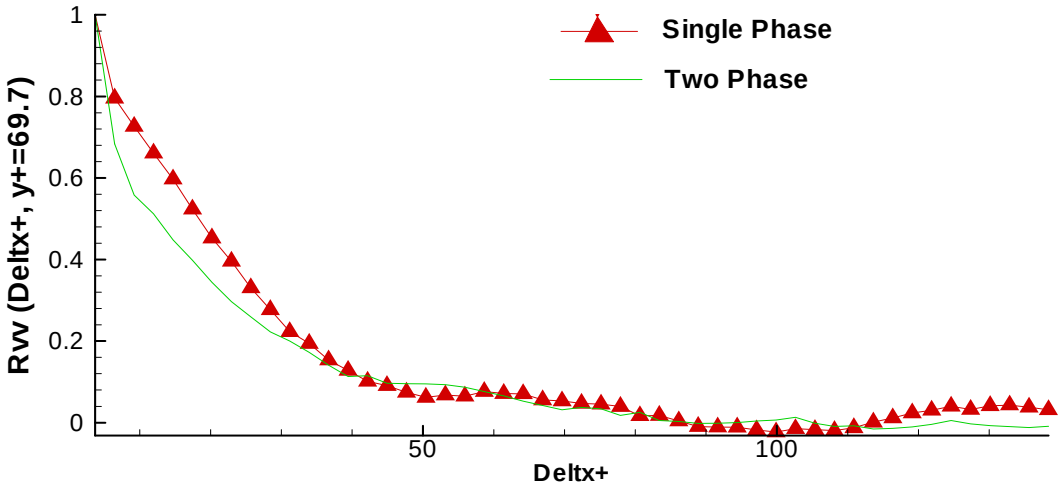

FIGURE 5.13 (b) Two-point correlation coefficient in the longitudinal direction at y+ = 69.7 for normal fluctuating velocity.

Figures 5.14 (a) and 5.14 (b) give the wavelet cross-correlation map of (u u) using Mexican hat wavelet and Morlet wavelet in the longitudinal direction at y+ = 69.7 for streamwise fluctuating velocity.

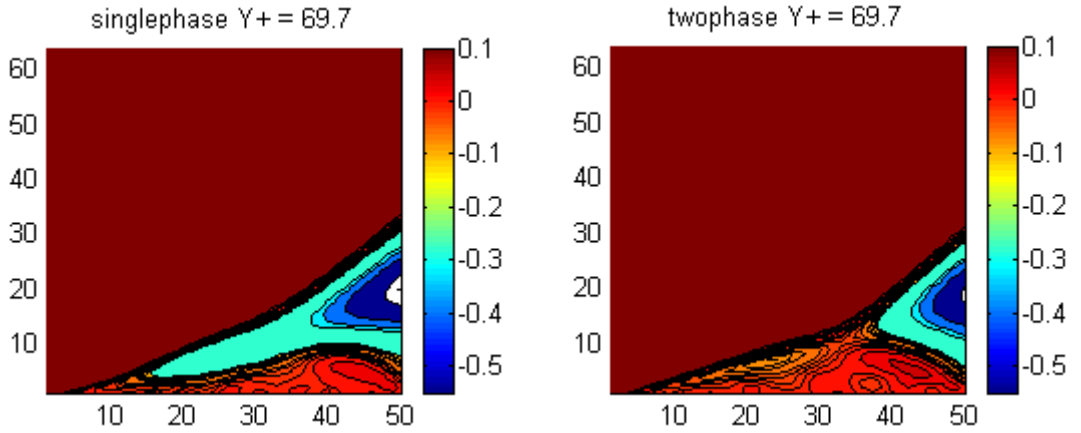

FIGURE 5.14 (a) Wavelet cross-correlation map of (u u) using Mexican hat wavelet in the longitudinal direction at y+ = 69.7 for streamwise fluctuating velocity.

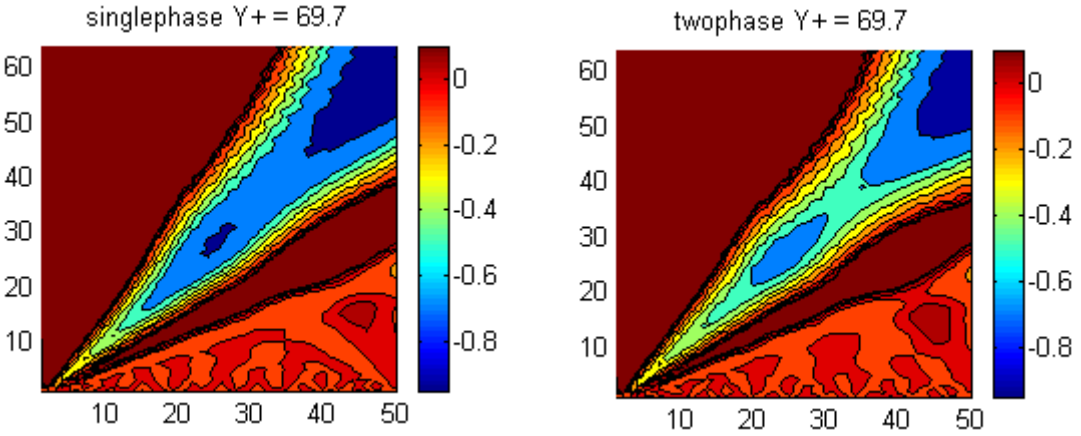

FIGURE 5.14 (b) Wavelet cross-correlation map of (u u) using Morlet wavelet in the longitudinal direction at y+ = 69.7 for streamwise fluctuating velocity.

Figures 5.15 (a) and 5.15 (b) give the wavelet cross-correlation map of (v v) using Mexican hat wavelet and Morlet wavelet in the longitudinal direction at y+ = 69.7 for normal fluctuating velocity.

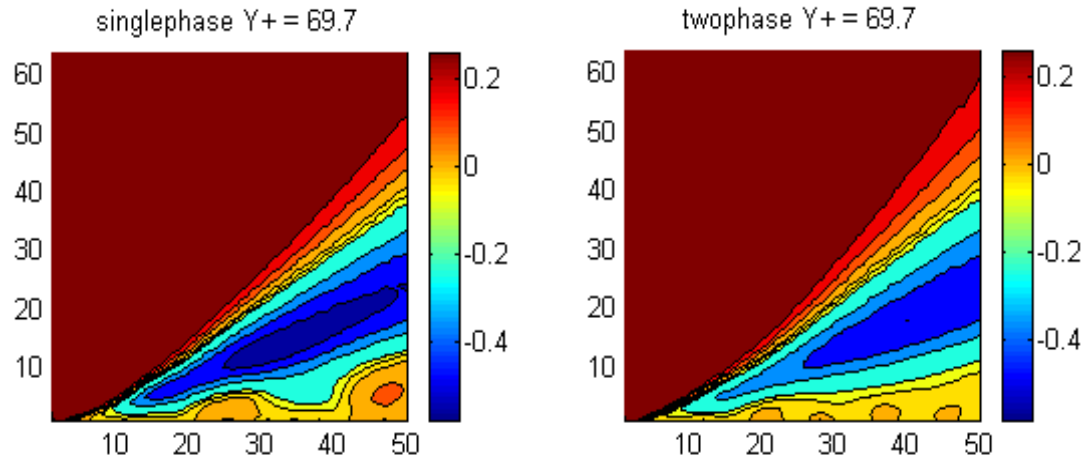

FIGURE 5.15 (a) Wavelet cross-correlation map of (v v) using Mexican hat wavelet in the longitudinal direction at y+ = 69.7 for normal fluctuating velocity.

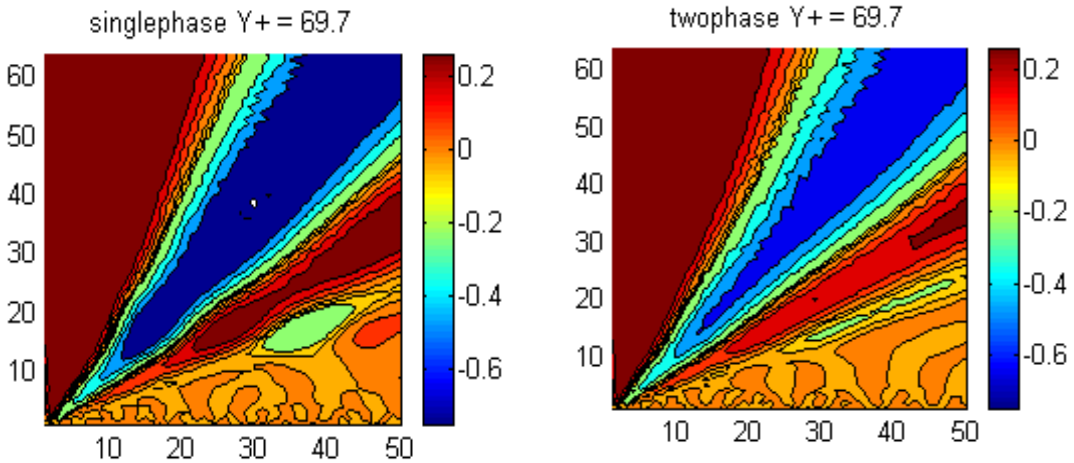

FIGURE 5.15 (b) Wavelet cross-correlation map of (v v) using Morlet wavelet in the longitudinal direction at y+ = 69.7 for normal fluctuating velocity.

In the wavelet cross-correlation map figures, the horizontal axis is Δx index which can be checked in Table 5.2.

Δx index	1	5	10	15	20	25	30	35	40	45	50
Δx	0.32	1.27	2.45	3.64	4.82	6.01	7.19	8.37	9.56	10.74	11.93
Δx+	3.71	14.7	28.4	42.2	55.9	69.7	83.4	97.1	110.9	124.6	138.4

TABLE 5.2 Δx index, Δx, Δx+ check table.

The vertical axis is the scale number. Large scale corresponds to low wavenumber, large eddy size. Small scale number corresponds to high wavenumber, small eddies. It can be seen that the area for the large eddy is increased from the Wavelet cross-correlation map for (u u) in two phase flow conditions. For five y+ locations 9.2, 14.7, 17.4, 25.7, 69.7, both Mexican hat wavelet and Morlet wavelet give the consistent changing tendency for streamwise fluctuating velocity. It can also be seen that the contrast between single phase and two phase flow is better by using Mexican hat wavelet than using Morlet wavelet. As stated in Chapter IV, the Mexican hat wavelet has good resolution in low frequency and Morlet wavelet has good resolution in high frequency. This kind of area increase from single phase to two phase flow shows that the drag reduction should not be simply explained as the damping of turbulence intensity. Actually, for four y+ locations 14.7, 17.4, 25.7, 69.7, the area for the large eddy is decreased from the Wavelet cross-correlation map for (v v). These show that

the correlation between velocities at different x locations change from single phase flow to two phase flow not in a simple way of increasing or damping. Wavelet cross-correlation map show that the correlation in the longitudinal direction between streamwise velocities increase in the low frequency range and the correlation in the longitudinal direction between normal velocities decrease in the low frequency range. This result works well with what Gutierrez Torres (2004) found in her thesis by using length scale method. Wavelet cross-correlation map provide more space-wavenumber information.

5.2 Wavelet cross-correlation map in the normal direction

Figures 5.16 (a) and 5.16 (b) give the cross correlation coefficient in the transverse direction at x+ = 3.7 for streamwise fluctuating velocity and normal fluctuating velocity.

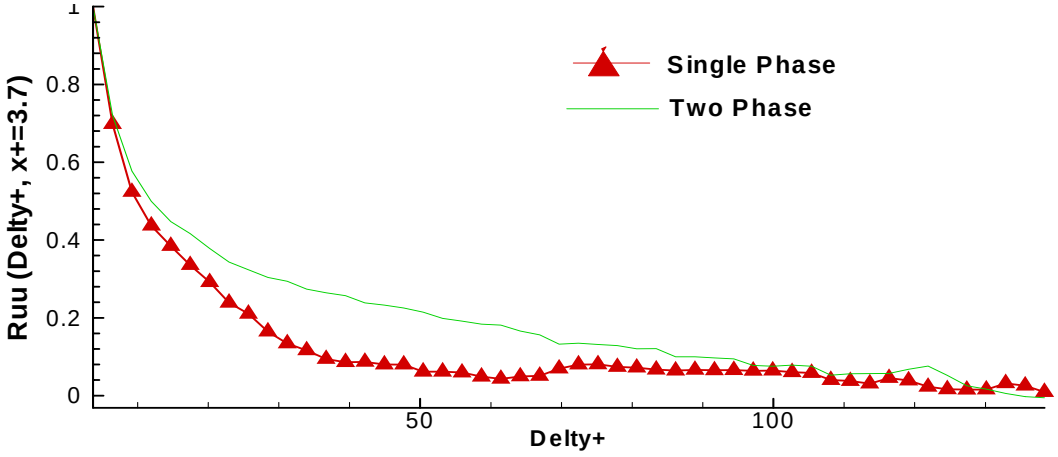

FIGURE 5.16 (a) Two-point correlation coefficient in the transverse direction at x+ = 3.7 for streamwise fluctuating velocity.

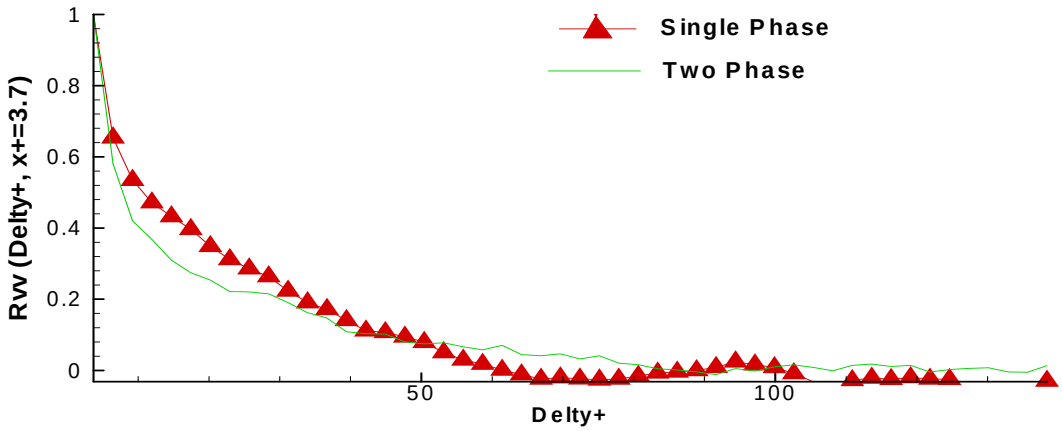

FIGURE 5.16 (b) Two-point correlation coefficient in the transverse direction at x+ = 3.7 for normal fluctuating velocity.

Figures 5.17 (a) and 5.17 (b) give the wavelet cross-correlation map of (u u) using Mexican hat wavelet and Morlet wavelet in the transverse direction at x+ = 3.7 for streamwise fluctuating velocity.

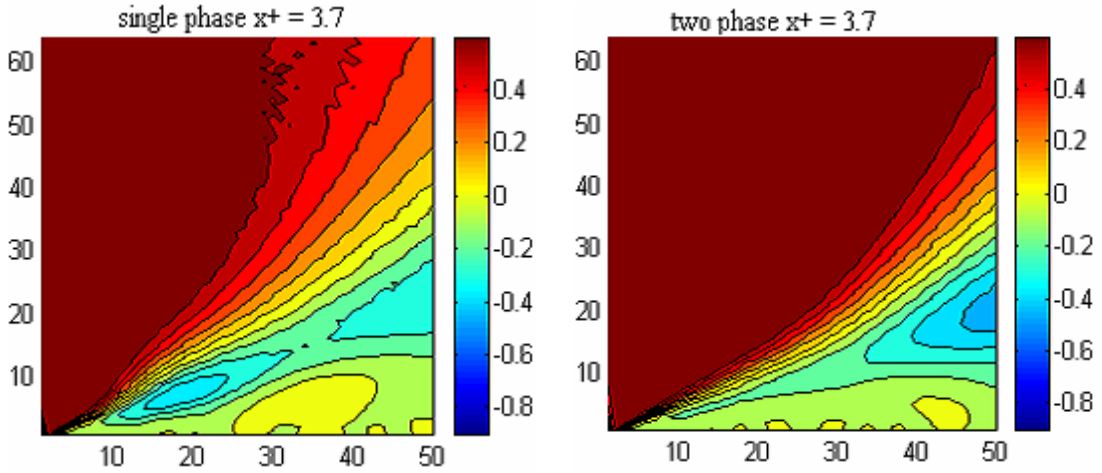

FIGURE 5.17 (a) Wavelet cross-correlation map of (u u) using Mexican hat wavelet in the transverse direction at x+ = 3.7 for streamwise fluctuating velocity.

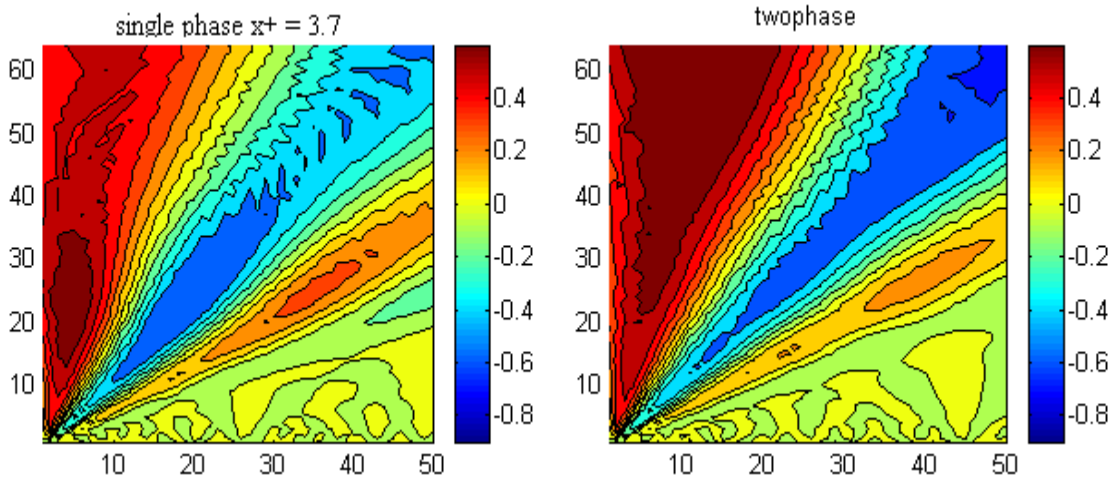

FIGURE 5.17 (b) Wavelet cross-correlation map of (u u) using Morlet wavelet in the transverse direction at x+ = 3.7 for streamwise fluctuating velocity.

Figures 5.18 (a) and 5.18 (b) give the wavelet cross-correlation map of (v v) using Mexican hat wavelet and Morlet wavelet in the transverse direction at x+ = 3.7 for normal fluctuating velocity.

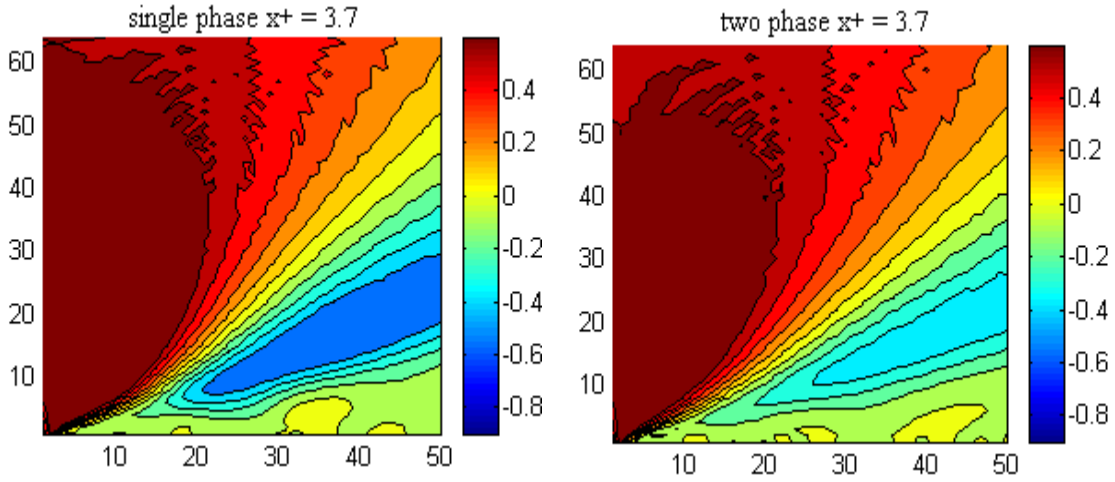

FIGURE 5.18 (a) Wavelet cross-correlation map of (v v) using Mexican hat wavelet in the transverse direction at x+ = 3.7 for normal fluctuating velocity.

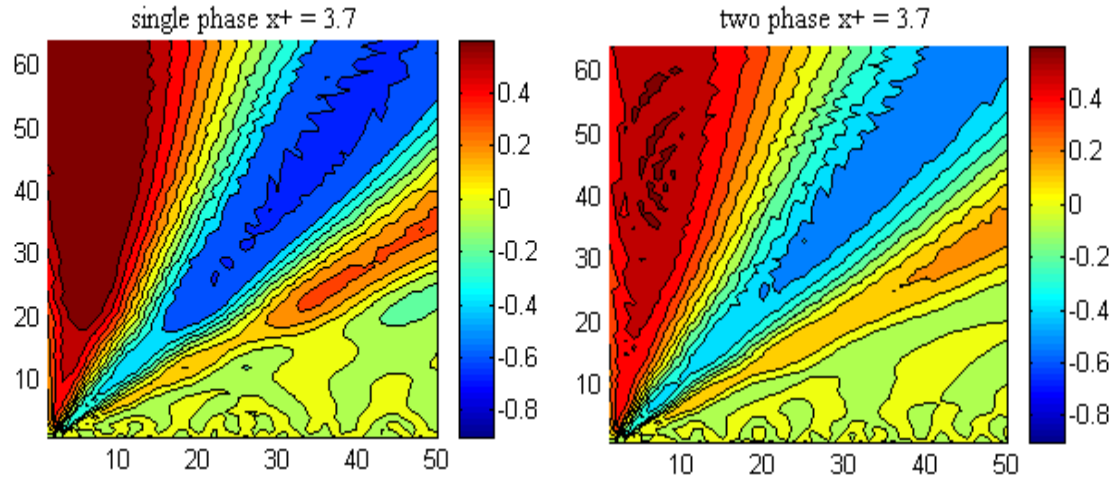

FIGURE 5.18 (b) Wavelet cross-correlation map of (v v) using Morlet wavelet in the transverse direction at x+ = 3.7 for normal fluctuating velocity.

Figures 5.19 (a) and 5.19 (b) give the cross correlation coefficient in the transverse direction at x+ = 28.4 for streamwise fluctuating velocity and normal fluctuating velocity.

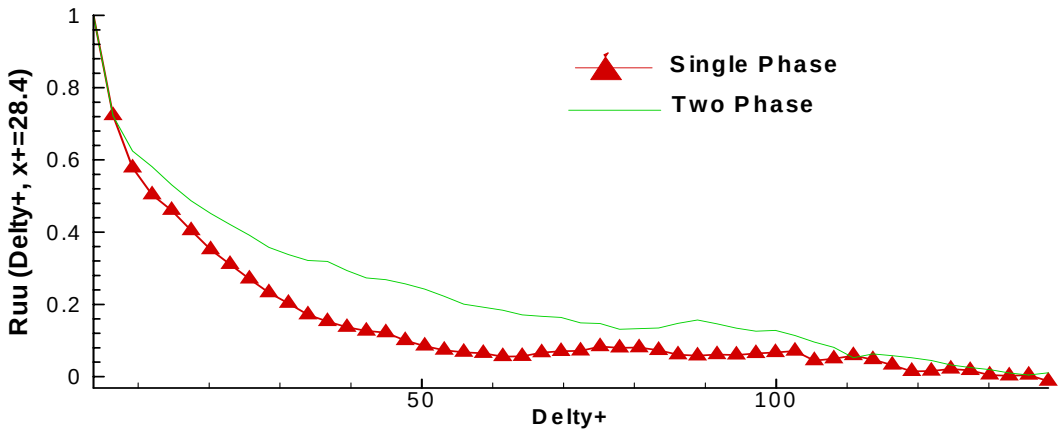

FIGURE 5.19 (a) Two-point correlation coefficient in the transverse direction at x+ = 28.4 for streamwise fluctuating velocity.

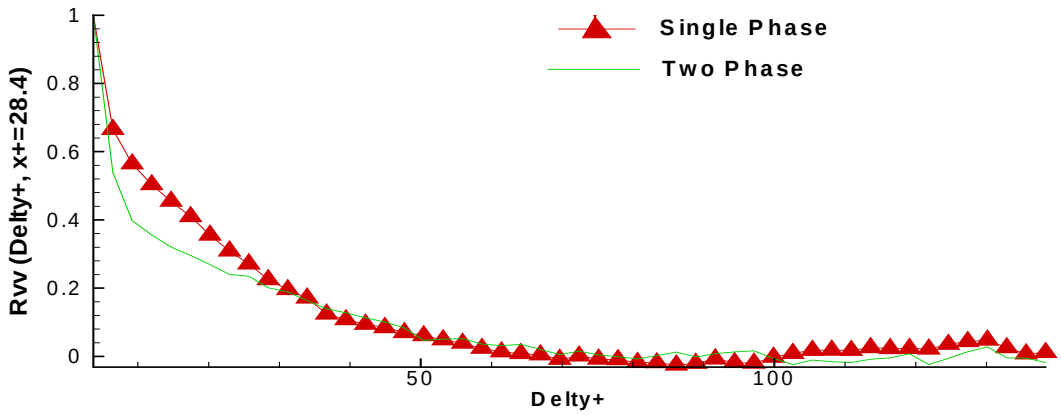

FIGURE 5.19 (b) Two-point correlation coefficient in the transverse direction at x+ = 28.4 for normal fluctuating velocity.

Figures 5.20 (a) and 5.20 (b) give the wavelet cross-correlation map of (u u) using Mexican hat wavelet and Morlet wavelet in the transverse direction at x+ = 28.4 for streamwise fluctuating velocity.

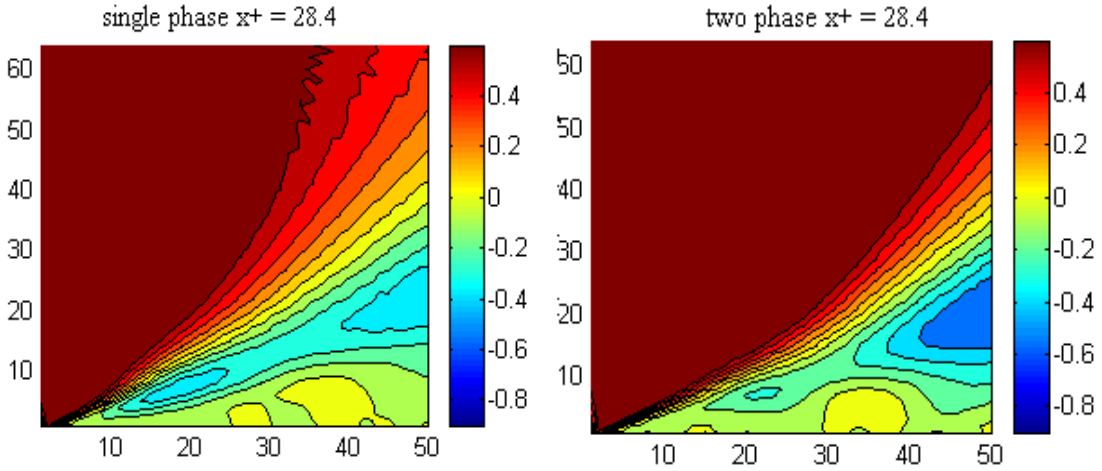

FIGURE 5.20 (a) Wavelet cross-correlation map of (u u) using Mexican hat wavelet in the transverse direction at x+ = 28.4 for streamwise fluctuating velocity.

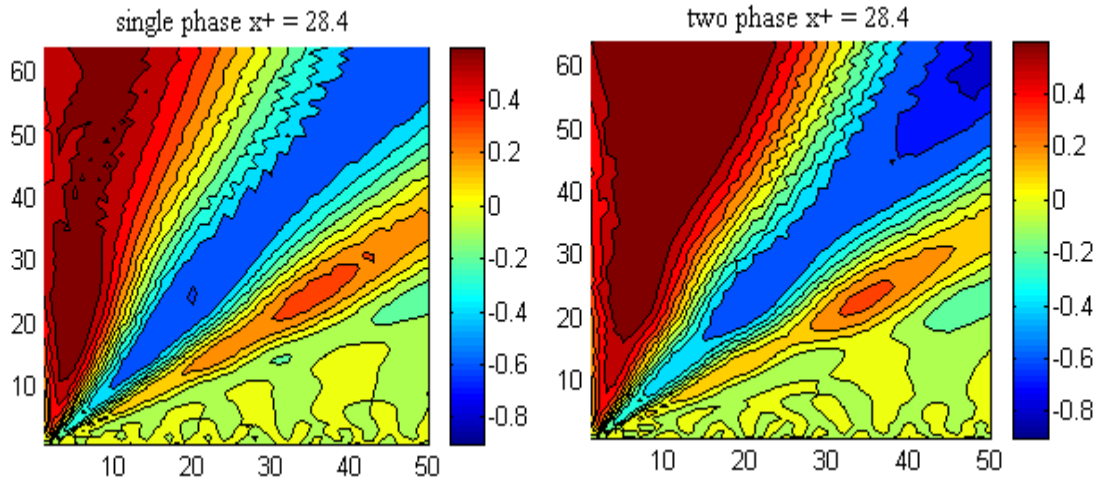

FIGURE 5.20 (b) Wavelet cross-correlation map of (u u) using Morlet wavelet in the transverse direction at x+ = 28.4 for streamwise fluctuating velocity.

Figures 5.21 (a) and 5.21 (b) give the wavelet cross-correlation map of (v v) using Mexican hat wavelet and Morlet wavelet in the transverse direction at x+ = 28.4 for normal fluctuating velocity.

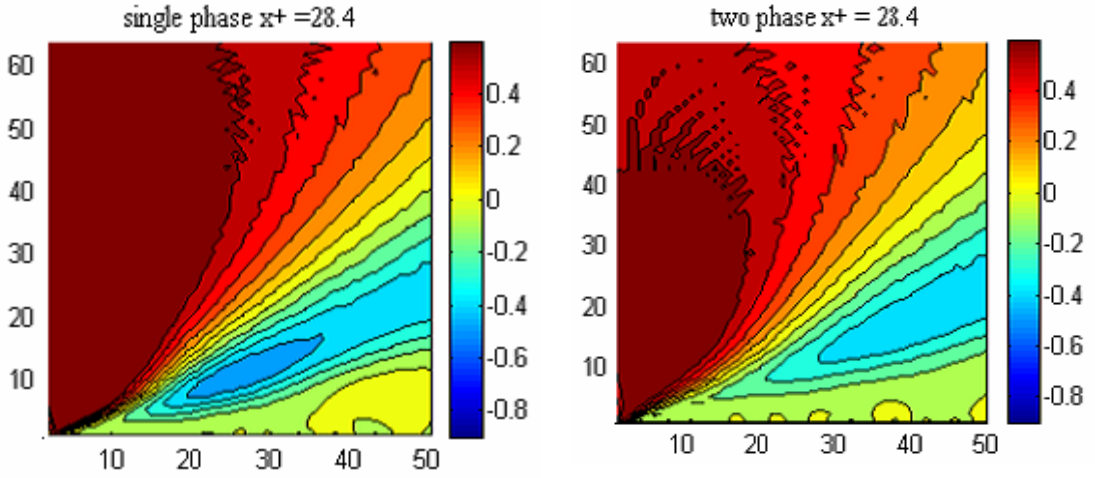

FIGURE 5.21 (a) Wavelet cross-correlation map of (v v) using Mexican hat wavelet in the transverse direction at x+ = 28.4 for normal fluctuating velocity.

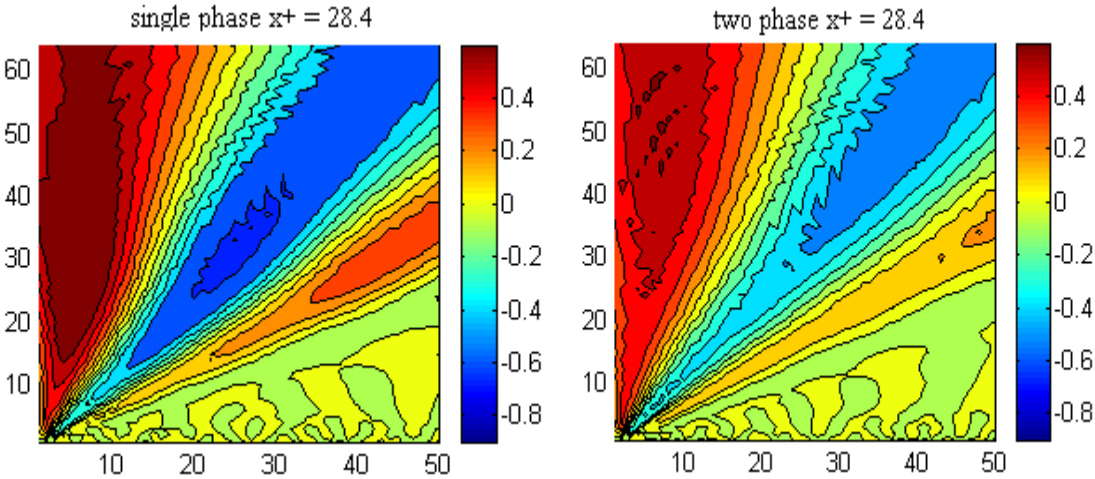

FIGURE 5.21 (b) Wavelet cross-correlation map of (v v) using Morlet wavelet in the transverse direction at x+ = 28.4 for normal fluctuating velocity.

Figures 5.22 (a) and 5.22 (b) give the cross correlation coefficient in the transverse direction at x+ = 72.4 for streamwise fluctuating velocity and normal fluctuating velocity.

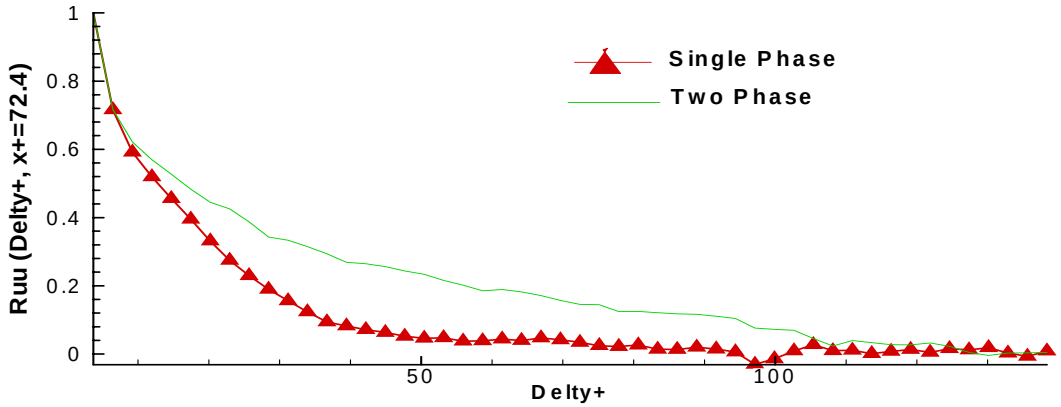

FIGURE 5.22 (a) Two-point correlation coefficient in the transverse direction at x+ = 72.4 for streamwise fluctuating velocity.

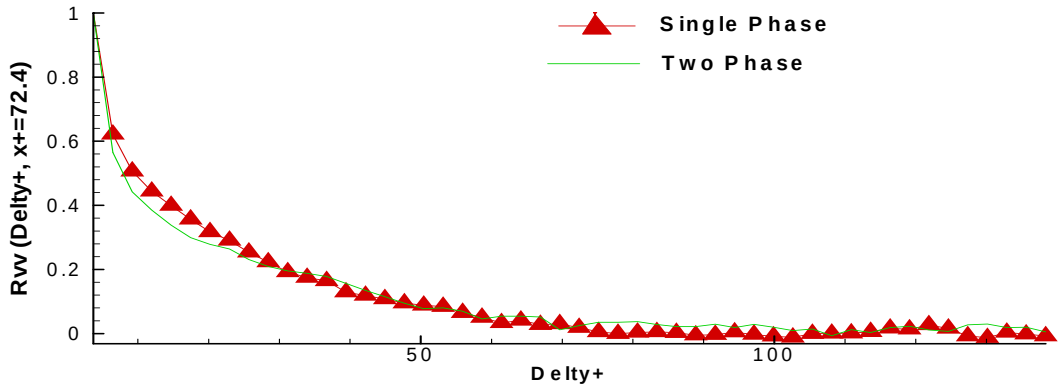

FIGURE 5.22 (b) Two-point correlation coefficient in the transverse direction at x+ = 72.4 for normal fluctuating velocity.

Figures 5.23 (a) and 5.23 (b) give give the wavelet cross-correlation map of (u u) using Mexican hat wavelet and Morlet wavelet in the transverse direction at x+ = 72.4 for streamwise fluctuating velocity.

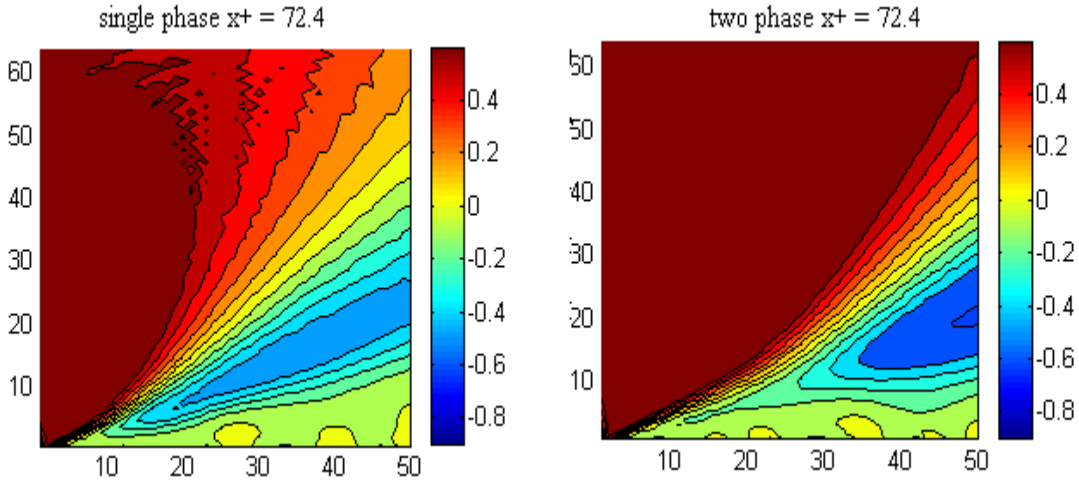

FIGURE 5.23 (a) Wavelet cross-correlation map of (u u) using Mexican hat wavelet in the transverse direction at x+ = 72.4 for streamwise fluctuating velocity.

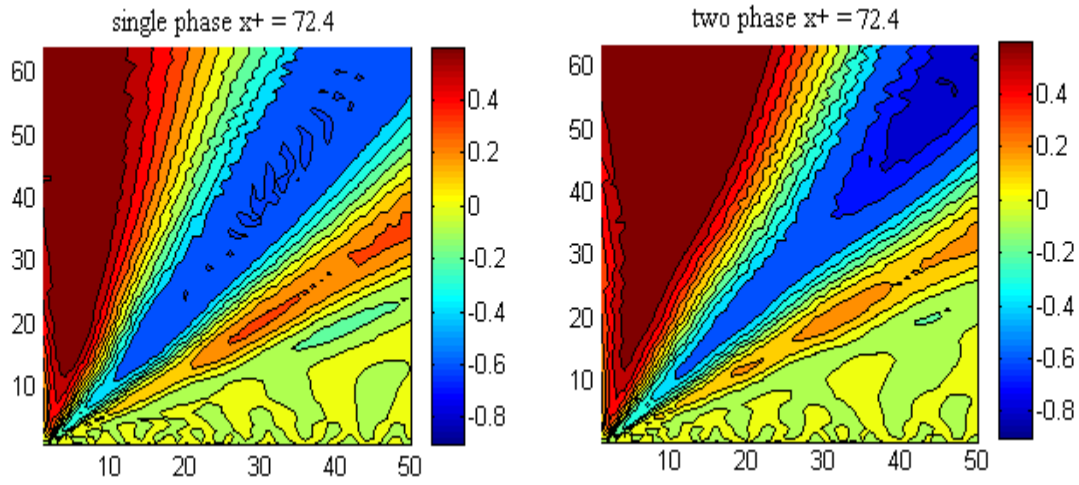

FIGURE 5.23 (b) Wavelet cross-correlation map of (u u) using Morlet wavelet in the transverse direction at x+ = 72.4 for streamwise fluctuating velocity.

Figures 5.24 (a) and 5.24 (b) give give the wavelet cross-correlation map of (u u) using Mexican hat wavelet and Morlet wavelet in the transverse direction at x+ = 72.4 for streamwise fluctuating velocity.

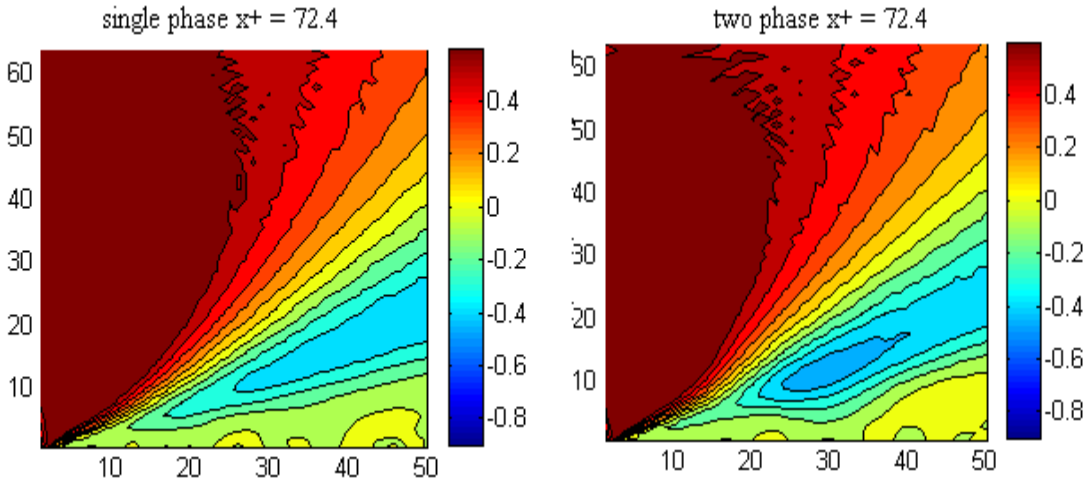

FIGURE 5.24 (a) Wavelet cross-correlation map of (v v) using Mexican hat wavelet in the transverse direction at x+ = 72.4 for normal fluctuating velocity.

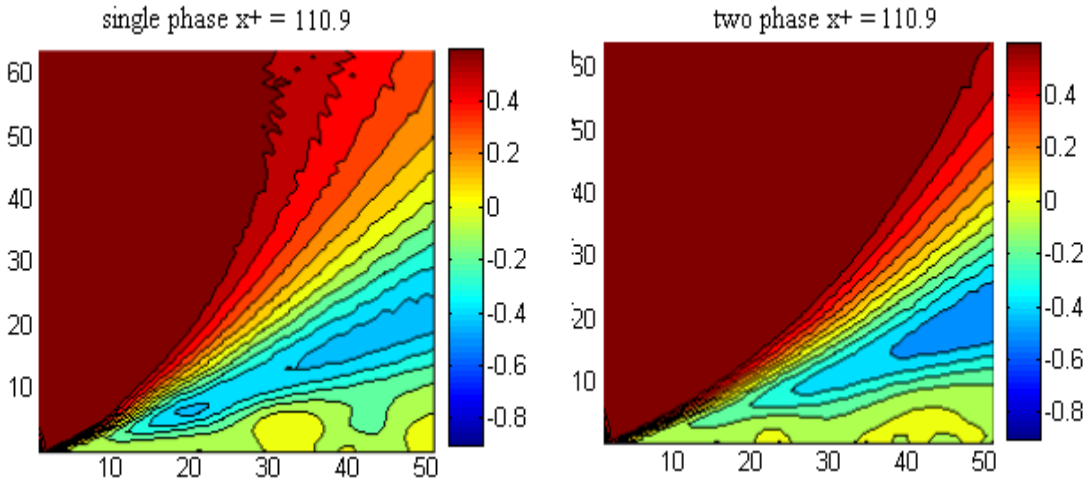

FIGURE 5.24 (b) Wavelet cross-correlation map of (v v) using Morlet wavelet in the transverse direction at x+ = 72.4 for normal fluctuating velocity.

Figures 5.22 (a) and 5.22 (b) give the cross correlation coefficient in the transverse direction at x+ = 72.4 for streamwise fluctuating velocity and normal fluctuating velocity.

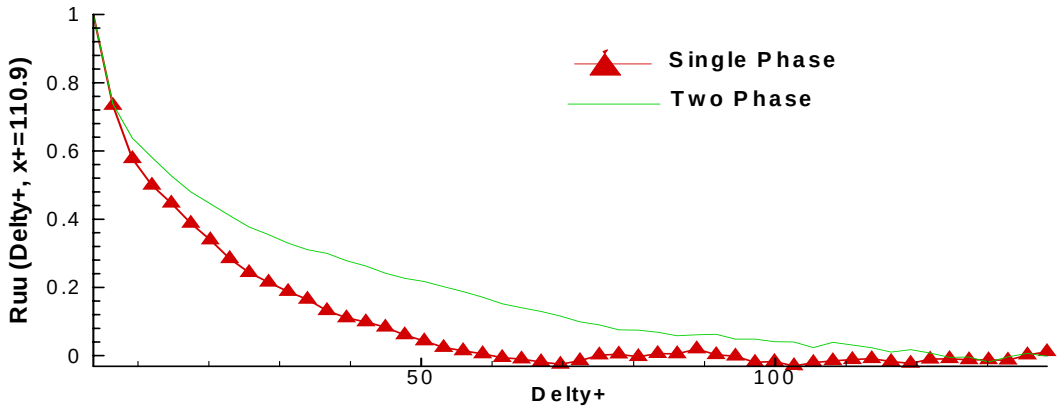

FIGURE 5.25 (a) Two-point correlation coefficient in the transverse direction at x+ = 110.9 for streamwise fluctuating velocity.

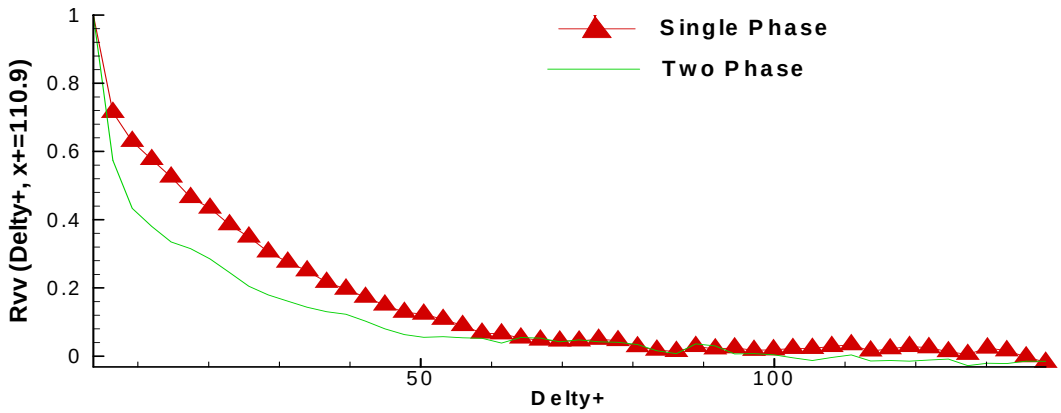

FIGURE 5.25 (b) Two-point correlation coefficient in the transverse direction at x+ = 110.9 for normal fluctuating velocity.

Figures 5.23 (a) and 5.23 (b) give give the wavelet cross-correlation map of (u u) using Mexican hat wavelet and Morlet wavelet in the transverse direction at x+ = 72.4 for streamwise fluctuating velocity.

.

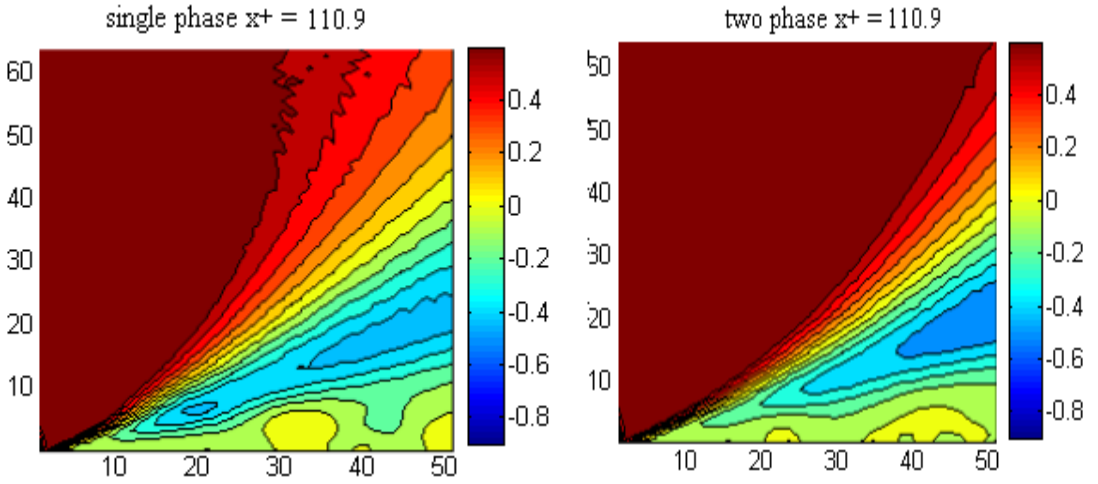

FIGURE 5.26 (a) Wavelet cross-correlation map of (u u) using Mexican hat wavelet in the transverse direction at x+ = 110.9 for streamwise fluctuating velocity.

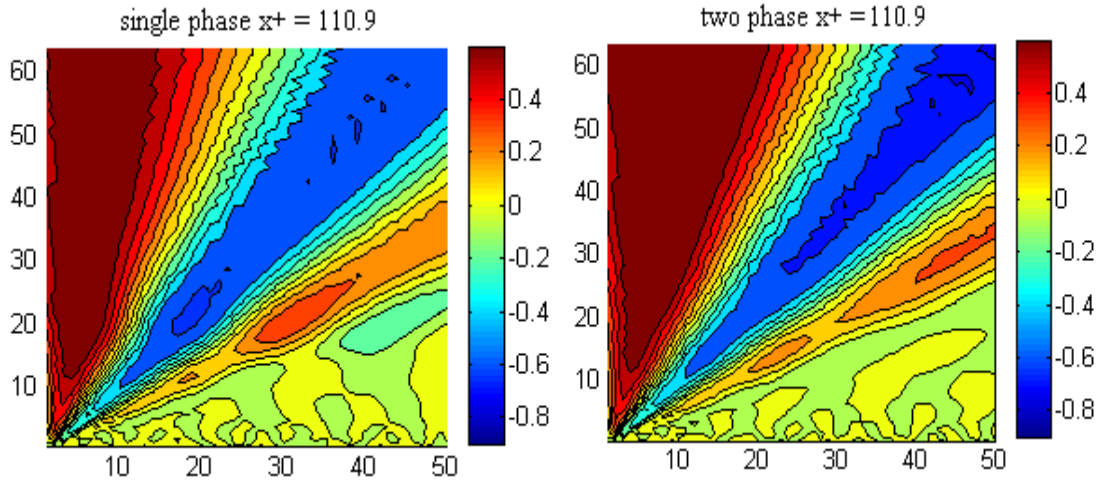

FIGURE 5.26 (b) Wavelet cross-correlation map of (u u) using Morlet wavelet in the transverse direction at x+ = 110.9 for streamwise fluctuating velocity.

Figures 5.24 (a) and 5.24 (b) give give the wavelet cross-correlation map of (u u) using Mexican hat wavelet and Morlet wavelet in the transverse direction at x+ = 72.4 for streamwise fluctuating velocity.

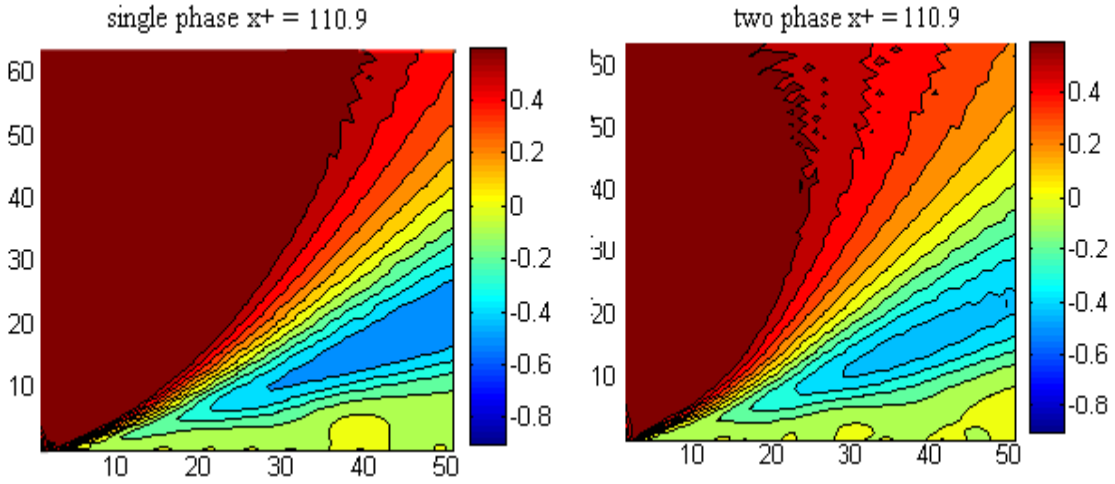

FIGURE 5.27 (a) Wavelet cross-correlation map of (v v) using Mexican hat wavelet in the transverse direction at x+ = 110.9 for normal fluctuating velocity.

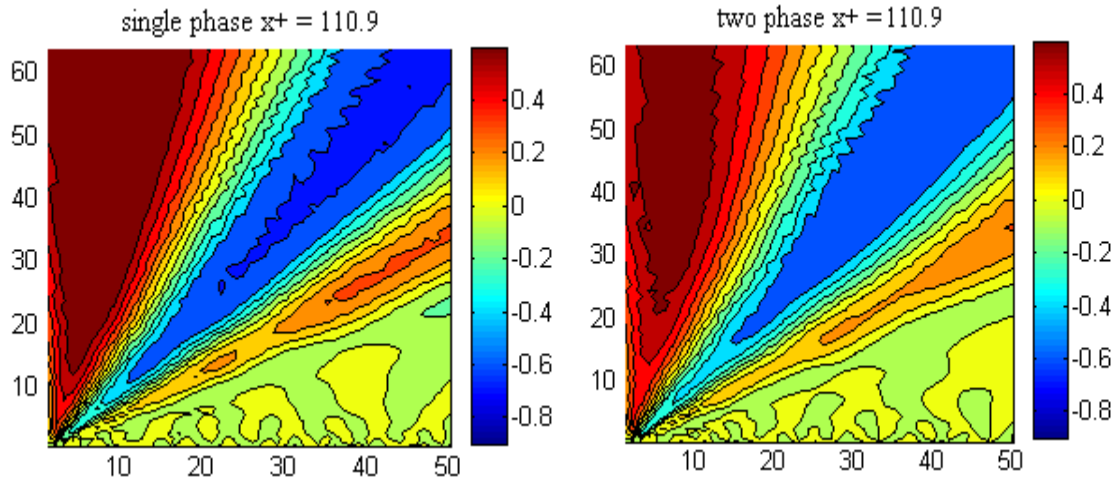

FIGURE 5.27 (b) Wavelet cross-correlation map of (v v) using Morlet wavelet in the transverse direction at x+ = 110.9 for normal fluctuating velocity.

Since the transverse direction correlation was processed at this time, the wavelet cross-correlation map 's horizontal axis is Δy index, which can be checked in Table 5.3. The vertical axis is the scale number. Large scale corresponds to low wavenumber, large eddy size. Small scale number corresponds to high wavenumber, small eddies.

Δy index	1	5	10	15	20	25	30	35	40	45	50
Δy	0.32	1.27	2.45	3.64	4.82	6.01	7.19	8.37	9.56	10.74	11.93
Δy+	3.71	14.7	28.4	42.2	55.9	69.7	83.4	97.1	110.9	124.6	138.4

TABLE 5.3 Δy index, Δy, Δy+ check table.

For four x+ locations 3.7, 28.4, 72.4, 110.9, both Mexican hat wavelet and Morlet wavelet give the consistent changing tendency for streamwise fluctuating velocity. It can also be seen that the contrast between single phase and two phase flow is better by using Mexican hat wavelet than using Morlet wavelet. This kind of increase from single phase to two phase flow shows that the drag reduction should not be simply explained as the damping of turbulence intensity. Actually, for x+ locations 3.7, 28.4, 72.4, 110.9, the area for the large eddy is decreased from the Wavelet cross-correlation map for (v v). These show that the correlation between velocities at different y locations change from single phase flow to two phase flow not in a simple way of increasing or damping. Wavelet cross-correlation map show that the correlation in the transverse direction between streamwise velocities increase in the low frequency range

and the correlation in the longitudinal direction between normal velocities decrease in the low frequency range. This result also works well with what Gutierrez Torres (2004) found in her thesis by using length scale method. Wavelet cross-correlation map provide more space-wavenumber information.

5.3 Three-D wavelet cross-correlation energy map and wavelet cross-correlation density spectrum

Using the algorithm of wavelet cross-correlation energy map discussed in Chapter IV, the data from single phase flow and two phase flow are calculated. And three-D plot was used. Figures 5.28 (a), (b) give the (u u) Wavelet cross-correlation Energy map in longitudinal direction Mexican hat for single phase and two phase. And figures 5.29 (a), (b) give the (v v) Wavelet cross-correlation Energy map in longitudinal direction Mexican hat for single phase and two phase. Figures 5.30 (a), (b), 5.31(a), (b) follow the same idea but using Morlet wavelet function. In figures 5.28 (a), the energy distribution was plotted at five y+ locations. And in each y+ plane, the energy strength was expressed by the color of the contour. The energy strength was located in wavenumber-Δx plane. It can be seen that the energy distribution from near the wall was lower than the energy distribution far from the wall. In figure 5.28 (b), the same 3-D plot was given. The difference between these two 3-D plots was obvious. The energy distribution in the longitudinal direction from streamwise direction was increased in microbubbles injected conditions.

Using the algorithm of wavelet cross-correlation density spectra discussed in Chapter IV, the data from single phase flow and two phase flow are calculated. Figures 5.32, 5.33 give the (u u) and (v v) Wavelet cross-correlation density spectra in longitudinal direction using Morlet wavelet. It can be seen that at the large eddy range, the density for (u u) was increased and the density for (v v) was decreased.

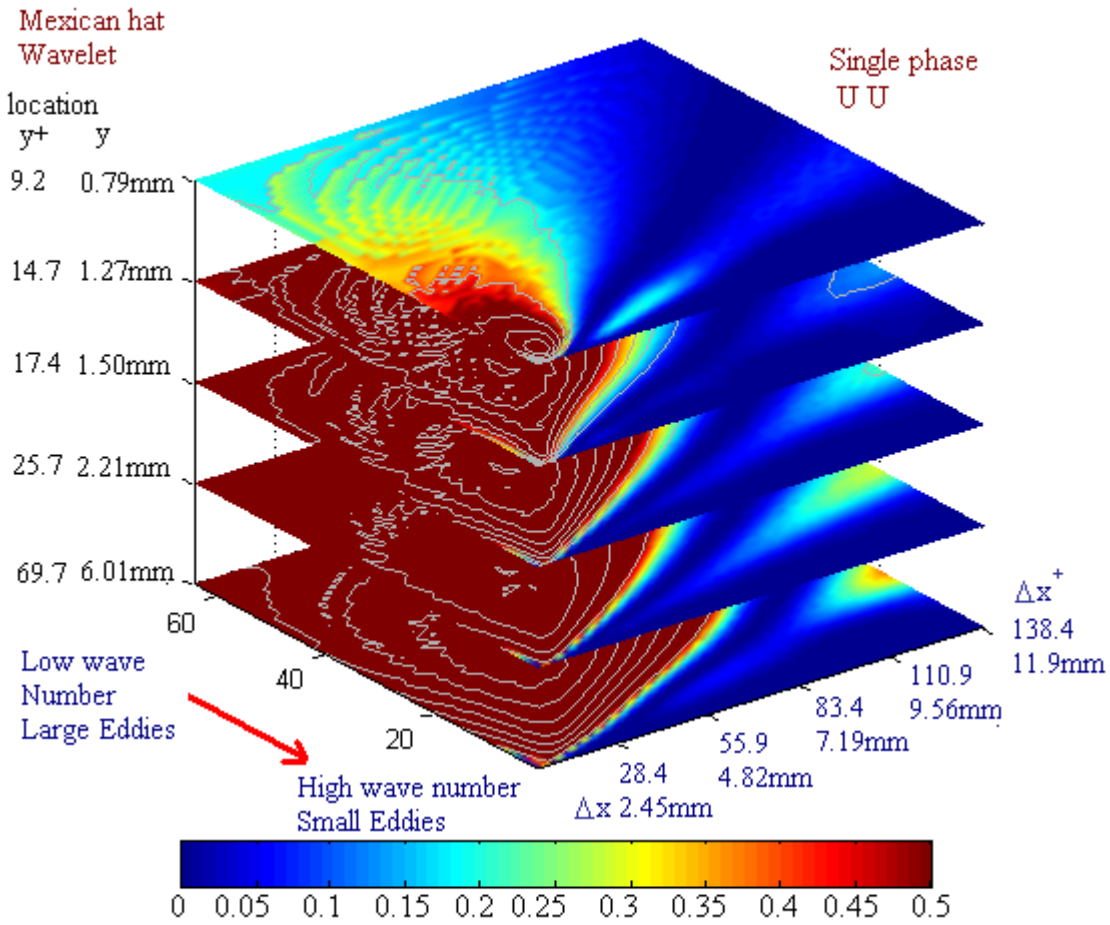

FIGURE 5.28 (a) Wavelet cross-correlation energy map of (u u) in longitudinal direction using Mexican hat for single phase.

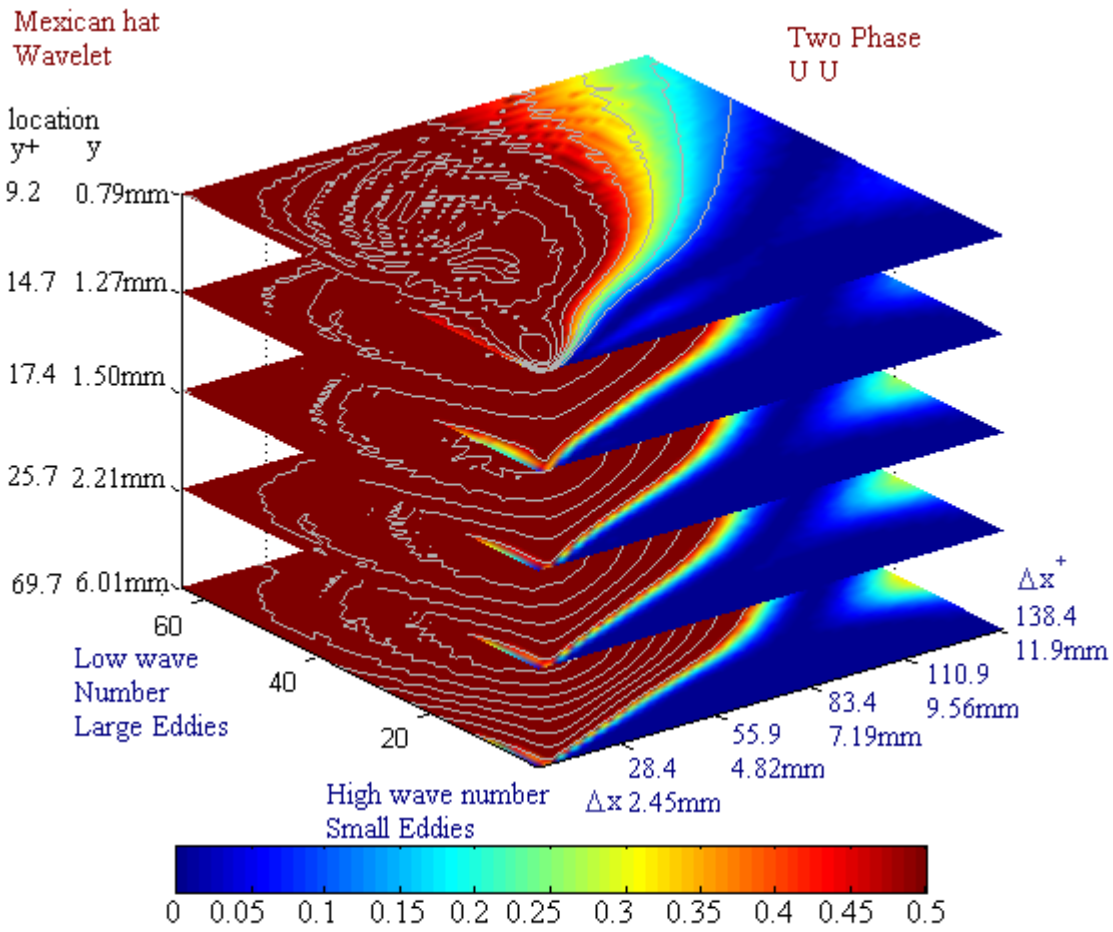

FIGURE 5.28 (b) Wavelet cross-correlation energy map of (u u) in longitudinal direction using Mexican hat for two phase.

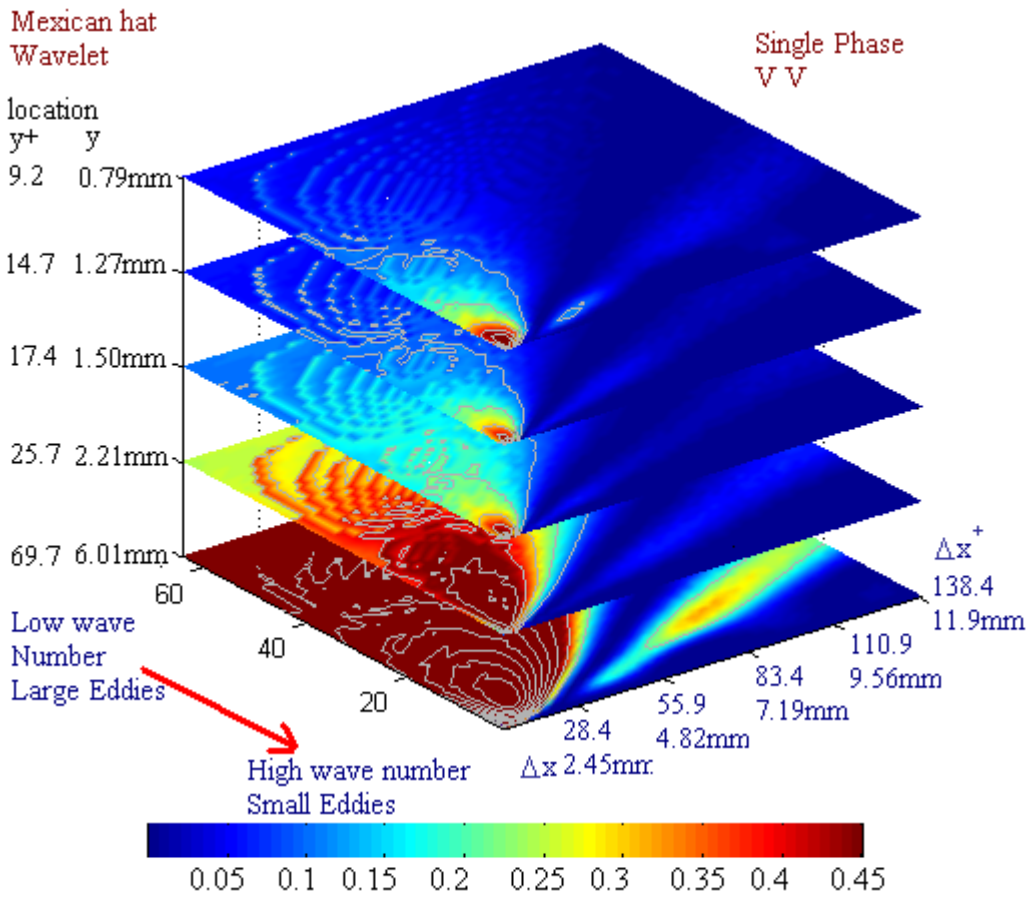

FIGURE 5.29 (a) Wavelet cross-correlation energy map of (v v) in longitudinal direction using Mexican hat for single phase.

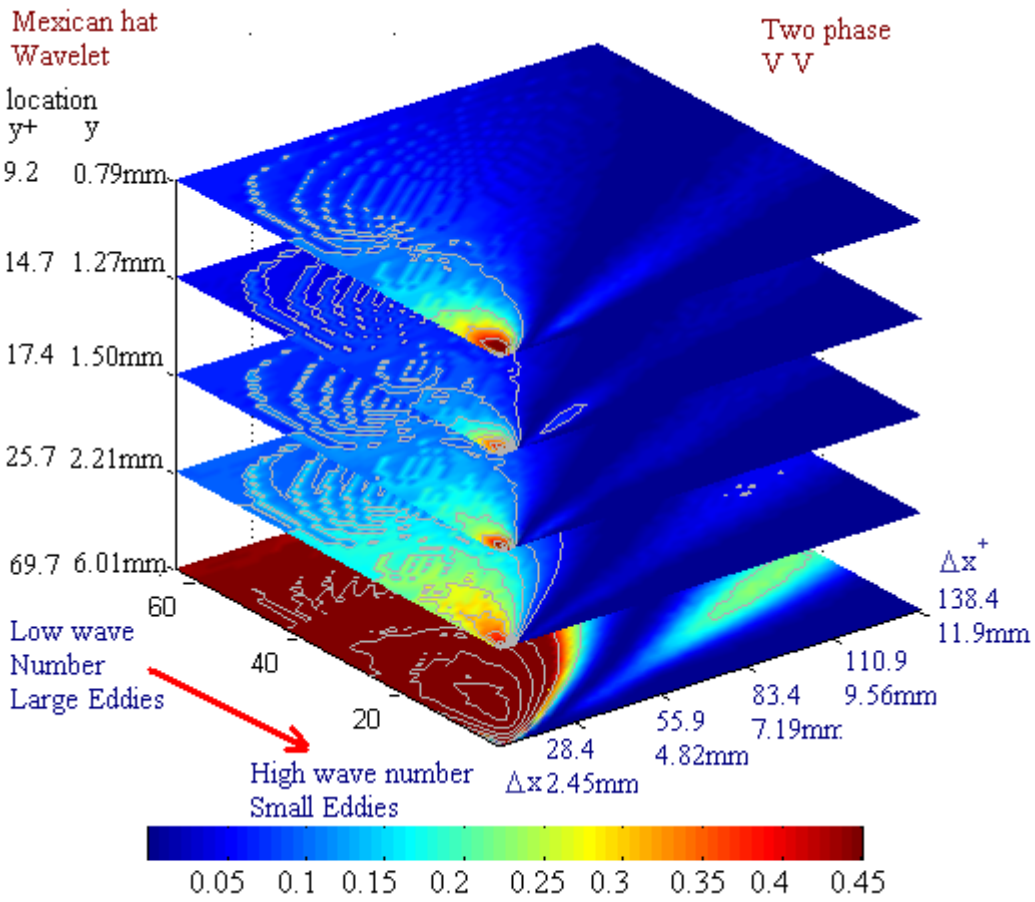

FIGURE 5.29 (b) Wavelet cross-correlation energy map of (v v) in longitudinal direction using Mexican hat for two phase.

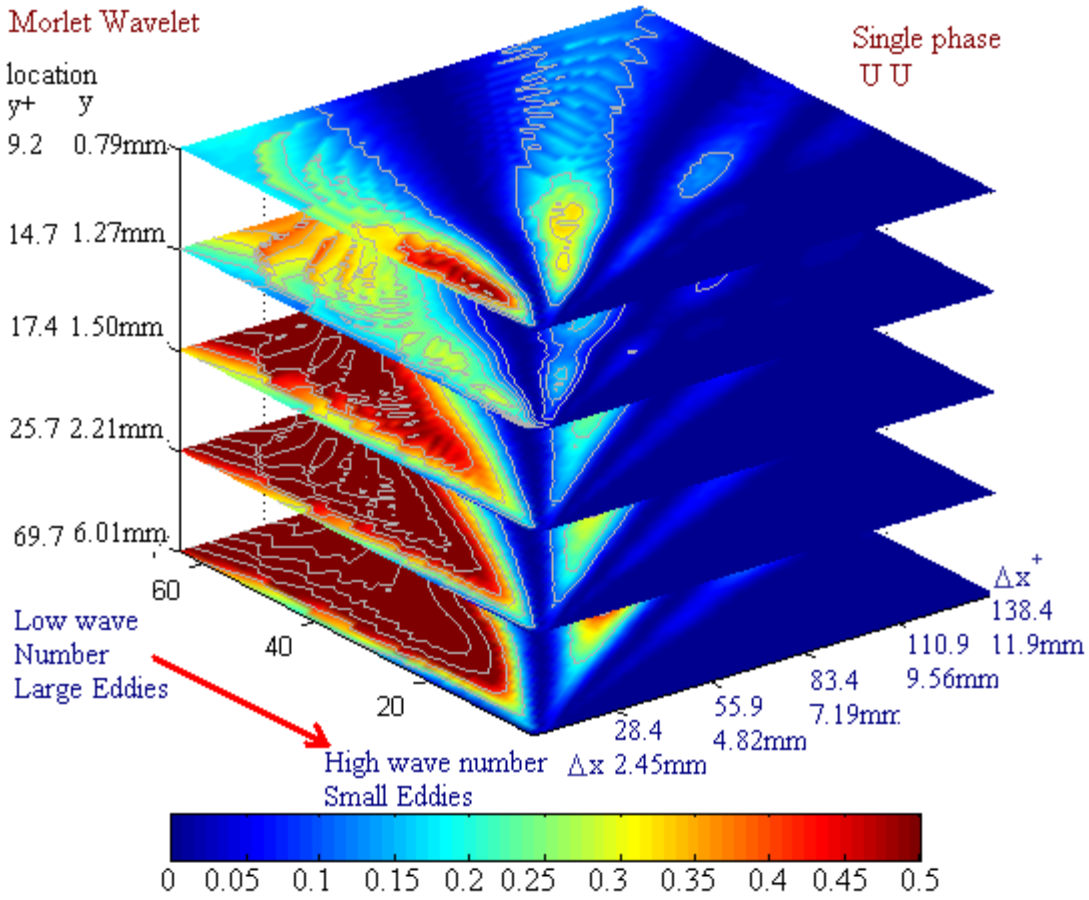

FIGURE 5.30(a) Wavelet cross-correlation energy map of (u u) in longitudinal direction using Morlet wavelet for single phase.

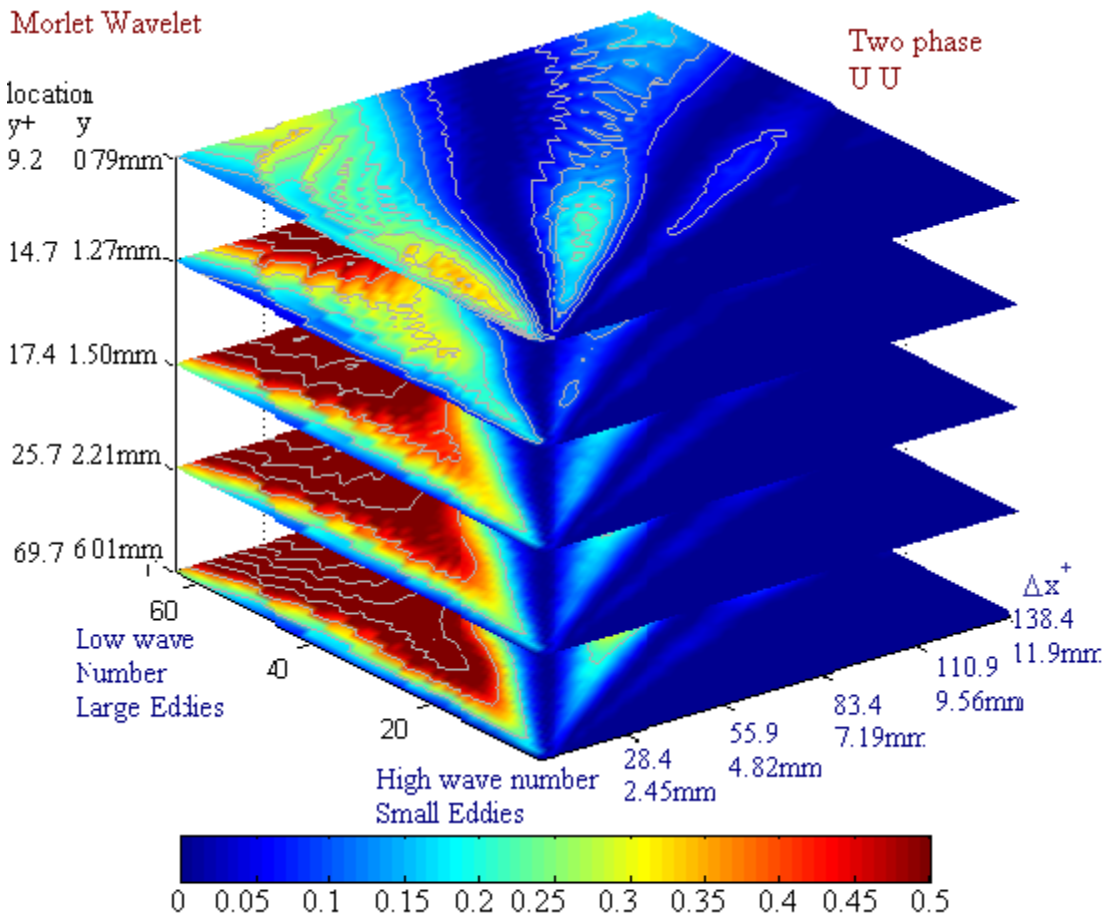

FIGURE 5.30(b) Wavelet cross-correlation energy map of (u u) in longitudinal direction using Morlet wavelet for single phase.

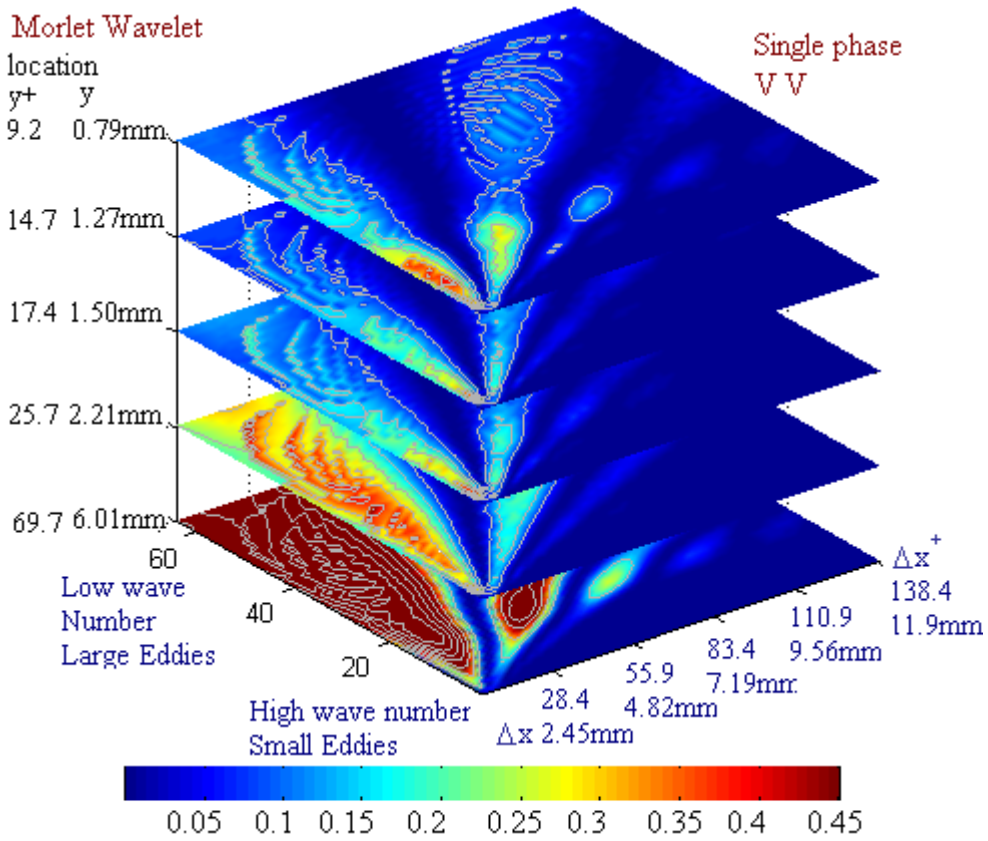

FIGURE 5.31 (a) Wavelet cross-correlation energy map of (v v) in longitudinal direction using Morlet wavelet for single phase.

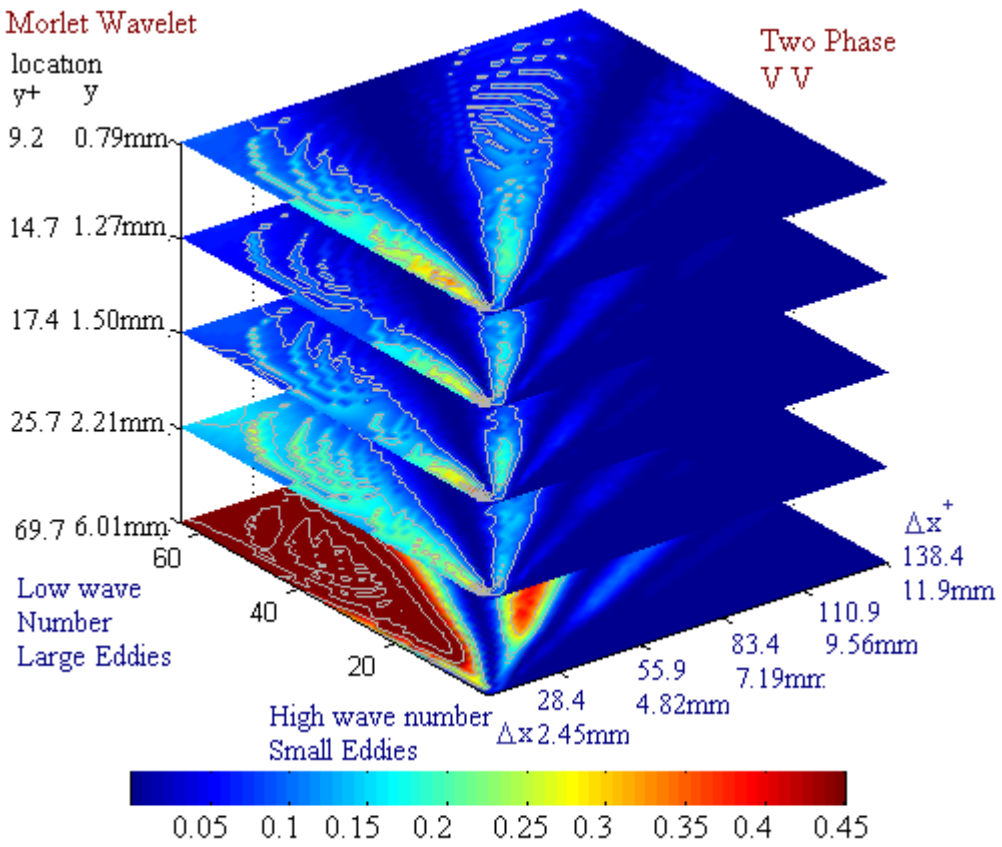

FIGURE 5.31 (b) Wavelet cross-correlation energy map of (v v) in longitudinal direction using Morlet wavelet for two phase.

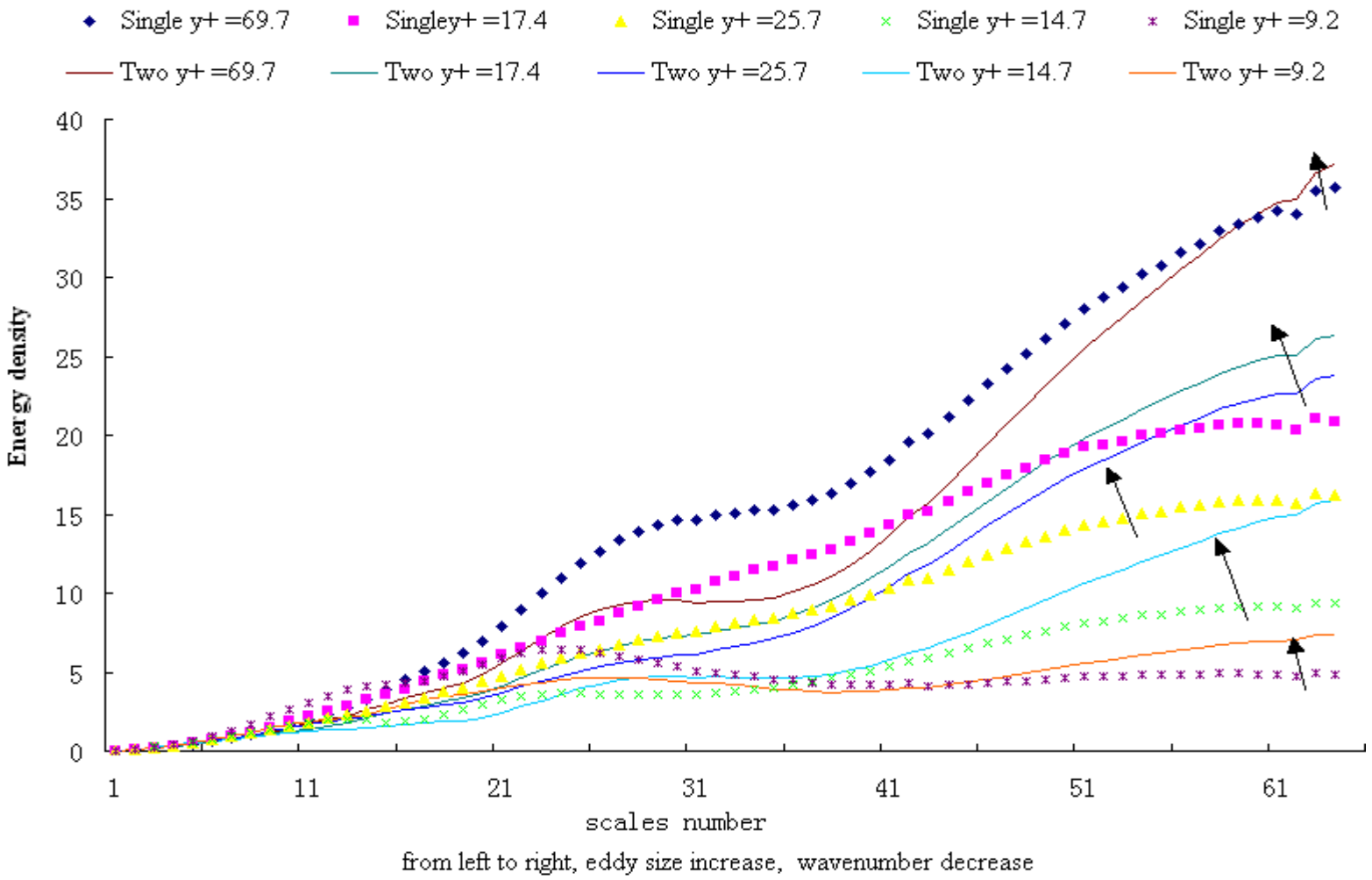

FIGURE 5.32 Wavelet cross-correlation density spectra of (u u) in longitudinal direction using Morlet wavelet.

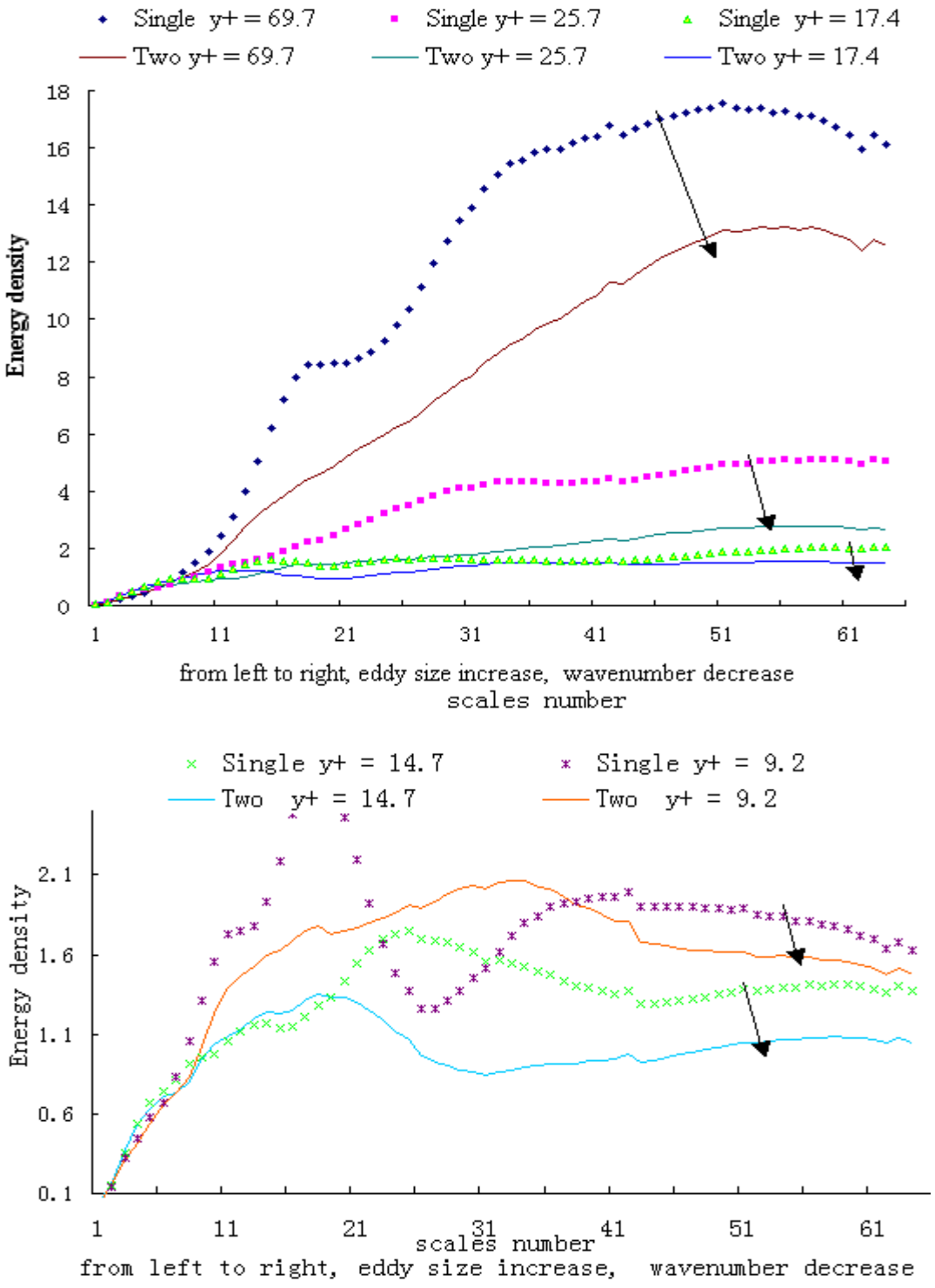

FIGURE 5.33 Wavelet cross-correlation density spectra of (v v) in longitudinal direction using Morlet wavelet.

Figures 5.34 (a), (b) give the (u u) Wavelet cross-correlation Energy map in transverse direction Mexican hat for single phase and two phase. And figures 5.35 (a), (b) give the (v v) Wavelet cross-correlation Energy map in transverse direction Mexican hat for single phase and two phase. Figures 5.36(a), (b), 5.37(a), (b) follow the same idea but using Morlet wavelet function. In figure 5.34 (a), the energy distribution was plotted at five x+ locations. And in each x+ plane, the energy strength was expressed by the color of the contour. The energy strength was located in wavenumber-Δy plane. The energy distribution follows the direction of the flow can be seen. In figure 5.34 (b), the same 3-D plot was given. The difference between these two 3-D plots was obvious. The energy distribution in the normal direction from streamwise direction velocities was increased in microbubbles injected conditions. Figures 5.35 (a) and (b) showed that the energy distribution in the transverse direction from normal direction velocities decreased in microbubbles injected conditions.

Using the algorithm of wavelet cross-correlation density spectra discussed in Chapter IV, the data from single phase flow and two phase flow are calculated. Figures 5.38, 5.39 give the (u u) and vv Wavelet cross-correlation density spectra in the transverse direction using Morlet wavelet. It can be seen that at the large eddy range, the density for (u u) was increased and the density for (v v) was decreased. It can also be seen that at the small eddy range, the density for (u u) was decreased and the density for (v v) was decreased.

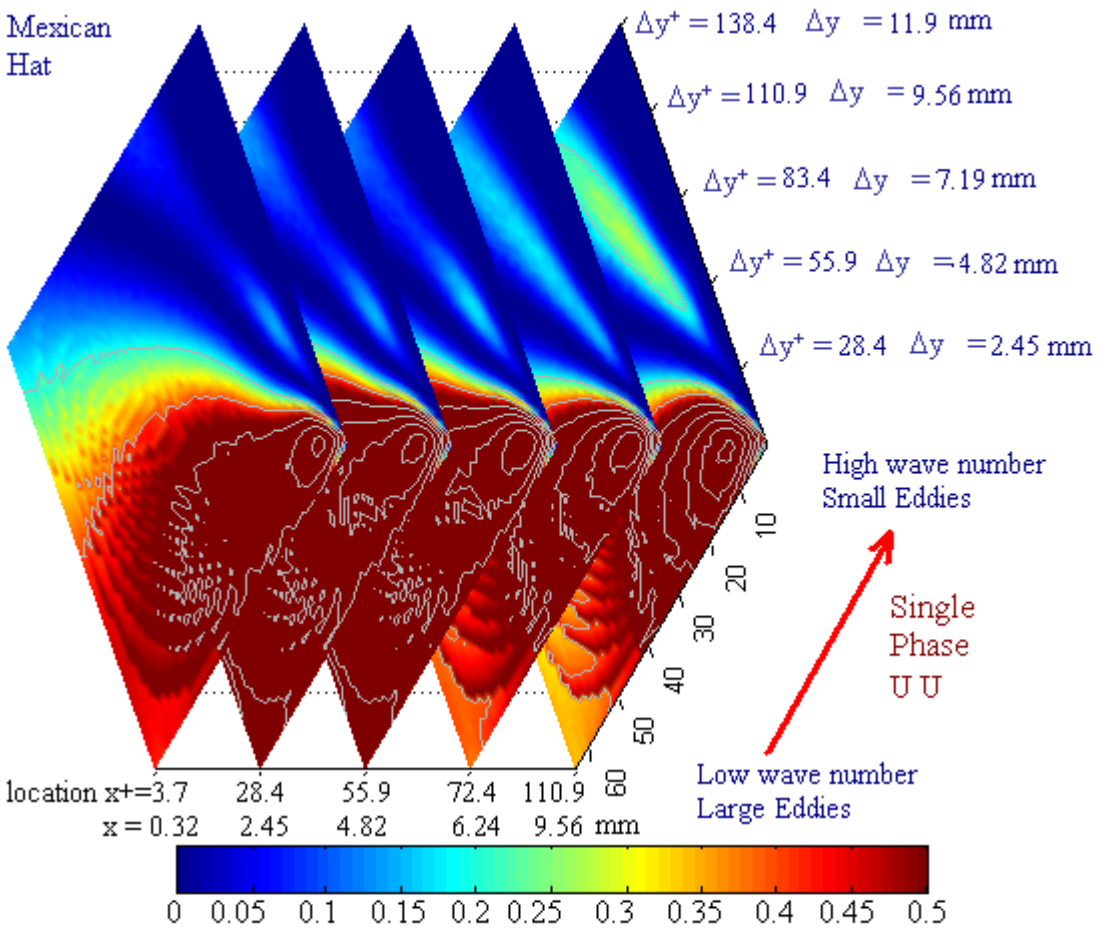

FIGURE 5.34 (a) Wavelet cross-correlation energy map of (u u) in transverse direction using Mexican hat for single phase.

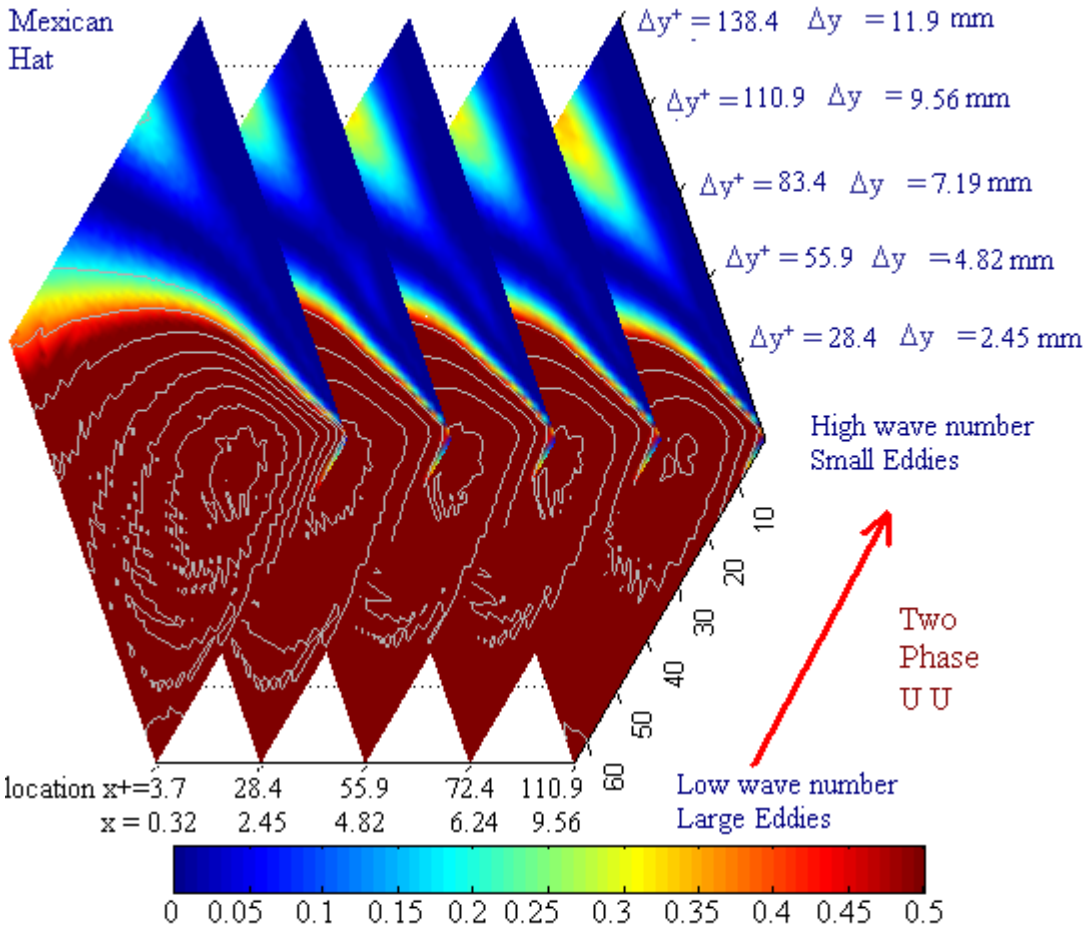

FIGURE 5.34 (b) Wavelet cross-correlation energy map of (u u) in transverse direction using Mexican hat for two phase.

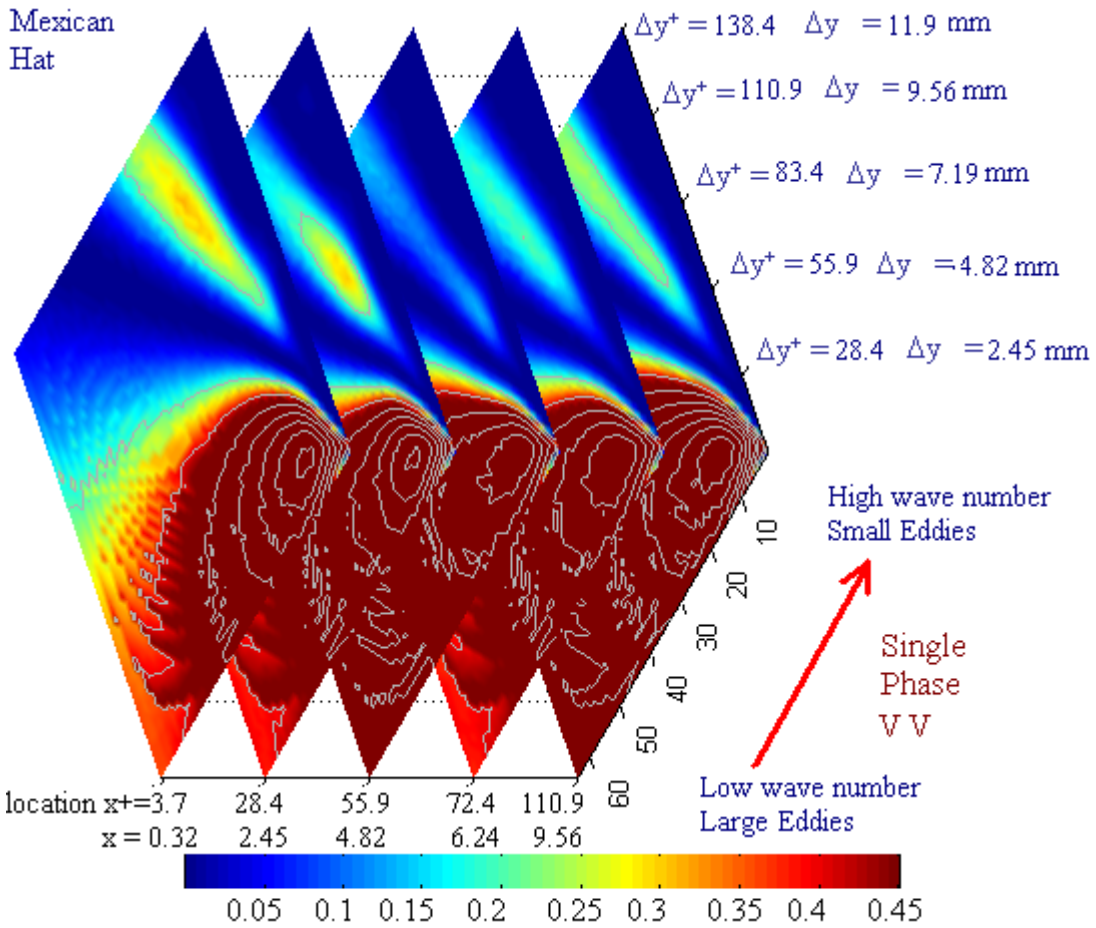

FIGURE 5.35 (a) Wavelet cross-correlation energy map of (v v) in transverse direction using Mexican hat for single phase.

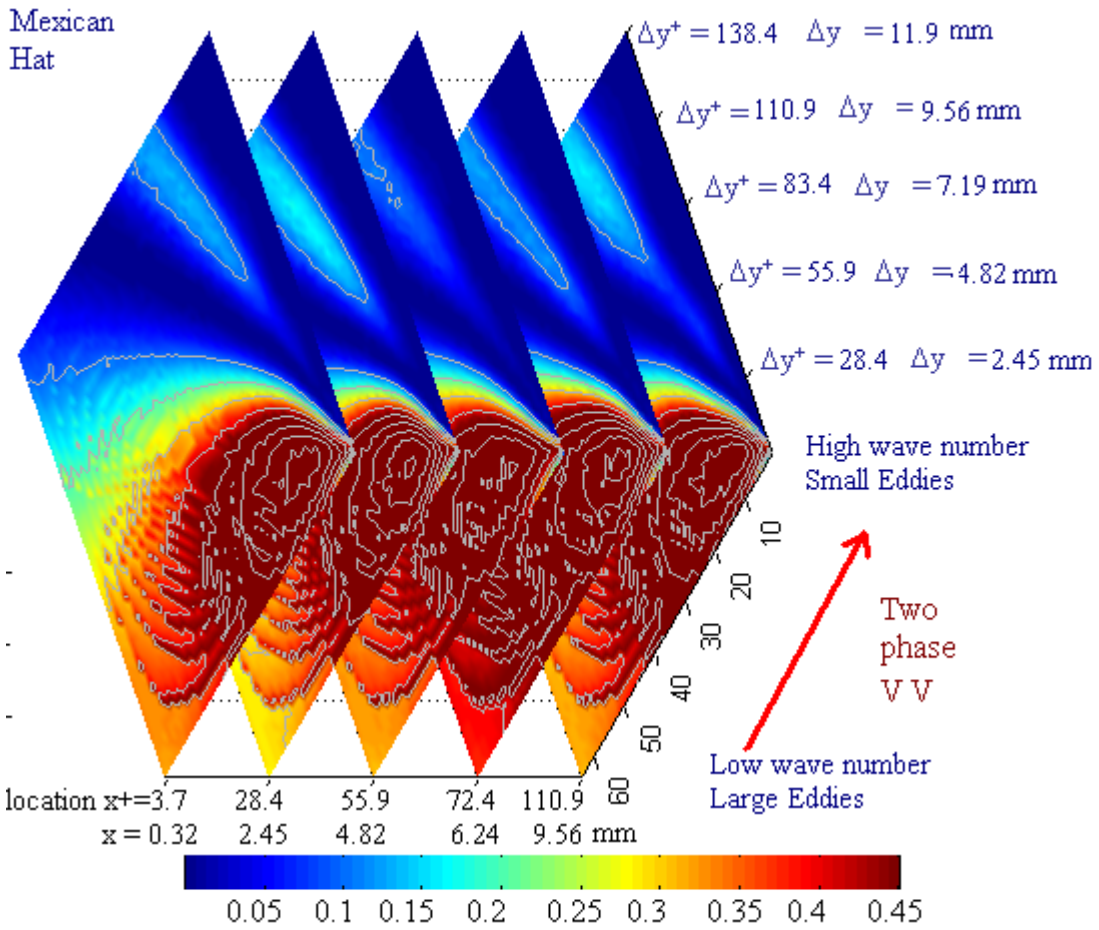

FIGURE 5.35 (b) Wavelet cross-correlation energy map of (v v) in transverse direction using Mexican hat for two phase.

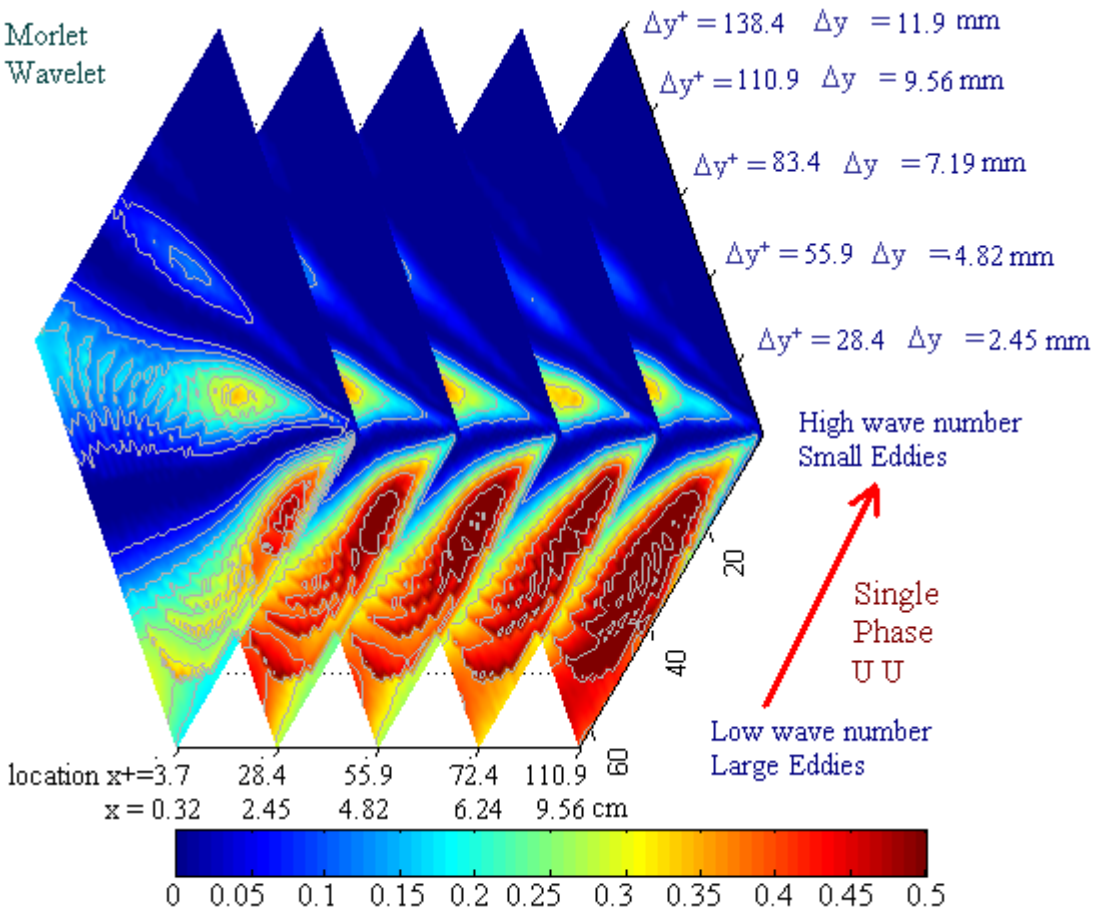

FIGURE 5.36 (a) Wavelet cross-correlation energy map of (u u) in transverse direction using Morlet wavelet for single phase.

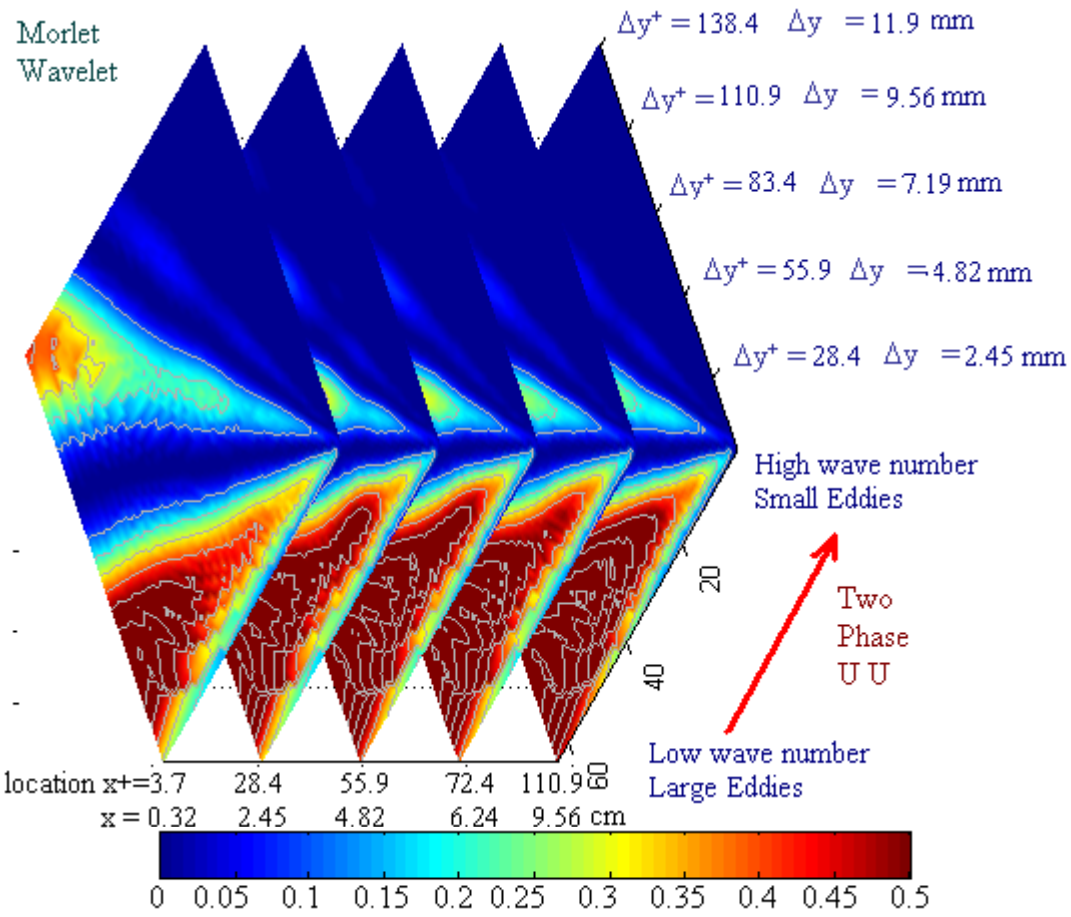

FIGURE 5.36 (b) Wavelet cross-correlation energy map of (u u) in transverse direction using Morlet wavelet for two phase.

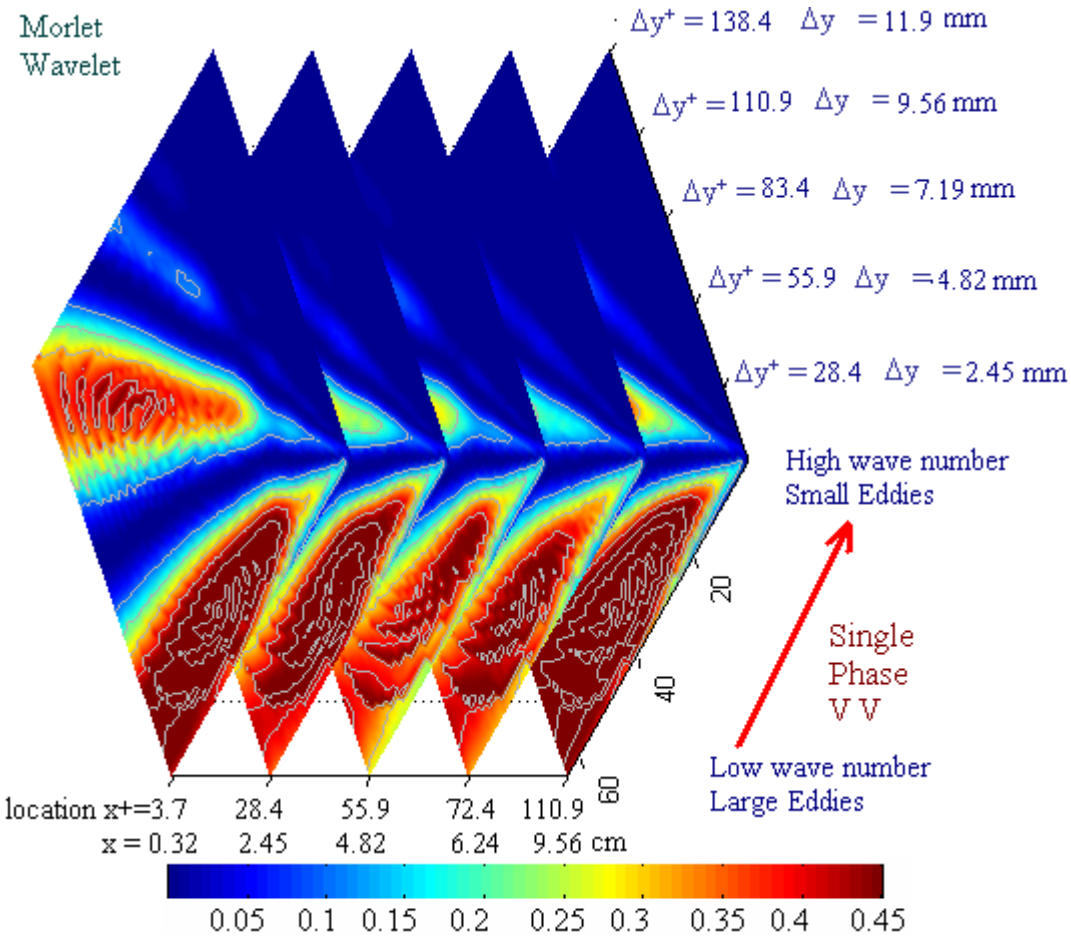

FIGURE 5.37 (a) Wavelet cross-correlation energy map of (v v) in transverse direction using Morlet wavelet for single phase.

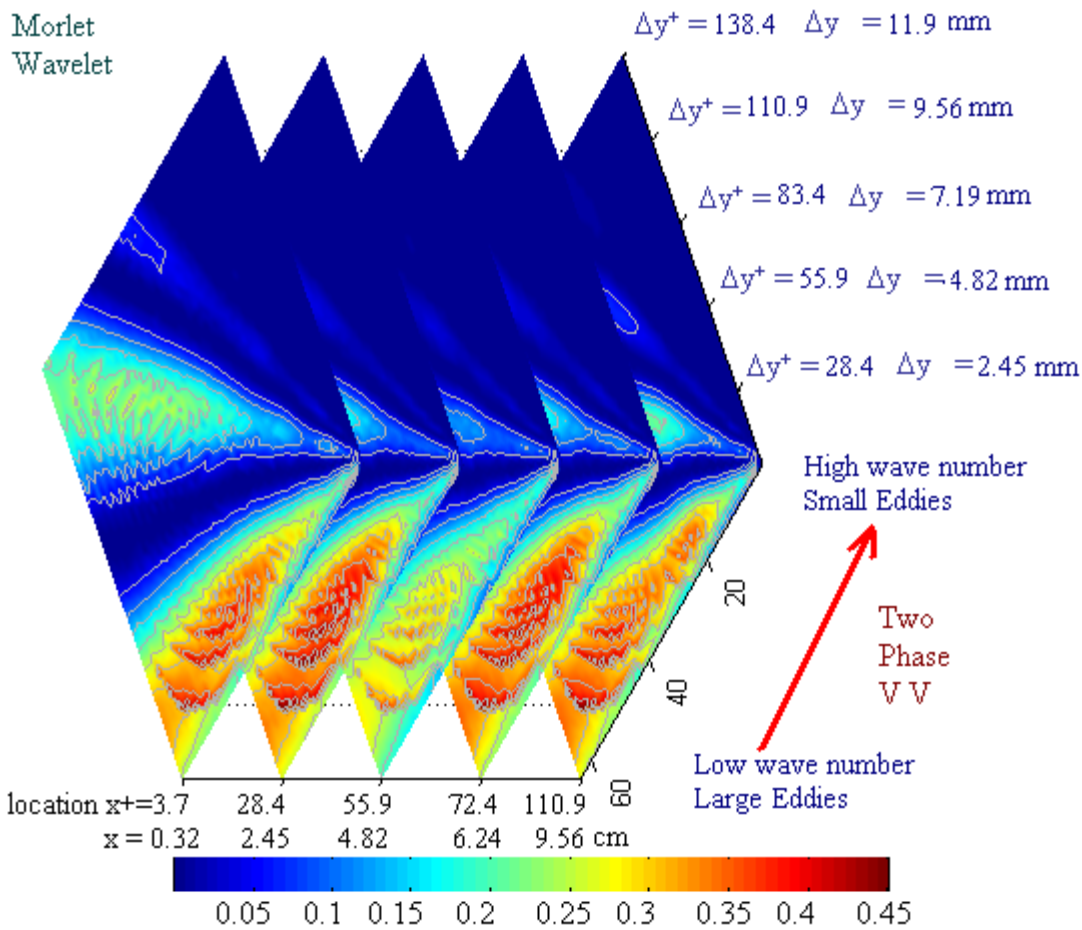

FIGURE 5.37 (b) Wavelet cross-correlation energy map of (v v) in transverse direction using Morlet wavelet for two phase.

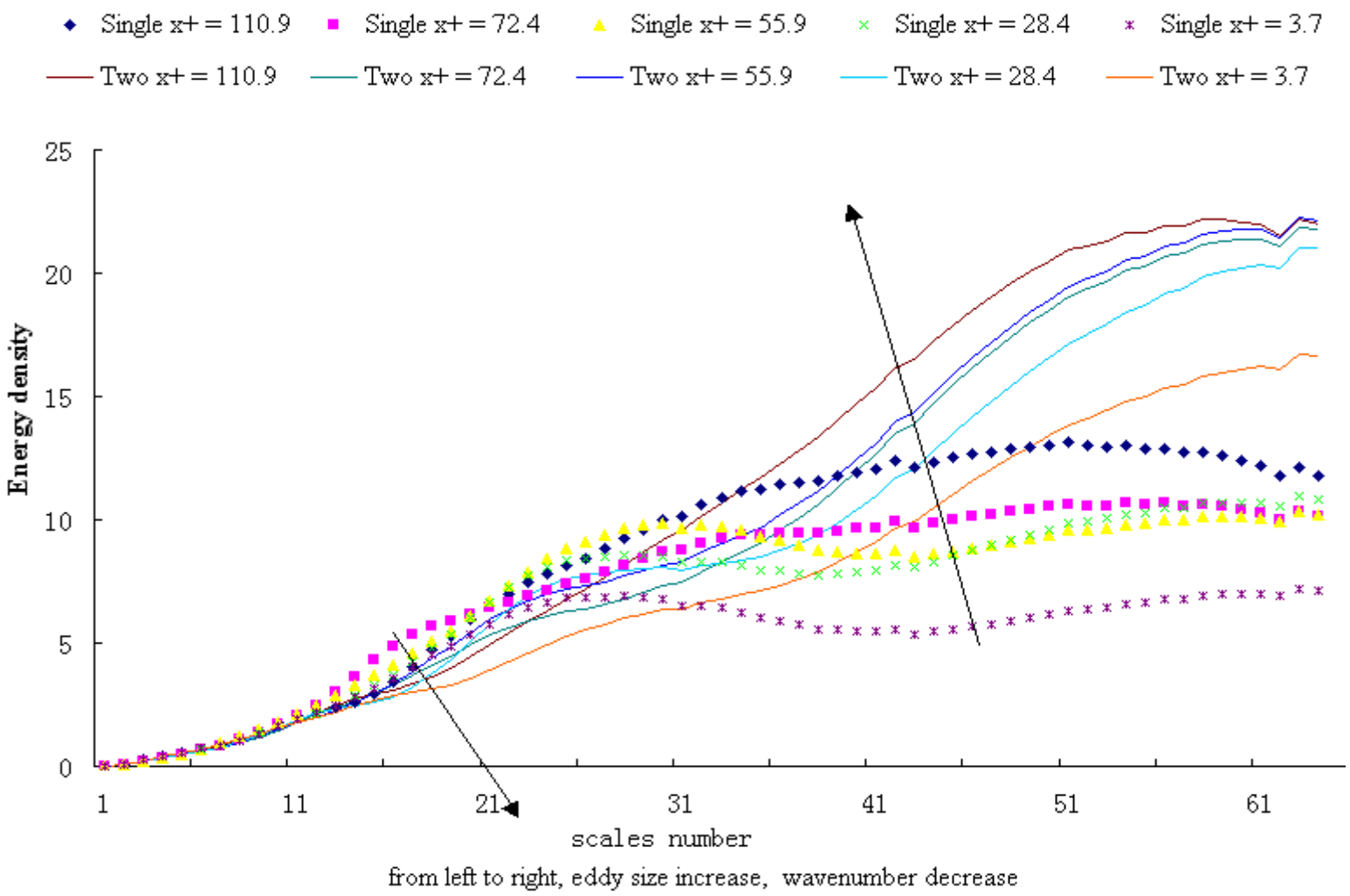

FIGURE 5.38 Wavelet cross-correlation density spectra of (u u) in transverse direction using Morlet wavelet.

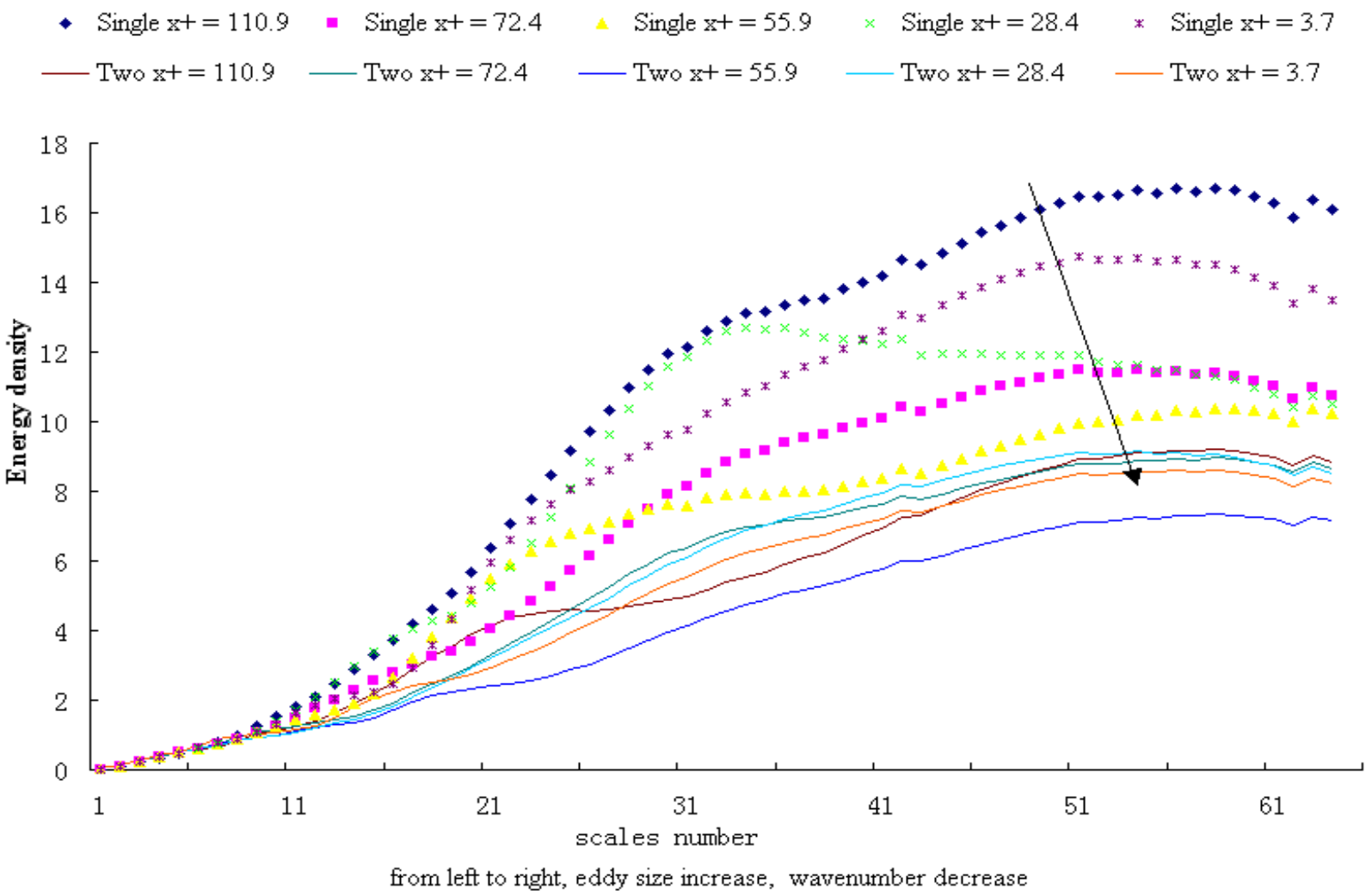

FIGURE 5.39 Wavelet cross-correlation density spectra of (v v) in transverse direction using Morlet wavelet.

5.4 Wavelet auto-correlation map at y+ =14.7

Figures 5.40 (a) give the auto-correlation for (u u) at x+ = 47.7, y+ = 14.7 for single phase flow and two phase flow. Figures 5.40 (b) give the corresponding wavelet auto-correlation map.

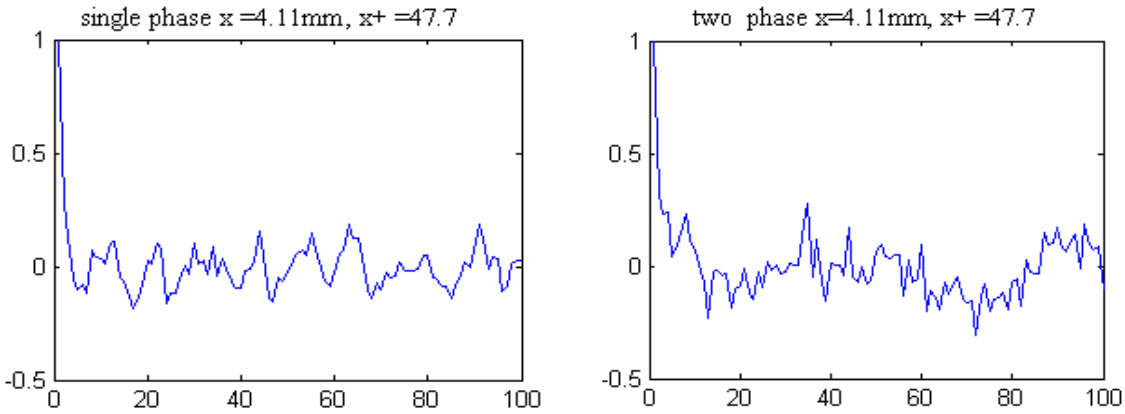

FIGURE 5.40 (a) Auto-correlation for (u u) at y= 1.27mm, y+ =14.7, x=4.11mm, x+ =47.7.

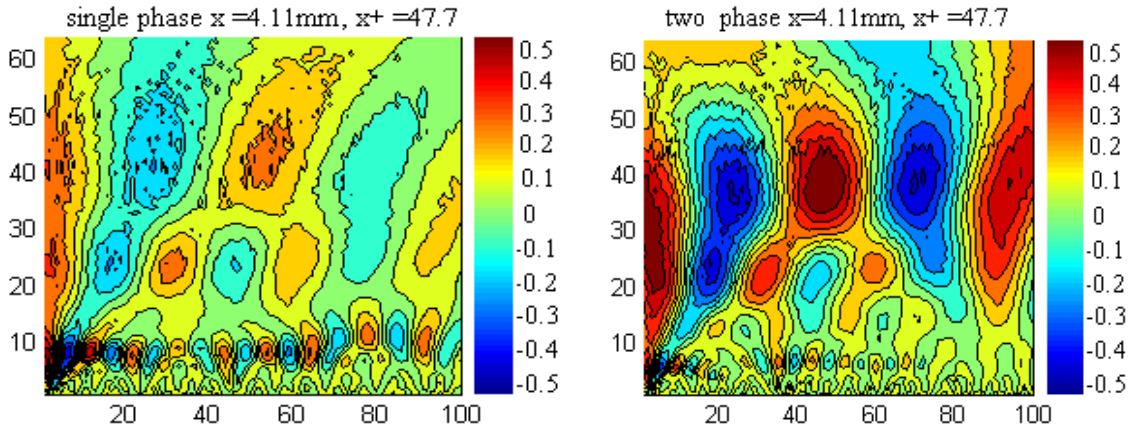

FIGURE 5.40 (b) Wavelet auto-correlation map for (u u) at y= 1.27mm, y+ =14.7, x=4.11mm, x+ =47.7.

Figures 5.41 (a) give the auto-correlation for (u u) at x+ = 53.2, y+ = 14.7 for single phase flow and two phase flow. Figures 5.41 (b) give the corresponding wavelet auto-correlation map.

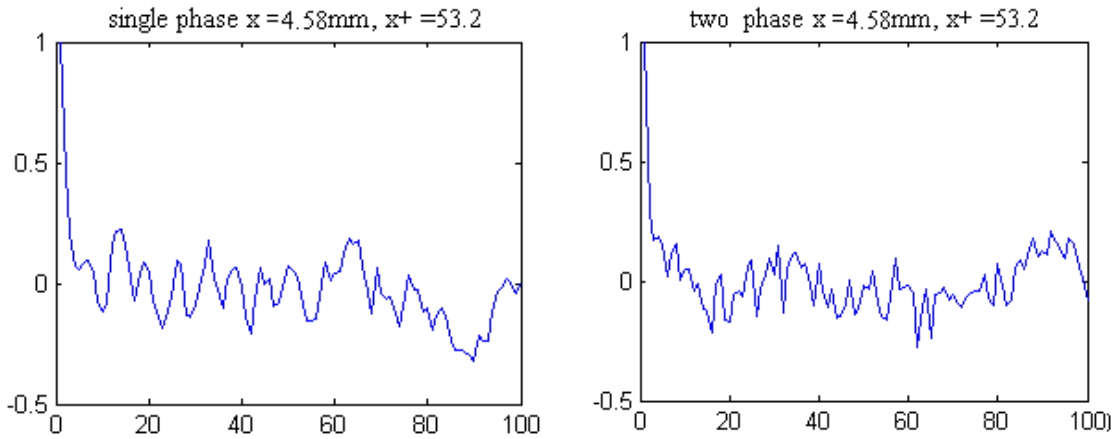

FIGURE 5.41 (a) Auto-correlation for (u u) at y= 1.27mm, y+ =14.7, x=4.58mm, x+ =53.2.

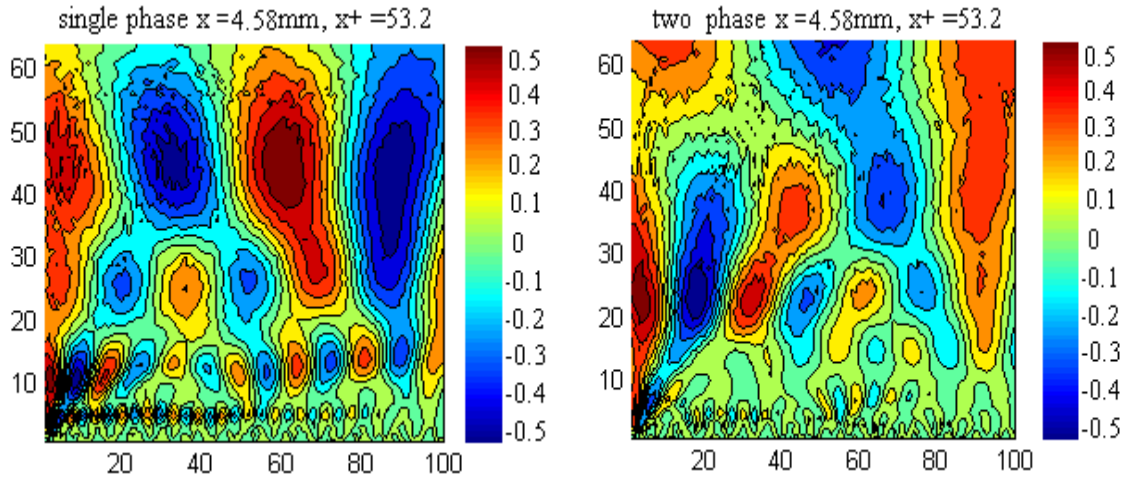

FIGURE 5.41 (b) Wavelet auto-correlation map for (u u) at y= 1.27mm, y+ =14.7, x=4.58mm, x+ =53.2.

Figures 5.42 (a) give the auto-correlation for (u u) at x+ = 58.7, y+ = 14.7 for single phase flow and two phase flow. Figures 5.42 (b) give the corresponding wavelet auto-correlation map.

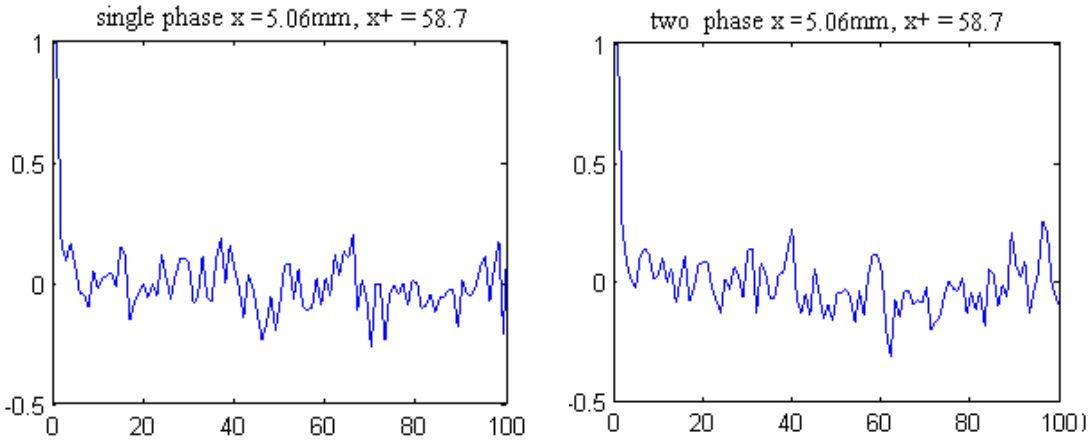

FIGURE 5.42(a) Auto-correlation for (u u) at y= 1.27mm, y+ =14.7, x=5.06mm, x+ =58.7.

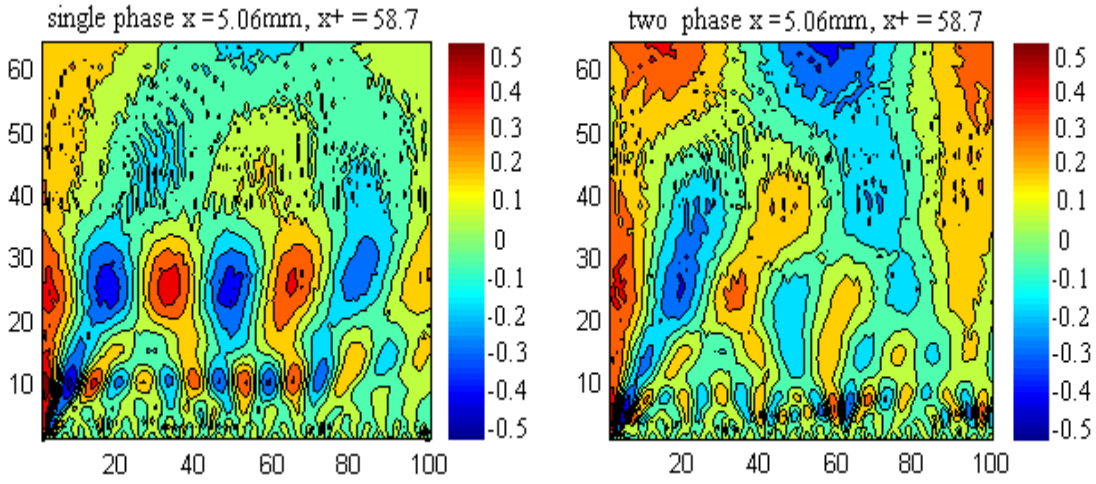

FIGURE 5.42 (b) Wavelet auto-correlation map for (u u) at y= 1.27mm, y+ =14.7, x=5.06mm, x+ =58.7.

Figures 5.43 (a) give the auto-correlation for (u u) at x+ = 64.2, y+ = 14.7 for single phase flow and two phase flow. Figures 5.43 (b) give the corresponding wavelet auto-correlation map.

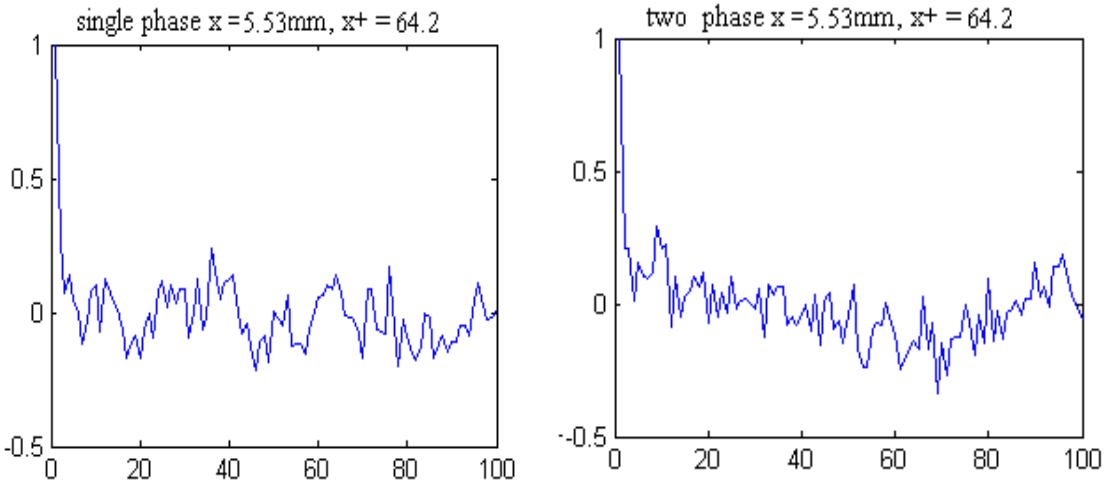

FIGURE 5.43(a) Auto-correlation for (u u) at y= 1.27mm, y+ =14.7, x=5.53mm, x+ =64.2.

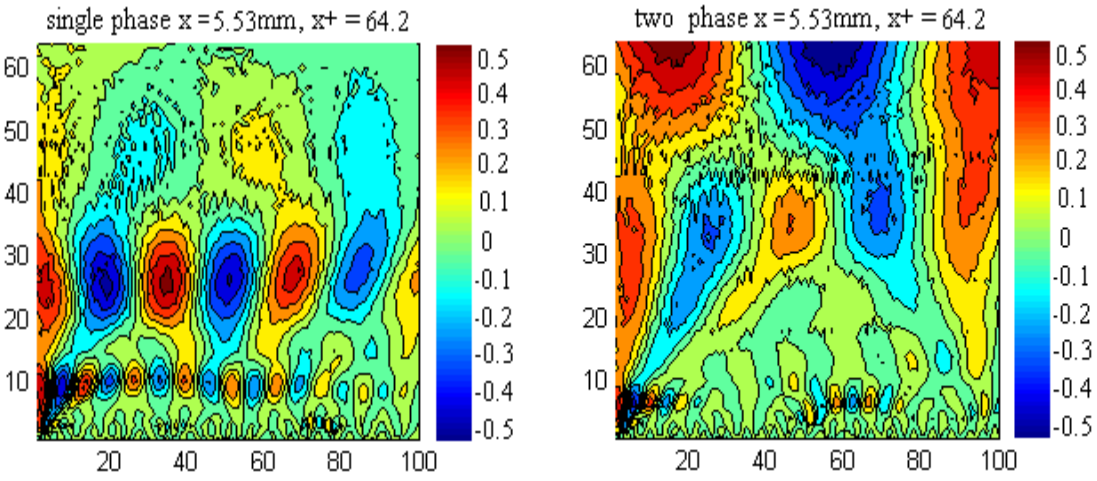

FIGURE 5.43 (b) Wavelet auto-correlation map for (u u) at y= 1.27mm, y+ =14.7, x=5.53mm, x+ =64.2.

Figures 5.44 (a) give the auto-correlation for (u u) at x+ = 69.7, y+ = 14.7 for single phase flow and two phase flow. Figures 5.44 (b) give the corresponding wavelet auto-correlation map.

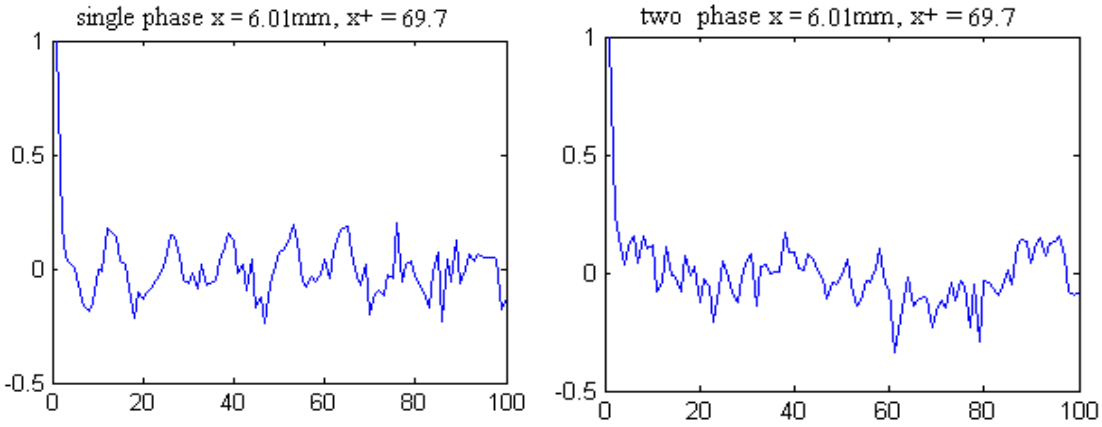

FIGURE 5.44 (a) Auto-correlation for (u u) at y= 1.27mm, y+ =14.7, x=6.01mm, x+ =69.7.

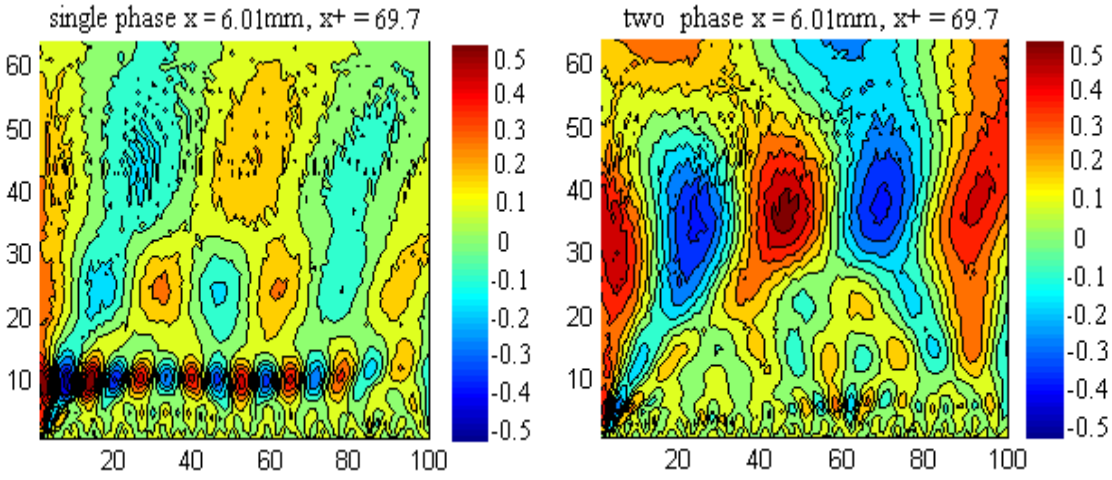

FIGURE 5.44 (b) Wavelet auto-correlation map for (u u) at y= 1.27mm, y+ =14.7, x=6.01mm, x+ =69.7.

Figures 5.45 (a) give the three-D plot of wavelet auto-correlation map for (u u) at y= 1.27mm, y+ =14.7 of single phase using Mexican hat wavelet.

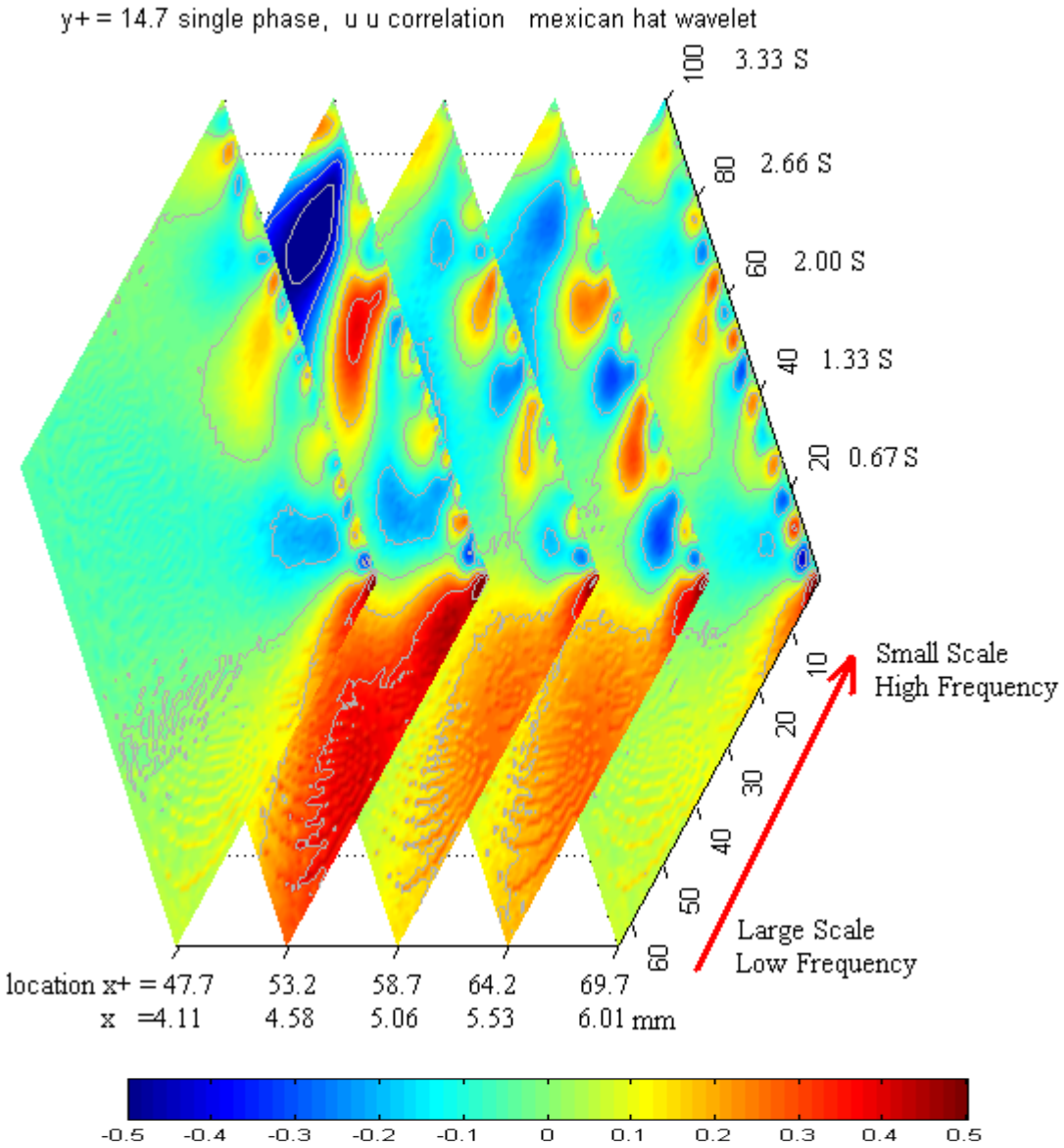

FIGURE 5.45 (a) Three-D plot of wavelet auto-correlation map for (u u) at y= 1.27mm, y+ =14.7 of single phase using Mexican hat wavelet.

Figures 5.45 (b) give the three-D plot of wavelet auto-correlation map for (u u) at y= 1.27mm, y+ =14.7 of two phase using Mexican hat wavelet.

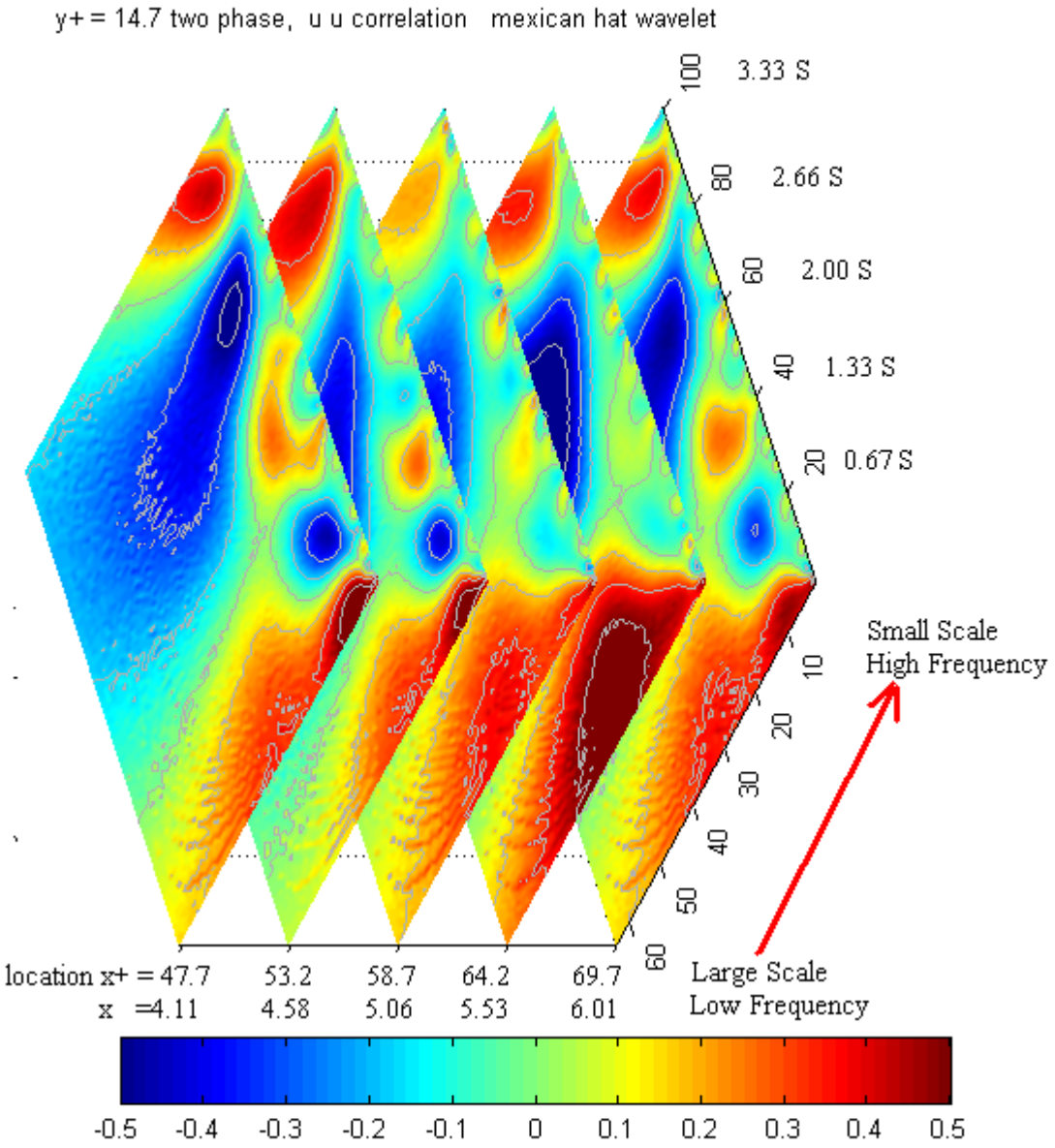

FIGURE 5.45 (b) Three-D plot of wavelet auto-correlation map for (u u) at y= 1.27mm, y+ =14.7 of two phase using Mexican hat wavelet.

Figures 5.46 (a) give the three-D plot of wavelet auto-correlation map for (v v) at y= 1.27mm, y+ =14.7 of single phase using Mexican hat wavelet.

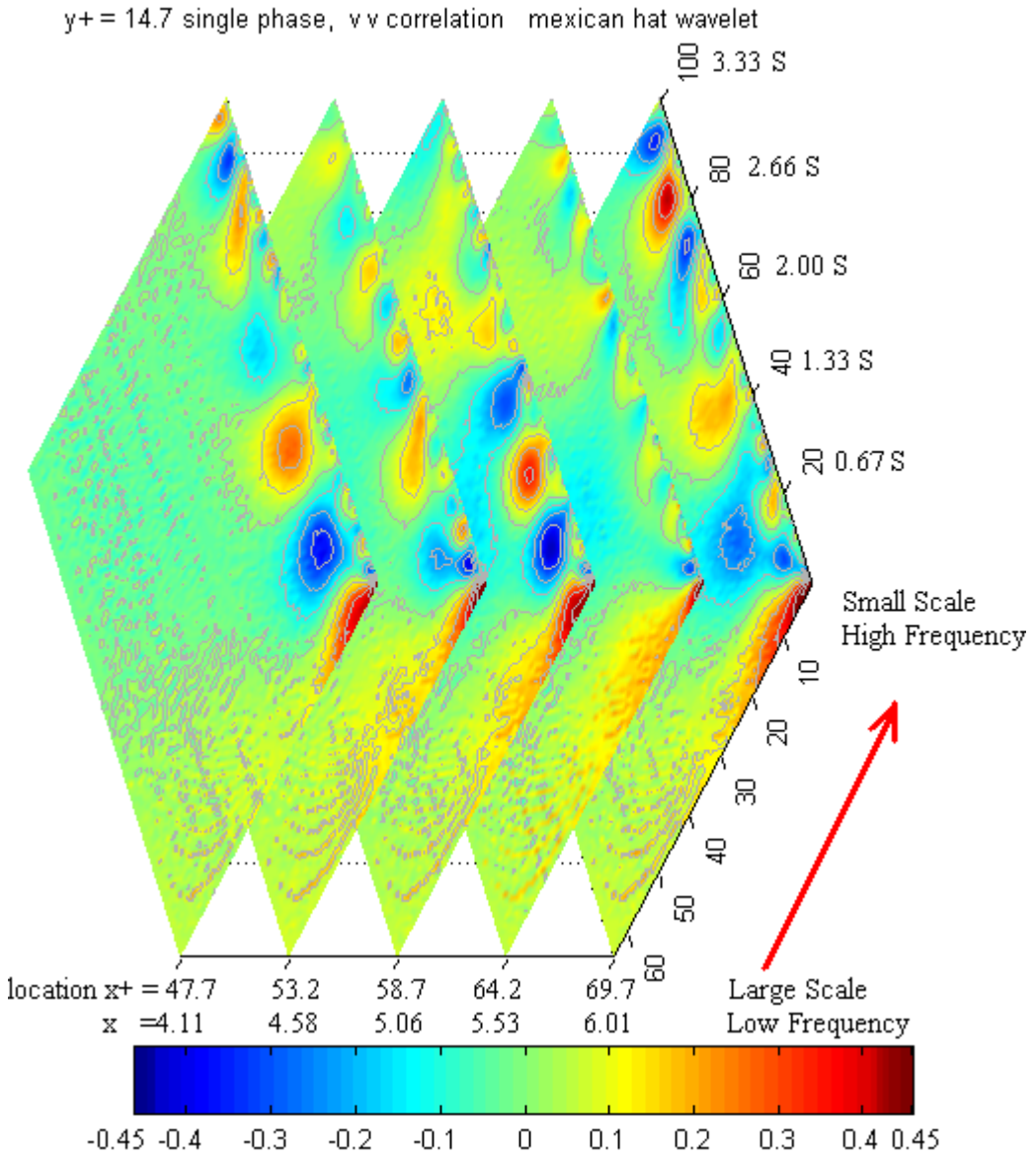

FIGURE 5.46 (a) Three-D plot of wavelet auto-correlation map for (v v) at y= 1.27mm, y+ =14.7 of single phase using Mexican hat wavelet.

Figures 5.46 (b) give the three-D plot of wavelet auto-correlation map for (v v) at y= 1.27mm, y+ =14.7 of two phase using Mexican hat wavelet.

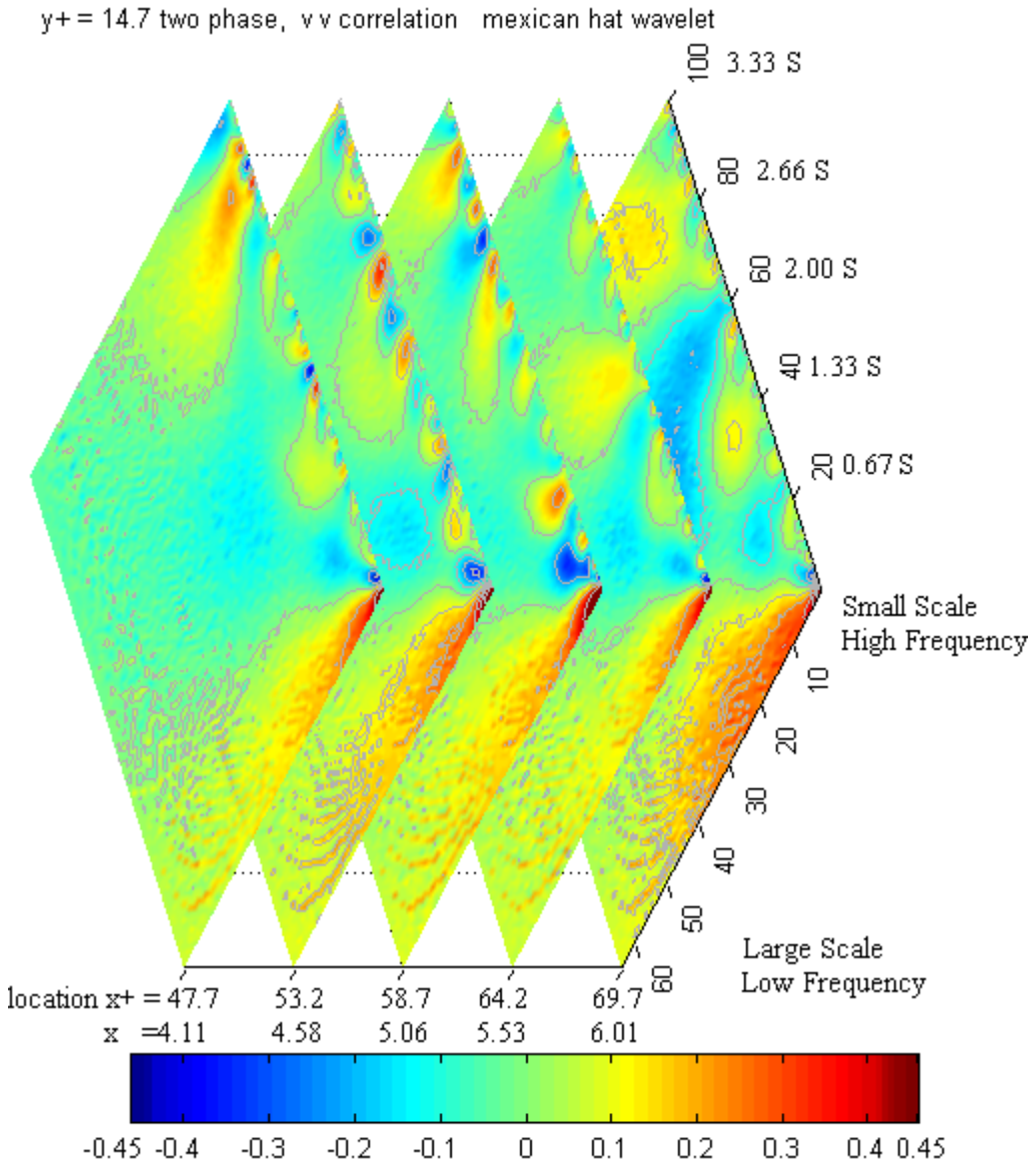

FIGURE 5.46 (b) Three-D plot of wavelet auto-correlation map for (v v) at y= 1.27mm, y+ =14.7 of two phase using Mexican hat wavelet.

Figures 5.47 (a) give the three-D plot of wavelet cross-correlation map for u v at y= 1.27mm, y+ =14.7 of single phase using Mexican hat wavelet.

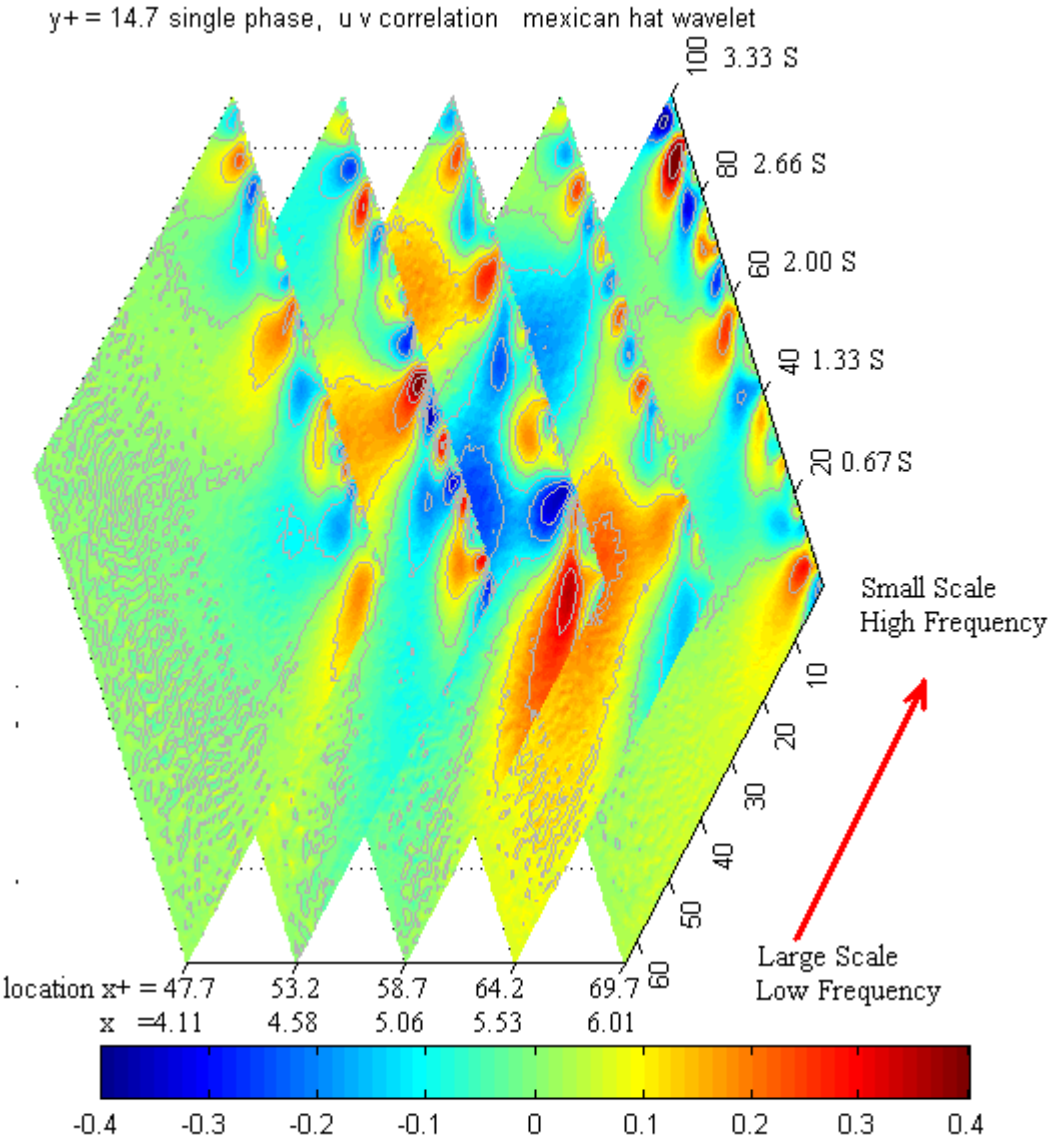

FIGURE 5.47 (a) Three-D plot of wavelet cross-correlation map for u v at y= 1.27mm, y+ =14.7 of single phase using Mexican hat wavelet.

Figures 5.47 (b) give the three-D plot of wavelet cross-correlation map for u v at y= 1.27mm, y+ =14.7 of single phase using Mexican hat wavelet.

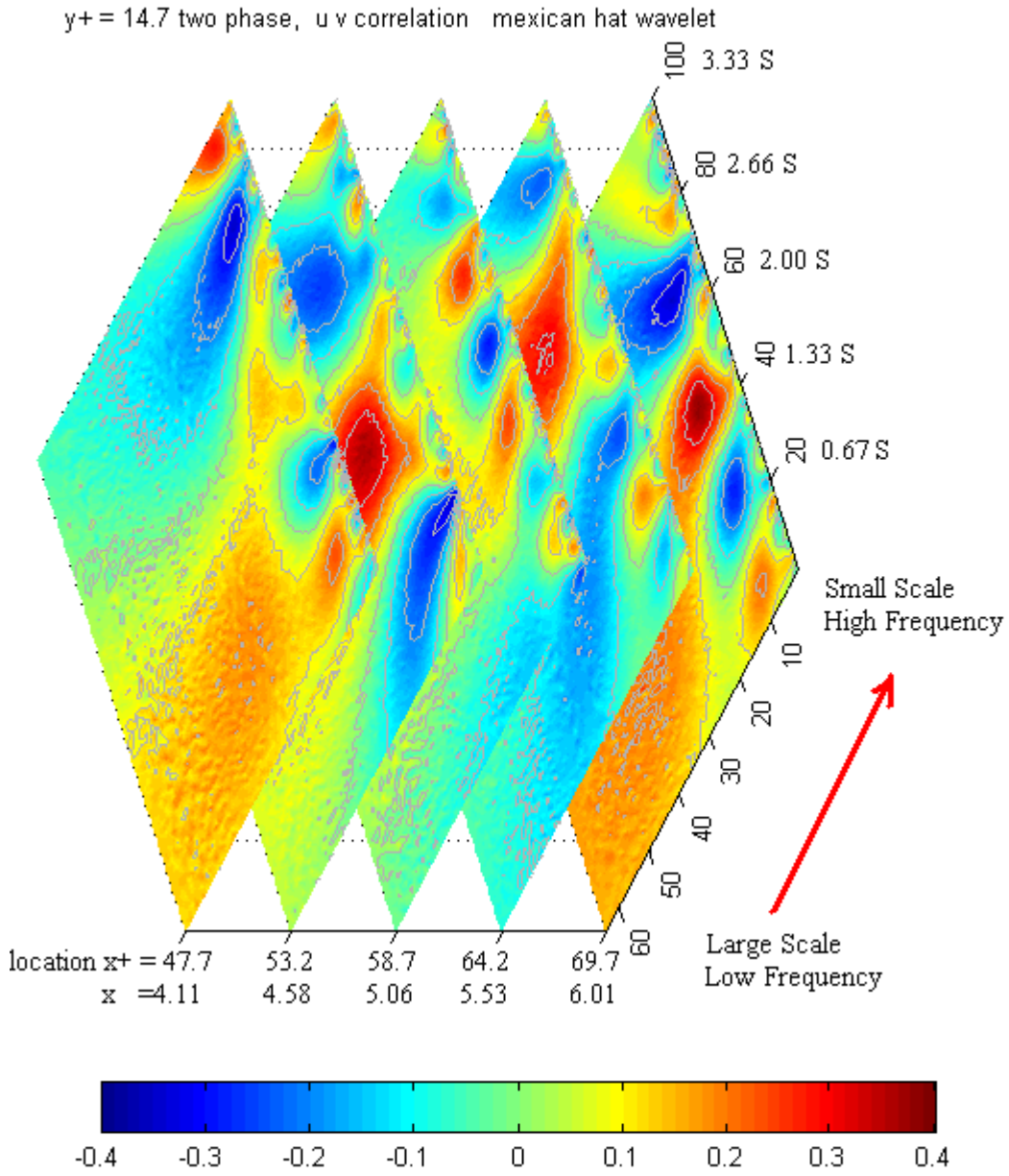

FIGURE 5.47 (b) Three-D plot of wavelet cross-correlation map for u v at y= 1.27mm, y+ =14.7 of two phase using Mexican hat wavelet.

Figures 5.48 (a) give the three-D plot of wavelet auto-correlation map for (u u) at y= 1.27mm, y+ =14.7 of single phase using Morlet wavelet.

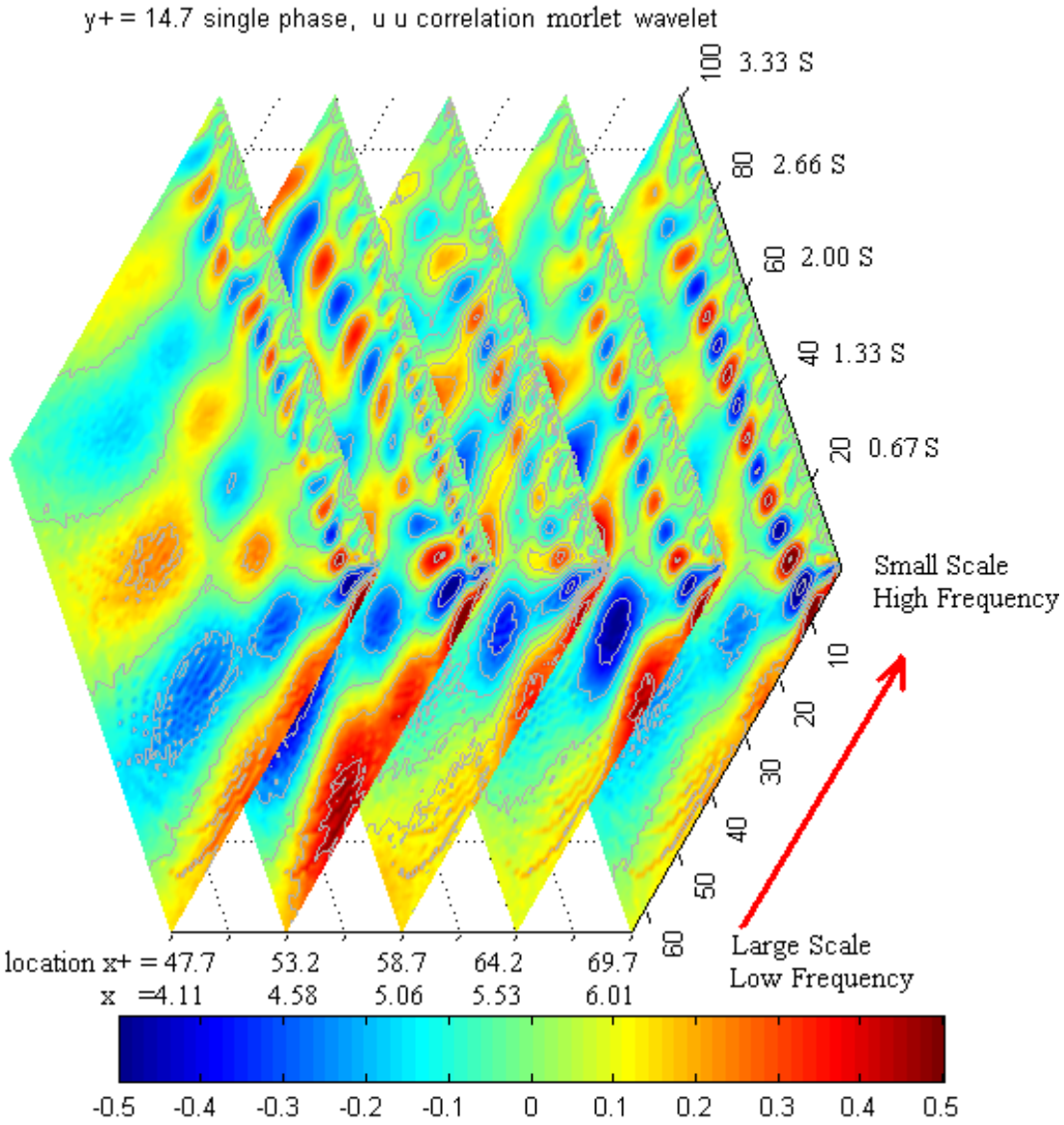

FIGURE 5.48 (a) Three-D plot of CWT map for (u u) at y= 1.27mm, y+ =14.7 of single phase using Morlet wavelet.

Figures 5.48 (b) give the three-D plot of wavelet auto-correlation map for (u u) at y= 1.27mm, y+ =14.7 of two phase using Morlet wavelet.

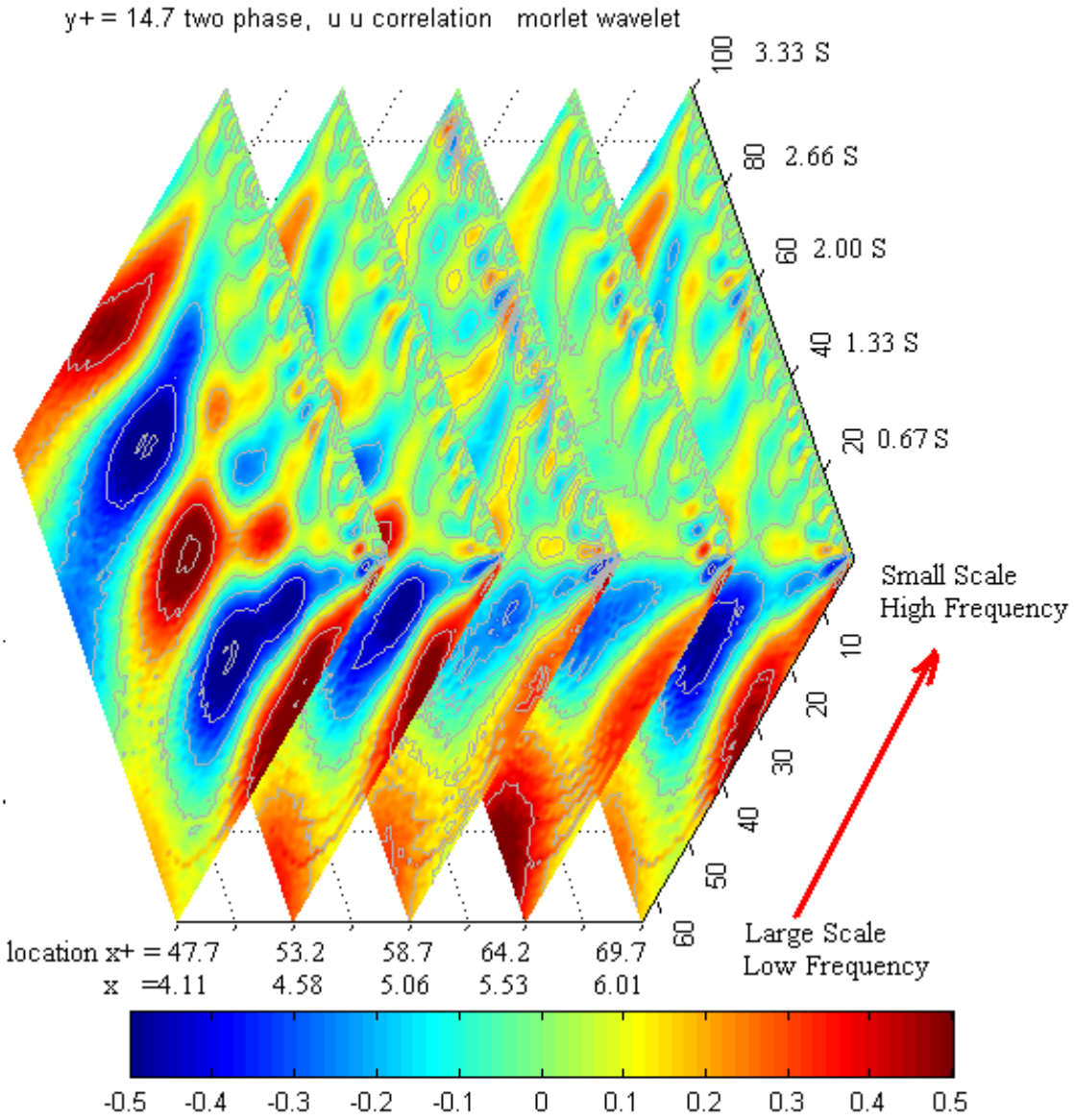

FIGURE 5.48 (b) Three-D plot of wavelet auto-correlation map for (u u) at y= 1.27mm, y+ =14.7 of two phase using Morlet wavelet.

Figures 5.49 (a) give the three-D plot of wavelet auto-correlation map for (v v) at y= 1.27mm, y+ =14.7 of single phase using Morlet wavelet.

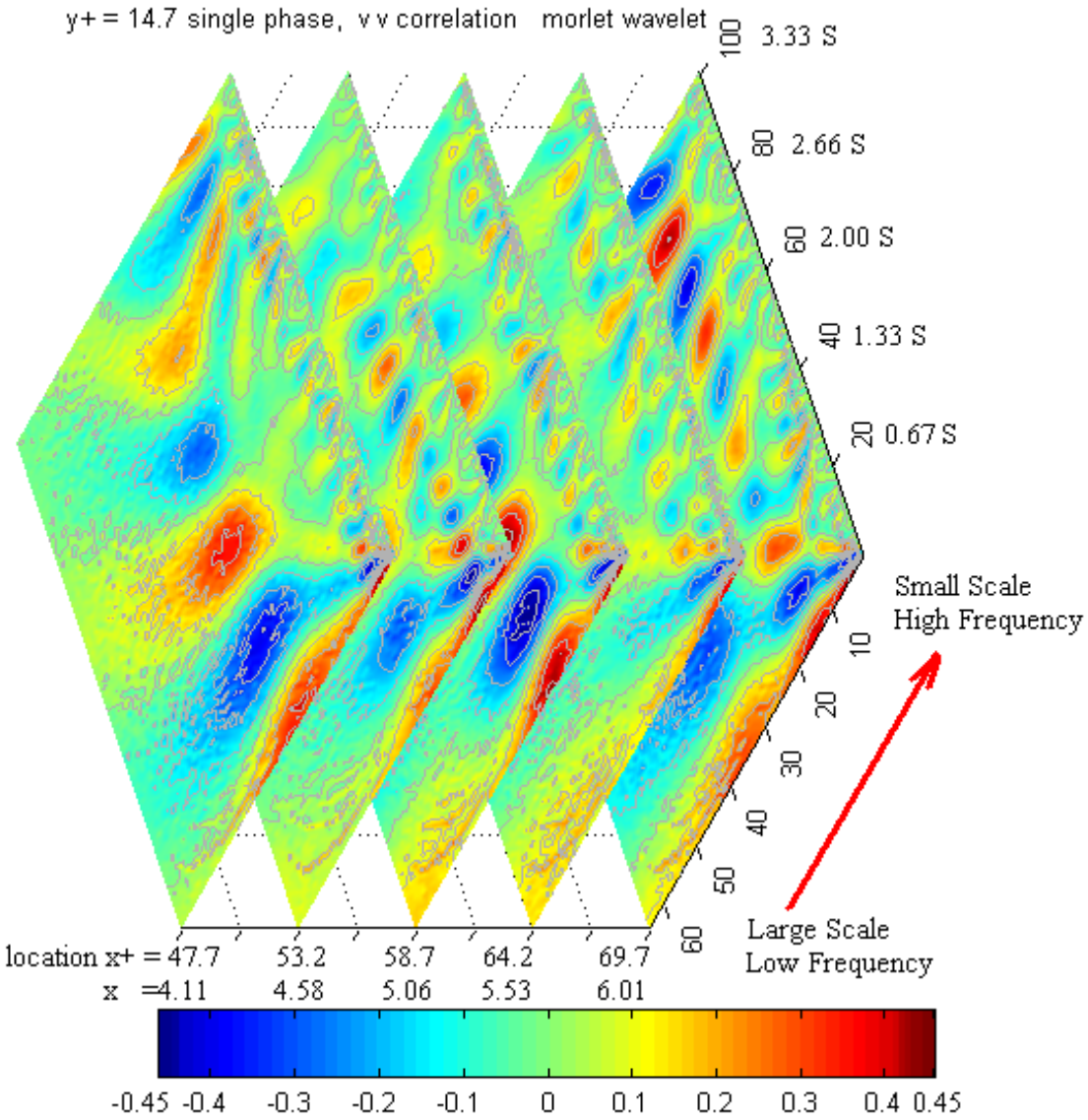

FIGURE 5.49 (a) Three-D plot of wavelet auto-correlation map for (v v) at y= 1.27mm, y+ =14.7 of single phase using Morlet wavelet.

Figures 5.49 (b) give the three-D plot of wavelet auto-correlation map for (v v) at y= 1.27mm, y+ =14.7 of two phase using Morlet wavelet.

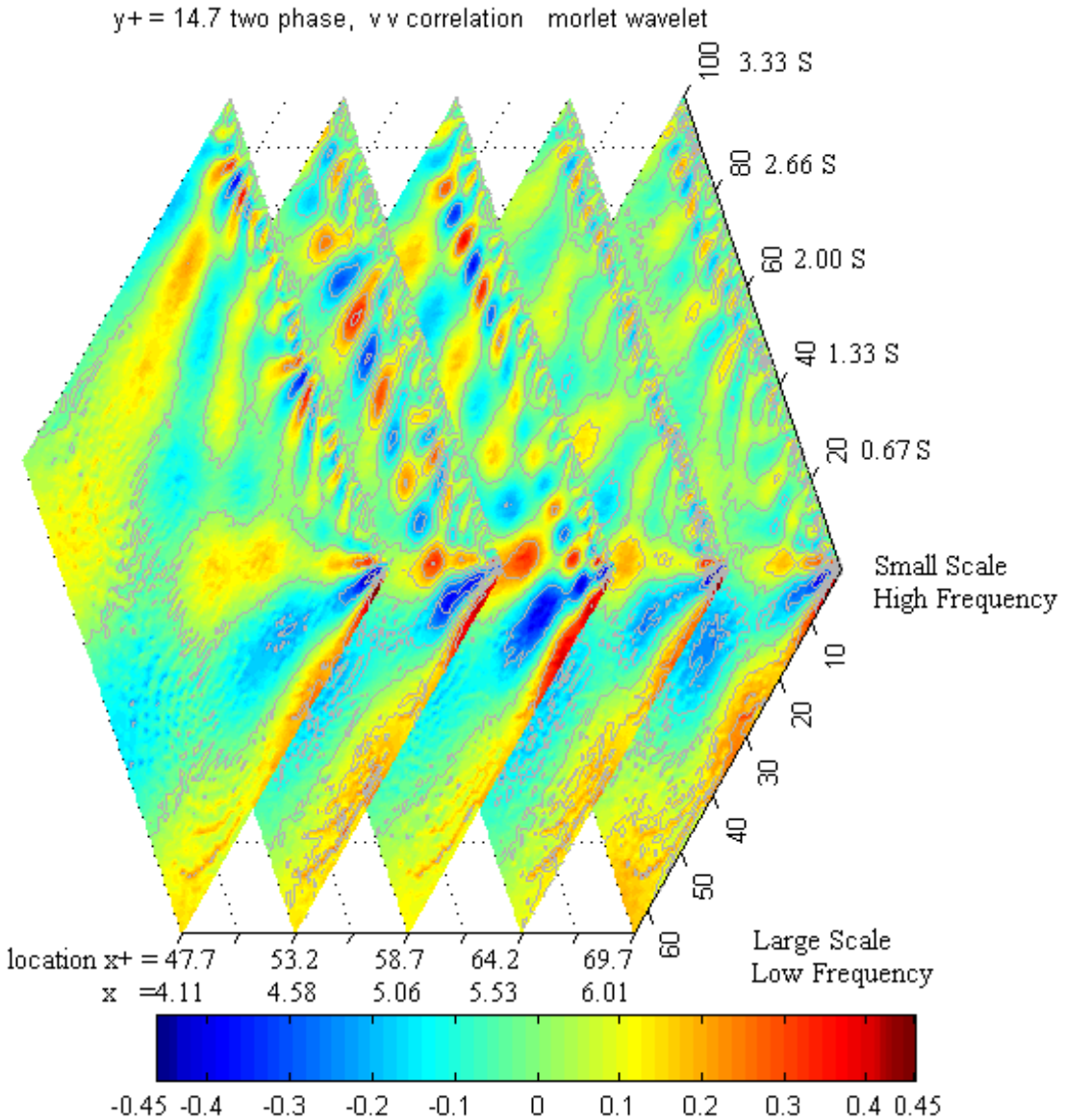

FIGURE 5.49 (b) Three-D plot of wavelet auto-correlation map for (v v) at y= 1.27mm, y+ =14.7 of two phase using Morlet wavelet.

Figures 5.50 (a) give the three-D plot of wavelet cross-correlation map for u v at y= 1.27mm, y+ =14.7 of two phase using Morlet wavelet.

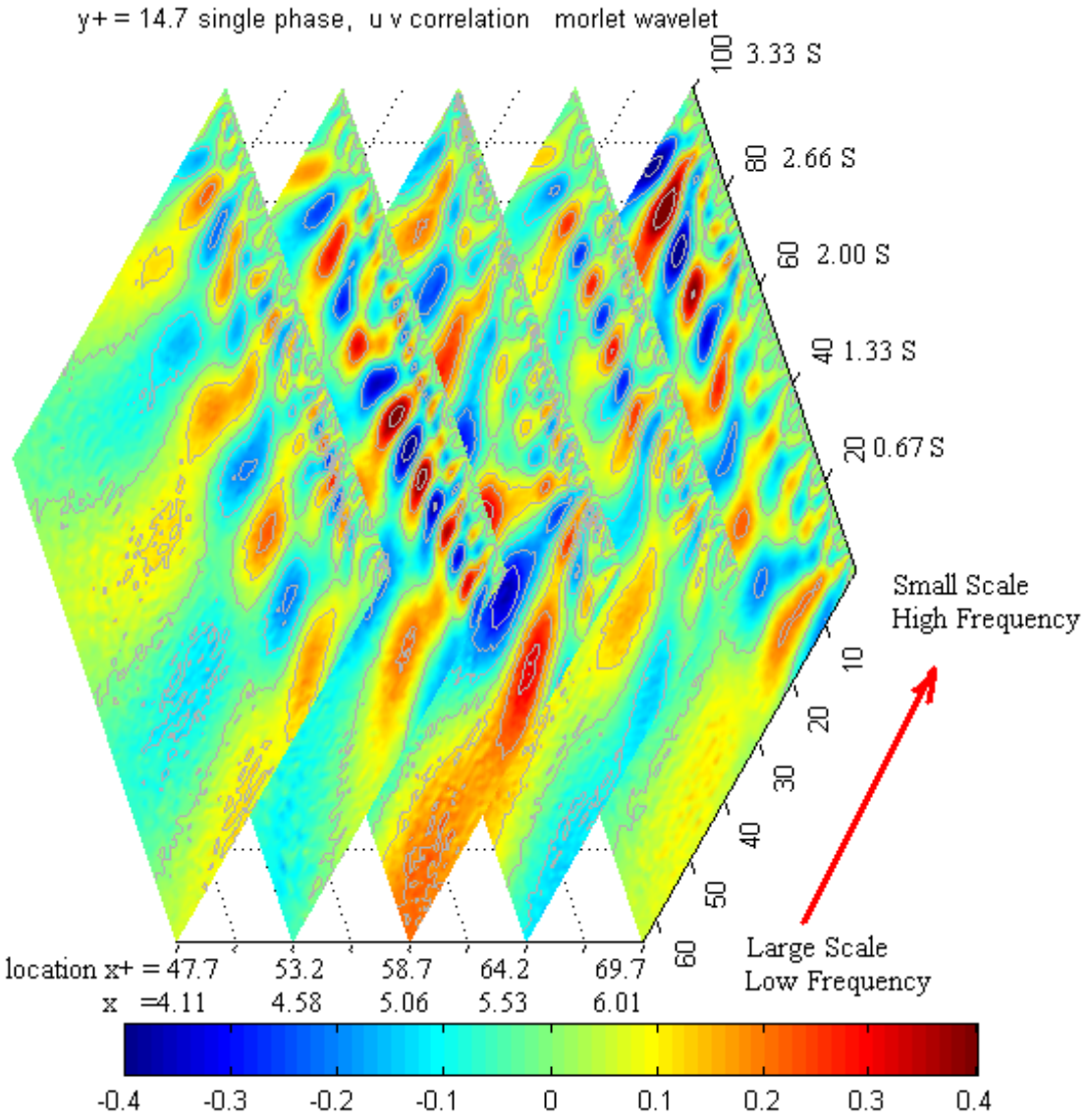

FIGURE 5.50 (a) Three-D plot of wavelet cross-correlation map for u v at y= 1.27mm, y+ =14.7 of single phase using Morlet wavelet.

Figures 5.50 (b) give the three-D plot of wavelet cross-correlation map for u v at y= 1.27mm, y+ =14.7 of two phase using Morlet wavelet.

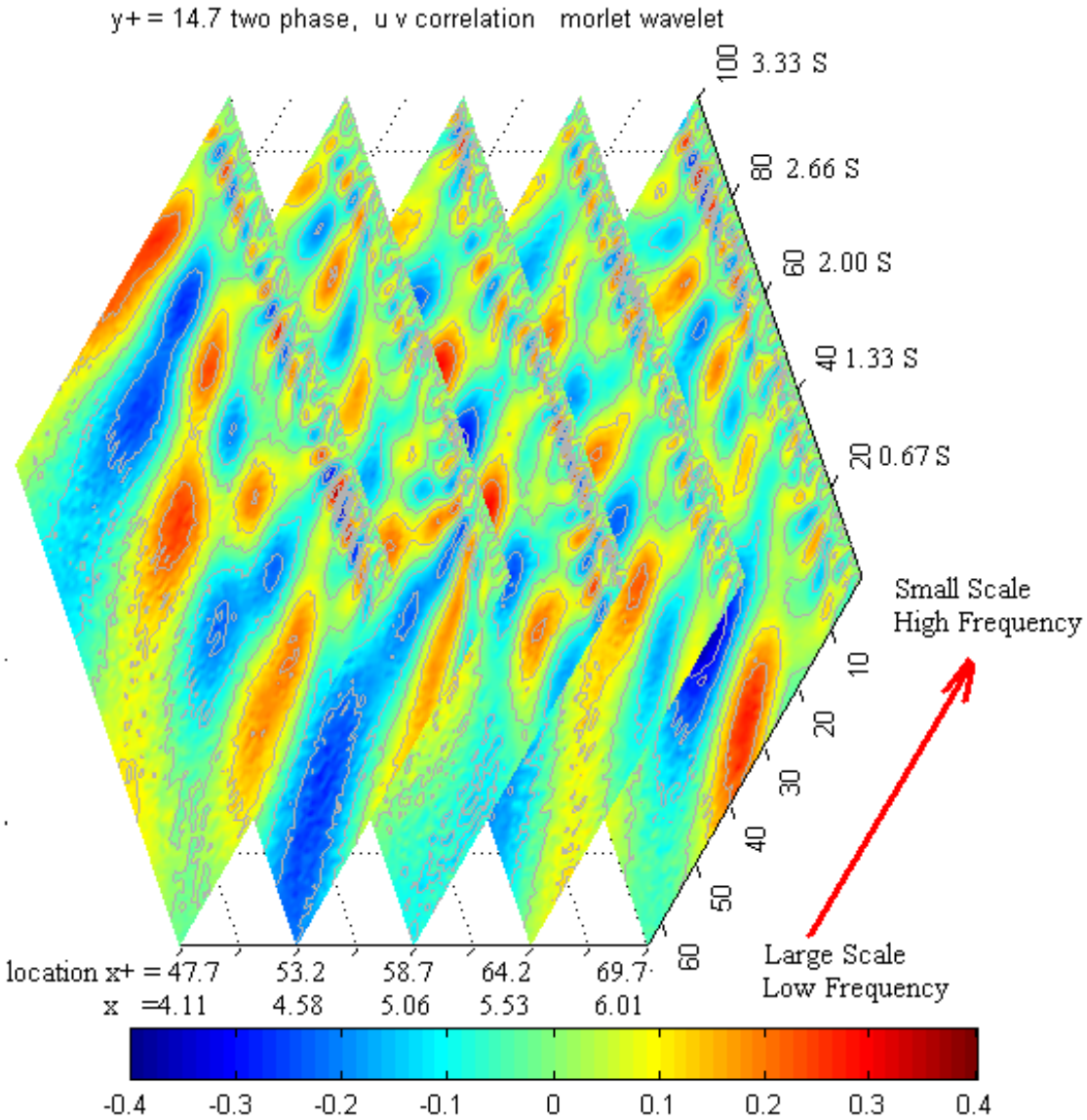

FIGURE 5.50 (b) Three-D plot of wavelet cross-correlation map for u v at y= 1.27mm, y+ =14.7 of two phase using Morlet wavelet.

Using the algorithm of wavelet auto-correlation map discussed in Chapter IV, the data from single phase flow and two phase flow are calculated. From figures 5.45 (a), 5.45 (b), 5.46 (a), 5.46 (b), 5.47 (a), 5.47 (b), 5.48 (a), 5.48 (b), 5.49 (a), 5.49 (b), 5.50 (a), 5.50 (b), the frequency shifting effect could be found. From single phase to two phase, the periodical coherent structures in the high frequency range disappeared or were damped and the periodical coherent structures in the low frequency range appeared or were strengthened.

In figure 5.45 (a), the wavelet auto-correlation map was plotted at five x+ locations. And in each x+ plane, the coherent structure magnitude was expressed by the color of the contour. The coherent structure magnitude was located in frequency-time plane. In figure 5.45 (b), the same 3-D plot was given. The difference between these two 3-D plots was obvious. The coherent structures at high frequency range were decreased in microbubbles injected conditions for the auto-correlation of streamwise fluctuating velocities. The coherent structures at low frequency range were increased in microbubbles injected conditions for the auto-correlation of streamwise fluctuating velocities. The coherent structures at high frequency range were decreased in microbubbles injected conditions for the auto-correlation of normal fluctuating velocities. From figures 5.48 (a), 5.48 (b), 5.49 (a), 5.49 (b), the difference between single phase and two phase was more clear.

As stated in Chapter IV, the Morlet wavelet has better resolution in high frequency. In figures 5.48 (a), 5.48 (b), it can be found that the coherent structures at low frequency range were increased in microbubbles injected conditions for the auto-correlation of

streamwise fluctuating velocities. The coherent structures at high frequency range were decreased in microbubbles injected conditions for the auto-correlation of streamwise fluctuating velocities. Furthermore, in figure 5.49, the coherent structures at both high frequency and low frequency range were decreased in microbubbles injected conditions for the auto-correlation of normal fluctuating velocities.

Using the algorithm of wavelet auto-correlation density spectra discussed in Chapter IV, the data from single phase flow and two phase flow are calculated. Figures 5.52, 5.53 give the (u u) and (v v) Wavelet auto-correlation density spectra using Morlet wavelet. It can be seen that at the low frequency, the density for (u u) was increased and the density for (v v) was decreased.

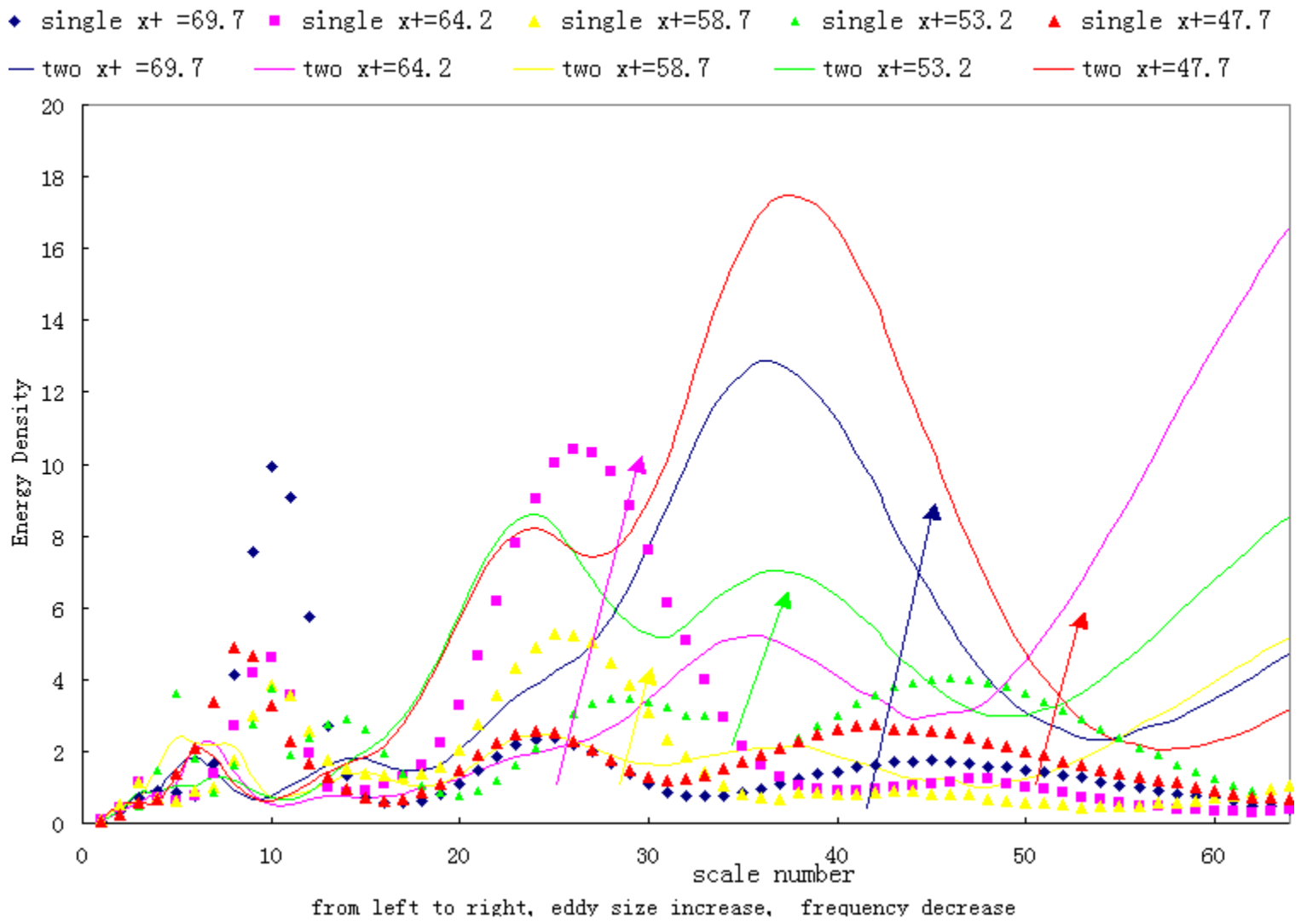

FIGURE 5.51 Wavelet auto-correlation density spectra of (u u) in transverse direction using Morlet wavelet.

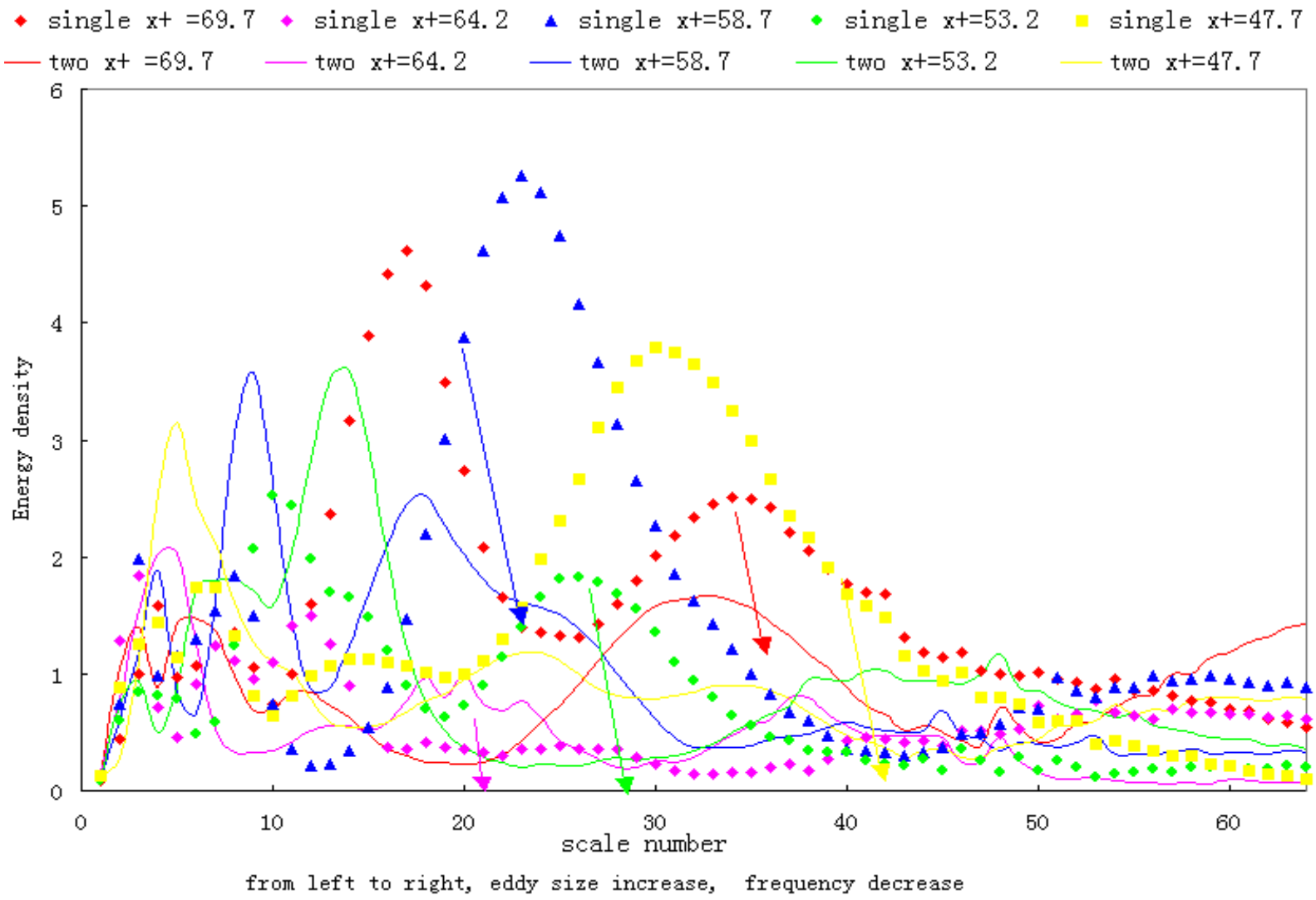

FIGURE 5.52 Wavelet auto-correlation density spectra of (v v) in transverse direction using Morlet wavelet.

5.5 Wavelet auto-correlation map at y+ =17.4

Figures 5.53 (a) give the auto-correlation for (u u) at x+ = 47.7, y+ = 17.4 for single phase flow and two phase flow. Figures 5.53 (b) give the corresponding wavelet auto-correlation map.

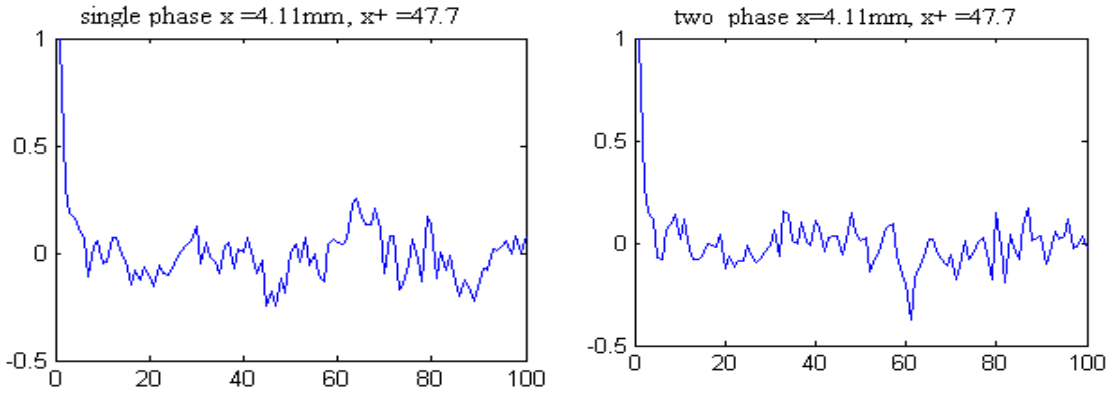

FIGURE 5.53 (a) Auto-correlation for (u u) at y= 1.50mm, y+ =17.4, x=4.11mm, x+ =47.7.

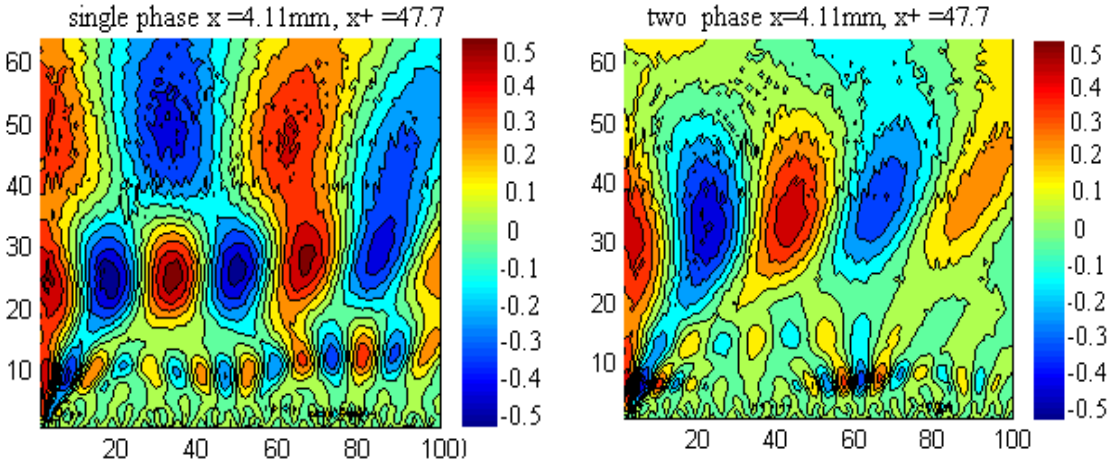

FIGURE 5.53 (b) Wavelet auto-correlation map for (u u) at y= 1.50mm, y+ =17.4, x=4.11mm, x+ =47.7.

Figures 5.54 (a) give the auto-correlation for (u u) at x+ = 53.2, y+ = 17.4 for single phase flow and two phase flow. Figures 5.54 (b) give the corresponding wavelet auto-correlation map.

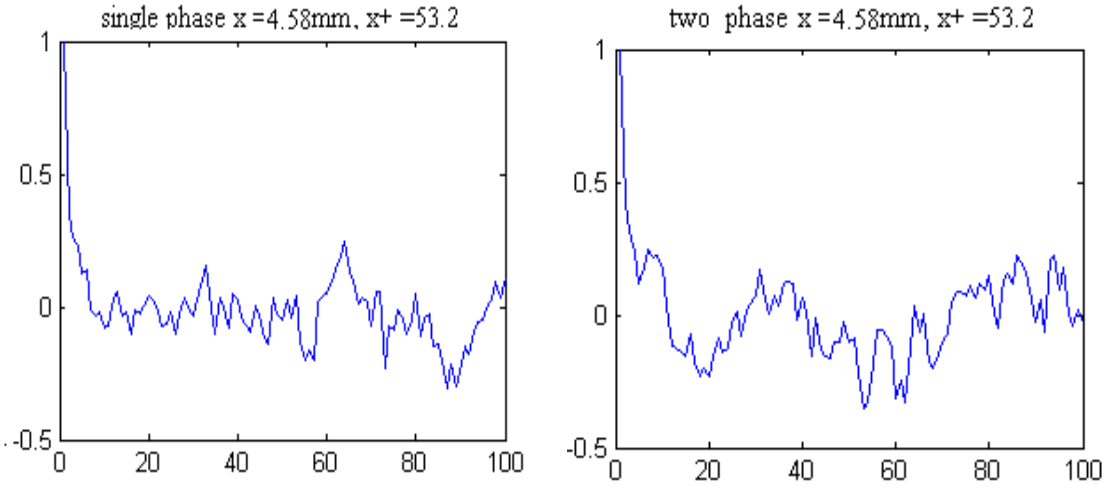

FIGURE 5.54 (a) Auto-correlation for (u u) at y= 1.50mm, y+ =17.4, x=4.58mm, x+ =53.2.

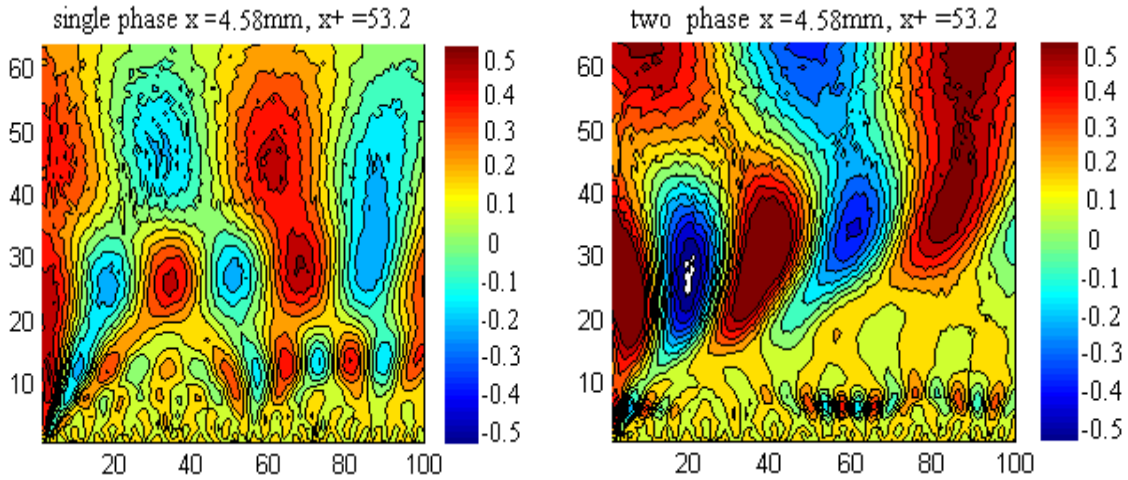

FIGURE 5.54 (b) Wavelet auto-correlation map for (u u) at y= 1.50mm, y+ =17.4, x=4.58mm, x+ =53.2.

Figures 5.55 (a) give the auto-correlation for (u u) at x+ = 58.7, y+ = 17.4 for single phase flow and two phase flow. Figures 5.55 (b) give the corresponding wavelet auto-correlation map.

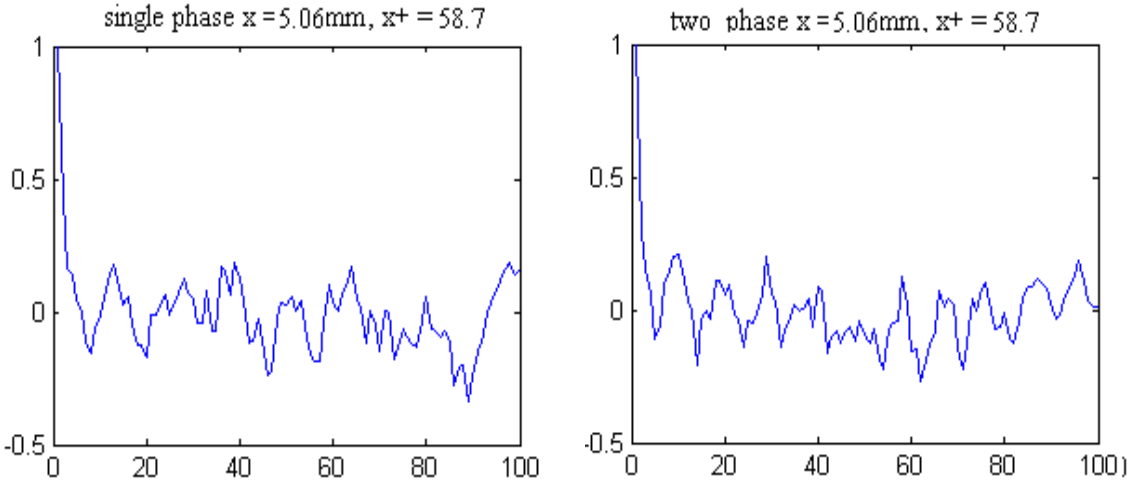

FIGURE 5.55 (a) Auto-correlation for (u u) at y= 1.50mm, y+ =17.4, x=5.06mm, x+ =58.7.

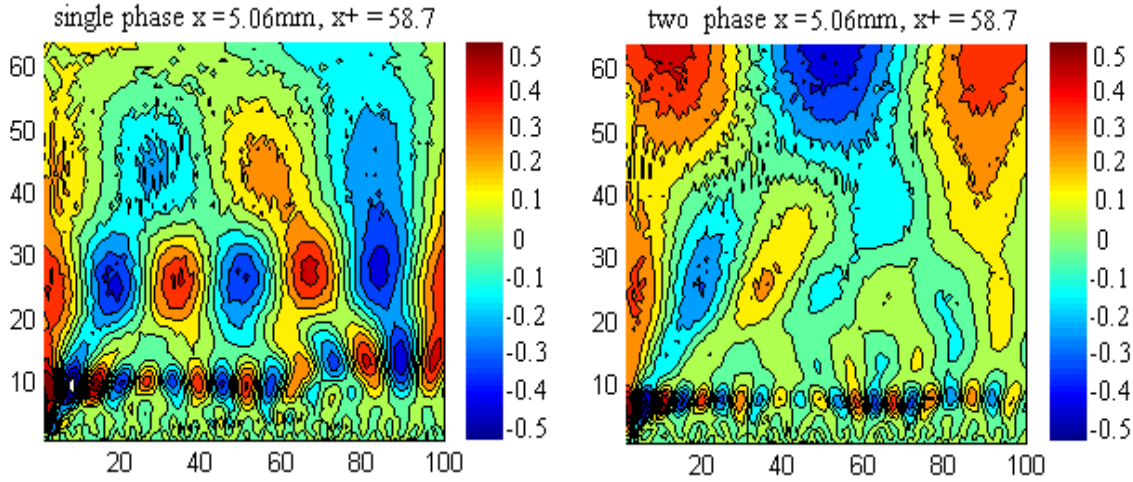

FIGURE 5.55 (b) Wavelet auto-correlation map for (u u) at y= 1.50mm, y+ =17.4, x=5.06mm, x+ =58.7.

Figures 5.56 (a) give the auto-correlation for (u u) at x+ = 64.2, y+ = 17.4 for single phase flow and two phase flow. Figures 5.56 (b) give the corresponding wavelet auto-correlation map.

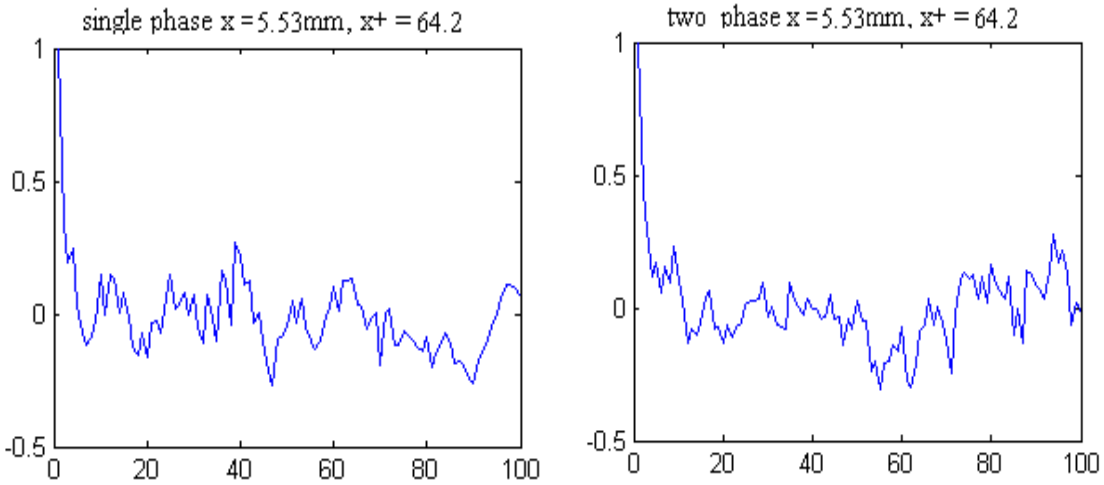

FIGURE 5.56 (a) Auto-correlation for (u u) at y= 1.50mm, y+ =17.4, x=5.53mm, x+ =64.2.

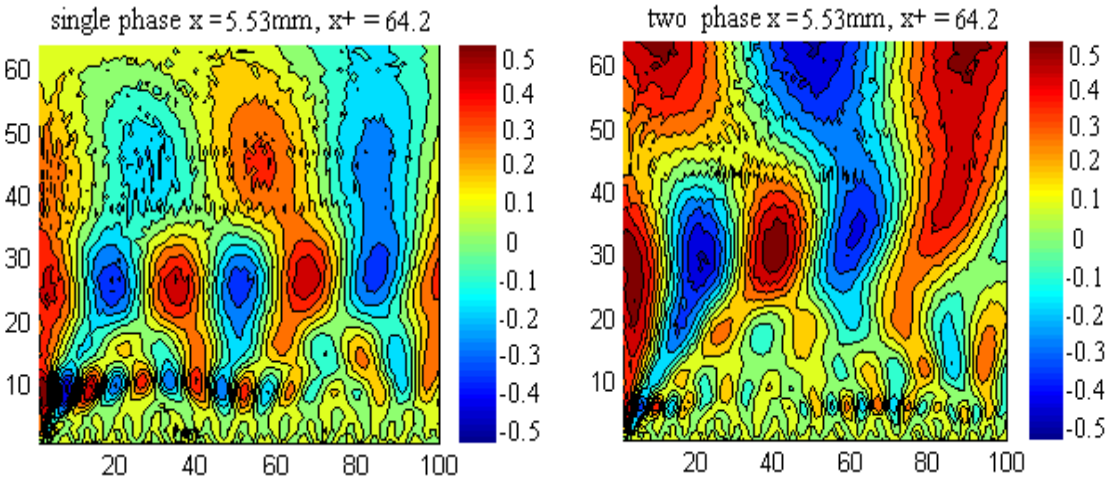

FIGURE 5.56 (b) Wavelet auto-correlation map for (u u) at y= 1.50mm, y+ =17.4, x=5.53mm, x+ =64.2.

Figures 5.57 (a) give the auto-correlation for (u u) at x+ = 69.7, y+ = 17.4 for single phase flow and two phase flow. Figures 5.57 (b) give the corresponding wavelet auto-correlation map.

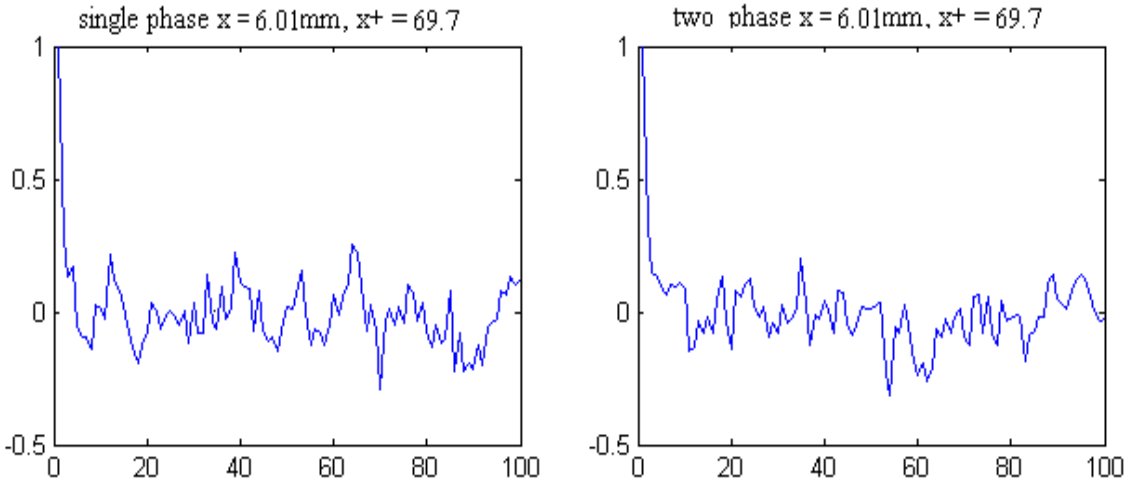

FIGURE 5.57 (a) Auto-correlation for (u u) at y= 1.50mm, y+ =17.4, x=6.01mm, x+ =69.7.

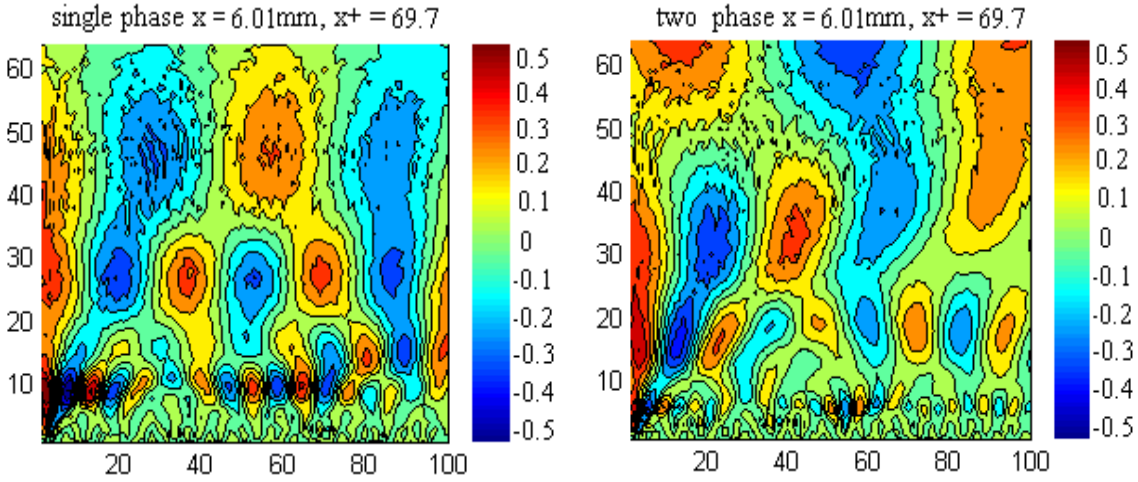

FIGURE 5.57 (b) Wavelet auto-correlation map for (u u) at y= 1.50mm, y+ =17.4, x=6.01mm, x+ =69.7.

Figures 5.58 (a) give the three-D plot of wavelet auto-correlation map for (u u) at y= 1.27mm, y+ =17.4 of single phase using Mexican hat wavelet.

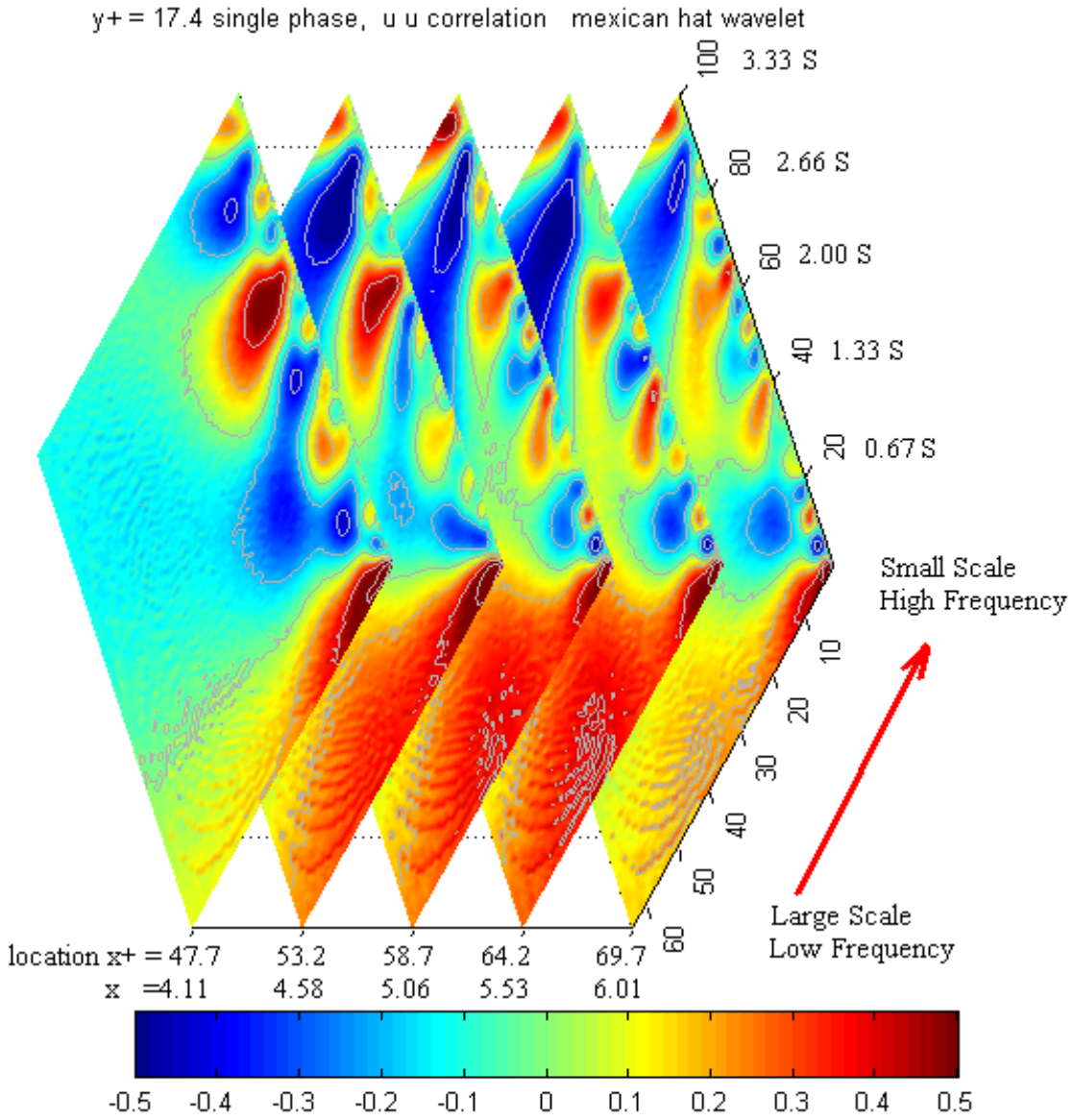

FIGURE 5.58 (a) Three-D plot of wavelet auto-correlation map for (u u) at y= 1.50mm, y+ =17.4 of single phase using Mexican hat wavelet.

Figures 5.58 (b) give the three-D plot of wavelet auto-correlation map for (u u) at y= 1.27mm, y+ =14.7 of two phase using Mexican hat wavelet.

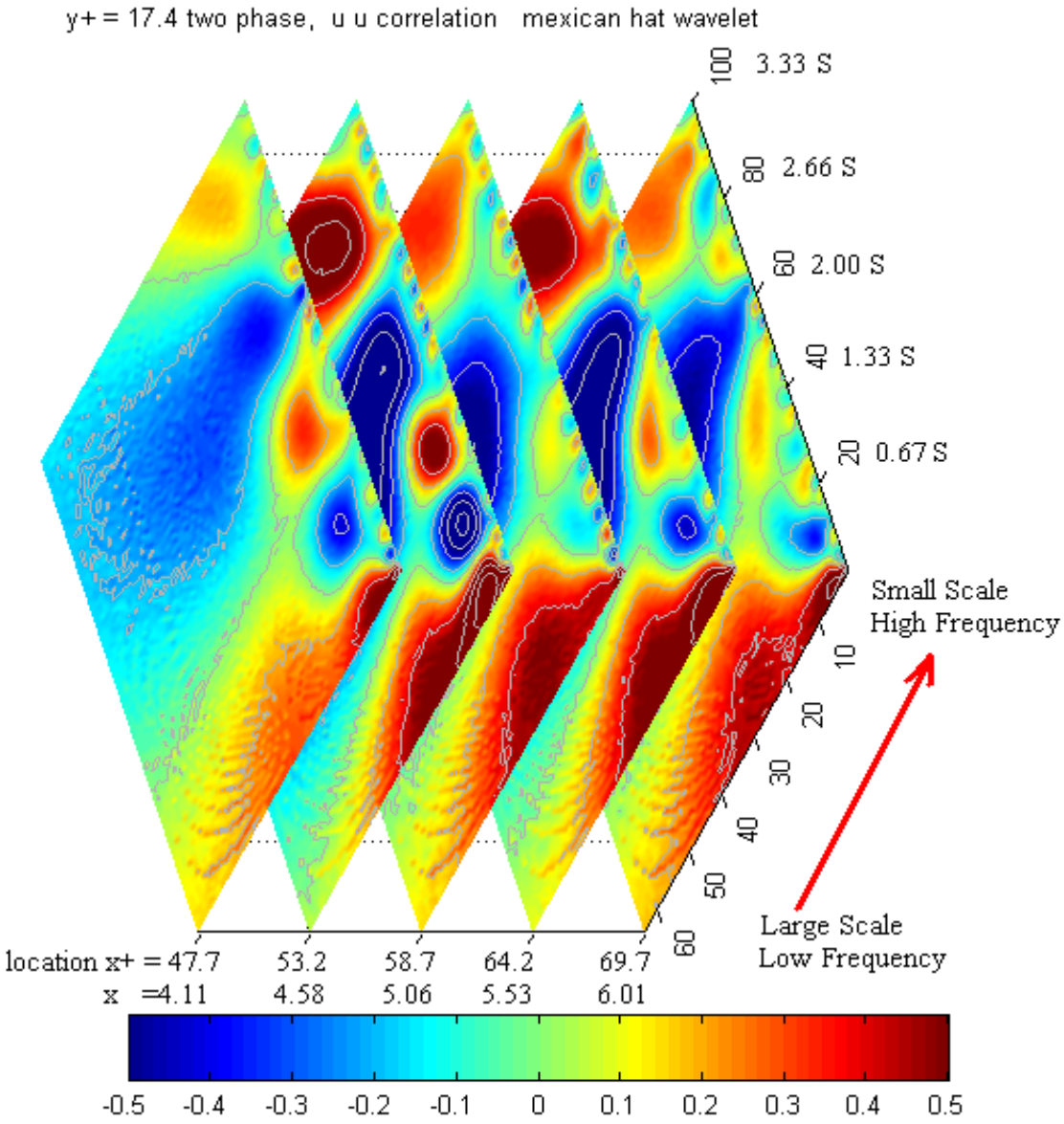

FIGURE 5.58 (b) Three-D plot of wavelet auto-correlation map for (u u) at y= 1.50mm, y+ =17.4 of two phase using Mexican hat wavelet.

Figures 5.59 (a) give the three-D plot of wavelet auto-correlation map for (v v) at y= 1.27mm, y+ =14.7 of single phase using Mexican hat wavelet.

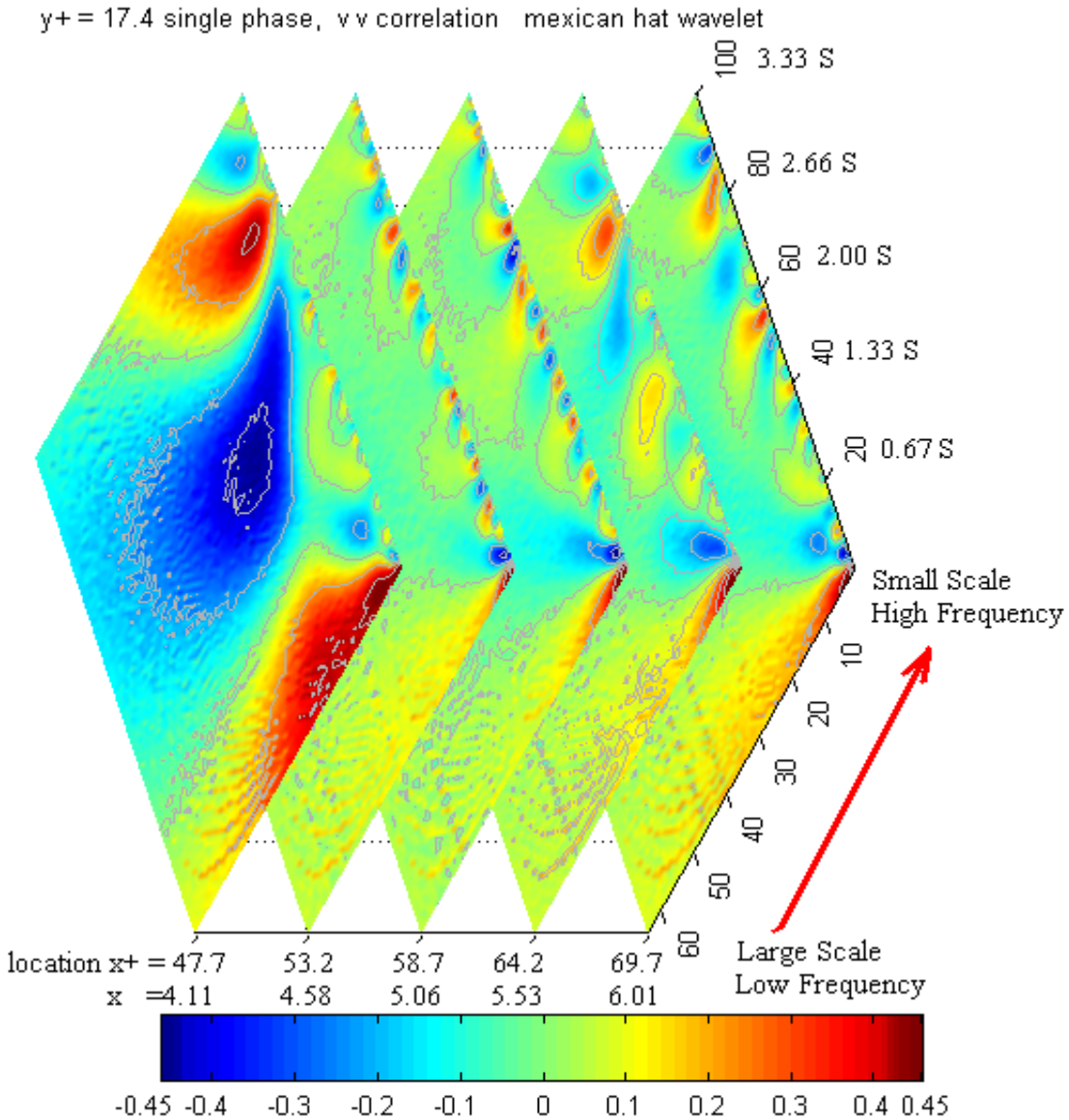

FIGURE 5.59 (a) Three-D plot of wavelet auto-correlation map for (v v) at y= 1.50mm, y+ =17.4 of single phase using Mexican hat wavelet.

Figures 5.59 (b) give the three-D plot of wavelet auto-correlation map for (v v) at y= 1.27mm, y+ =14.7 of two phase using Mexican hat wavelet.

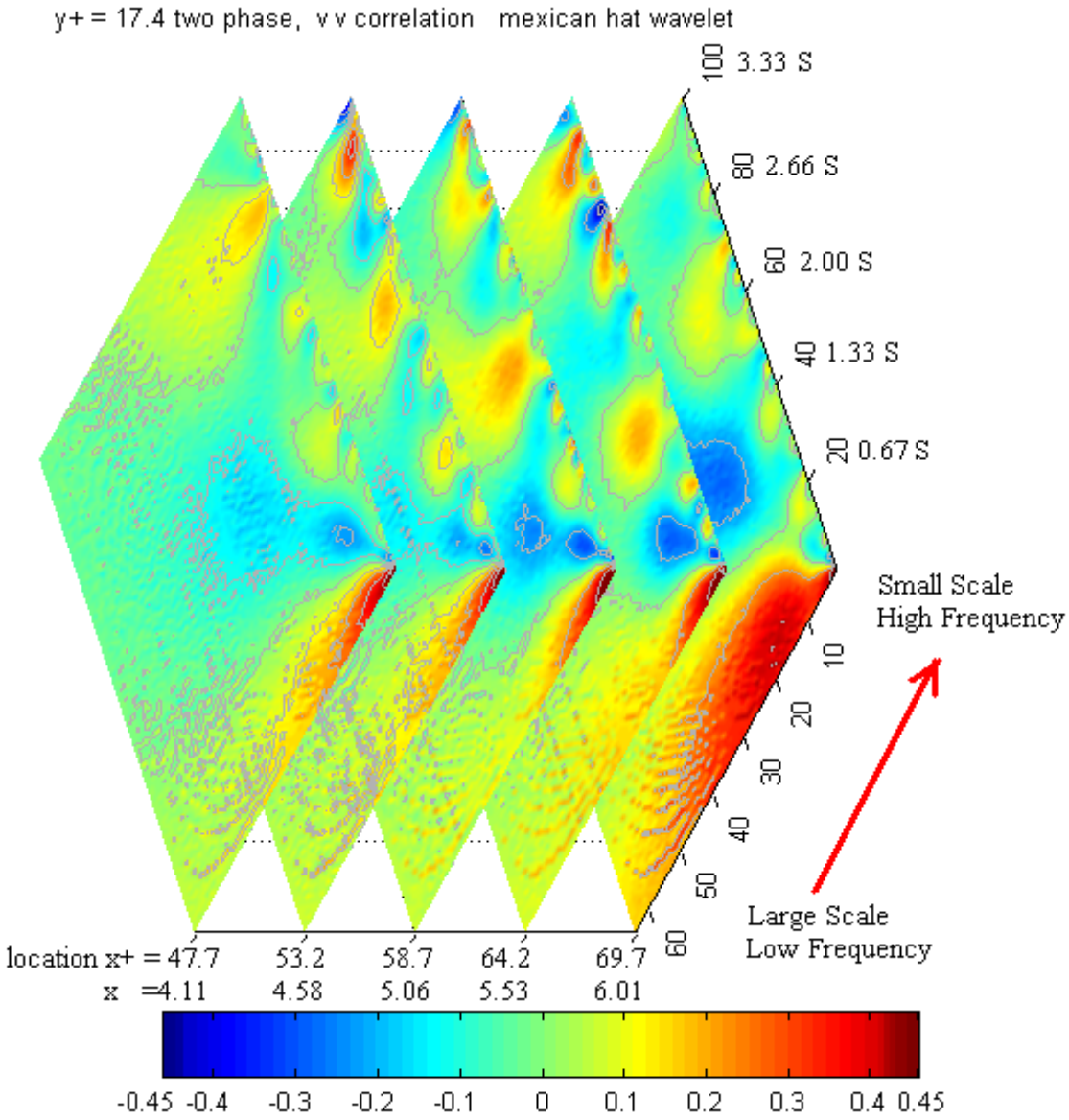

FIGURE 5.59 (b) Three-D plot of wavelet auto-correlation map for (v v) at y= 1.50mm, y+ =17.4 of two phase using Mexican hat wavelet.

Figures 5.60 (a) give the three-D plot of wavelet cross-correlation map for u v at y= 1.27mm, y+ =14.7 of single phase using Mexican hat wavelet.

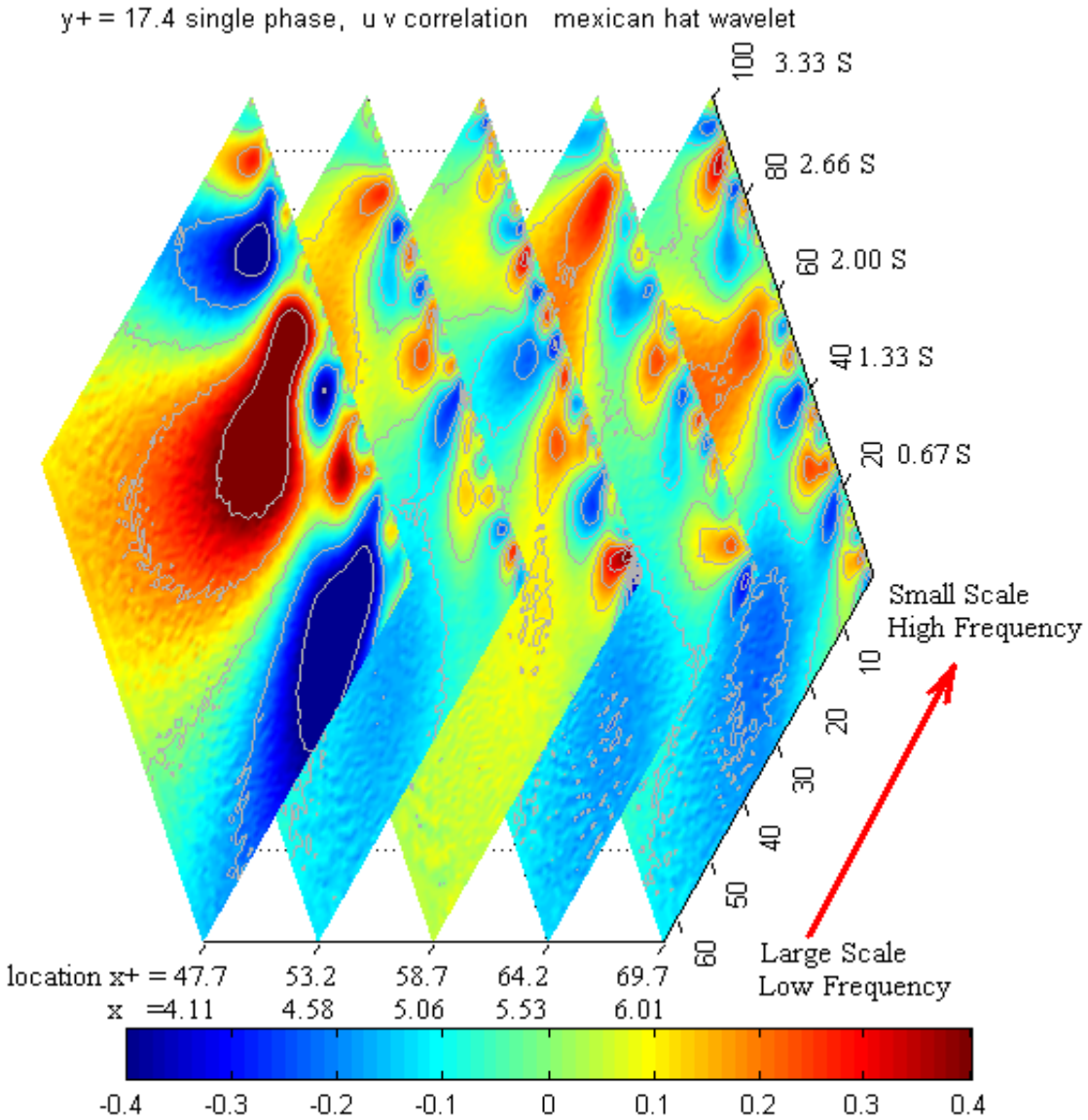

FIGURE 5.60 (a) Three-D plot of wavelet cross-correlation map for u v at y= 1.50mm, y+ =17.4 of single phase using Mexican hat.

Figures 5.60 (b) give the three-D plot of wavelet cross-correlation map for u v at y= 1.27mm, y+ =14.7 of single phase using Mexican hat wavelet.

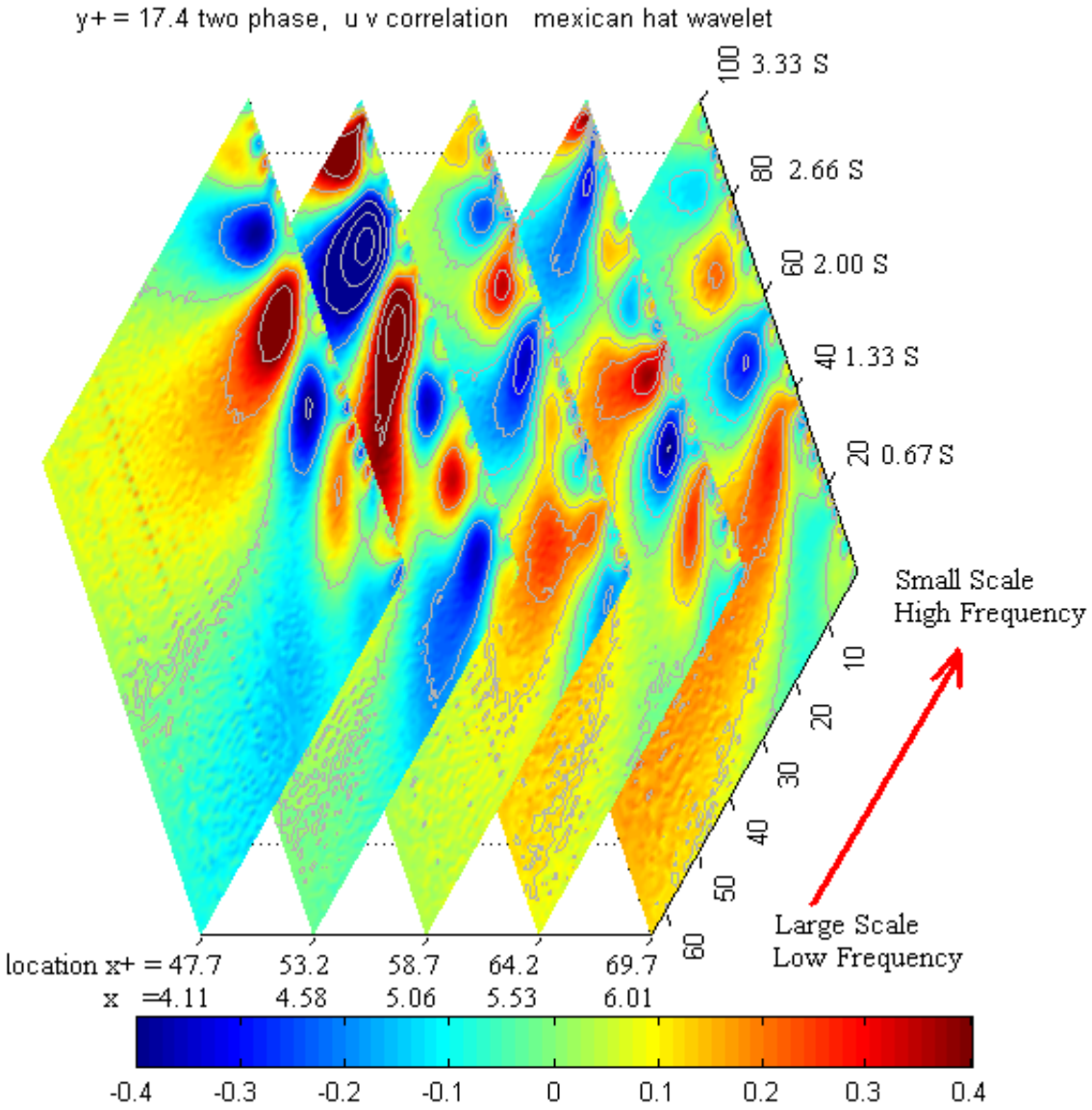

FIGURE 5.60 (b) Three-D plot of wavelet cross-correlation map for u v at y= 1.50mm, y+ =17.4 of two phase using Mexican hat wavelet.

Figures 5.61 (a) give the three-D plot of wavelet auto-correlation map for (u u) at y= 1.27mm, y+ =14.7 of single phase using Morlet wavelet.

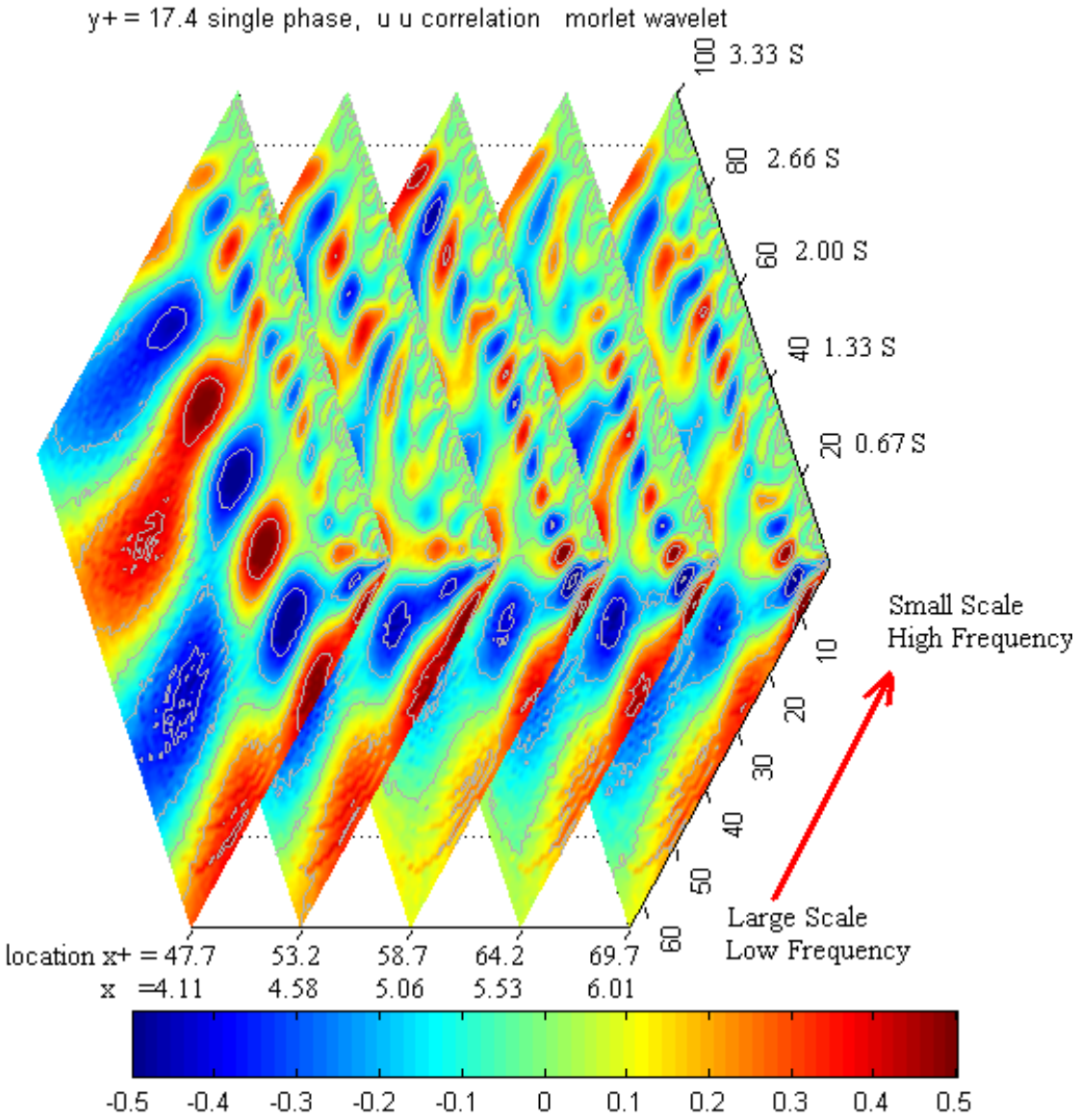

FIGURE 5.61 (a) Three-D plot of wavelet auto-correlation map for (u u) at y= 1.50mm, y+ =17.4 of single phase using Morlet wavelet.

Figures 5.61 (b) give the three-D plot of wavelet auto-correlation map for (u u) at y= 1.27mm, y+ =14.7 of two phase using Morlet wavelet.

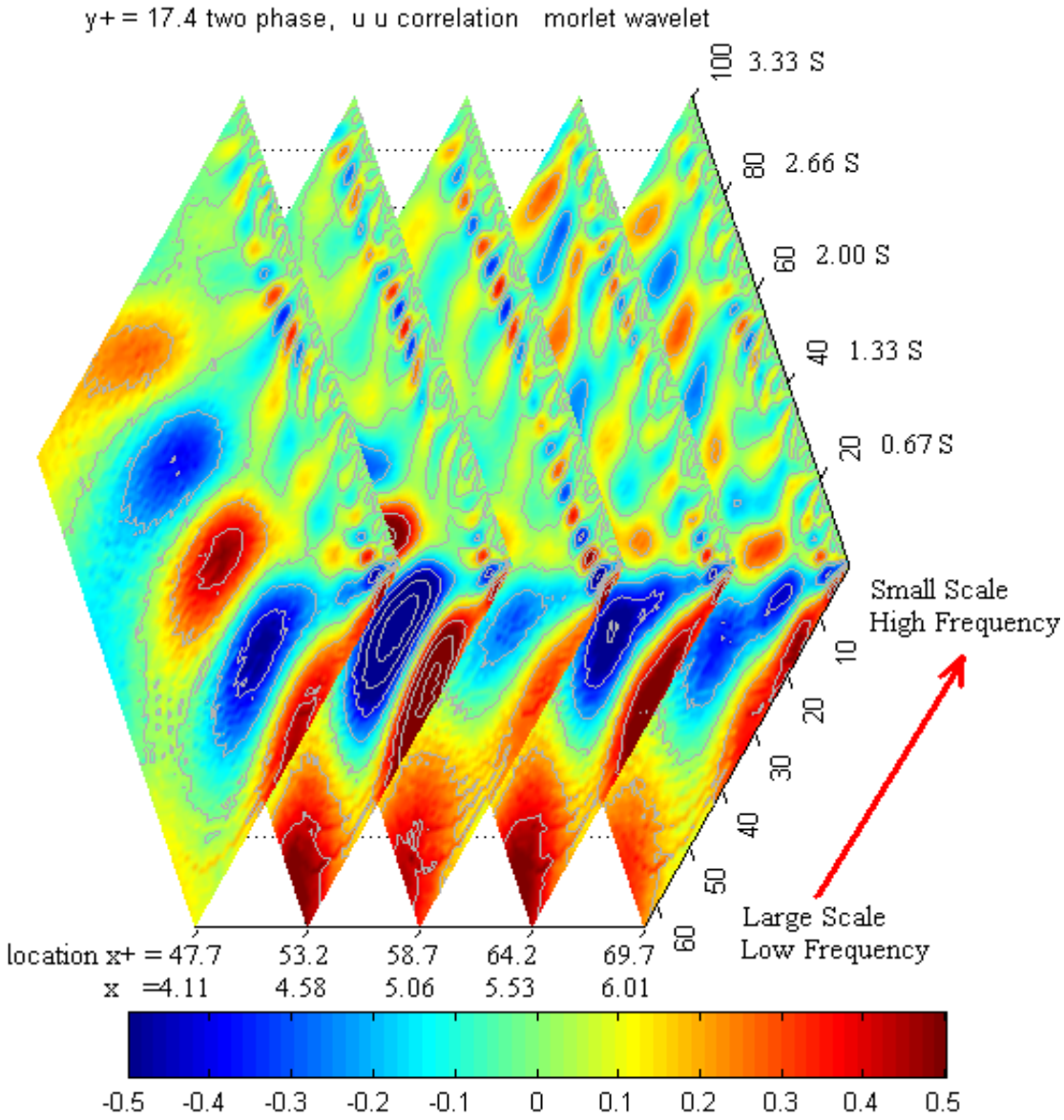

FIGURE 5.61 (b) Three-D plot of wavelet auto-correlation map for (u u) at y= 1.50mm, y+ =17.4 of two phase using Morlet wavelet.

Figures 5.62 (a) give the three-D plot of wavelet auto-correlation map for (v v) at y= 1.27mm, y+ =14.7 of single phase using Morlet wavelet.

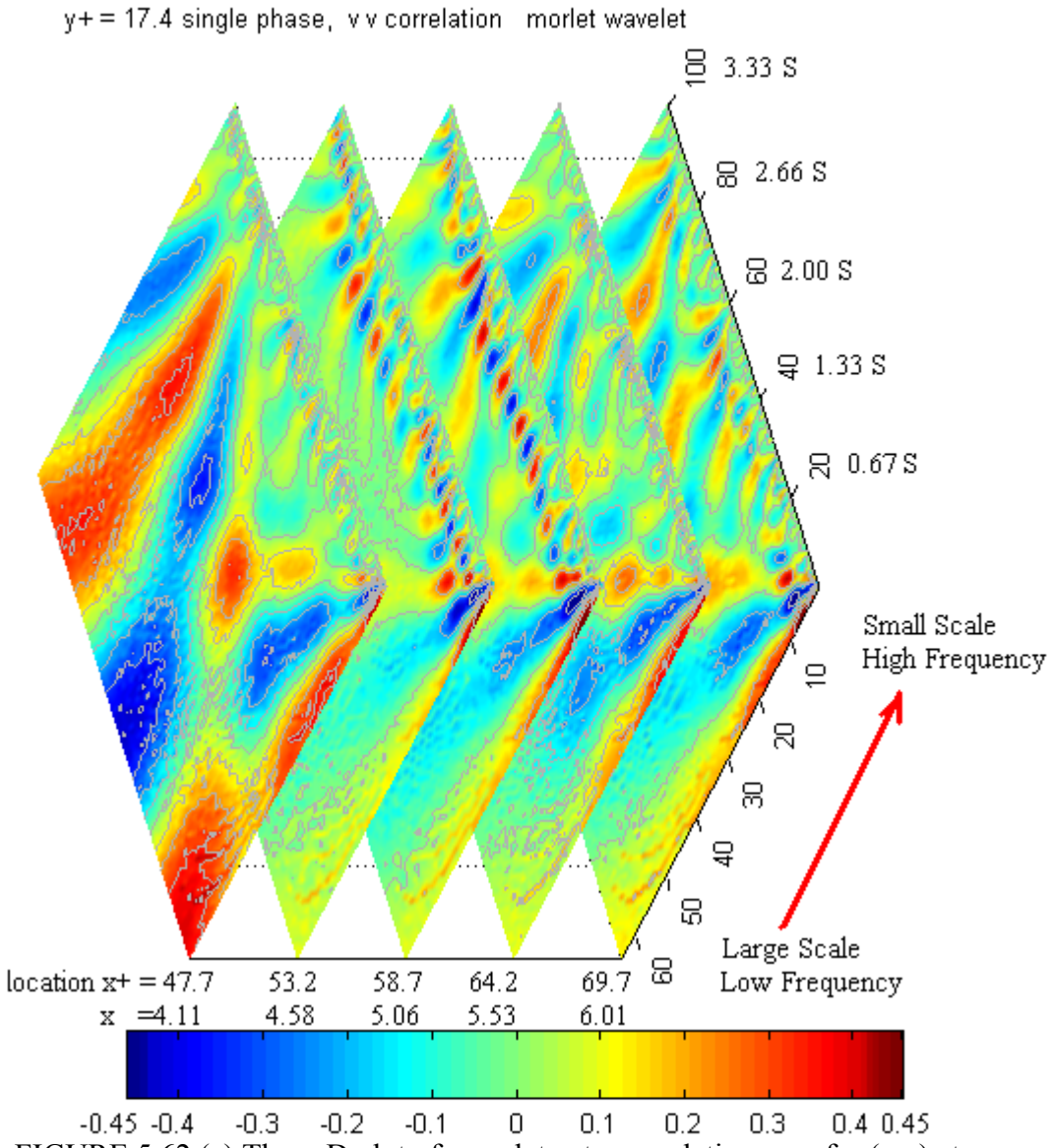

FIGURE 5.62 (a) Three-D plot of wavelet auto-correlation map for (v v) at y= 1.50mm, y+ =17.4 of single phase using Morlet wavelet.

Figures 5.62 (b) give the three-D plot of wavelet auto-correlation map for (v v) at y= 1.27mm, y+ =14.7 of two phase using Morlet wavelet.

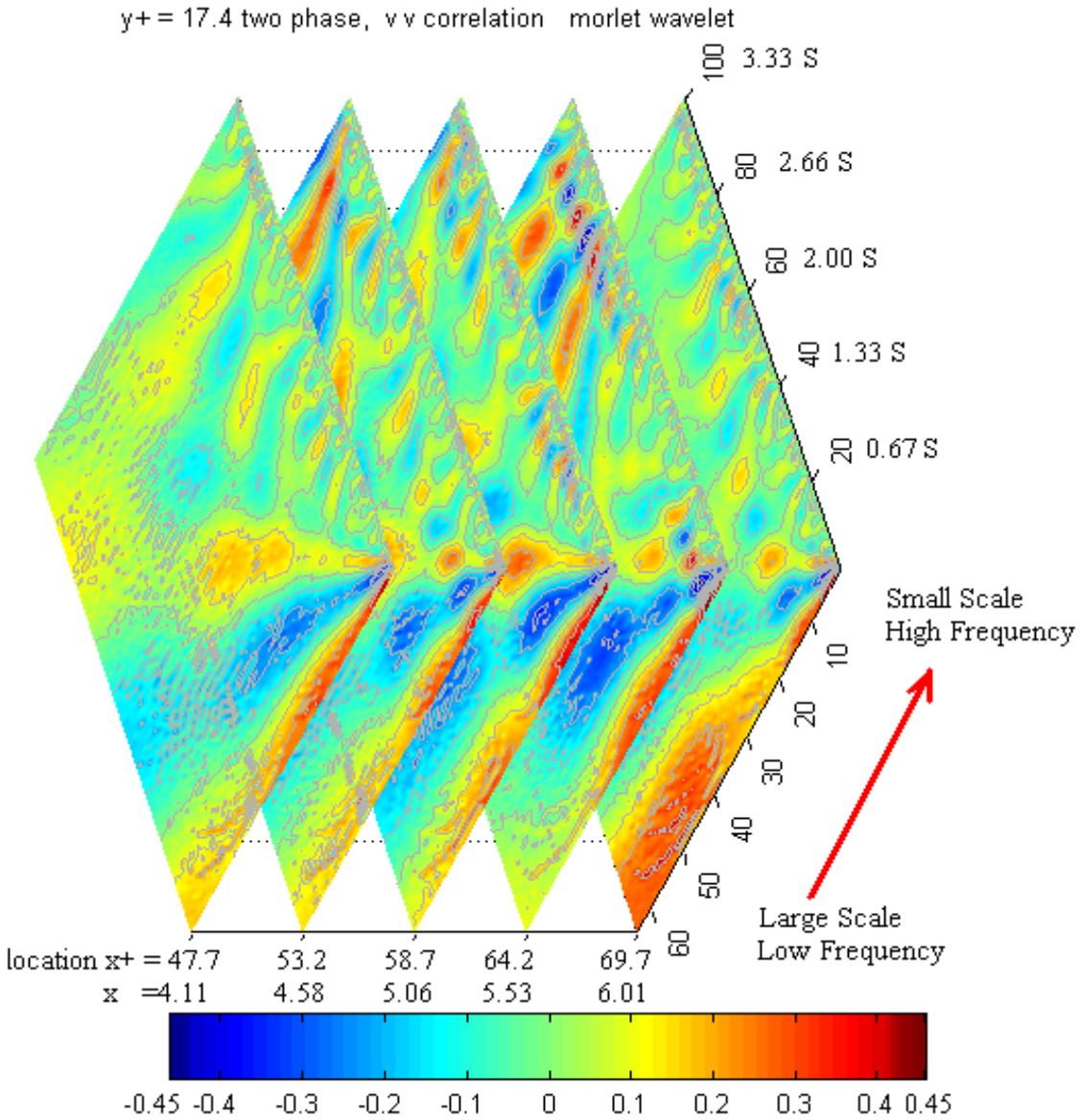

FIGURE 5.62 (b) Three-D plot of Wavelet auto-correlation map for (v v) at y= 1.50mm, y+ =17.4 of two phase using Morlet wavelet.

Figures 5.63 (a) give the three-D plot of wavelet cross-correlation map for u v at y= 1.27mm, y+ =14.7 of two phase using Morlet wavelet.

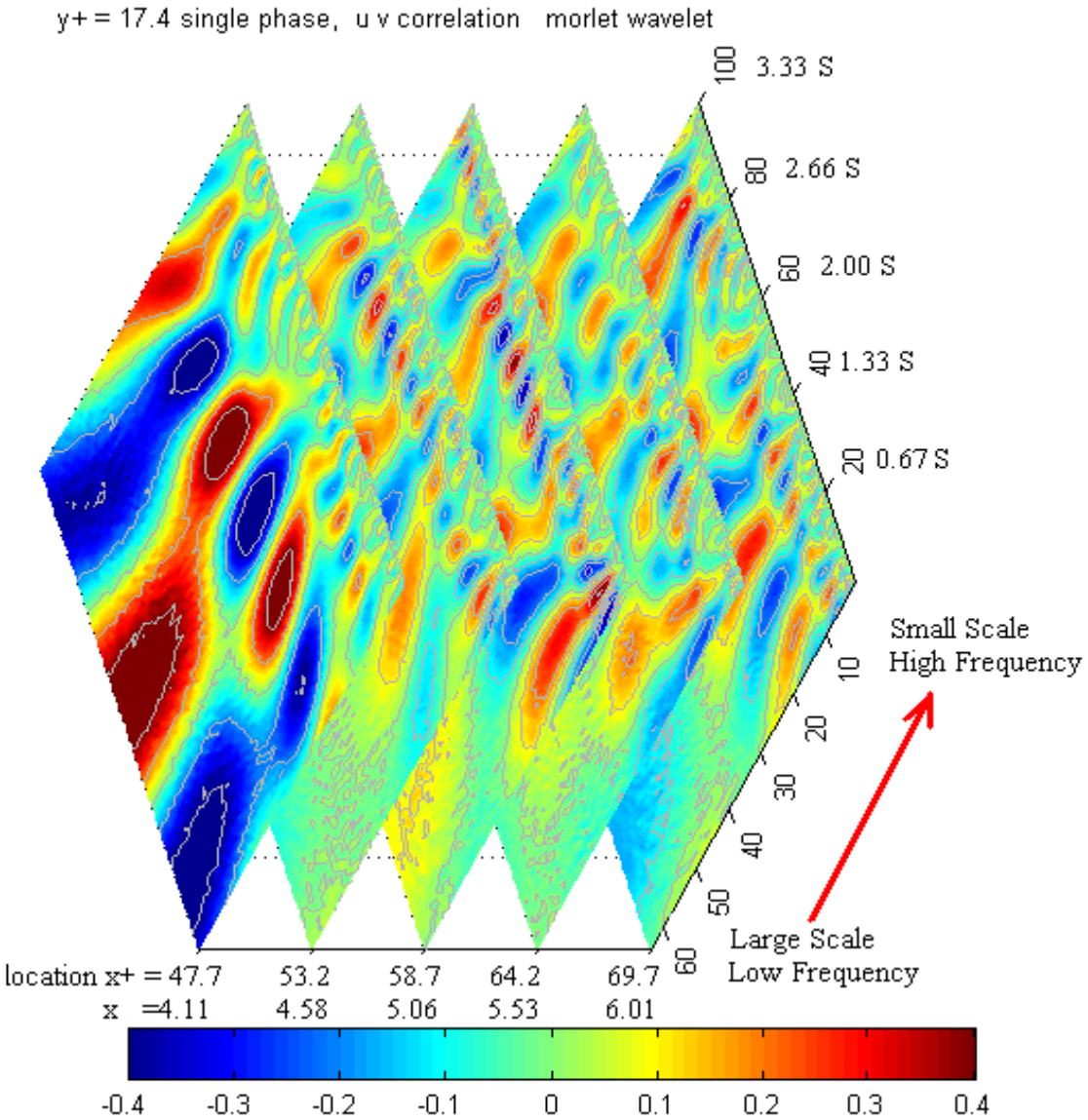

FIGURE 5.63 (a) Three-D plot of Wavelet auto-correlation map for u v at y= 1.50mm, y+ =17.4 of single phase using Morlet wavelet.

Figures 5.63 (b) give the three-D plot of wavelet cross-correlation map for u v at y= 1.27mm, y+ =14.7 of two phase using Morlet wavelet.

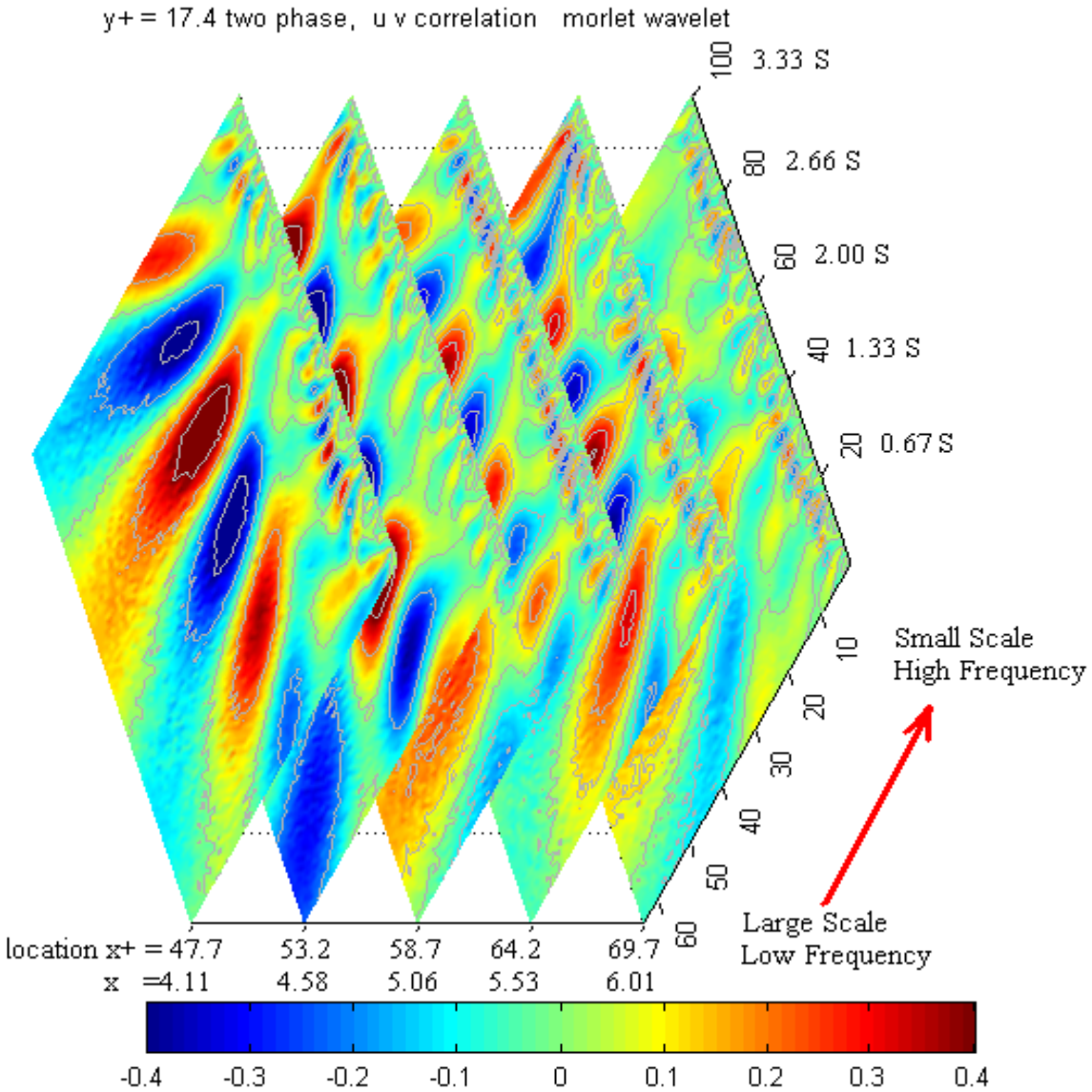

FIGURE 5.63 (b) Three-D plot of Wavelet auto-correlation map for u v at y= 1.50mm, y+ =17.4 of two phase using Morlet wavelet.

Using the algorithm of wavelet auto-correlation map discussed in Chapter IV, the data from single phase flow and two phase flow are calculated. From figures 5.58 (a), 5.58 (b), 5.59 (a), 5.59 (b), 5.60 (a), 5.60 (b), 5.61 (a), 5.61 (b), 5.62 (a), 5.62 (b), 5.63 (a), 5.63 (b), the frequency shifting effect could be found. From single phase to two phase, the periodical coherent structures in the high frequency range disappeared or were damped and the periodical coherent structures in the low frequency range appeared or were strengthened.

In figure 5.58 (a), the wavelet auto-correlation map was plotted at five x+ locations. And in each x+ plane, the coherent structure magnitude was expressed by the color of the contour. The coherent structure magnitude was located in frequency-time plane. In figure 5.58 (b), the same 3-D plot was given. The difference between these two 3-D plots was obvious. The coherent structures at high frequency range were decreased in microbubbles injected conditions for the auto-correlation of streamwise fluctuating velocities. The coherent structures at low frequency range were increased in microbubbles injected conditions for the auto-correlation of streamwise fluctuating velocities. The coherent structures at high frequency range were decreased in microbubbles injected conditions for the auto-correlation of normal fluctuating velocities. From figures 5.61 (a), 5.61 (b), 5.62 (a), 5.62 (b), the difference between single phase and two phase was more clear.

As stated in Chapter IV, the Morlet wavelet has better resolution in high frequency. In figures 5.61 (a), 5.61 (b), it can be found that the coherent structures at low frequency range were increased in microbubbles injected conditions for the auto-correlation of

streamwise fluctuating velocities. The coherent structures at high frequency range were decreased in microbubbles injected conditions for the auto-correlation of streamwise fluctuating velocities. Furthermore, in figures 5.62 (a), 5.62 (b), the coherent structures at both high frequency and low frequency range were decreased in microbubbles injected conditions for the auto-correlation of normal fluctuating velocities.

Using the algorithm of wavelet auto-correlation density spectra discussed in Chapter IV, the data from single phase flow and two phase flow are calculated. Figures 5.64, 5.65 give the (u u) and vv Wavelet auto-correlation density spectra using Morlet wavelet. It can be seen that at the low frequency, the density for (u u) was increased and the density for (v v) was decreased.

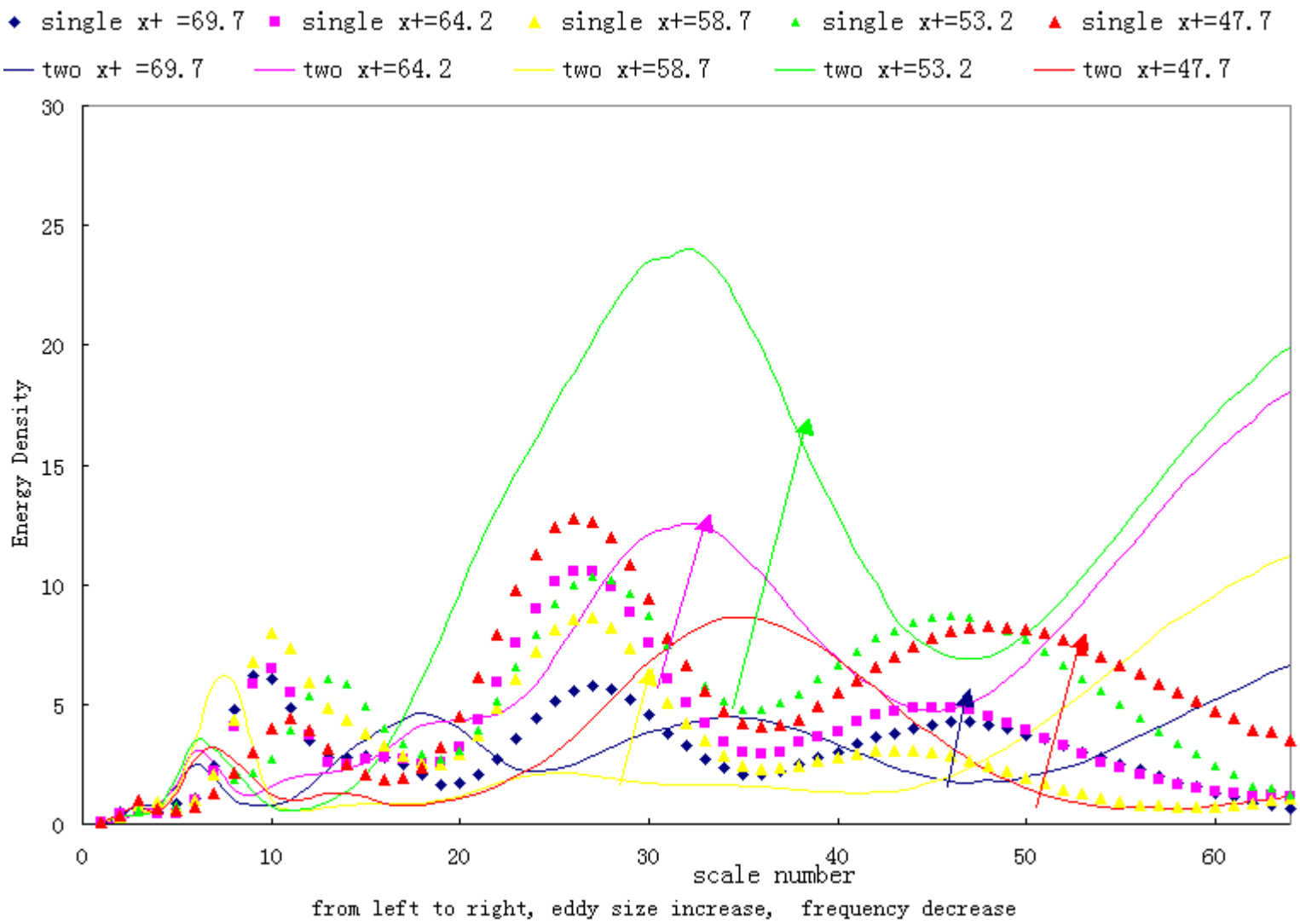

FIGURE 5.64 Wavelet auto-correlation density spectra of (u u) in transverse direction using Morlet wavelet.

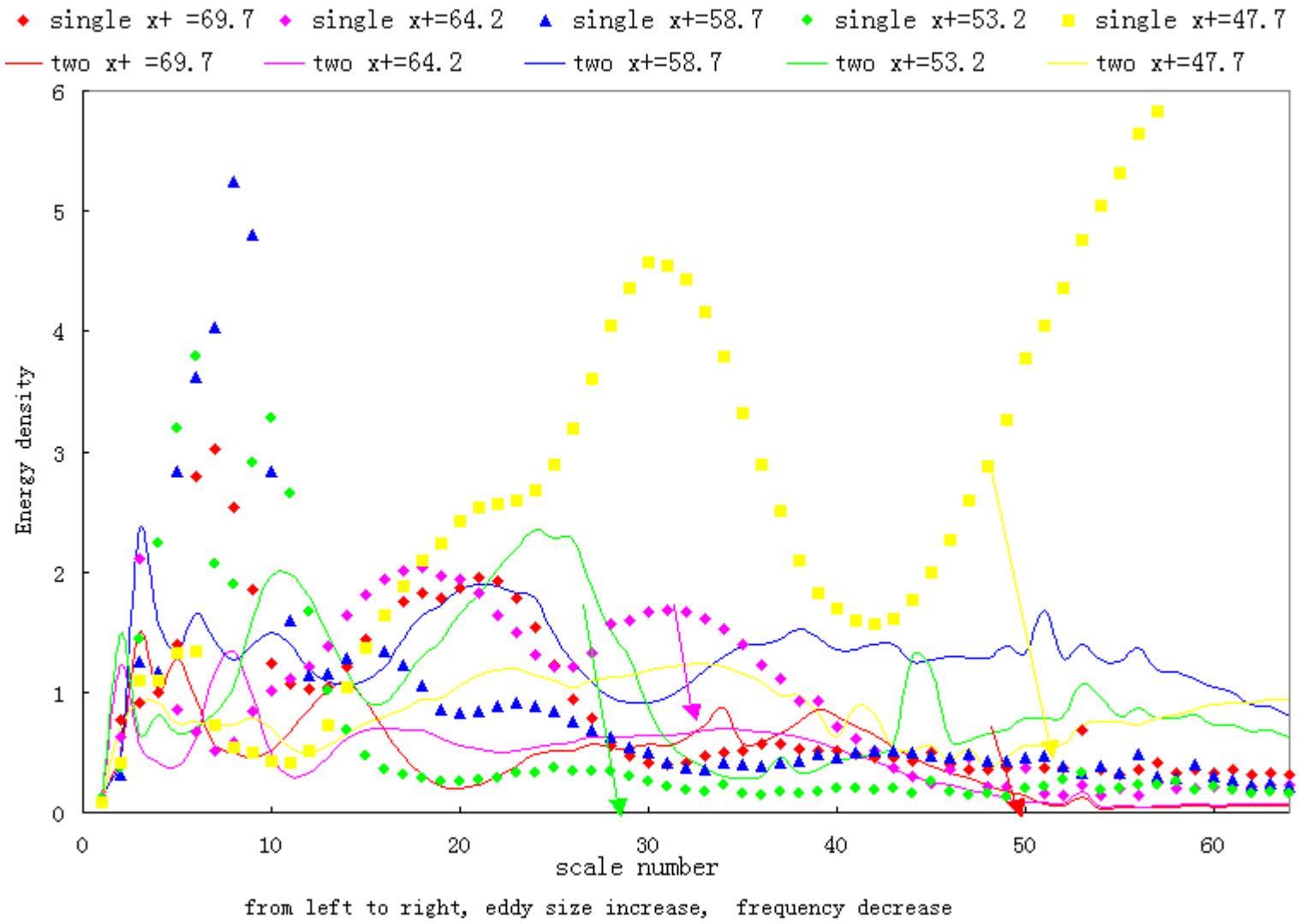

FIGURE 5.65 Wavelet auto-correlation density spectra of (v v) in transverse direction using Morlet wavelet.

CHAPTER VI

CONCLUSIONS

In this study, the experimental analysis in the near upper wall of a rectangular channel was carried out. Microbubbles with an average diameter of 30 μm, were produced by electrolysis and injected in the near wall region. Particle Image Velocimetry (PIV) measurement technique was used to measure instantaneous two dimensional x-y velocity fields. New time-frequency analysis technique was used.

The drag reduction due to microbubble injection in the boundary layer of a fully developed turbulent channel flow was investigated. Particle Image Velocimetry (PIV) and pressure measurement techniques were taken. Two-dimensional velocity components in an x-y plane at Reynolds number of 5128 based on the half height of the channel were measured. The effects of the presence of microbubbles in the boundary layer were assessed. A drag reduction of 38.4% was obtained with void fraction of 4.9%.

The turbulence quantities such as the streamwise and normal turbulent intensities, the Reynolds shear stresses, correlation and spectra were calculated to assess the difference between single phase flow and microbubble injected two phase flow. Relatively consistent conclusions were achieved. However, one shortcoming of these techniques is the lack of coherent structures detection. With correlation or spectra techniques, the processing for data would be presented only in time or in frequency domain respectively.

The algorithms of wavelet cross-correlation and wavelet auto-correlation maps were applied to the PIV velocity field measurement. Modifications in the wavelet cross-correlation and wavelet auto-correlation maps due to the presence of microbubbles were studied and compared in two- and three-dimensions. Wavelet cross- and auto-correlation maps provide an easy coherent structure detection method. Using 3-D plotting routines, the wavelet cross-correlation maps in different locations were presented to aid in evaluation of the turbulent coherent structures at various locations. Furthermore, Wavelet auto-correlation map would provide the coherent structures detection at different transient time. The following observations were deduced from this study:

1. The microbubble injection within the boundary layer increases the turbulent energy of the streamwise velocity components of the large scale (large eddy size, low frequency) range and decreases the energy of the small scale (small eddy size, high frequency) range.
2. The wavelet cross-correlation maps of the normal velocities indicate that the microbubble presence decrease the turbulent energy of normal velocity components for both the large scale (large eddy size, low frequency) and the small scale (small eddy size, high frequency) ranges.
3. The wavelet auto-correlation maps of streamwise velocity shows that the intensities at low frequency range were increased with microbubble presence and the intensities at high frequency range were decreased.

4. The turbulent intensities for the normal fluctuating velocities at both low frequency and high frequency range were decreased with microbubble injection.

All the above analysis can give visualized explanation to the drag reduction phenomena. Further studies by using wavelet technique can definitely help to answer some long-standing questions about the nature of the drag reduction.

.

REFERENCES

ADRIAN, R. J. 1991 Particle-imaging techniques for experimental fluid mechanics. *Annu. Rev.Fluid Mech*. **23**, 261-304.

ARGOUL, F., ARNÉODO, A., GRASSEAU, G., GAGNE, Y., HOPFINGER, E. J. & FRISCH, U. 1989 Wavelet analysis of turbulence reveals the multifractal nature of the Richardson cascade. *Nature* **338**, 51-53.

BANNASCH, R. 1998 Hydrodynamics of wave-like curvature on bodies of swimming animals. *Proc. of the International Symposium on Seawater Drag Reduction*, Newport, RI, 435-442.

BARON, A. & QUADRIO, M. 1993 Some preliminary results on the influence of riblets on the structure of a turbulent boundary layer. *Int. J. Heat and Fluid Flow* **14**, 223-230.

BEATY, W. R., JOHNSTON, R. L., KRAMER, R. L., WARNOCK, L. G. & WHEELER, G. R. 1984 Drag reducers increase flow in offshore pipelines without additional expansion. *Oil & Gas Journal*, **82** 71-74.

BECHERT, D. W., BRUSE, M. & HAGE, W. 2000 Experiments with three-dimensional riblets as an idealized model of shark skin. *Experiments in Fluids* **28**, 403-412.

BECHERT, D. W., BRUSE, M., HAGE, W., VAN DER HOEVEN, J. G. T. & HOPPE, G. 1997 Experiments on drag-reducing surfaces and their optimization with an adjustable geometry. *J. Fluid Mech.* **338**, 59-87.

BIJAOUI, A. E., SLEZAK, F. RUE & LEGA, E. 1996 Wavelets and the study of the distant universe, *Proc. of the IEEE*, **84**, No. 4, 670-679.

BUSHNELL, D. M. & MOORE, K. J. 1991 Drag reduction in nature, *Ann. Rev. Fluid Mech.* **23**, 65-79.

CAMUSSI, R. 2002 Coherent structure identification from wavelet analysis of particle image velocimetry data. *Experiments in Fluid.* **32**, 76-86.

CARPENTER, P. W. 1990 Status of transition delay using compliant walls, In *Viscous Drag Reduction in Boundary Layers* (ed. Bushnell, D.M. & Hefner, J.N.), AIAA 79-113.

CHOI, K. S. & ORCHARD, D. M. 1997 Turbulence management using riblets for heat and momentum transfer. *Experimental Thermal and Fluid Science* **15**, 109-124.

DALLARD, T., BROWAND, F. K. 1993 The growth of large scales at defect sites in the plane mixing layer. *J. Fluid Mech* **247,** 339-368.

DAUBECHIES, I. 1992 *Ten Lectures on Wavelets.* Society for Industrial and Applied Mathematics.

DE GENNES, P. G. 1990 *Introduction to Polymer Dynamics.* Cambridge University Press.

DEN TOONDER, J. M. J., HULSEN, M. A., KUIKEN, G. D. C. & NIEUWSTADT, F. T. M. 1997 Drag reduction by polymer additives in a turbulent pipe flow: numerical and laboratory experiments. *J. Fluid Mech*. **337**, 193-231.

EVERSON, R. & SIROVICH, L. 1990 Wavelet analysis of the turbulent jet, *Phys. Lett,* **145**, 314-322.

FARGE, M. 1992 Wavelet transforms and their applications to turbulence. *Annual Review of Fluid Mechanics.* **24**, 395-457.

FARGE, M., PELLEGRINO, G. & SCHNEIDER, K. 2001 Coherent vortex extraction in 3D turbulent flows using orthogonal wavelets. *Phys. Rev. Lett.* **87**, 054501.

FARGE, M., SCHNEIDER, K., PELLEGRINO, G., WRAY, A. A. & ROGALLO, R. S. 2003 Coherent vortex extraction in three-dimensional homogeneous isotropic turbulence: comparison between CVS- wavelets and POD-Fourier decompositions, *Physics of Fluids* **15**, 2886-2896.

FEIN, J. A. 1998 Dolphin drag reduction: myth or magic. *Proc. of the International Symposium on Seawater Drag Reduction*, Newport, RI, 429-433.

FISH, F. E. 1991 Dolphin swimming-a review. *Mamm. Rev*. **21**, 181-195.

FISH, F. E. 1998 Imaginative solutions by marine organisms for drag reduction. *Proc. of the International Symposium on Seawater Drag Reduction*, Newport, RI, 443-452.

FONTAINE, A. A., DEUTSCH, S., BRUNGART, T. A., PETRIE, H. L. & FENSTERMACKER, M. 1999 Drag reduction by coupled systems: microbubble

injection with homogeneous polymer and surfactant solutions. *Experiments in Fluids*, **26**, 397-403.

GRAY, J. 1936 Studies of animal locomotion. *Journ. of Exp. Biol*. **13**, 192-199.

GROSSMAN, A. & MORLET, J., 1984 Decompositions of hardy functions into square-integrable wavelets of constant shape, *SIAM Journal of Mathematical Analysis*, **15**, 723-736.

GUTIERREZ TORRES, C. D. C. 2004 Modification of turbulent structure in channel flow by microbubble injection close to the wall. PhD dissertation, Texas A&M University, College Station.

HARDER, K. J. & TIEDERMAN, W. G. 1991 Drag reduction and turbulent structure in two-dimensional channel flows. *Phil. Trans. R. Soc. Lond*. *A* **336**, 19-34.

HASSAN, Y. A., BLANCHAT, T. K. & SEELEY, C. H. 1992 PIV flow visualization using particle tracking techniques. *Meas. Sci. Technol.* **3**, 633-642.

HASSAN, Y., ORTIZ-VILLAFUERTE, J., 2003 Investigation of microbubble boundary layer using particle image velocimetry. *Proc. of ASME FEDSM'03 -45639,* [CD-ROM], *4th ASME-JSME Joint Fluids Engineering Conference,* Honolulu, HI.

HUBBARD, B. B. 1996 *The World According to Wavelets.* AK Peters, Wellesley Mass.

JIMENEZ BERNAL, J. A. 2004 Microbubble drag reduction phenomenon study in a channel flow, PhD dissertation, Texas A&M University, College Station.

JORDAN, D. A., HAJJ, M. R., TIELEMAN, H. W. 1997 Characterization of turbulence scales in the atmospheric surface layer with the continuous wavelet transform. *Journal of Wind Engineering and Industrial Aerodynamics* **69-71**, 709-716.

KATO, H., MIYANAGA, M., HARAMOTO, Y. & GUIN, M. M. 1994 Frictional drag reduction by injecting bubbly water into turbulent boundary layer. *Proc. 1994 Cavitation and Gas-Liquid Flow in Fluid Machinery and Devices ASME* **190**, 185-194.

KITAGAWA, A., SUGIYAMA, K., ASHIHARA, M., HISHIDA, K. & KODAMA, Y. 2003 Measurement of turbulence modification by microbubbles causing frictional drag reduction. *Proc. of ASME FEDSM ' 03*. [CD-ROM], Honolulu, HI.

KODAMA, Y., KAKUGAWA, A., TAKAHASHI, T. & KAWASHIMA, H. 2000 Experimental study on microbubbles and their applicability to ship for skin friction reduction. *International Journal of Heat and Fluid Flow* **21**, 582-588.

KOELTZSCH, K., DINKEKACKER, A. & GRUNDMANN, R., 2002 Flow over convergent and divergent wall riblets. *Experiments in Fluids* **33**, 346-350.

LEE, S. J. & LEE, S. H. 2001 Flow field analysis of a turbulent boundary layer over a riblet surface. *Experiments in Fluids* **30**, 153-166.

LI, H. 1997a, Wavelet analysis on coherent structure dynamics in a plane turbulent jet. *Experimental Heat Transfer, Fluid Mechanics and Thermodynamics. Edizioni ETS.* PISA, 1175-1782.

LI, H. 1997b Wavelet Reynolds stress analysis of two-dimensional vortex flow. *Proc. of ASME FEDSM'97,* [CD-ROM], VANCOUVER, CANADA, 3040-3045.

LI, H. 1997c Wavelet velocity correlation analysis in a plane turbulent jet. *Proc. of the 11th Symposium on Turbulent Shear Flows*. **3**, 101-106.

LI, H. 1997d Turbulent structure analysis of a two-dimensional jet using wavelets. *Proc. of the 5th Triennial International Symposium on Fluid Control Measurement and Visualization*, 589-594.

LI, H. & NOZAKI, T. 1995 Wavelet analysis for the plane turbulent jet (analysis of large eddy structure). *JSME International Journal, Fluids and Thermal Engineering.* **38**, 525-531.

LI, H., NOZAKI, T., TABATA, T. & OSHIGE, S., 1997 Wavelet analysis of flow structure in a bounded jet. *Proc. of International Conference on Fluid Engineering.* **2**, 589-594.

LI, H., TAKEI, M., OCHI, M., SAITO, Y. & HORII, K., 1998a Velocity correlation analysis in the near-field of a turbulent jet with help of discrete wavelet transform. *Proc. of ASME FEDSM'* 98, [CD-ROM], WASHINGTON, DC.

LI, H., TAKEI, M., OCHI, M., SAITO, Y. & HORII, K., 1998b Effect of different orthogonal wavelet basis on multiresolution image analysis of a turbulent flow. *Proc. of International Conference on Optical Technology and Image*. [CD-ROM].

Li, H. & TOMITA, Y. 1998 Wavelet analysis of gas-solid two-phase flow in a horizontal pipe. *Proceedings of the Third International Conference on Multiphase Flow*, Lyon, France, June, Paper Number 122.

LI, H., HU, H., KOBAYASHI, T., SAGA, T. & TANIGUCHI, N., 2000 Extraction of multi-scale turbulent structure from PIV results based on wavelet vector multiresolution technique. *9TH. International Symposium on Flow Visualization.* Edinburgh, UK.

LI, H., HU, H., KOBAYASHI, T., SAGA, T. & TANIGUCHI, N. 2001a Wavelet multi-resolution analysis of dual-plane stereoscopic PIV measurement results in a lobed jet. *4th International Symposium on Particle Image Velocimetry.* GÖTTINGEN, GERMANY.

LI, H., HU, H., KOBAYASHI, T., SAGA, T. & TANIGUCHI, N. 2001b Application of wavelet vector multi-resolution technique to PIV measurements. *AIAA Paper 2001-0696.*

LI, H., HU, H., KOBAYASHI, T., SAGA, T. & TANIGUCHI, N. 2002 Wavelet multi-resolution analysis of stereoscopic particle-image-velocimetry measurements in lobed jet. *AIAA Journal* **40**, 1037-1046.

LIANDRAT, J. & MORET-BAILLY, F. 1990, The wavelet transform: some application to fluid dynamics and turbulence, *European Journal of Mechanics B/Fluids*, **9**, 1-19.

LUMLEY, J. & BLOSSEY, P. 1998 Control of turbulence. *Annu. Rev. Fluid Mech.* **30,** 311-327.

MADAVAN, N. K., DEUTSCH, S., MERKLE, C. L. 1984 Reduction of turbulent skin friction by microbubbles. *Phys. Fluids* **27**, 356-363.

MADAVAN, N. K., MERKLE, C. L., DEUTSCH, S. 1985 Numerical investigations into the mechanisms of microbubble drag reduction. *Journal of Fluids Engineering* **107**, 370-377.

MCCORMICK, M. E. & BHATTACHARYYA, R. 1973 Drag reduction of a submersible hull by electrolysis. *Naval Engineering Journal,* **85**, 11-16.

MIN, T., YOO, Y. Y., CHOI, H. & JOSEPH, D. D. 2003 Drag reduction by polymer additives in a turbulent channel flow. *J. Fluid Mech*. **486**, 213-238.

MOIN, P. & KIM, J. 1997 Tackling turbulence with supercomputers. *Sci. Amer.,* **276,** 62-68.

MUZY, J., BACRY E. & ARNEODO, A. 1991 Wavelets and multifractal formalism for singular signals: application to turbulence data. *Physical Review Letters*, **67**, 3515.

PINHO, F. T. & WHITELAW, J. H. 1990 Flow of non-Newtonian fluids in a pipe. *J. Non-Newtonian Fluid Mech.* **34**, 129-144.

POLIKAR, R., GREER, M., UDPA, L. & KEINERT, F. 1997 Multiresolution wavelet analysis of ERPs for the detection of Alzheimer's disease, *Proc. of the IEEE 19th Intl. Conf. of Engineering in Medicine and Biology Society*, 1301-1304. Chicago IL.

POLIKAR, R., UDPA, L., UDPA, S. S. & TAYLOR, T. 1998 Frequency invariant classification of weld inspection signals, *IEEE Transactions on Ultrasonics, Ferroelectrics and Frequency Control,* **45**, 614-625.

PROTAS, B., SCHNEIDER, K. & FARGE, M. 2002 Geometrical alignment properties in Fourier- and wavelet-filtered statistically stationary two-dimensional turbulence. *Physical Review E* **66**, 046307.

RAFFEL, M., WILLERT, C. E. & KOMPENHANS, J. 1998 *Particle Image Velocimetry:* A *Practical Guide,* Springer.

ROSEN, M. W. & CORNFORD, N. E. 1971. Fluid friction of fish slimes. *Nature*, **234**, 49-51.

SCHLICHTHING, H. & GERSTEN, K. 2000 *Boundary Layer Theory.* Springer.

SELLIN, R.H.J. 1988 Application of polymer drag reduction to sewer flow problems. *AIAA Paper* 88-3666.

TOMS, B. A. 1977 On the early experiments on drag reduction by polymers. *Phys. Fluids* **20**, S3-S5.

TSINOBER, A. 2001 *An Informal Introduction to Turbulence.* Kluwer Academic Publishers.

UEMURA, T., YAMAMOTO, F. & OHMI, K. 1989 A high speed algorithm of image analysis for real time measurement of two-dimensional velocity distribution. *Proc. of ASME FED-85 Flow Visualization,* 129-134, NewYork.

UNTHANK, J. L., LALKA, S. G., NIXON, J. C. & SAWCHUK, A. P. 1992 Drag-reducing polymers selectively improve blood flow through arterial stenoses. *FASEB J.,* **6**, A1471.

VIDELER, J. 1992 Comparing the cost of flight: aircraft designers can still learn from nature In: W. Nachtigall (ed.): BIONA-report 8 I.Bionic-Kongress, Wiesbaden, GERMANY, 53-72.

VIRK, P. S. 1975 Drag reduction fundamentals. *AIChE Journal* **21**, 625-656.

WANG, J., LAN, S., CHEN, G. 2000 Experimental study of the turbulent boundary layer flow over riblets surface. *Fluid Dynamics Research* **27**, 217-229.

WARHOLIC, M. D. 1997 Modification of turbulent channel flow by passive and additive devices. PhD dissertation, University of Illinois, Urbana.

WARHOLIC, M. D., MASSAH, H. & HANRATTY, T. J. 1999 Influence of drag-reducing polymers on turbulence: effects of Reynolds number, concentration and mixing. *Experiments in Fluids* **27**, 461-472.

WARHOLIC, M. D., HEIST D.K., KATCHER. M. & HANRATTY T. J. 2001 A study with particle-image velocimetry of the influence of drag-reducing polymers on the structure of turbulence. *Experiments in Fluids* **31**, 474-483.

WEI, T. & WILLMARTH, W. W. 1992 Modifying turbulent structure with drag-reducing polymer additives in turbulent channel flows. *J. Fluid Mech.* **245**, 619-641.

WHITE, C. M., SOMANDEPALLI, V. S. R. & MUNGAL, M. G. 2003 The turbulence structure of drag-reduced boundary layer flow. *Experiments in Fluids* **36**, 62-69.

WOOD, R. M., 2003 Aerodynamic drag and drag reduction: energy and energy savings (Invited), *AIAA Paper 2003-209*.

YAMADA, M. & OHKITANI, K. 1990 Orthonormal wavelet expansion and its application to turbulence. *Prog. Theor. Phys.,* **83**, 819-823.

VITA

Ling Zhen was born on October 24, 1977, in China. She received a Bachelor of Science in electrical engineering from Zhejiang University in June 1999.

She received a Master of Science degree in electrical engineering from the same university in March 2002. In 2002, while attending Zhejiang University, she was selected to receive the most prestigious scholarship- the Chinese Academy of Sciences Scholarship being chosen from more than 4,000 graduate students in Zhejiang University.

In January 2003, she joined the master's program in nuclear engineering at Texas A&M University under the supervision of Dr. Hassan.

Contact Information: Nuclear Engineering Department

Texas A&M University

College Station, TX. 77843-3133

(Dr. Yassin A. Hassan)

lingzhenmiss@yahoo.com